CHIMERA STATES IN COMPLEX NETWORKS

EDITED BY: Eckehard Schöll, Anna Zakharova and Ralph G. Andrzejak
PUBLISHED IN: Frontiers in Applied Mathematics and Statistics

frontiers Research Topics

frontiers

ISSN 1664-8714
ISBN 978-2-88963-311-1
DOI 10.3389/978-2-88963-311-1

About Frontiers

Frontiers is more than just an open-access publisher of scholarly articles: it is a pioneering approach to the world of academia, radically improving the way scholarly research is managed. The grand vision of Frontiers is a world where all people have an equal opportunity to seek, share and generate knowledge. Frontiers provides immediate and permanent online open access to all its publications, but this alone is not enough to realize our grand goals.

Frontiers Journal Series

The Frontiers Journal Series is a multi-tier and interdisciplinary set of open-access, online journals, promising a paradigm shift from the current review, selection and dissemination processes in academic publishing. All Frontiers journals are driven by researchers for researchers; therefore, they constitute a service to the scholarly community. At the same time, the Frontiers Journal Series operates on a revolutionary invention, the tiered publishing system, initially addressing specific communities of scholars, and gradually climbing up to broader public understanding, thus serving the interests of the lay society, too.

Dedication to Quality

Each Frontiers article is a landmark of the highest quality, thanks to genuinely collaborative interactions between authors and review editors, who include some of the world's best academicians. Research must be certified by peers before entering a stream of knowledge that may eventually reach the public - and shape society; therefore, Frontiers only applies the most rigorous and unbiased reviews.
Frontiers revolutionizes research publishing by freely delivering the most outstanding research, evaluated with no bias from both the academic and social point of view. By applying the most advanced information technologies, Frontiers is catapulting scholarly publishing into a new generation.

What are Frontiers Research Topics?

Frontiers Research Topics are very popular trademarks of the Frontiers Journals Series: they are collections of at least ten articles, all centered on a particular subject. With their unique mix of varied contributions from Original Research to Review Articles, Frontiers Research Topics unify the most influential researchers, the latest key findings and historical advances in a hot research area! Find out more on how to host your own Frontiers Research Topic or contribute to one as an author by contacting the Frontiers Editorial Office: researchtopics@frontiersin.org

CHIMERA STATES IN COMPLEX NETWORKS

Topic Editors:
Eckehard Schöll, Technische Universität Berlin, Germany
Anna Zakharova, Technische Universität Berlin, Germany
Ralph G. Andrzejak, Universitat Pompeu Fabra Barcelona, Spain

Citation: Schöll, E., Zakharova, A., Andrzejak, R. G., eds. (2020). Chimera States in Complex Networks. Lausanne: Frontiers Media SA. doi: 10.3389/978-2-88963-311-1

Table of Contents

frontiers in Applied Mathematics and Statistics

EDITORIAL
published: 29 November 2019
doi: 10.3389/fams.2019.00062

Editorial: Chimera States in Complex Networks

Eckehard Schöll[1], *Anna Zakharova*[1] *and Ralph G. Andrzejak*[2]*

[1] *Institut für Theoretische Physik, Technische Universität Berlin, Berlin, Germany,* [2] *Department of Information and Communication Technologies, Universitat Pompeu Fabra, Barcelona, Spain*

Keywords: chimera states, networks, synchronization, multilayer network, complex

Editorial on the Research Topic

Chimera States in Complex Networks

Dynamics of complex networks is a central issue in non-linear science with applications to different fields ranging from natural to technological and socio-economic systems. The interplay of non-linear dynamics, network topology, naturally arising delays, and random fluctuations results in a plethora of spatio-temporal synchronization patterns. Chimera states in dynamical networks consist of coexisting domains of spatially coherent (synchronized) and incoherent (desynchronized) behavior. They are a manifestation of spontaneous symmetry-breaking in systems of identical oscillators, and occur in a variety of physical, chemical, biological, neuronal, ecological, technological, or socio-economic systems.

In this Research Topic, we focus on recent developments with future promising perspectives, for instance, chimera patterns in small networks, adaptive networks, complex coupling topologies like modular, fractal, or multilayer connectivity, coupled phase and amplitude dynamics, information flow in chimera states, as well as filtering and control methods for stabilizing chimera states.

In particular, multilayer networks where the nodes are distributed in different layers offer better representation of the topology and dynamics of real-world systems in comparison with one-layer structures. One of the most promising applications of the multilayer approach is the study of the brain, where the neurons can form different layers depending on their connectivity through chemical or electrical synapses, or technological interdependent systems, i.e., those systems in which the correct functioning of one of them strongly depends on the status of the others. For instance, multilayer networks with interconnected layers naturally occur in transportation systems and electrical power grids. The intriguing dynamics of multiplex networks includes relay synchronization and partial synchronization patterns like chimera states.

The articles in this Research Topic are grouped such that we start from theoretical aspects and methods, and then proceed to various applications in physics, chemistry, neurosciences, ecology, and social dynamics. The first six articles focus on theoretical advances. Deschle et al. quantify the directed flow of information within and between two coupled subpopulations of a phase oscillator network in a chimera state. For this purpose they apply the delayed mutual information to the time points at which the individual phases pass through their respective Poincaré sections. The authors report on a functional flow of information from the desynchronized to the synchronized subpopulation of the phase oscillator network. Banerjee et al. study amplitude chimeras, which are distinct from conventional phase chimeras, since the coexistence of coherent and incoherent domains here refers not to the correlation of the oscillator phases, but of their amplitudes: all the oscillators have the same phase velocity, however, the oscillators in the incoherent domain show periodic oscillations with randomly shifted origin. The authors investigate the effect of local low-pass or all-pass filtering in the coupling path, and show that filtering can suppress amplitude chimeras and give rise to global synchrony, in a generic model of Stuart-Landau oscillators.

OPEN ACCESS

Edited and reviewed by:
Axel Hutt,
German Weather Service, Germany

Correspondence:
Ralph G. Andrzejak
ralph.andrzejak@upf.edu

Specialty section:
This article was submitted to Dynamical Systems, a section of the journal Frontiers in Applied Mathematics and Statistics

Received: *07 November 2019*
Accepted: *15 November 2019*
Published: *29 November 2019*

Citation:
Schöll E, Zakharova A and Andrzejak RG (2019) Editorial: Chimera States in Complex Networks. Front. Appl. Math. Stat. 5:62. doi: 10.3389/fams.2019.00062

The paper by Sathiyadevi et al. investigates imperfect amplitude mediated chimeras and shows that these states occur due to competing attractive and repulsive interactions in non-locally coupled networks of Stuart-Landau oscillators. The distinctive feature of these patterns is that the oscillators constituting the synchronized and desynchronized groups drift randomly in time between the homogeneous and inhomogeneous regimes. The authors demonstrate the robustness of the observed amplitude mediated chimera state against Gaussian white noise. Dmitrichev et al. study the mechanism of chimera state cloning in a large two-layer multiplex network of coupled relaxation oscillators with short-term interactions. In more detail, for certain values of strength and time of multiplex coupling, in the initially disordered layer, the authors detect a chimera state with the same characteristics, like the chimera which has been set in the other layer. The authors show that the cloning is not related to synchronization, but arises from the competition of oscillations in pairs of elements from different layers. Sawicki et al. explore chimera states in a three-layer network of FitzHugh-Nagumo oscillators, where each layer represents a non-locally coupled ring. In particular, the role of time delays introduced in both inter- and intra-layer interactions is investigated. In the parameter plane of the two delay times, the authors determine the regions where chimera patterns occur, alternating with regimes of coherent states. It turns out that a proper choice of time delay allows for achieving the desired state of the network: chimera states or coherent patterns, full or relay inter-layer synchronization. The work of Omelchenko et al. deals with the control of chimera states in multilayer networks. In small-size networks, chimera states usually exhibit short lifetimes and erratic drifting of the spatial position of the incoherent domain. A tweezer control scheme combining both symmetric and asymmetric feedback loops can stabilize and fix the position of chimera states. Here this control method is applied to a two-layer network of Van der Pol oscillators. Tweezer control, applied to only one layer, successfully stabilizes chimera patterns in the other, uncontrolled layer.

The next seven articles feature various applications. Rode et al. apply chimera states to chemical oscillators combining numerical simulations with experiments on photo-coupled relaxation oscillators. Focusing on the case of strong interactions the authors find in chemical experiments that beyond weak coupling chimera patterns consist of different coexisting cluster states. Moreover, numerical modeling reveals that the observed cluster states result from a phase-dependent excitability that is also commonly observed in neural tissue and cardiac pacemaker cells. Ocampo-Espindola et al. investigate the formation of weak chimera states in modular networks of electrochemical oscillators. Two globally coupled populations of highly non-linear oscillators which are weakly coupled through a collective resistance are studied experimentally and numerically. The authors find very robust chimera states and conclude that they could provide a mechanism for the generation of chimeras in biological systems. The modular multilayer topology of the connectome of *C. elegans* is studied by Pournaki et al. They consider a network consisting of two synaptic (electrical and chemical) layers and one extrasynaptic (wireless) layer. Synchronization patterns and chimera-like states are investigated using metrics of synchronization based on Euclidean distances and a new method of finding clustered nodes by correlating their dynamical variables. Their findings allow them to relate the dynamics of the model neurons to biological neuronal functions such as motor activities. Argyropoulos and Provata apply chimera states to neural networks of coupled Leaky Integrate-and-Fire models. They investigate the formation of chimera states in 2D lattices with hierarchical (fractal) connectivity that has the form of a deterministic or a random Sierpinski carpet. Their findings confirm previous studies on symmetric deterministic hierarchical connectivities and extend them to slanted and random fractals. Hizanidis et al. analyze chimera states in network models of locally and non-locally coupled superconducting quantum interference devices (SQUIDs). They demonstrate numerically that for both types of coupling, chimera states as well as other spatially non-uniform states can be generated under time-dependent applied magnetic flux for appropriately chosen initial conditions. Furthermore, chimera states can be achieved in the presence of a constant (DC) flux gradient with the SQUID meta-material initially at rest. Saha et al. apply chimera states to an ecological network. The population dynamics of different species, dispersed in patches and connected by weighted mean-field diffusion, is described by a modified Rosenzweig-MacArthur predator-prey model. Various complex population patterns emerge, namely multicluster and chimera states, besides synchrony and homogeneous steady states. Lugo et al. study chimera states in learning dynamics. An agent-based two-layer model of the social dynamics in which the state of the agents corresponds to one of two possible strategies is used to find new configurations which do not exist in a single isolated social network. They include chimera states in which two different collective states coexist in the network, namely, one with full coordination and one with coexistence of strategies.

AUTHOR CONTRIBUTIONS

This editorial was written by ES, AZ, and RA.

Conflict of Interest: The authors declare that the research was conducted in the absence of any commercial or financial relationships that could be construed as a potential conflict of interest.

frontiers in Applied Mathematics and Statistics

ORIGINAL RESEARCH
published: 25 June 2019
doi: 10.3389/fams.2019.00028

Directed Flow of Information in Chimera States

Nicolás Deschle[1,2]*, *Andreas Daffertshofer*[1]*, *Demian Battaglia*[3] and *Erik A. Martens*[4,5]*

[1] Faculty of Behavioural and Movement Sciences, Amsterdam Movement Sciences and Institute for Brain and Behavior Amsterdam, Vrije Universiteit Amsterdam, Amsterdam, Netherlands, [2] Institute for Complex Systems and Mathematical Biology, University of Aberdeen, King's College, Aberdeen, United Kingdom, [3] Institute for Systems Neuroscience, University Aix-Marseille, Marseille, France, [4] Department of Applied Mathematics and Computer Science, Technical University of Denmark, Kongens Lyngby, Denmark, [5] Department of Biomedical Sciences, University of Copenhagen, Copenhagen, Denmark

We investigated interactions within chimera states in a phase oscillator network with two coupled subpopulations. To quantify interactions within and between these subpopulations, we estimated the corresponding (delayed) mutual information that—in general—quantifies the capacity or the maximum rate at which information can be transferred to recover a sender's information at the receiver with a vanishingly low error probability. After verifying their equivalence with estimates based on the continuous phase data, we determined the mutual information using the time points at which the individual phases passed through their respective Poincaré sections. This stroboscopic view on the dynamics may resemble, e.g., neural spike times, that are common observables in the study of neuronal information transfer. This discretization also increased processing speed significantly, rendering it particularly suitable for a fine-grained analysis of the effects of experimental and model parameters. In our model, the delayed mutual information within each subpopulation peaked at zero delay, whereas between the subpopulations it was always maximal at non-zero delay, irrespective of parameter choices. We observed that the delayed mutual information of the desynchronized subpopulation preceded the synchronized subpopulation. Put differently, the oscillators of the desynchronized subpopulation were "driving" the ones in the synchronized subpopulation. These findings were also observed when estimating mutual information of the full phase trajectories. We can thus conclude that the delayed mutual information of discrete time points allows for inferring a *functional* directed flow of information between subpopulations of coupled phase oscillators.

Keywords: chimera states, phase oscillators, coupled networks, mutual information, information flow

OPEN ACCESS

Edited by:
Ralph G. Andrzejak,
Universitat Pompeu Fabra, Spain

Reviewed by:
Jan Sieber,
University of Exeter, United Kingdom
Hiromichi Suetani,
Oita University, Japan

***Correspondence:**
Nicolás Deschle
n.deschle@vu.nl
Andreas Daffertshofer
a.daffertshofer@vu.nl
Erik A. Martens
eama@dtu.dk

Specialty section:
This article was submitted to Dynamical Systems, a section of the journal Frontiers in Applied Mathematics and Statistics

Received: *15 December 2018*
Accepted: *21 May 2019*
Published: *25 June 2019*

Citation:
Deschle N, Daffertshofer A, Battaglia D and Martens EA (2019) Directed Flow of Information in Chimera States. Front. Appl. Math. Stat. 5:28. doi: 10.3389/fams.2019.00028

1. INTRODUCTION

Oscillatory units are found in a spectacular variety of systems in nature and technology. Examples in biology include flashing fireflies [1], cardiac pacemaker cells [2–6], and neurons [7–11]; in physics one may think of Josephson junctions [12–14], electric power grids [15–21], and, of course, pendulum clocks [22]. Synchronization plays an important role in the collective behavior of and the communication between individual units [23–25]. In the last two decades or so, many studies addressed the problem of synchronization in networks with complex structure, such as networks of networks, hierarchical networks and multilayer networks [26–29]. Alongside efforts

studying synchronization on networks, a new symmetry breaking regime coined *chimera state* has been observed. In a chimera state an oscillator population "splits" into two parts, one being synchronized and the other being desynchronized [30–32], or more generally, different levels of synchronization [33]. This state is a striking manifestation of symmetry breaking, as it may occur even if oscillators are identical and coupled symmetrically; see [34, 35] for recent reviews. Chimera states have spurred much interest resulting in many theoretical investigations, but they have also been demonstrated in experimental settings using, e.g., mechanical and (electro-)chemical oscillators or lasers [36–39], and electronic circuits implementing FitzHugh-Nagumo neurons [40].

Chimera states can be considered patterns of localized synchronization. As such they may contribute to the coding of information in a network. This is particularly interesting since systems with chimera states typically display multi-stability, i.e., different chimera configurations may co-exist for identical parameters [41–44]. Such a network may hence be able to encode different stimuli through different chimera states without the need for adjusting parameters or altering network structure. It is even possible to dynamically switch between different synchronization patterns, thus allowing for dynamic coding of information [45, 46].

The mere existence of different levels of synchronization in the same network can also facilitate the transfer of information across a network, especially between subpopulations. Coherent oscillations between neurons or neural populations have been hypothesized to provide a communication mechanism while full neural synchronization is usually considered pathological [24, 47, 48]. A recent study reported chimera-like states in neuronal networks in humans, more specifically in electro-encephalographic patterns during epileptic seizures [49]. Admittedly, our understanding of these mechanism is still in its infancy also because the (interpretations of) experimental studies often lack mathematical rigor, both regarding the description of synchronization processes and the resulting implications for the network's capacity for information processing. *What is the information transfer within and between synchronized and desynchronized populations?* We investigated the communication channels between two subpopulations in a system of coupled phase oscillators. Since we designed that system to exhibit chimera states, we expected non-trivial interactions between the subpopulations. To tackle this, we employed the delayed version of mutual information which measures the rate at which information can be sent and recovered with vanishingly low probability of error [50]. Furthermore, assuming symmetry of our configuration, any directionality found in the system should be regarded of functional nature. With this we sought not only to answer the aforementioned question but to contribute to a more general understanding of how information can be transferred between subpopulations of oscillators. In view of potential applicability in other (experimental) studies, we also investigated whether we could gain sufficient insight into this communication by looking at the passage times through the oscillators' Poincaré sections rather than evaluating the corresponding continuous-time data. Such data may resemble, e.g., spike trains in neurophysiological assessments.

Our paper is structured as follows. First, we introduce our model in the study of chimera states [32, 51–53]. It consists of two subpopulations that either can be synchronized or desynchronized. We generalize this model by including distributed coupling strengths among the oscillatory units as well as additive Gaussian white noise. We briefly sketch the conditions under which chimera states can exist. Second, we outline the concept of *delayed* mutual information and detail how to estimate this for "event-based" data where we define events via Poincaré sections of the phase oscillators' trajectories. With this tool at hand, we finally investigate the flow of information within and between the two subpopulations, and characterize its dependency on the essential model parameters.

2. MODEL

We build on a variant of the noisy Kuramoto-Sakaguchi model [54], generalized to M subpopulations of phase oscillators [55]. The phase $\phi_{j,\mu}(t)$ of oscillator $j = 1,\ldots,N$ in population $\mu = 1,\ldots,M$ evolves according to

$$d\phi_{j,\mu}(t) = \left[\omega_{j,\mu} + \sum_{\nu=1}^{M}\sum_{k=1}^{N_\mu} C_{\mathrm{jk},\mu\nu}\sin\left(\phi_{k,\nu}(t) - \phi_{j,\mu}(t) - \alpha_{\mu\nu}\right)\right]dt + dW_{j,\mu}(t), \tag{1}$$

where $\omega_{j,\mu}$ is the natural frequency of the oscillator j in subpopulation μ. Throughout our study $\omega_{j,\mu}$ is drawn from a zero-centered Gaussian distribution with variance σ_ω^2. Oscillator j in population μ and oscillator k in population ν interact sinusoidally with coupling strength $C_{\mathrm{jk},\mu\nu}$ and a phase lag α. The phase lag α varies the interaction function between more cosine ($\alpha \to \pi/2$) or more sine like-behavior ($\alpha \to 0$) and can be interpreted as a (small) transmission delay between units [34]. The additive noise term $dW_{j,\mu}(t)$ represents mean-centered Gaussian noise with variance (strength) σ_W^2, i.e., $\langle dW_{j,\mu}(t)dW_{k,\nu}(t')\rangle_t = \sigma_W^2\delta_{jk}\delta_{\mu\nu}\delta(t-t')$.

For the sake of legibility, we restrict this model to the case of $M = 2$ subpopulations of equal size $N_1 = N_2 = N$, as illustrated in **Figure 1A**. In the absence of noise and in the case of identical oscillators, uniform phase lag and homogeneous coupling, i.e., for $\sigma_W = 0$, $\sigma_\omega = 0$, $\alpha_{\mu\nu} \coloneqq \alpha$, and $\sigma_C = 0$, respectively, the aforementioned studies establishes corresponding bifurcation diagrams [32, 51, 52].

To generalize the model toward more realistic, experimental setting, we included distributed coupling strengths via a non-uniform, (statistically) symmetric coupling between subpopulations. This can be cast in the following coupling matrix:

$$C = \frac{1}{N}\begin{pmatrix} C_\zeta & C_\eta \\ C_\eta & C_\zeta \end{pmatrix} \in \mathbb{R}^{2N\times 2N} \tag{2}$$

with block matrices $C_\zeta, C_\eta \in R^{N\times N}$. The self-coupling within the subpopulation and the neighbor coupling between

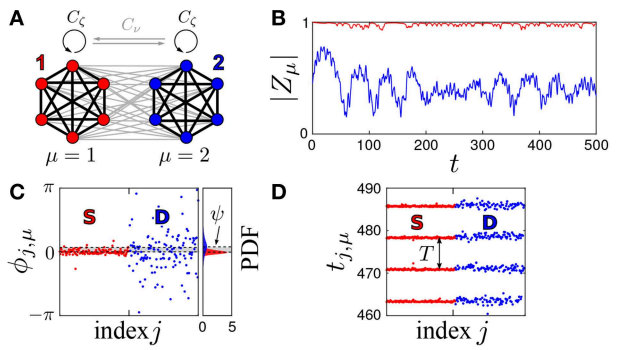

FIGURE 1 | (A) Chimera state in a network with $M = 2$ oscillator subpopulations and non-uniform coupling, simulated using Equation (1). **(B)** The time evolution of the order parameter, $|Z_\mu(t)|$, $\mu = 1, 2$, reflects the fluctuations driven by the coupling and the external field. Despite temporary deviations off the synchronization manifold $|Z_1| = 1$, the system remains near the chimera state attractor. That is, chimera states appear robust to both coupling heterogeneity and additive noise. Considering the time-average of the order parameters, the state may be classified as a stable chimera. **(C)** Snapshot in time of the phases $\phi_{j,\mu}(t)$. The probability density distributions (PDF) of the phases reveal a phase shift between subpopulations 1 and 2, given by $\psi := \arg(Z_2/Z_1)$, which remains on average constant in time, $\psi = 0.26$. **(D)** Times $t'_{j,\mu}$ correspond to the Poincaré sections of the phases i.e., $t'_{j,\mu}$ such that $\phi_j(t'_{j,\mu}) = 0$. The time period of collective oscillation is defined as $T := 1/\Omega$ and $\Omega := \langle\langle \frac{d\phi}{dt} \rangle_t\rangle_j$ where $\langle\cdot\rangle_t$ and $\langle\cdot\rangle_j$ denote averages over time and oscillators, respectively. Parameters are: $A = 0.275$, $\beta = 0.125$, $\sigma_C = 0.01$, $\sigma_\omega = 0.01$, $\sigma_W^2 = 0.001$.

subpopulations are represented by C_ζ and C_η, respectively. Each block C_ζ (or C_η) is composed of random numbers drawn from a normal distribution with mean ζ (or η) and variance σ_C^2. By this, we can tune the heterogeneity in the network. We would like to note that, in general, the chosen coupling is only symmetric for $\sigma_C > 0$ in the sense of a statistical average, and that the expected coupling values ζ and η in each block only can be retrieved by the mean in the limit of large numbers. Although the symmetry between the two subpopulations $1 \leftrightarrow 2$ is broken and only preserved in a statistical sense in the limit of large numbers, we verified that chimera states appeared in both configurations. That is, subpopulation 1 is synchronized and subpopulation 2 is desynchronized (SD) and subpopulation 2 is synchronized and subpopulation 1 is desynchronized (DS), for a particular choice of parameters using numerical simulations. Another consequence of distributed coupling strengths is that only a very few oscillators may have experienced negative (inhibitory) coupling, which can be neglected.

Following Abrams et al. [51], we parametrize the relation between strengths by $A = \zeta - \eta$ with $\zeta + \eta = 1$ and the phase lag $\alpha_{\mu,\nu}$ by $\beta_{\mu,\nu} = \frac{\pi}{2} - \alpha_{\mu,\nu}$ which here can be kept homogeneous for the entire network, i.e., $\beta_{\mu,\nu} := \beta$. By this, we may recover the results reported in Montbrió et al. [32] and Abrams et al. [51], in the limit $\sigma_C \to 0$, under the proviso of $\sigma_W = \sigma_\omega = 0$. In brief, increasing A from 0 while fixing α (or $\beta := \pi/2 - \alpha$) yields the following bifurcation scheme: a "stable chimera" is born through a saddle-node bifurcation and becomes unstable in a supercritical Hopf bifurcation with a stable limit cycle corresponding to a "breathing chimera," which eventually is destroyed in a homoclinic bifurcation. For all parameter values, the fully synchronized state exists and is a stable attractor; see also **Figure A1**. Subsequent studies demonstrated robustness of chimera states against non-uniformity of delays ($\alpha_{\mu\nu} \neq \alpha$) [33], heterogeneity of oscillator frequencies ($\sigma_\omega > 0$) [56], and additive noise [57]. Although non-uniform phase lags lead to less degenerate dynamics and give room for more complex dynamics [33, 53], we restrict ourselves to the case of uniform phase lags without compromising the essential phenomenology of chimera states.

The macroscopic behavior, i.e., the synchronization of the two populations, may be characterized by complex-valued order parameters, which are either defined on the population level, i.e., $Z_\mu := N^{-1}\sum_{j=1}^{N} e^{i\theta_{\mu,j}}$, or globally, i.e., $Z = (2N)^{-1}\sum_{\mu=1}^{M}\sum_{j=1}^{N} e^{i\theta_{\mu,j}}$. As common in the studies of coupled phase oscillators, the level of synchrony can be given by $R_\mu := |Z_\mu|$. Thus, $R_\mu = 1$ implies that oscillators in population μ are perfectly phase synchronized (S), while for $R_\mu < 1$ the oscillators are imperfectly synchronized or de-synchronized (D). For our two-subpopulation case, full synchrony (SS) hence occurs when $R_1 \lessapprox 1$ and $R_2 \lessapprox 1$, and chimera states are present if $R_1 < 1$ and $R_2 \lessapprox 1$ or vice versa. The angular order parameter, $\Phi_\mu := \arg Z_\mu$ keeps track of the average phase of the (sub)population. Fluctuations inherent to the model may affect the order parameter as illustrated in **Figure 1B** (please refer to section 3.1 for the numerical specifications). We therefore always considered averages over time, $\langle R_\mu\rangle_t$, when discussing the stability of a state. In fact, in our model chimera states remain stable for relatively large coupling heterogeneity, $\sigma_C > 0$ presuming $\sigma_\omega > 0$ and $\sigma_W > 0$, as is evidenced by numerical simulations; see also **Figure A1**. The perfect synchronization manifold with $R = 1$ cannot be achieved; see **Figure 1B**. Further aspects of these noisy dynamics will be presented elsewhere.

Adding noise and heterogeneity to the system may alter its dynamics. In the present work we concentrated on parameter regions characterized by the occurrence of dynamic states that did resemble stable chimeras, i.e., $\langle R_1\rangle_t > \langle R_2\rangle_t$, where $\langle\cdot\rangle_t$ denotes the average over a duration of $T = 9 \cdot 10^6$ time steps (after removing a transient of $T = 10^5$ time steps). **Figure A1** provides an overview and explanation of how parameter points A and β were selected.

3. IMPLEMENTATION AND ANALYSIS

3.1. Simulations

For the numerical implementation we employed a Euler-Maruyama scheme with $\Delta t = 10^{-2}$ for $N = 128$ phase oscillators per subpopulation that were evolved for $T = 10^6$ [54]. We varied the coupling parameter A and the phase lag parameter β, while we fixed the width (standard deviation) of the natural frequency distribution to $\sigma_\omega = 0.01$ and of the coupling distribution to $\sigma_C = 0.01$. The additive noise had variance $\sigma_W^2 = 0.001$.

3.2. Mutual Information

Mutual information $I(X; Y)$, first introduced by Shannon and Weaver [58], is meant to assess the dependence between two random variables X and Y. It measures the amount of

information that X contains about Y. In terms of communication theory, Y can be regarded as output of a *communication channel* which depends probabilistically on its input, X. By construction, $I(X;Y)$ is non-negative; it is equal to zero if and only if X and Y are independent. Moreover, $I(X;Y)$ is symmetric, i.e., $I(X;Y) = I(Y;X)$ implying that it is not directional. The mutual information may also be considered as a measure of the reduction in the uncertainty of X(Y) due to the knowledge of Y(X) or, in terms of communication, the rate at which information is being shared between the two [50]. The maximum rate at which one can send information over the channel and recover it at the output with a vanishingly low probability of error is called *channel capacity*, $c = \max_{p(x)} I(X;Y)$. In networks with oscillatory nodes, the random variables are the degree of synchronization of different subpopulations, and the rate of information shared will depend on the state of the system for each of the subpopulations.

Mutual information can be defined via the Kullback-Leibler divergence or in terms of entropies,

$$\begin{aligned} I(X;Y) &= H(X) - H(X|Y) \\ &= H(X) + H(Y) - H(X,Y). \end{aligned} \tag{3}$$

where $H(X)$ is the entropy of the random variable X, i.e., $H(X) = -\int dx\ p_X(x)\log p_X(x)$ with $p_X(x)$ being the corresponding probability density.

3.3. Delayed Mutual Information

For time-dependent random variables, one may generalize this definition to that of a *delayed mutual information*. This variant dates back to Fraser and Swinney [59], who used the delayed mutual information for estimating the embedding delay in chaotic systems—in that context the delayed *auto*-mutual information is often considered a "generalization" of the auto-correlation function [60]. Applications range from the study of coupled map lattices [61] via spatiotemporal [62] and general dependencies between time series [63] to the detection of synchronization [64]. With the notation $I_{XY} := I(X;Y)$ and $H_X := H(X)$, the delayed mutual information for a delay τ may read

$$\begin{aligned} I_{XY}(\tau) &= I(X(t);Y(t+\tau)) \\ &= H_X + H_Y - H_{XY}(\tau) \end{aligned} \tag{4}$$

which has the symmetry $I_{XY}(\tau) = I_{YX}(-\tau)$[1]. With this definition, one can measure the rate of information shared between X and Y as a function of time delay τ. In fact, we are not particularly interested in the specific value of the mutual information but rather focus here on the time delay at which the mutual information is maximal. Hence, we define $\tau_{\max} := \arg\max_\tau I_{XY}(\tau)$. A positive (negative) value of $\tau_{\max}$ implies that Y shares more information with a delayed (advanced) X. This means there is an information flow from X(Y) to Y(X).

[1]This follows because of: $I_{XY}(\tau) = I\big(X(t);Y(t+\tau)\big) = I\big(X(t-\tau);Y(t)\big) = I\big(Y(t);X(t-\tau)\big) = I_{YX}(-\tau)$.

3.4. Delayed Mutual Information Between Subpopulations

3.4.1. Estimates Using Continuous-Time Data

When the time-dependent random variables are continuous time series $u_\mu(t)$ and $u_\nu(t)$ associated to populations μ and ν, the delayed mutual information can be estimated from Equation (4) for $X(t) = u_\mu(t)$ and $Y(t) = u_\nu(t)$,

$$\tilde{I}_{\mu\nu}(\tau) = \tilde{I}\left(u_\mu(t);u_\nu(t+\tau)\right). \tag{5}$$

We determined the probability densities using kernel density estimators with Epanetchnikov kernels with bandwidths given through a uniform maximum likelihood cross-validation search. For our parameter settings (254 oscillators and 10^6 samples), the resulting bandwidths ranged from about 0.10 to 0.18 rad. This software implementation is part of the KDE-toolbox; cf. [65] and Thomas et al. [66] for alternative schemes.

3.4.2. Estimates Using Event-Based Time Data

For the aforementioned event signals in the subpopulations 1 and 2, i.e., discrete time points are defined as passing moments through the respective Poincaré sections. The probability densities to incorporate when estimating the mutual information are densities of events, or densities of times. We implemented the probability estimates as follows. Let S_μ be a set of event times, i.e., $S_\mu = \{t_{\mu,1}^{(m)},\ldots,t_{\mu,N_\mu}^{(m')}\}$ where $t_{\mu,i}^{(m)}$ stands for the time of the m-th event of oscillator i in subpopulation μ. Then, the probability density for an event to happen at time t in subpopulation μ is $p_\mu(t) = P(t \in S_\mu)$ and the probability of an event to happen at time t in subpopulation μ and time $t+\tau$ in subpopulation ν is

$$\begin{aligned} p_{\mu\nu}(t,t+\tau) &= P\left(\left\{t \in S_\mu\right\} \cap \{t+\tau \in S_\nu\}\right) \\ &= P\left(t \in S_\mu\right) + P\left(t+\tau \in S_\nu\right) \\ &\quad - P\left(\left\{t \in S_\mu\right\} \cup \{t+\tau \in S_\nu\}\right). \end{aligned} \tag{6}$$

The delayed mutual information can be given as

$$\begin{aligned} I_{\mu\nu}(\tau) &= \int dt\, p_{\mu\nu}(t,t+\tau)\log\frac{p_{\mu\nu}(t,t+\tau)}{p_\mu(t)p_\nu(t)} \\ &= H_\mu + H_\nu - H_{\mu\nu}(\tau). \end{aligned} \tag{7}$$

We again computed the probability densities using kernel density estimators [65] but now involving Gaussian kernels. We also adjusted the bandwidth selection to a spherical, local maximum likelihood cross-validation due to the sparsity of the data and the resulting bandwidths ranged from about 25 to 35 time units. These results appeared robust when using the aforementioned uniform search; again we employed the KDE-toolbox.

3.5. Events Defined Via Poincaré Sections

We analyzed the times $t_{1,\mu}, t_{2,\mu}, \ldots t_{N,\mu}$ at which the individual phases $\phi(t)_{j,\mu}$ passed through their respective Poincaré sections. The latter were defined as $t_{j,\mu} \in \mathbb{R}_0^+ : \phi_{j,\mu}(t_{j,\mu})/2\pi \in \mathbb{Z}$. As mentioned above, every subpopulation μ generated an "event sequence" $S_\mu = \{t_{\mu,1}^{(m)},\ldots,t_{\mu,N_\mu}^{(m')}\}$; which, as already said, may be considered reminiscent of spike trains; cf. **Figure 1C**.

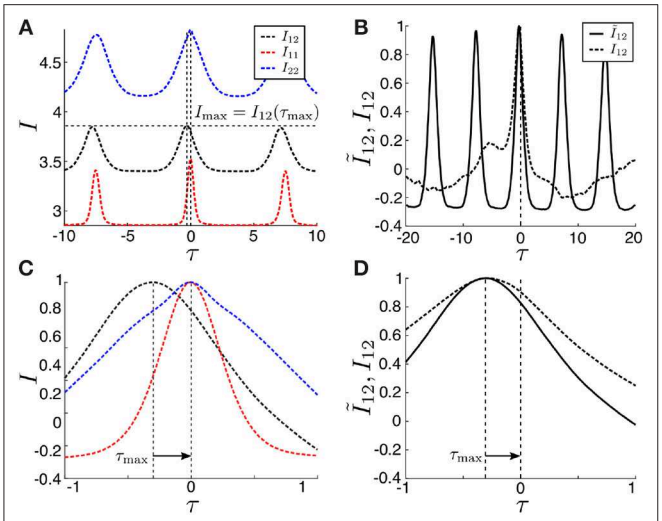

FIGURE 2 | (A) Mutual informations $I_{\mu\nu}$ as a function of τ between and within the two subpopulations μ and ν. **(C)** The range-zoomed curve reveals a directionality in the mutual information $I_{12}(\tau)$ between the two subpopulations 1 and 2, with a maximum peak $I_{\max} \coloneqq I_{12}(\tau_{\max})$ located at $\tau_{\max} < 0$. **(B,D)** Comparison of the average mutual information obtained from continuous time data (solid), $\tilde{I}_{12}$, vs. event time data (dotted), I_{12}. Obviously, locations of the peaks agree very well. **(B–D)** display the average mutual information $(I - \langle I \rangle_t)/\max_t (I - \langle I \rangle_t)$ with $\langle I \rangle_t$ denoting the average over time after discarding a transient (see text for details). Parameters across panels are $A = 0.275$, $\beta = 0.125$, $\sigma_\omega = 0.01$, $\sigma_C = 0.01$, $\sigma_W^2 = 0.001$.

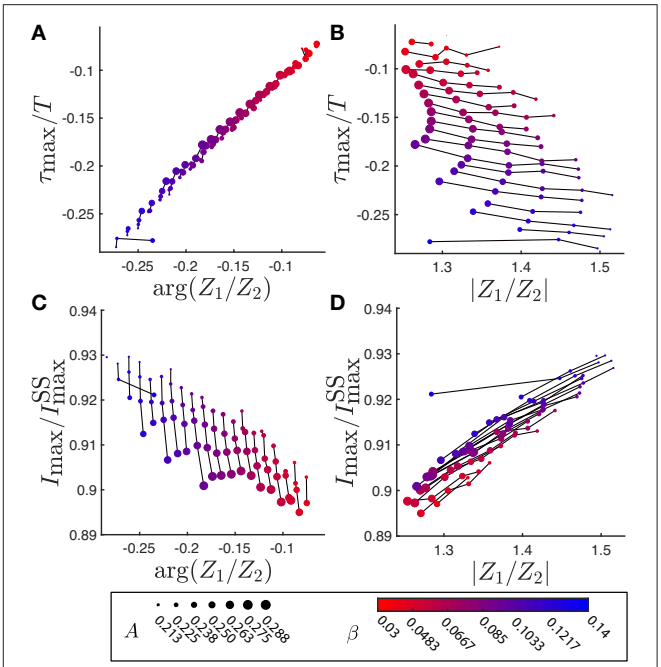

FIGURE 3 | Dependency of ($I_{\max}$, $\nu_{\max}$) on the synchronization level and on the parameters β and A. **(A)** The maximizing time delay $\tau_{\max}$ has a nearly linear dependency on the angular phase difference of order parameters $\arg(Z_1/Z_2)$. **(B)** $\tau_{\max}$ appears largely independent of the ratio of the magnitude of order parameters $|Z_1/Z_2|$, though results are weakly dependent on β. **(C,D)** The normalized maximum peak of mutual information I_{max}/I_{max}^{SS} shows a weak dependency on the ratio of order parameters. All other parameters are fixed at $\sigma_\omega = 0.01, \sigma_C = 0.01, \sigma_W^2 = 0.001$.

4. RESULTS

To determine the directionality of the information flow in the network we computed the time lagged mutual information within the subpopulations, $I_{11}(\tau)$ and $I_{22}(\tau)$ and between them, $I_{12}(\tau) = I_{21}(-\tau)$.

The first results for the event data outlined in section 3.5 are shown in **Figure 2A**. Since the recurrence of events mimicked the mean frequency of the phase oscillators, the mutual information turned out periodic. As expected, we observed (average) values of the mutual information that differed between I_{11} (red), I_{22} (blue), I_{12} (black). This relates to the difference in entropy of the subpopulations, with the less synchronized one ($\mu = 2$) being more disordered. The latter, hence, contained more entropy. However, since we were not interested in the explicit values of $I_{\mu\nu}(\tau)$, we could rescale the mutual information to maximum value which allowed for a comparative view when zooming in to the neighborhood of $\tau \approx 0$; see **Figure 2C**. The off-zero peak of $I_{\max} \coloneqq I_{12}(\tau_{\max})$ in $\tau = \tau_{\max}$ clearly indicated a directed information flow, i.e., there is a *functional directionality despite the structural symmetry* of our model.

When comparing the estimates for the mutual information obtained from the event data, I, with those from the continuous-time, $\tilde{I}$, we found little to no difference in peak location. That is, the positions $\tau_{\max}$ of the maximum peaks, $\tilde{I}_{\max}$ and $I_{\max}$, were nearly identical using either method as shown in **Figures 2B,D**. Thus, to study the effects of varying model parameters on $I_{\mu\nu}(\tau)$, our subsequent analysis may solely rely on the event data approach.

Varying the values of A and β revealed a strong relation between the location of the peak of the delayed mutual information $\tau_{\max}$ and the relative phase $\arg(Z_1/Z_2)$ between the two subpopulations; see **Figure 3A**. This convincingly shows that our approach to analyze the event-based data reveals important information about the (otherwise continuous) dynamics of the subpopulations, here given by the phases (arguments) of the local order parameters. By contrast, the relative strength of local synchronization $|Z_1/Z_2|$ had little to no effect on $\tau_{\max}$; see **Figure 3B**. These dependencies were inverted when looking at the value of mutual information, I_{max}/I_{max}^{SS}; see **Figures 3C,D**. Consequently, the value of mutual information was affected by relative strength of local synchronization $|Z_1/Z_2|$ | after all the more a subpopulation is synchronized, the lower the corresponding entropy. However, effects were small and probably negligible when transferring to (selected) experimental data. More details about the normalization factor I_{max}^{SS} are discussed in **Appendix B**.

5. DISCUSSION

The delayed mutual information from event data, here, the passing times through the oscillators' Poincaré sections, agreed with that of the continuous data. This is an important finding as it shows that studying discrete event time series

allows for inferring information-related properties of continuous dynamics. This offers the possibility to bring our approach to experimental studies, be that in neuroscience, where spike trains are a traditional measure of continuous neuronal activity, or economics, where stroboscopic assessments of stocks are common practice. Here, we used this approach to explore the information flow within and between subpopulations of a network of coupled phase oscillators. This information flow turned out to be directed.

Mutual information is the traditional measure of shared information between the two systems [58]. Our findings relied on the introduction of a time delay τ, which readily allows for identifying a direction of flow of information. This concept is much related to the widely used transfer entropy [67, 68]. In fact, transfer entropy is the delayed *conditional* mutual information [69, 70]. It therefore differs from our approach primarily by a normalization factor. Since here we were not interested in the absolute amount of information (flow), we could simplify assessments and focus on delayed mutual information | adding the conditional part jeopardizes the approximation of probabilities, i.e., estimating transfer entropy in a reliable manner typically requires more data than our delayed mutual information. A detailed discussion of these differences is beyond the scope of the current study.

For our model we found that the delayed mutual information between the synchronized subpopulation and the less synchronized one peaked at a finite delay $\tau_{\max} \neq 0$. Hence, there was a directed flow of information between the two subpopulations. Since we found that $\tau_{\max} < 0$ for $I_{12}(\tau)$, the direction of this flow was from the less synchronized subpopulation to the fully synchronized one, i.e., $2 \rightarrow 1$ or $\mathrm{D} \rightarrow \mathrm{S}$. In fact, the delay largely resembled the relative phase between the corresponding local order parameters, as shown in of **Figure 3A**. We could not only readily identify the relative phase by encountering event data only, but our approach also allowed for attaching a meaningful interpretation in an information theoretic sense. This is promising since event data are, as stated repeatedly, conventional outcome parameters in many experimental settings. This is particularly true for studies in neuroscience, for which the quest on information processing is often central. There, networks are typically complex and modular. The complex collective dynamics switches at multiple scales, rendering neuronal networks especially exciting when it comes to information routing [71]. As of yet, our approach does not allow for unraveling dynamics information routing. This will require extending the (time-lagged) mutual information to a time-dependent version, e.g., by windowing the data under study. We plan to incorporate this in future studies.

6. CONCLUSION

Estimating the delayed mutual information based on time points at which the individual phases passed through their respective Poincaré sections allows for identifying the information flow between subpopulations of networks. If the network displays chimera states, the information flow turns out to be directed. In our model of coupled phase oscillators, the flow of information was directed from the less synchronized subpopulation to the fully synchronized one since the first preceded the latter. Our approach is a first step to study information transfer between spike trains. It can be readily adopted to static well-defined modular networks and needs to be upgraded to a time dependent version to be applied to real, biological data.

AUTHOR CONTRIBUTIONS

ND conducted the simulations and analysis and wrote the manuscript. AD set up the study, incorporated the kernel density estimation and wrote the manuscript. DB contributed to the first concepts of the study and wrote the manuscript. EM set up the study, conducted simulations and wrote the manuscript.

FUNDING

This study received funding from the European Union's Horizon 2020 research and innovation program under the Marie Skłodowska-Curie grant agreement #642563 (COSMOS).

ACKNOWLEDGMENTS

ND and AD want to thank to Rok Cestnik and Bastian Pietras for fruitful discussions.

SUPPLEMENTARY MATERIAL

The Supplementary Material for this article can be found online at: https://www.frontiersin.org/articles/10.3389/fams.2019.00028/full#supplementary-material

REFERENCES

1. Ermentrout GB, Rinzel J. Beyond a pacemaker's entrainment limit: phase walk-through. *Am J Physiol-Regul Integr Compar. Physiol.* (1984) **246**:R102–6. doi: 10.1152/ajpregu.1984.246.1.R102
2. Guevara MR, Glass L, Shrier A. Phase locking, period-doubling bifurcations, and irregular dynamics in periodically stimulated cardiac cells. *Science.* (1981) **214**:1350–3. doi: 10.1126/science.7313693
3. Guevara MR, Alonso F, Jeandupeux D, Van Ginneken ACG. Alternans in periodically stimulated isolated ventricular myocytes: experiment and model. Goldbeter A. In: Faculté des Sciences, Université Libre de Bruxelles, Brussels, editor. *Cell to Cell Signalling.* New York, NY: Elsevier; Academic Press (1989). p. 551–63.
4. Glass L, Mackey MC. *From Clocks to Chaos: The Rhythms of Life.* Princeton, NJ: Princeton University Press (1988).
5. Zeng WZ, Courtemanche M, Sehn L, Shrier A, Glass L. Theoretical computation of phase locking in embryonic atrial heart cell aggregates. *J Theor Biol.* (1990) **145**:225–44. doi: 10.1016/S0022-5193(05)80128-6
6. Glass L, Shrier A. Low-dimensional dynamics in the heart. In: *Theory of Heart.* New York, NY: Springer-Verlag (1991). p. 289–312.
7. Singer W. Neurobiology: striving for coherence. *Nature.* (1999) **397**:391. doi: 10.1038/17021

8. Gray CM, König P, Engel AK, Singer W. Oscillatory responses in cat visual cortex exhibit inter-columnar synchronization which reflects global stimulus properties. *Nature*. (1989) **338**:334. doi: 10.1038/338334a0
9. MacKay WA. Synchronized neuronal oscillations and their role in motor processes. *Trends Cogn Sci*. (1997) **1**:176–83.
10. Singer W, Gray CM. Visual feature integration and the temporal correlation hypothesis. *Annu Rev Neurosci*. (1995) **18**:555–86. doi: 10.1146/annurev.ne.18.030195.003011
11. Stern EA, Jaeger D, Wilson CJ. Membrane potential synchrony of simultaneously recorded striatal spiny neurons *in vivo*. *Nature*. (1998) **394**:475. doi: 10.1038/28848
12. Jain AK, Likharev K, Lukens J, Sauvageau J. Mutual phase-locking in Josephson junction arrays. *Phys Rep*. (1984) **109**:309–426. doi: 10.1016/0370-1573(84)90002-4
13. Saitoh K, Nishino T. Phase locking in a double junction of Josephson weak links. *Phys Rev B*. (1991) **44**:7070. doi: 10.1103/PhysRevB.44.7070
14. Valkering T, Hooijer C, Kroon M. Dynamics of two capacitively coupled Josephson junctions in the overdamped limit. *Physica D Nonlinear Phenomena*. (2000) **135**:137–53. doi: 10.1016/S0167-2789(99)00116-5
15. Menck PJ, Heitzig J, Kurths J, Schellnhuber HJ. How dead ends undermine power grid stability. *Nat Commun*. (2014) **5**:3969. doi: 10.1038/ncomms4969
16. Nardelli PHJ, Rubido N, Wang C, Baptista MS, Pomalaza-Raez C, Cardieri P, et al. Models for the modern power grid. *Eur Phys J Spec Top*. (2014) **223**:2423–37. doi: 10.1140/epjst/e2014-02219-6
17. Motter AE, Myers SA, Anghel M, Nishikawa T. Spontaneous synchrony in power-grid networks. *Nat Phys*. (2013) **9**:191. doi: 10.1038/nphys2535
18. Dörfler F, Chertkov M, Bullo F. Synchronization in complex oscillator networks and smart grids. *Proc Natl Acad Sci USA*. (2013) **110**:2005–10. doi: 10.1073/pnas.1212134110
19. Lozano S, Buzna L, Díaz-Guilera A. Role of network topology in the synchronization of power systems. *Eur Phys J B*. (2012) **85**:231. doi: 10.1140/epjb/e2012-30209-9
20. Susuki Y, Mezic I. Nonlinear koopman modes and coherency identification of coupled swing dynamics. *IEEE Trans Power Syst*. (2011) **26**:1894–904. doi: 10.1109/TPWRS.2010.2103369
21. Rohden M, Sorge A, Timme M, Witthaut D. Self-organized synchronization in decentralized power grids. *Phys Rev Lett*. (2012) **109**:064101. doi: 10.1103/PhysRevLett.109.064101
22. Huygens C. *Horologium Oscillatorium Sive de Motu Pendulorum ad Horologia Aptato Demonstrationes Geometricae*. Paris: F. Muguet (1673).
23. Pikovsky A, Rosenblum M, Kurths J, Kurths J. *Synchronization: A Universal Concept in Nonlinear Sciences. Vol. 12*. Cambridge, UK: Cambridge University Press (2003).
24. Buzsaki G. *Rhythms of the Brain*. New York, NY: Oxford University Press (2006).
25. Strogatz SH. *SYNC: The Emerging Science of Spontaneous Order*. New York, NY: Hachette (2003).
26. Boccaletti S, Bianconi G, Criado R, Del Genio CI, Gómez-Gardenes J, Romance M, et al. The structure and dynamics of multilayer networks. *Phys Rep*. (2014) **544**:1–122. doi: 10.1016/j.physrep.2014.07.001
27. Arenas A, Díaz-Guilera A, Kurths J, Moreno Y, Zhou C. Synchronization in complex networks. *Phys Rep*. (2008) **469**:93–153. doi: 10.1016/j.physrep.2008.09.002
28. Kivelä M, Arenas A, Barthelemy M, Gleeson JP, Moreno Y, Porter MA. Multilayer networks. *J Complex Netw*. (2014) **2**:203–71. doi: 10.1093/comnet/cnu016
29. Rodrigues FA, Peron TKD, Ji P, Kurths J. The Kuramoto model in complex networks. *Phys. Rep*. (2016) **610**:1–98. doi: 10.1016/j.physrep.2015.10.008
30. Kuramoto Y, Battogtokh D. Coexistence of coherence and incoherence in nonlocally coupled phase oscillators. *Nonlinear Phenomena Complex Syst*. (2002) **4**:380–5. Available online at: http://www.j-npcs.org/abstracts/vol2002/v5no4/v5no4p380.html
31. Abrams DM, Strogatz SH. Chimera states for coupled oscillators. *Phys Rev Lett*. (2004) **93**:174102. doi: 10.1103/PhysRevLett.93.174102
32. Montbrió E, Kurths J, Blasius B. Synchronization of two interacting populations of oscillators. *Phys Rev E*. (2004) **70**:056125. doi: 10.1103/PhysRevE.70.056125
33. Martens EA, Bick C, Panaggio MJ. Chimera states in two populations with heterogeneous phase-lag. *Chaos*. (2016) **26**:094819. doi: 10.1063/1.4958930
34. Panaggio MJ, Abrams DM. Chimera states: coexistence of coherence and incoherence in networks of coupled oscillators. *Nonlinearity*. (2015) **28**:R67. doi: 10.1088/0951-7715/28/3/R67
35. Schöll E. Synchronization patterns and chimera states in complex networks: Interplay of topology and dynamics. *Euro Phys J Spec Top*. (2016) **225**:891–919. doi: 10.1140/epjst/e2016-02646-3
36. Martens EA, Thutupalli S, Fourriere A, Hallatschek O. Chimera states in mechanical oscillator networks. *Proc Natl Acad Sci USA*. (2013) **110**:10563–7. doi: 10.1073/pnas.1302880110
37. Tinsley MR, Nkomo S, Showalter K. Chimera and phase-cluster states in populations of coupled chemical oscillators. *Nat Phys*. (2012) **8**:1–4. doi: 10.1038/nphys2371
38. Hagerstrom AM, Murphy TE, Roy R, Hövel P, Omelchenko I, Schöll E. Experimental observation of chimeras in coupled-map lattices. *Nat Phys*. (2012) **8**:1–4. doi: 10.1038/nphys2372
39. Wickramasinghe M, Kiss IZ. Spatially organized dynamical states in chemical oscillator networks: synchronization, dynamical differentiation, and chimera patterns. *PLoS ONE*. (2013) **8**:e80586. doi: 10.1371/journal.pone.0080586
40. Gambuzza LV, Buscarino A, Chessari S, Fortuna L, Meucci R, Frasca M. Experimental investigation of chimera states with quiescent and synchronous domains in coupled electronic oscillators. *Phys Rev E*. (2014) **90**:032905. doi: 10.1103/PhysRevE.90.032905
41. Martens EA. Bistable chimera attractors on a triangular network of oscillator populations. *Phys Rev E*. (2010) **82**:016216. doi: 10.1103/PhysRevE.82.016216
42. Martens EA. Chimeras in a network of three oscillator populations with varying network topology. *Chaos*. (2010) **20**:043122. doi: 10.1063/1.3499502
43. Shanahan M. Metastable chimera states in community-structured oscillator networks. *Chaos*. (2010) **20**:013108. doi: 10.1063/1.3305451
44. Bick C. Heteroclinic switching between chimeras. *Phys Rev E*. (2018) **97**:050201. doi: 10.1103/PhysRevE.97.050201
45. Bick C, Martens EA. Controlling chimeras. *New J Phys*. (2015) **17**:033030. doi: 10.1088/1367-2630/17/3/033030
46. Martens EA, Panaggio MJ, Abrams DM. Basins of attraction for chimera states. *New J Phys*. (2016) **18**:022002. doi: 10.1088/1367-2630/18/2/022002
47. Fries P. A mechanism for cognitive dynamics: neuronal communication through neuronal coherence. *Trends Cogn Sci*. (2005) **9**:474–80. doi: 10.1016/j.tics.2005.08.011
48. Fell J, Axmacher N. The role of phase synchronization in memory processes. *Nat Rev Neurosci*. (2011) **12**:105. doi: 10.1038/nrn2979
49. Andrzejak RG, Rummel C, Mormann F, Schindler K. All together now: analogies between chimera state collapses and epileptic seizures. *Sci Rep*. (2016) **6**:23000. doi: 10.1038/srep23000
50. Cover TM, Thomas JA. *Elements of Information Theory*. New York, NY: John Wiley and Sons (2012).
51. Abrams DM, Mirollo RE, Strogatz SH, Wiley DA. Solvable model for chimera states of coupled oscillators. *Phys Rev Lett*. (2008) **101**:084103. doi: 10.1103/PhysRevLett.101.084103
52. Panaggio MJ, Abrams DM, Ashwin P, Laing CR. Chimera states in networks of phase oscillators: the case of two small populations. *Phys Rev E*. (2016) **93**:012218. doi: 10.1103/PhysRevE.93.012218
53. Bick C, Panaggio MJ, Martens EA. Chaos in Kuramoto oscillator networks. *Chaos*. (2018) **28**:071102. doi: 10.1063/1.5041444
54. Acebrón J, Bonilla L, Pérez Vicente C, et al. The Kuramoto model: a simple paradigm for synchronization phenomena. *Rev Mod Phys*. (2005) **77**:137. doi: 10.1103/RevModPhys.77.137
55. Bick C, Laing C, Goodfellow M, Martens EA. Understanding synchrony patterns in biological and neural oscillator networks through mean-field reductions: a review. *arXiv.[preprint] arXiv:1902(05307v2)*. (2019).
56. Laing CR. Chimera states in heterogeneous networks. *Chaos*. (2009) **19**:013113. doi: 10.1063/1.3068353
57. Laing CR. Disorder-induced dynamics in a pair of coupled heterogeneous phase oscillator networks. *Chaos*. (2012) **22**:043104. doi: 10.1063/1.4758814
58. Shannon CE, Weaver W. *The Mathematical Theory of Communication*. Urbana, IL: University of Illinois Press (1949).

59. Fraser AM, Swinney HL. Independent coordinates for strange attractors from mutual information. *Phys Rev A*. (1986) **33**:1134–40. doi: 10.1103/PhysRevA.33.1134
60. Abarbanel H. *Analysis of Observed Chaotic Data*. New York, NY: Springer Science and Business Media (2012).
61. Kaneko K. Lyapunov analysis and information flow in coupled map lattices.Pdf. *Physica D Nonlinear Phenomena*. (1986) **23D**:436–47. doi: 10.1016/0167-2789(86)90149-1
62. Vastano JA, Swinney HL. Information transport in spatial-temporal system. *Phys Rev Lett*. (1988) **60**:1773–6. doi: 10.1103/PhysRevLett.60.1773
63. Green ML, Savit R. Dependent variables in broad band continuous time series. *Physica D Nonlinear Phenomena*. (1991) **50**:521–44. doi: 10.1016/0167-2789(91)90013-Y
64. Paluš M. Detecting phase synchronization in noisy systems. *Phys Lett A*. (1997) **235**:341–51. doi: 10.1016/S0375-9601(97)00635-X
65. Ihler A, Mandel M. *Kernel Density Estimation (KDE) Toolbox for Matlab*. (2003). Available online at: http://www.ics.uci.edu/~ihler/code
66. Thomas RD, Moses NC, Semple EA, Strang AJ. An efficient algorithm for the computation of average mutual information: validation and implementation in Matlab. *J Math Psychol*. (2014) **61**:45–59. doi: 10.1016/j.jmp.2014.09.001
67. Schreiber T. Measuring information transfer. *Phys Rev Lett*. (2000) **85**:461. doi: 10.1103/PhysRevLett.85.461
68. Wibral M, Pampu N, Priesemann V, Siebenhühner F, Seiwert H, Lindner M, et al. Measuring information-transfer delays. *PLoS ONE*. (2013) **8**:e55809. doi: 10.1371/journal.pone.0055809
69. Dobrushin RL. A general formulation of the fundamental theorem of Shannon in the theory of information. *Uspekhi Matematicheskikh Nauk*. (1959) **14**:3–104.
70. Wyner AD. A definition of conditional mutual information for arbitrary ensembles. *Inform Control*. (1978) **38**:51–9.
71. Kirst C, Timme M, Battaglia D. Dynamic information routing in complex networks. *Nat Commun*. (2016) **7**:11061. doi: 10.1038/ncomms11061

Conflict of Interest Statement: The authors declare that the research was conducted in the absence of any commercial or financial relationships that could be construed as a potential conflict of interest.

frontiers in Applied Mathematics and Statistics

ORIGINAL RESEARCH
published: 11 February 2019
doi: 10.3389/fams.2019.00008

Filtering Suppresses Amplitude Chimeras

Tanmoy Banerjee[1]*, *Biswabibek Bandyopadhyay*[1], *Anna Zakharova*[2] and *Eckehard Schöll*[2]*

[1] Chaos and Complex Systems Research Laboratory, Department of Physics, University of Burdwan, Burdwan, India,
[2] Institut für Theoretische Physik, Technische Universität Berlin, Berlin, Germany

Amplitude chimera (AC) is an interesting chimera pattern that has been discovered recently and is distinct from other chimera patterns, like phase chimeras and amplitude mediated phase chimeras. Unlike other chimeras, in the AC pattern all the oscillators have the same phase velocity, however, the oscillators in the incoherent domain show periodic oscillations with randomly shifted origin. In this paper we investigate the effect of local filtering in the coupling path on the occurrence of AC patterns. Our study is motivated by the fact that in the practical coupling channels filtering effects come into play due to the presence of dispersion and dissipation. We show that a low-pass or all-pass filtering is actually detrimental to the occurrence of AC. We quantitatively establish that with decreasing cut-off frequency of the filter, an AC transforms into a synchronized pattern. We also show that the symmetry-breaking steady state, i.e., the oscillation death state can be revoked and rhythmogenesis can be induced by local filtering. Our study will shed light on the understanding of many biological systems where spontaneous symmetry-breaking and local filtering occur simultaneously.

Keywords: chimera, amplitude chimera, oscillation death, filtering, control, rhythmogenesis, all-pass filter

OPEN ACCESS

Edited by:
Ulrich Parlitz,
Max-Planck-Institute for Dynamics and Self-Organisation, Max Planck Society (MPG), Germany

Reviewed by:
Isao T. Tokuda,
Ritsumeikan University, Japan
Anastasiia Panchuk,
Institute of Mathematics (NAN Ukraine), Ukraine

***Correspondence:**
Tanmoy Banerjee
tbanerjee@phys.buruniv.ac.in
Eckehard Schöll
schoell@physik.tu-berlin.de

Specialty section:
This article was submitted to Dynamical Systems, a section of the journal Frontiers in Applied Mathematics and Statistics

Received: *30 November 2018*
Accepted: *24 January 2019*
Published: *11 February 2019*

Citation:
Banerjee T, Bandyopadhyay B, Zakharova A and Schöll E (2019) Filtering Suppresses Amplitude Chimeras. Front. Appl. Math. Stat. 5:8. doi: 10.3389/fams.2019.00008

1. INTRODUCTION

Networks of coupled identical oscillators show various cooperative behaviors. From the symmetry considerations they can be categorized into two broad types: (i) symmetric (or symmetry preserving) states, like synchronization, phase locking, and amplitude death (AD) state [1, 2], and (ii) symmetry-breaking states, such as oscillation death (OD) [2] and chimera states [3]. Among all these cooperative behaviors, in the center of recent research is the chimera state [4, 5] discovered by Kuramoto and Battoghtokh in 2002. Chimera is a counterintuitive spatiotemporal pattern in which coherence and incoherence coexist in a network of identical oscillators [3, 6]. In the initial years studies on chimeras focused on exploring several aspects of chimera theoretically (see two recent reviews on chimeras in [3, 6] for a detailed discussion). Later on experimental observations of chimeras established their robustness in real systems. After the first experimental evidence of chimeras in optical systems [7] and chemical oscillators [8], they have been observed experimentally in several other systems also, e.g., in mechanical systems [9, 10], electronic [11, 12], optoelectronic delayed-feedback [13–16], electrochemical [17–19] oscillator systems and Boolean networks [20]. Studies on chimeras are continuing to be a vibrant area of research owing to its connection to various natural phenomena and systems, including epileptic seizure [21], unihemispheric sleep [22, 23], ecological synchrony [24, 25], social systems [26], and quantum systems [27].

Although chimeras were discovered in phase oscillators, later on the notion was extended to the general class of oscillators having both phase as well as amplitude dynamics. Those oscillators

may show amplitude mediated phase chimeras (AMC) [28], which is the coexistence of synchrony and asynchrony in both phase and amplitude: here in the incoherent (coherent) domain oscillators have disparate (same) phase velocities. Recently, a new type of chimera has been discovered by Zakharova et al. [29] called amplitude chimera (AC), in which all the oscillators of the network are correlated in phase, however, in the incoherent domain nodes have uncorrelated amplitude. The distinct signature of an AC state is that in its coherent domain nodes oscillate around the origin and have equal amplitude, however, nodes belonging to the incoherent domain show limit cycles of disparate amplitude and those limit cycles are shifted from the origin.

In contrast to other chimera patterns, AC has strong connections to another symmetry-breaking *steady* state, namely the oscillation death state (OD) [2, 30–34]. The bridge between AC and OD is mediated by an interesting emergent spatial pattern called chimera death [29, 35], which carries the attributes of both AC and OD. Since AC is the coexistence of spatially homogeneous and inhomogeneous limit cycles, therefore, it is believed to have relevance in the underlying mechanism for cellular differentiation [36, 37] and ecological oscillations [24, 25, 38, 39] where coexistence of inhomogeneity and homogeneity appears naturally.

As amplitude chimeras are a recently discovered variant of chimera patterns, therefore, it is less explored: the effect of node dynamics and coupling on the occurrence of AC demands further investigations. Specifically, in realistic networks, where signals often suffer from time delay [40], noise, dispersion and dissipation [41], their effect on the AC pattern will be important to explore. Although, the effect of noise and time delay has recently been explored in detail in Loos et al. [42] and Gjurchinovski et al. [43], however, the effect of dispersion and dissipation on the AC state has not been studied yet. In the presence of dispersion, signals having different frequencies propagate with different velocities. Whereas, dissipation causes attenuation and signal loss. A channel having both dispersion and dissipation is said to behave like a low-pass filter. On the other hand, a channel having only dispersion is said to behave as an all-pass filter [44]. Several physical and biological systems contain inherent *local* low-pass filters (LPFs): For example, the musculoskeletal system of human body acts as low-pass filter [45], the abdominal ganglion of crayfish contains local LPFs [46], LPF is one of the building blocks of phase-locked loops [47]. On the other hand, in the case of electronic communications and neuronal systems the presence of local amplifiers or ion channels [48], respectively, compensate for the dissipation, however, in those systems signals still suffer dispersions making the coupling path to behave as an all-pass filter (APF). The effect of low-pass filtering was studied before in the context of synchronization [49, 50] and rhythmogenesis from an amplitude or oscillation death state [41] (by rhythmogenesis we mean the process by which the rhythmic behavior of individual nodes in a network of coupled oscillators is restored from the state of suppressed oscillations without changing the intrinsic parameters associated with the individual nodes); Banerjee et al. [51] reported a novel transition from homogeneous to inhomogeneous limit cycle as a consequence of low-pass or all-pass filtering. However, hitherto the effect of filtering on the chimera state in coupled oscillators has not been explored.

Motivated by the above discussion, in this paper we study the effect of local filtering on the occurrence of amplitude chimera (AC) in a network of nonlocally coupled Stuart-Landau oscillators. By local filtering we mean that the filtering effect is considered in the self-feedback path only. We consider local low-pass and all-pass filters in the network and for the first time we show that both types of filtering have a detrimental effect on the occurrence of amplitude chimeras: filtering always suppresses amplitude chimeras. With the variation of a filtering parameter (namely, the corner or cut-off frequency) we observe transitions from the oscillation death and amplitude chimera state to the globally synchronized state.

2. WITHOUT FILTERING

We consider $N = 200$ Stuart-Landau oscillators interacting through nonlocal symmetry-breaking coupling (i.e., only through the x-variable). The mathematical model of the coupled system is given by,

$$\dot{x}_i = (1 - x_i^2 - y_i^2)x_i - y_i\omega + \frac{\varepsilon}{2P}\sum_{j=i-P}^{i+P}(x_j - x_i), \qquad (1a)$$

$$\dot{y}_i = (1 - x_i^2 - y_i^2)y_i + x_i\omega, \qquad (1b)$$

with $i = 1 \cdots 200$. The individual Stuart-Landau oscillators have unit amplitude and eigenfrequency ω. Here ε denotes the coupling strength and P is the coupling range of the nonlocal coupling.

To explore the dynamics of the coupled network we numerically solve Equation (1) using the fourth-order Runge-Kutta method (step size $= 0.01$). Throughout this paper we consider $\omega = 2$ and use the following initial conditions [29]: $x_i = 1$ and $y_i = -1$ for $1 \leq i \leq \frac{N}{2}$ and $x_i = -1$ and $y_i = 1$ for $\frac{N}{2} < i \leq N$.

Figure 1A shows the phase diagram in the $P - \varepsilon$ space: we can see that the amplitude chimera (AC) state is interspersed in between the completely synchronized oscillation zone (Sync) and the oscillation death (OD) zone. This is in accordance with the results of Zakharova et al. [29], Schneider et al. [52], Zakharova et al. [53], and Tumash et al. [54] where this system was studied in detail. **Figures 1B–D** illustrate the spatiotemporal evolution of the synchronized state ($\varepsilon = 5$), AC pattern ($\varepsilon = 20$) and multicluster OD state ($\varepsilon = 30$) at $P = 10$. **Figure 2** depicts the manifestation of AC and OD in the phase space for an exemplary coupling range $P = 10$. **Figure 2** (Left panel) shows AC for $\varepsilon = 20$: here the small amplitude and shifted-origin limit cycles represent incoherent nodes and those having large amplitude oscillating around the origin represent the coherent nodes (for clarity only a few nodes from coherent and incoherent domains are shown). For higher coupling strengths a symmetry-breaking steady state (OD state) emerges, which is shown in **Figure 2**

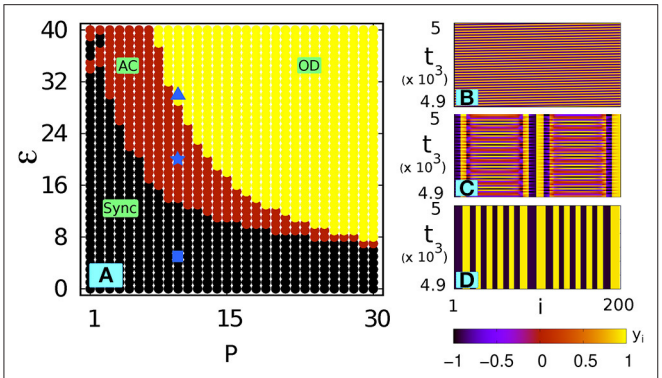

FIGURE 1 | Without filtering: **(A)** phase diagram in the $P - \varepsilon$ space for $N = 200$ nonlocally coupled Stuart-Landau oscillators ($\omega = 2$). Sync, synhronized state; AC, amplitude chimera; OD, oscillation death. **(B–D)** The spatiotemporal plots at $P = 10$ for three different coupling strengths ε: **(B)** synchronized state for $\varepsilon = 5$ [shown by ■ in **(A)**], **(C)** AC for $\varepsilon = 20$ [shown by ★ in **(A)**] and **(D)** multicluster OD for $\varepsilon = 30$ [shown in ▲ in **(A)**].

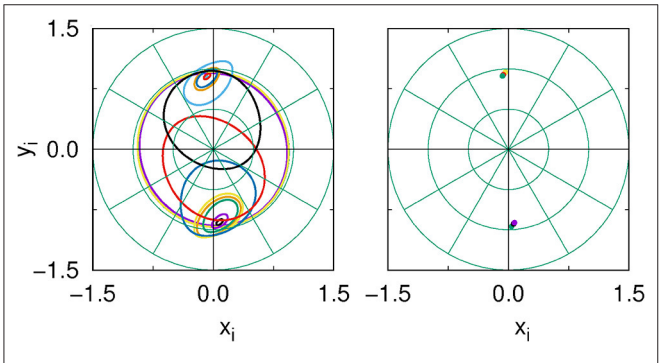

FIGURE 2 | Without filtering: Phase-space plot of a few nodes of the network from the coherent and incoherent domains **(Left panel)** AC ($\varepsilon = 20$, ★ point in **Figure 1A**), and **(Right panel)** OD ($\varepsilon = 30$, ▲ point of **Figure 1A**). Other parameter values are $P = 10$, $\omega = 2$, $N = 200$.

(Right panel) for $\varepsilon = 30$. In the next section we will explore how filtering affects this dynamical landscape in parameter space.

3. EFFECT OF LOW-PASS FILTERING

3.1. Mathematical Model

We consider $N = 200$ Stuart-Landau oscillators interacting through nonlocal symmetry-breaking coupling as in Equation (1), but here we consider local low-pass filter in the coupling path. The mathematical model of the coupled system is given by,

$$\dot{x}_i = (1 - x_i^2 - y_i^2)x_i - y_i\omega + \frac{\varepsilon}{2P}\sum_{j=i-P}^{i+P}(x_j - z_i), \qquad (2a)$$

$$\dot{y}_i = (1 - x_i^2 - y_i^2)y_i + x_i\omega, \qquad (2b)$$

$$\dot{z}_i = \alpha(-z_i + x_i). \qquad (2c)$$

Equation ((2c)) is the mathematical equation of a low-pass filter whose input is x_i and output is z_i. This z_i is fed to the coupling part of Equation (2a). Here α represents the corner or cut-off frequency of the LPF: the lower is the value of α, the higher is the effect of filtering. For larger α, filtering effects become lesser: if we put $\alpha \to \infty$ in Equation (2a), it simply gives $z_i = x_i$, i.e., no filtering effect is present and Equation (2) reduces to the original Equation (1). Since in the literature of filters we are conversant with the frequency domain representation, therefore, at first it is difficult to realize the role of α in Equation (2c). However, a close inspection reveals that α controls both phase and amplitude of the output signal z_i by the following way: the phase shift between input and output is given by $\phi_i = arctan(\omega\alpha^{-1})$, the ratio of output and input (called gain of the filter) is $G = \frac{1}{\sqrt{1+\omega^2\alpha^{-2}}}$ (see [51] for details). Another equivalent form is the representation of Equation (2c) as a distributed delayed coupling term in Equation (2a) with an exponential delay kernel $exp(-\alpha\tau)$ [55, 56].

3.2. Results

We investigate the effect of local low-pass filtering on the occurrence of amplitude chimera. Since α is the only control parameter, we will explore the effect of α on the dynamics of the network. We keep all the parameters and initial conditions the same as in the unfiltered case; the initial conditions for the filter variable z_i are chosen the same as those of x_i for the unfiltered case.

Figures 3A,B demonstrate the phase diagram of the network in the $P - \varepsilon$ space for three different (decreasing) values of α. It can be observed from **Figure 3** that the smaller the value of α is, the more the network dynamics deviates from the original scenario shown in **Figure 1A**. It is apparent from **Figure 3** that with decreasing α (i.e., increasing filtering effect) the synchronized portion dominates and therefore suppresses the AC and OD regions: a lower α shifts the AC and OD zone to a higher P region and also quenches the area of the AC and OD zone. Eventually, below a critical value of α (say α_c) the AC and OD state disappear and only the synchronized state prevails in the whole $P - \varepsilon$ space. This suppression of the AC and OD zone is shown in **Figure 3C** for $\alpha = 10$.

The scenario can be understood more clearly in the $\varepsilon - \alpha$ space for a fixed P. **Figure 4A** shows this for $P = 10$: we can observe that for comparatively high values of α the dynamics of the system remains unchanged. However, as the value of α is decreased the system goes to a synchronized state irrespectively of ε. It also shows that there exists a critical value α_c of α, below which the synchronized state is the only possible state. **Figures 4B–D** illustrate how decreasing α leads to the transition from OD to synchrony via AC ($\varepsilon = 25$ and $P = 10$): for $\alpha = 45$ the network shows a multi-clustered OD state (**Figure 4B**), and the AC state is shown for $\alpha = 35$ (**Figure 4C**), and finally global synchrony (a coherent traveling wave or a splay state) appears for further lowering of α (**Figure 4D** for $\alpha = 25$). It is noteworthy that in a range of lower ε, no OD state occurs and in this zone a decreasing α leads to a direct transition from AC to synchrony.

Figure 4E shows the scenario in the $P - \alpha$ space ($\varepsilon = 35$): here also we can see that at lower α values the completely

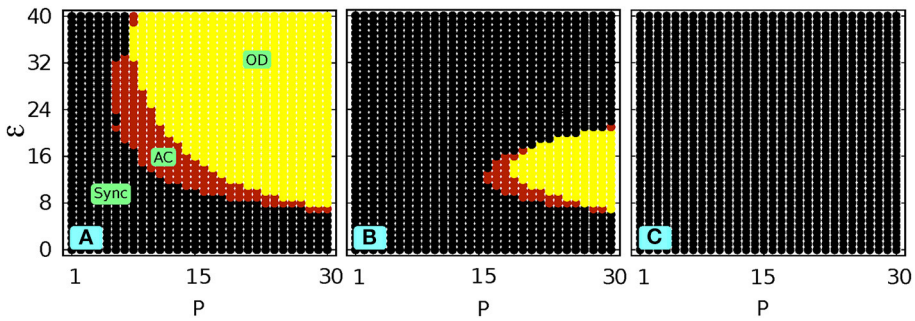

FIGURE 3 | With local low-pass filtering: Phase diagram in the P vs ε space ($N = 200$, $\omega = 2$) for **(A)** $\alpha = 50$ and **(B)** $\alpha = 20$. **(C)** shows complete suppression of AC for $\alpha = 10$.

synchronized state emerges out of either AC or OD. From **Figures 4A,E** we see that OD state is predominant for higher coupling strength (ε) and near-global coupling range (i.e., $P \to N/2$): it is interesting to note that a suitably chosen filtering parameter α can suppress the steady state and therefore results in rhythmogenesis in the network. In Zou et al. [41] and Banerjee et al. [51] filtering-induced rhythmogenesis in coupled oscillators was reported, however, in contrast to Zou et al. [41] and Banerjee et al. [51] here we show the existence of a broad parameter zone where OD does not transform into oscillation (SYNC) directly, but another symmetry-breaking emergent state, i.e., an amplitude chimera, mediates the transition. Therefore, filtering plays an important role in networks of physical, biological, and physiological systems where the occurrence of oscillation suppression often leads to a fatal system degradation and an irrecoverable malfunctioning [57–59]. A similar enhancement of the stability domain of the synchronized solutions for small α was found for distributed delayed coupling with an exponential kernel [56].

In the above results we use suitable measures, such as the measure of spatial correlation (g_0) and the center of mass (y_{cm_i}) to ensure the occurrence of the synchronized state and AC state and also to distinguish them (distinction of the OD state is relatively simple as we have to check whether a steady state is reached or not). According to Kemeth et al. [60], the *measure of spatial correlation* is defined in terms of the normalized probability density function g as

$$g_0(t) \equiv \sum_{|\hat{L}\psi_i(t)|=0}^{\delta_{th}} g(|\hat{L}\psi_i(t)|). \tag{3}$$

Here $\hat{L}\psi_i(t)$ represents the local curvature at each node i at time t given by

$$\hat{L}\psi_i(t) = \psi_{(i-1)}(t) - 2\psi_i(t) + \psi_{(i+1)}(t), \tag{4}$$

where $\hat{L}$ is the discrete Laplacian operator on each snapshot $\{\psi_i\}$. In our present case the state variable $\psi_i(t) = y_i$ (one can use x_i as well). In Equation (3) we consider a threshold value $\delta_{th} = 0.01L_{max}$, where L_{max} is the maximum curvature in the network [60]. The measure of spatial correlation $g_0(t) = 1$ for a fully synchronized network and $g_0(t) = 0$ for a completely unsynchronized network. Therefore, $0 < g_0(t) < 1$ represents partial synchronization ensuring the occurrence of chimera state. Although $g_0(t)$ can ensure the occurrence of a chimera state, it cannot distinguish between phase and amplitude chimeras. To ensure that AC indeed emerges in the network, we compute the *center of mass* of each oscillator defined by [29]

$$y_{cm_i} = \frac{1}{T}\int_0^T y_i dt, \tag{5}$$

where y_i represents the state of the i-th oscillator and T is a sufficiently large time. The quantity y_{cm_i} gives a measure of the shift of a limit cycle from the origin. Therefore, it can distinguish the homogeneous limit cycles from inhomogeneous ones.

Figures 5A,C, respectively, show $g_0(t)$ and y_{cm_i} of each oscillator corresponding to the synchronized state of **Figure 4D** ($\alpha = 25$): we observe that all the oscillators in the network have $g_0(t) = 1$ and $y_{cm_i} = 0$ indicating that the whole network is synchronized. On the other hand, **Figures 5B,D**, respectively, show $g_0(t)$ and y_{cm_i} corresponding to the AC state of **Figure 4C** ($\alpha = 35$): we can see that $0 < g_0(t) < 1$ indicating the occurrence of chimeras and at the same time y_{cm_i} in the incoherent region exhibits a random sequence of shifts to positive and negative values, however, in the coherent region $y_{cm_i} = 0$ indicating that the resulting chimera is indeed an AC pattern.

According to Tumash et al. [54], a strong measure that distinguishes an AC state from the synchronized state is the Floquet exponent. We study the stability of the periodic solution of nonlocally coupled Stuart-Landau oscillators given by (2) using Floquet theory [54]. We rewrite (2) as

$$\dot{\mathbf{x}} = f(\mathbf{x}(t)), \tag{6}$$

with $\mathbf{x}(t) \in \mathbf{R}^n$ and also consider that a periodic solution $\psi(t) = \psi(t+T)$ exists. In our case, we have three equations, therefore, $n = 3N$. The linearized equation is written as,

$$\delta\dot{\mathbf{x}}(t) = \mathbf{J}(\psi(t))\delta\mathbf{x}(t), \tag{7}$$

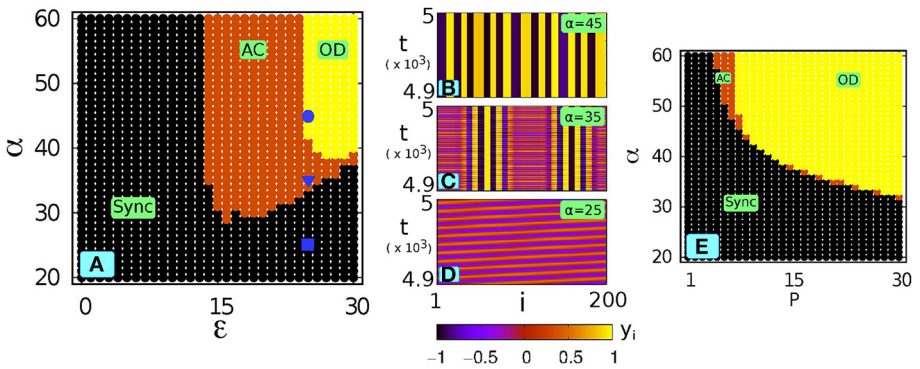

FIGURE 4 | With local low-pass filtering: **(A)** phase diagram in the $\varepsilon - \alpha$ space for $P = 10$ ($\omega = 2$). Three points at three α values at a particular $\varepsilon = 25$ are marked by • ($\alpha = 45$), ▼ ($\alpha = 35$) and ■ ($\alpha = 25$). **(B–D)** spatiotemporal plots corresponding to those three points (decreasing α): **(B)** multicluster OD, **(C)** AC, **(D)** synchronized state (coherent traveling wave or splay state). **(E)** phase diagram in the $P - \alpha$ space for $\varepsilon = 35$.

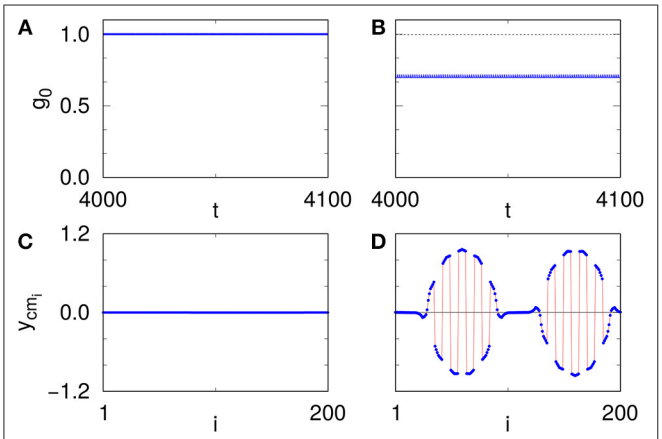

FIGURE 5 | With local low-pass filtering: **(A,B)** The time evolution of g_0 corresponding to the synchronized **(A)** and AC **(B)** state as marked in **Figure 4A** by (■) ($\alpha = 25$) and (▼) ($\alpha = 35$), respectively. **(C,D)** The corresponding center of mass (y_{cm_i}) for the above two points, showing synchronized **(C)** and AC **(D)** states, respectively. Other parameters are $P = 10$, $\varepsilon = 25$ and $\omega = 2$.

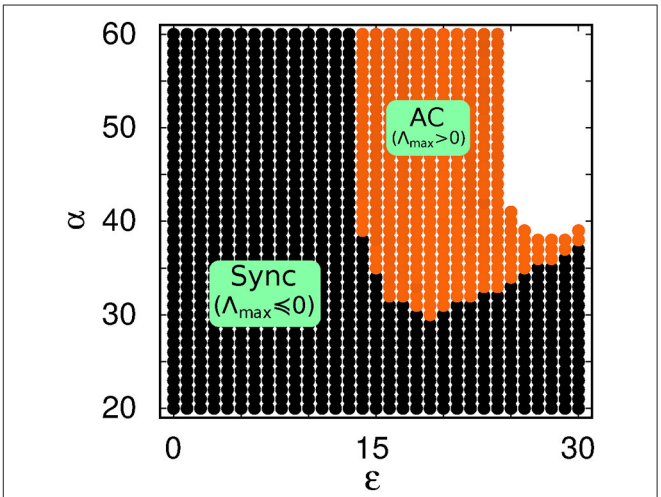

FIGURE 6 | With local low-pass filtering: Phase diagram of the periodic solutions (Sync and AC) in $\varepsilon - \alpha$ space based on the Floquet exponent. For the synchronized region (black), at each point, the largest real part of the Floquet exponents (Λ_{max}) is negative (for the Goldstone mode it is approximately equal to zero). For the AC region (orange) at each point it is greater than zero (i.e., $\Lambda_{max} > 0$). Other parameters are $P = 10$, $\omega = 2$, $N = 200$.

where $\mathbf{J}(\psi(t))$ is the Jacobian matrix evaluated at $\psi(t)$ and has the following solution:

$$\delta\mathbf{x}(t) = \mathbf{M}(t)\delta\mathbf{x}(0). \tag{8}$$

Here $\delta\mathbf{x}(0)$ is the initial condition. The fundamental matrix $\mathbf{M}(t)$ obeys the equation,

$$\dot{\mathbf{M}}(t) = \mathbf{J}(\psi(t))\mathbf{M}(t), \tag{9}$$

where $\mathbf{M}(0) = 1$, and $\mathbf{M}(t + T) = \mathbf{M}(t)\mathbf{M}(T)$. $\mathbf{M}(T)$ is the monodromy matrix whose eigenvalues are called Floquet multipliers (μ_k). Each Floquet multiplier can be expressed as $\mu_k = exp((\Lambda_k + i\Omega_k)T)$, where $(\Lambda_k + i\Omega_k)$ is the Floquet exponent. The stability of the periodic orbit can be analyzed by determining the sign of the real part of these exponents. When the real parts of all the Floquet exponents are less than zero (i.e., $\Lambda_k < 0$) except the Goldstone mode (which is equal to zero) then the periodic solution is stable indicating a synchronized solution [54]. But according to Tumash et al. [54] when at least one or two of them are greater than zero ($\Lambda_k > 0$), then the solution becomes unstable indicating a saddle cycle in phase space which corresponds to an AC state. In our computation we average the exponents over $200T$ (where $T = \pi$). **Figure 6** shows the zone in black where all the exponents are negative (except the Goldstone mode), which indicates the synchronized state; Again, at every point in the orange region, a few Λ_ks have small (< 0.5) positive values, which means that the system is in the AC state. Note the agreement between **Figure 4A** and **Figure 6**, which confirms

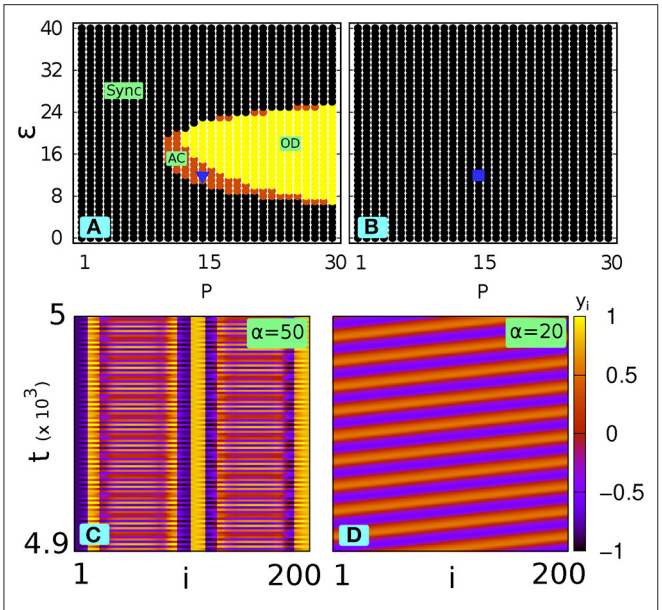

FIGURE 7 | With all-pass filtering: Phase diagram in the $P-\varepsilon$ space for **(A)** $\alpha = 50$ and **(B)** $\alpha = 20$. **(C)** spatiotemporal plot of AC corresponding to $\alpha = 50$ (shown by ▼ in **A**). **(D)** spatiotemporal plot of the synchronized state (coherent traveling wave) corresponding to $\alpha = 20$ (shown by ■ in **B**). In both **(C,D)** $\varepsilon = 12$, $P = 15$, $\omega = 2$.

that a transition from AC to synchrony indeed occurs with decreasing α.

4. EFFECT OF ALL-PASS FILTERING

Next we consider the effect of all-pass filtering (APF) in the network of Stuart-Landau oscillators described in Equation (1). The mathematical model of the coupled system is given by

$$\dot{x}_i = (1 - x_i^2 - y_i^2)x_i - y_i\omega + \frac{\varepsilon}{2P}\sum_{j=i-P}^{i+P}(x_j - U_i) \tag{10a}$$

$$\dot{y}_i = (1 - x_i^2 - y_i^2)y_i + x_i\omega \tag{10b}$$

$$\dot{z}_i = \alpha(-z_i + x_i) \tag{10c}$$

$$U_i = 2z_i - x_i \tag{10d}$$

Equations (10c, 10d) jointly represent the differential algebraic equation of an all-pass filter, whose input is x_i and output is U_i [51]. In this case α has the same meaning as in Equation (2c), but the effect of α is different on U_i: Here α does not affect the amplitude of U_i, it only affects the phase part by introducing a phase shift between the input and output signals, given by $\theta = 2arctan(\omega\alpha^{-1})$. Note that for the same α the phase shift introduced by a LPF (i.e., ϕ) is half of that of an APF (i.e., θ).

In **Figure 7** the effect of an all-pass filter is shown in the $P-\varepsilon$ space for two α values: **Figure 7A** is for $\alpha = 50$ and **Figure 7B** is for $\alpha = 20$. **Figures 7C,D** show the spatiotemporal representation of AC (for $\alpha = 50$) and synchronized state (coherent traveling wave for $\alpha = 20$), respectively: it shows that α acts as an efficient control parameter for the suppression of AC. Here it is evident that local all-pass filtering can also suppress AC (and OD) and gives rise to the synchronized state. Comparing **Figures 7A,B** of the low-pass filtering case with **Figures 7A,B**, respectively, it is interesting to note that for the same α an APF is more effective than a LPF as far as the suppression of amplitude chimeras (and OD) is concerned: see for example at $\alpha = 20$, low-pass filtering only quenches the AC and OD zone in $P-\varepsilon$ space (**Figure 3B**), however, all-pass filtering completely suppresses the AC and OD zone (**Figure 7B**). We ensure that α_c, the critical value below which AC and OD are completely suppressed, is much higher for an APF compared to that of a LPF (not shown here): therefore even a relatively weak all-pass local filtering is equivalent to a stronger local low-pass filtering, as far as suppressing AC and OD is concerned. This is the consequence of the fact that at a particular value of α, the phase shift introduced by an APF is twice of that of a LPF [51]. Therefore, all the results suggest that α which is the control parameter of local filters, also controls the dynamics of the whole network.

5. CONCLUSION

In this paper, we have revealed that the presence of local filtering (either low-pass or all-pass) suppresses the amplitude chimera state and therefore gives rise to global synchrony (coherent traveling waves). Further, it has been shown that local filtering causes rhythmogenesis by suppressing the steady state behavior (i.e., OD state), which has immense importance in many biological and engineering systems [58, 61]. Collectively, our study has a broad significance: it establishes that local filtering is detrimental for the symmetry-breaking states (AC and OD) and favors restoration of the symmetry in the network.

Our study reveals that the cut-off frequency α of the local filter acts as an efficient control parameter of the network that can be tuned to achieve a desired symmetry-breaking state or synchronized state without changing coupling strength or range. Several control methods to stabilize phase or amplitude mediated phase chimeras have recently been proposed [62–64]. In Gjurchinovski et al. [43] it has been shown that a constant time delay in the coupling path can stabilize amplitude chimeras. In contrast, here we established that the local filtering has a destabilizing effect on the occurrence of amplitude chimeras. In the case of rhythmogenesis, the value of α that suppresses the steady state depends upon the system and coupling parameters in a nontrivial manner (see [51] for two mean-field coupled oscillators). It has been observed that if one wants to *ensure* rhythmogenesis (irrespectively of other parameters) the typical value of α is of the order of the intrinsic frequency of an individual oscillator (here ω). However, depending upon system and coupling parameters, α (filtering) need not be so small

(strong): rhythmogenesis appears much before that, i.e., for $\alpha > \omega$.

From the perspective of dynamical systems the role of α can be understood in the following way: α actually controls the dissipative property of the whole network by controlling the dissipation and dispersion in the coupling path; a smaller α imposes a larger filtering effect and therefore smaller dissipation, which favors synchrony and rhythmogenesis. In this context we observe that filtering does not affect the pattern of phase chimera appreciably. This may be due to the fact that additional phase shift and/or attenuation caused by filtering has lesser effect on the mean frequency than on the amplitude dynamics (note that in the phase chimera the mean frequency is the determining factor that distinguishes the coherent and incoherent domains, whereas in the amplitude chimera, the amplitude of the nodes matters).

In this paper we have considered a network of Stuart-Landau oscillators. However, we verified that the filtering affects the amplitude chimera in a similar way in other systems also, for example, in a network of Rayleigh oscillators [65] (results not shown). Since the Stuart-Landau oscillator is a generic model for systems near a Hopf bifurcation and since filtering naturally arises in many biological and physical systems, we believe that our results can also be extended to those systems.

AUTHOR CONTRIBUTIONS

TB, ES, and AZ formulated the problem. BB and TB carried out the analysis. BB performed the computations. All authors discussed the results and contributed to writing the manuscript, read and approved the final manuscript.

ACKNOWLEDGMENTS

BB acknowledges University of Burdwan for providing financial support through the state funded research fellowship. AZ and ES acknowledge the financial support by DFG in the framework of SFB 910.

REFERENCES

1. Pikovsky AS, Rosenblum MG, Kurths J. *Synchronization. A Universal Concept In Nonlinear Science*. Cambridge: Cambridge University Press (2001).
2. Koseska A, Volkov E, Kurths J. Oscillation quenching mechanisms: Amplitude vs oscillation death. *Physics Reports* (2013) **531**:173. doi: 10.1016/j.physrep.2013.06.001
3. Schöll E. Synchronization patterns and chimera states in complex networks: Interplay of topology and dynamics. *Eur Phys J Special Topics* (2016) **225**: 891. doi: 10.1140/epjst/e2016-02646-3
4. Kuramoto Y, Battogtokh D. Coexistence of coherence and incoherence in nonlocally coupled phase oscillators. *Nonlin Phen Complex Sys.* (2002) **5**:380.
5. Abrams DM, Strogatz SH. Chimera states for coupled oscillators. *Phys. Rev. Lett.* **93** (2004):174102. doi: 10.1103/PhysRevLett.93.174102
6. Panaggio MJ, Abrams DM. Chimera states: Coexistence of coherence and incoherence in networks of coupled oscillators. *Nonlinearity* (2015) **28**:R67–87. doi: 10.1088/0951-7715/28/3/R67
7. Hagerstrom AM, Murphy TE, Roy R, Hövel P, Omelchenko I, Schöll E. Experimental observation of chimeras in coupled-map lattices. *Nat Phys.* (2012) **8**:658–61. doi: 10.1038/nphys2372
8. Tinsley MR, Nkomo S, Showalter K. Chimera and phase-cluster states in populations of coupled chemical oscillators. *Nat Phys.* (2012) **8**:662–65. doi: 10.1038/nphys2371
9. Martens EA, Thutupalli S, Fourriere A, Hallatschek O. Chimera states in mechanical oscillator networks. *Proc Nat Acad Sci USA.* (2013) **110**:10563–7. doi: 10.1073/pnas.1302880110
10. Kapitaniak T, P Kuzma JW, Czolczynski K, Maistrenko Y. Imperfect chimera states for coupled pendula. *Sci Rep.* (2014) **4**:6379. doi: 10.1038/srep06379
11. Larger L, Penkovsky B, Maistrenko Y. Virtual chimera states for delayed-feedback systems. *Phys Rev Lett.* (2013) **111**:054103. doi: 10.1103/PhysRevLett.111.054103
12. Gambuzza LV, Buscarino A, Chessari S, Fortuna L, Meucci R, Frasca M. Experimental investigation of chimera states with quiescent and synchronous domains in coupled electronic oscillators. *Phys Rev E* (2014) **90**:032905. doi: 10.1103/PhysRevE.90.032905
13. Larger L, Penkovsky B, Maistrenko Y. Laser chimeras as a paradigm for multistable patterns in complex systems. *Nat Commun.* (2015) **6**:7752. doi: 10.1038/ncomms8752
14. Hart JD, Bansal K, Murphy TE, Roy R. Experimental observation of chimeras in a minimal globally coupled network. *Chaos* (2016) **26**:094801. doi: 10.1063/1.4953662
15. Hart J, Larger L, Murphy T, Roy R. Delayed dynamical systems: networks, chimeras and reservoir computing. *arXiv* **1808.04596** (2018).
16. Brunner D, Penkovsky B, Levchenko R, Schöll E, Larger L, Maistrenko Y. Two-dimensional spatiotemporal complexity in dual-delayed nonlinear feedback systems: chimeras and dissipative solitons. *Chaos* (2018) **28**:103106. doi: 10.1063/1.5043391
17. Wickramasinghe M, Kiss IZ. Spatially organized dynamical states in chemical oscillator networks: synchronization, dynamical differentiation, and chimera patterns. *PLoS ONE* (2013) **8**:e80586. doi: 10.1371/journal.pone.0080586
18. Wickramasinghe M, Kiss IZ. Spatially organized partial synchronization through the chimera mechanism in a network of electrochemical reactions. *Phys Chem Chem Phys.* (2014) **16**:18360. doi: 10.1039/C4CP02249A
19. Schmidt L, Schönleber K, Krischer K, Garcia-Morales V. Coexistence of synchrony and incoherence in oscillatory media under nonlinear global coupling. *Chaos* (2014) **24**:013102. doi: 10.1063/1.4858996
20. Rosin DP, Rontani D, Haynes ND, Schöll E, Gauthier DJ. Transient scaling and resurgence of chimera states in networks of boolean phase oscillators. *Phys Rev E* (2014) **90**:030902(R). doi: 10.1103/PhysRevE.90.030902
21. Rothkegel A, Lehnertz K. Irregular macroscopic dynamics due to chimera states in small-world networks of pulse-coupled oscillators. *New J Phys.* (2014) **16**:055006. doi: 10.1088/1367-2630/16/5/055006
22. Rattenborg NC, Amlaner CJ, Lima SL. Behavioral, neurophysiological and evolutionary perspectives on unihemispheric sleep. *Neurosci Biobehav Rev.* (2000) **24**:817. doi: 10.1016/S0149-7634(00)00039-7
23. Rattenborg NC, Voirin B, Cruz SM, Tisdale R, Dell'Omo G, Lipp HP, et al. Evidence that birds sleep in mid-flight. *Nat Commun.* (2016) **7**:12468. doi: 10.1038/ncomms12468
24. Banerjee T, Dutta PS, Zakharova A, Schöll E. Chimera patterns induced by distance-dependent power-law coupling in ecological networks. *Phys Rev E* (2016) **94**:032206. doi: 10.1103/PhysRevE.94.032206
25. Dutta PS, Banerjee T. Spatial coexistence of synchronized oscillation and death: a chimeralike state. *Phys Rev E* (2015) **92**:042919. doi: 10.1103/PhysRevE.92.042919
26. Gonzalez-Avella JC, Cosenza MG, Miguel MS. Localized coherence in two interacting populations of social agents. *Physica A* (2014) **399**:24. doi: 10.1016/j.physa.2013.12.035
27. Bastidas VM, Omelchenko I, Zakharova A, Schöll E, Brandes T. Quantum signatures of chimera states. *Phys Rev E* (2015) **92**:062924. doi: 10.1103/PhysRevE.92.062924
28. Sethia GC, Sen A, Johnston GL. Amplitude-mediated chimera states. *Phys Rev E* (2013) **88**:042917. doi: 10.1103/PhysRevE.88.042917

29. Zakharova A, Kapeller M, Schöll E. Chimera death: symmetry breaking in dynamical networks. *Phys Rev Lett.* (2014) **112**:154101. doi: 10.1103/PhysRevLett.112.154101
30. Zakharova A, Schneider I, Kyrychko YN, Blyuss KB, Koseska A, Fiedler B, et al. Time delay control of symmetry-breaking primary and secondary oscillation death. *Europhys Lett.* (2013) **104**:50004. doi: 10.1209/0295-5075/104/50004
31. Banerjee T, Ghosh D. Transition from amplitude to oscillation death under mean-field diffusive coupling. *Phys Rev E* (2014) **89**:052912. doi: 10.1103/PhysRevE.89.052912
32. Banerjee T, Ghosh D. Experimental observation of a transition from amplitude to oscillation death in coupled oscillators. *Phys Rev E* (2014) **89**:062902. doi: 10.1103/PhysRevE.89.062902
33. Ghosh D, Banerjee T. Transitions among the diverse oscillation quenching states induced by the interplay of direct and indirect coupling. *Phys Rev E* (2014) **90**:062908. doi: 10.1103/PhysRevE.90.062908
34. Ghosh D, Banerjee T, Kurths J. Mixed-mode oscillation suppression states in coupled oscillators. *Phys Rev E* (2015) **92**:052913. doi: 10.1103/PhysRevE.92.052913
35. Banerjee T. Mean-field diffusion induced chimera death state. *EPL* (2015) **110**:60003. doi: 10.1209/0295-5075/110/60003
36. Koseska A, Ullner E, Volkov E, Kurths J, Garcá-Ojalvo J. Cooperative differentiation through clustering in multicellular populations. *J Theoret Biol.* (2010) **263**:189–202. doi: 10.1016/j.jtbi.2009.11.007
37. Chickarmane V, Troein C, Nuber UA, Sauro HM, Peterson C. Transcriptional dynamics of the embryonic stem cell switch. *PLoS Comp Biol.* (2006) **2**:e123. doi: 10.1371/journal.pcbi.0020123
38. Banerjee T, Dutta PS, Gupta A. Mean-field dispersion-induced spatial synchrony, oscillation and amplitude death, and temporal stability in an ecological model. *Phys Rev E* (2015) **91**:052919. doi: 10.1103/PhysRevE.91.052919
39. Arumugam R, Dutta P, Banerjee T. Environmental coupling in ecosystems: from oscillation quenching to rhythmogenesis. *Phys Rev E* (2016) **94**:022206. doi: 10.1103/PhysRevE.94.022206
40. Biswas D, Banerjee T. *Time-Delayed Chaotic Dynamical Systems*. Springer International Publishing (2018).
41. Zou W, Zhan M, Kurths J. Revoking amplitude and oscillation deaths by low-pass filter in coupled oscillators. *Phys Rev E* (2017) **95**:062206. doi: 10.1103/PhysRevE.95.062206
42. Loos SAM, Claussen JC, Schöll E, Zakharova A. Chimera patterns under the impact of noise. *Phys Rev E* (2016) **93**:012209. doi: 10.1103/PhysRevE.93.012209
43. Gjurchinovski A, Schöll E, Zakharova A. Control of amplitude chimeras by time delay in dynamical networks. *Phys Rev E* (2017) **95**:042218. doi: 10.1103/PhysRevE.95.042218
44. Sedra AS, Smith KC. *Microelectronic Circuits*. Oxford: Oxford University Press. (2003).
45. Nakashima AM, Borland MJ, Abel SM. Measurement of noise and vibration in canadian forces armoured vehicles. *Ind Health* (2007) **45**:318. doi: 10.2486/indhealth.45.318
46. Stark L. *Neurological Control Systems: Studies in Bioengineering*. New York, NY: Plenum Press (1968).
47. Banerjee T, Paul B, Sarkar BC. Spatiotemporal dynamics of a digital phase-locked loop based coupled map lattice system. *Chaos* (2014) **24**:013116. doi: 10.1063/1.4863859
48. Izhikevich E. *Dynamical Systems in Neuroscience: The Geometry of Excitability and Bursting*. Cambridge, MA: The MIT press (2007).
49. Kim MY, Sramek C, Uchida A, Roy R. Synchronization of unidirectionally coupled mackey-glass analog circuits with frequency bandwidth limitations. *Phys Rev E* (2006) **74**:016211. doi: 10.1103/PhysRevE.74.016211
50. Soriano MC, Ruiz-Oliveras F, Colet P, Mirasso CR. Synchronization properties of coupled semiconductor lasers subject to filtered optical feedback. *Phys Rev E* (2008) **78**:046218. doi: 10.1103/PhysRevE.78.046218
51. Banerjee T, Biswas D, Ghosh D, Bandyopadhyay B, Kurths J. Transition from homogeneous to inhomogeneous limit cycles: effect of local filtering in coupled oscillators. *Phys Rev E* (2018) **97**:042218. doi: 10.1103/PhysRevE.97.042218
52. Schneider I, Kapeller M, Loos S, Zakharova A, Fiedler B, Schöll E. Stable and transient multi-cluster oscillation death in nonlocally coupled networks. *Phys Rev E* (2015) **92**:052915. doi: 10.1103/PhysRevE.92.052915
53. Zakharova A, Kapeller M, Schöll E. Amplitude chimeras and chimera death in dynamical networks. *J Phys Conf Ser.* (2016) **727**:012018. doi: 10.1088/1742-6596/727/1/012018
54. Tumash L, Zakharova A, Lehnert J, Just W, Schöll E. Stability of amplitude chimeras in oscillator networks. *EPL* (2017) **117**:20001. doi: 10.1209/0295-5075/117/20001
55. Kyrychko YN, Blyuss KB and Schöll E. Amplitude death in systems of coupled oscillators with distributed-delay coupling. *Eur Phys J B* (2011) **84**:307. doi: 10.1140/epjb/e2011-20677-8
56. Kyrychko YN, Blyuss KB and Schöll E. Synchronization of networks of oscillators with distributed-delay coupling. *Chaos* (2014) **24**:043117. doi: 10.1063/1.4898771
57. Zou W, Senthilkumar DV, Zhan M, Kurths J. Reviving oscillations in coupled nonlinear oscillators. *Phys Rev Lett.* (2013) **111**:014101. doi: 10.1103/PhysRevLett.111.014101
58. Zou W, Senthilkumar DV, Nagao R, Kiss IZ, Tang Y, Koseska A, et al. Restoration of rhythmicity in diffusively coupled dynamical networks. *Nat Commun.* (2015) **6**:7709. doi: 10.1038/ncomms8709
59. Ghosh D, Banerjee T, Kurths J. Revival of oscillation from mean-field-induced death: theory and experiment. *Phys Rev E* (2015) **92**:052908. doi: 10.1103/PhysRevE.92.052908
60. Kemeth FP, Haugland SW, Schmidt L, Kevrekidis IG, Krischer K. A classification scheme for chimera states. *Chaos* (2016) **26**:094815. doi: 10.1063/1.4959804
61. Motter AE, Myers SA, Anghel M, Nishikawa T. Spontaneous synchrony in power-grid networks. *Nat Phys.* (2013) **9**:191–7. doi: 10.1038/nphys2535
62. Sieber J, Omel'chenko O, Wolfrum M. Controlling unstable chaos: stabilizing chimera states by feedback. *Phys Rev Lett.* (2014) **112**:054102. doi: 10.1103/PhysRevLett.112.054102
63. Bick C, Martens EA. Controlling chimeras. *New J Phys.* (2015) **17**:033030. doi: 10.1088/1367-2630/17/3/033030
64. Omelchenko I, Omel'chenko OE, Zakharova A, Wolfrum M, Schöll E. Tweezers for chimeras in small networks. *Phys Rev Lett.* (2016) **116**:114101. doi: 10.1103/PhysRevLett.116.114101
65. Banerjee T, Biswas D, Ghosh D, Schöll E, Zakharova A. Networks of coupled oscillators: from phase to amplitude chimeras. *Chaos* (2018) **28**:113124. doi: 10.1063/1.5054181

Conflict of Interest Statement: The authors declare that the research was conducted in the absence of any commercial or financial relationships that could be construed as a potential conflict of interest.

frontiers in Applied Mathematics and Statistics

ORIGINAL RESEARCH
published: 29 November 2018
doi: 10.3389/fams.2018.00058

Imperfect Amplitude Mediated Chimera States in a Nonlocally Coupled Network

K. Sathiyadevi[1], *V. K. Chandrasekar*[1]*, *D. V. Senthilkumar*[2] *and M. Lakshmanan*[3]

[1] *Centre for Nonlinear Science and Engineering, School of Electrical and Electronics Engineering, SASTRA Deemed University, Thanjavur, India,* [2] *School of Physics, Indian Institute of Science Education and Research, Thiruvananthapuram, India,* [3] *Centre for Nonlinear Dynamics, School of Physics, Bharathidasan University, Tiruchirappalli, India*

We investigate the dynamical transitions in a network of nonlocally coupled Stuart-Landau oscillators with a combination of attractive and repulsive couplings. The competing interaction between the couplings plays a crucial role in many realistic situations, particularly in neuronal systems. We report that the employed attractive and repulsive couplings induce imperfect amplitude mediated chimera state which emerges as an intermediate between the oscillatory dynamics and the oscillation death state. Each oscillator in the synchronized and desynchronized groups constituting the imperfect amplitude mediated chimera drifts between both the homogeneous and inhomogeneous oscillations as a function of time. To distinguish the homogeneous and inhomogeneous oscillations, we use the finite-time average of each oscillator. The observed distinct dynamical states are further classified by finding the strength of the inhomogeneous oscillators in the corresponding dynamical states. We also find that the number of clusters in the cluster oscillation death states exponentially decays as a function of the coupling range and obeys a power law relation. Finally, we confirm the robustness of the observed amplitude mediated chimera state by introducing a Gaussian white noise in the system.

Keywords: nonlinear dynamics, coupled oscillators, dynamical transitions, synchronization, chimera states, oscillation death

OPEN ACCESS

Edited by:
Anna Zakharova, Technische Universität Berlin, Germany

Reviewed by:
Iryna Omelchenko, Technische Universität Berlin, Germany
Syamal Kumar Dana, Jadavpur University, India

***Correspondence:**
V. K. Chandrasekar
chandru25nld@gmail

Specialty section:
This article was submitted to Dynamical Systems, a section of the journal Frontiers in Applied Mathematics and Statistics

Received: *25 September 2018*
Accepted: *13 November 2018*
Published: *29 November 2018*

Citation:
Sathiyadevi K, Chandrasekar VK, Senthilkumar DV and Lakshmanan M (2018) Imperfect Amplitude Mediated Chimera States in a Nonlocally Coupled Network. Front. Appl. Math. Stat. 4:58. doi: 10.3389/fams.2018.00058

1. INTRODUCTION

During the past couple of decades studies on the emerging collective dynamical behavior of a given network of complex nonlinear systems has become an active area of research, due to its capability to mimic various natural phenomena such as clusters, synchronization, chimera, death states, etc. [1–4]. Among the intriguing collective dynamical behaviors exhibited by networks of coupled systems, chimera states have been receiving a wide attention in the recent literature both theoretically and experimentally. In particular, much focus has been paid toward understanding the onset of various types of chimeras. A flurry of research activities on the chimera states have been provoked due to the nonintuitive nature of the associated hybrid dynamical state. Chimera state is characterized by spatially coexisting coherent and incoherent dynamical behaviors arising out of an ensemble of identical systems. So far, chimera states have been found theoretically in limit cycle oscillators [5, 6], time discrete maps [7–9], chaotic models [10, 11], neural systems [10, 12, 13], quantum oscillators [14], population dynamics [15, 16], boolean networks [17] and so on. Chimera states have also been found experimentally in optical [18], electronic [18, 19], optoelectronic [20], chemical [21, 22], electrochemical [23, 24] and mechanical systems [25].

A diverse variety of chimera patterns have been identified depending on the coupling geometry, the strength of the interaction and the values of the parameters of the employed dynamical systems. Specifically, based on the spatial or spatio-temporal distribution of an ensemble of coupled identical systems, chimera states have been classified as amplitude chimera [26–30], globally clustered chimera [31], imperfect traveling chimera [32], breathing chimera [33, 34], spiral wave chimera [35], twisted chimera and multicore spiral chimera states [36]. Among the different types of chimeras, investigations on the onset of the amplitude mediated chimera has received a wide attention in the recent literature. Amplitude-mediated chimera was reported in a nonlocally coupled complex Ginzburg-Landau system in the strong coupling limit which may have potential applications in understanding spatio-temporal patterns in fluid flow experiments and in strongly coupled systems [6]. It is also reported in a system of globally coupled complex Ginzburg-Landau oscillators [37]. The robustness of amplitude mediated chimera state has also been examined in a globally coupled system of active and inactive Ginzburg-Landau oscillators by varying the fraction of active and inactive oscillators [38]. Interestingly, the notion of chimera state is not only restricted to oscillatory dynamics but has also been extended to include so called the death states which have been reported as chimera death [3]. Domains of inhomogeneous death states are termed as cluster oscillation death states whereas coexisting domains of coherent and incoherent death states (of the inhomogeneous death states) constitute the cluster chimera death state. The number of clusters in the death states are found to vary as a function of the coupling range and cluster initial conditions in nonlocally coupled networks [4, 39].

In this report, we unravel the emergence distinct collective dynamical behavior in a network of nonlocally coupled Stuart-Landau oscillators with competing attractive and repulsive couplings. The trade-off between the attractive and repulsive couplings in many natural systems has been revealed as an essential element in determining their functional and evolutionary processes [39, 40]. We find that the competing interaction between them facilitates the emergence of imperfect amplitude mediated chimera, which is characterized by a continuous drift of the oscillators between the homogeneous and the inhomogeneous oscillations as a function of time. Finite-time average of each of the oscillators elucidates the continuous shift between the homogeneous and the inhomogeneous states of the imperfect amplitude mediated chimera. Further, the homogeneous and inhomogeneous states can be distinguished by estimating the strength of inhomogeneous oscillators in each dynamical state. We find that the observed amplitude mediated chimera mediates the transition between the oscillatory and death states. Further, we will demonstrate the emergence of distinct cluster oscillation death and chimera death states as a function of the nonlocal coupling range. We have also found that the number of clusters in the network exponentially decays as a function of the coupling range and obeys a power-law relation.

The structure of the paper is organized as follows. In section 2, we introduce our model of nonlocally coupled Stuart-Landau oscillators with a combination of attractive and repulsive couplings. The emergence of imperfect amplitude mediated chimera state is demonstrated in section 3. The corresponding dynamical transitions are delineated in section 4 and the global dynamical behavior of the coupled systems is depicted in the section 5. Finally, we summarize the obtained results in section 6.

2. THE MODEL

We consider the paradigmatic model of Stuart-Landau limit cycle oscillators, which can be used to model a variety of weakly nonlinear systems near Hopf-bifurcation [41]. In addition, the limit cycle oscillations can be found in many biological and chemical systems such as heart beats, chemical oscillations, vibrations in bridges, etc. [42, 43]. Further, to demonstrate the complex dynamical behaviors in a network of coupled identical Stuart-Landau oscillators, we have employed the nonlocal attractive and repulsive couplings, which can be represented as

$$\begin{aligned}\dot{x}_i &= (\lambda - x_i^2 - y_i^2)x_i - \omega y_i + \frac{\epsilon}{2P}\sum_{k=i-P}^{i+P}(x_k - x_i),\\ \dot{y}_i &= (\lambda - x_i^2 - y_i^2)y_i + \omega x_i - \frac{\epsilon}{2P}\sum_{k=i-P}^{i+P}(y_k - y_i), \quad i = 1, 2, ..., N,\end{aligned} \tag{1}$$

where λ is the bifurcation parameter and ω is the natural frequency of the system. x_i and y_i are the state variables of the system. Here, the attractive and repulsive couplings are established via the state variables x_i and y_i ($i = 1, 2.., N$), respectively, and ϵ is the coupling strength. Throughout the work, the number of oscillators in the network has been chosen as $N = 100$, except for the cases mentioned specifically in the text, and the values of the parameters are fixed as $\lambda = 1.0$, $\omega = 1.0$. The numerical results are obtained through the Runge-Kutta fourth order scheme with a time step 0.01 and the initial states of the oscillators (x_i, y_i) are chosen such that they are independently distributed between -1 to +1 randomly.

3. AMPLITUDE MEDIATED CHIMERA

Amplitude chimera is characterized by a partial coherent and a partial incoherent spatio-temporal pattern with amplitude variations in their amplitude dynamics [26]. On the other hand the amplitude mediated chimera state suffers variations in both phase and frequency. Interestingly, we find that the system of nonlocally coupled Stuart-Landau oscillators also exhibit amplitude mediated chimera states, where the synchronized and desynchronized groups are imperfect over time exhibiting quasi-periodic oscillations. In particular, the synchronized group gives rise to inhomogeneous small oscillations populating both the upper and the lower branches of the inhomogeneous state while the desynchronized group oscillates with a larger amplitude. The space-time evolution in **Figure 1a** clearly illustrates that the oscillators at the boundaries of the upper (yellow/light gray) and the lower (blue/dark gray) branches of the inhomogeneous state exhibit large oscillations. In addition, the oscillators exhibiting

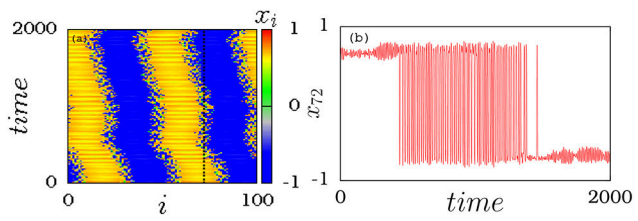

FIGURE 1 | (a) Spatio-temporal evolution of imperfect amplitude mediated chimera (after leaving transients of the order 1×10^4) and **(b)** time evolution of a representative oscillator x_{72}, a constituent of imperfect amplitude mediated chimera. Parameters: $r = 0.4$, $\omega = 1.0$, $\lambda = 1.0$, $\epsilon = 0.9$ and $N = 100$.

large oscillations suffer a drift to either one of the inhomogeneous states with small oscillations and vice versa as a function of time. Further, to elucidate that the oscillators in the network reside in the upper/lower branch of the inhomogeneous state for a finite-time interval and then transits to the homogeneous state for certain other time interval, we have depicted the time evolution of a typical oscillator, indicated along the dotted line in **Figures 1a,b**. The time evolution of the representative oscillator x_{72} elucidates that the corresponding oscillator oscillates in the upper branch of the inhomogeneous state for a certain time interval, then it manifests itself as a homogeneous oscillator. After a further finite time interval, the homogeneous oscillations with large amplitude transit to the lower branch of the inhomogeneous state exhibiting small oscillations. The homogeneous large oscillations re-emerge again after a finite time from the lower branch and then populate the upper branch of the inhomogeneous state after a while. These transitions in the dynamical nature of each oscillator takes place continuously as a function of time, thereby manifesting as an imperfect amplitude mediated chimera as a whole. The robust against initial conditions and system size of imperfect amplitude mediated chimera is discussed in the following.

3.1. Robustness of Imperfect Amplitude Mediated Chimera for Distinct Initial States and System Sizes

In order to show the robustness of the imperfect amplitude mediated chimeras with respect to various initial conditions, we have plotted the space-time evolution and snapshots of such dynamical states for the distribution of different initial states (see **Figure 2**). The menifestation of amplitude mediated chimeras is evident from the space-time plots, **Figures 2a–c**, which are plotted for random distribution of initial conditions between 0 to 1, symmetric cluster and asymmetric cluster initial states, respectively. The corresponding snapshots are shown in **Figures 2d–f**. From **Figure 2**, it is clear that the observed imperfect amplitude mediated states are robust against random and cluster initial conditions.

Further, it is also found that the observed imperfect amplitude mediated chimeras are robust againt system size (see **Figure 3**). The space-time plots and snapshots in **Figure 3** clearly depict the persistence of amplitude mediated chimera state even while increasing the system size to $N = 200$, $N = 500$ and $N = 1000$, respectively.

The dynamical transitions exhibited by the coupled Stuart-Landau oscillators will be described in the following as a function of the coupling strength.

4. DYNAMICAL TRANSITIONS IN COUPLED STUART-LANDAU OSCILLATORS

To start with, the dynamical behavior exhibited by the nonlocally coupled Stuart-Landau oscillators is inspected through the space-time and snapshot plots of the variables x_i, which are shown in **Figure 4**, for the coupling range $r = 0.4$. We find that a transition takes place from traveling wave (TW) state to imperfect amplitude mediated chimera (IAMC) state and finally to death states. In case of death states, the coupled Stuart-Landau oscillators exhibit multi-chimera death states (MCDs) through cluster oscillation death (COD) and cluster chimera death (CCD) states. As noted above, the network exhibits traveling wave (TW) state as shown in **Figures 4a,f** for the coupling strength $\epsilon = 0.7$. It is to be noted that here all the oscillators in the network oscillate homogeneously about the origin with the same frequency and constant velocity. The emergence of the imperfect amplitude mediated chimera (IAMC) state is observed for further increase in the coupling strength as depicted in **Figures 4b,g** for $\epsilon = 0.9$. In this state the oscillators in the network split into synchronized and desynchronized groups with amplitude variations. The oscillators hop between the synchronized and the desynchronized groups as a function of time, which can be clearly visualized in **Figure 1a** for sufficiently large time interval, but it resembles stationary amplitude mediated chimera for a short time interval (see **Figure 4b**). The synchronized group of oscillators oscillates with smaller amplitudes both in the upper and lower branches of the inhomogeneous state whereas the desynchronized group oscillates homogeneously about the origin. On increasing the coupling strength further, the oscillators with homogeneous oscillations populate either the lower or the upper branches of the inhomogeneous steady state, while the oscillators with small inhomogeneous oscillations settle as steady states in the respective branches resulting in a two cluster oscillation death (2COD) state. As a result, all the oscillators in the network occupy either the upper or lower branches of the inhomogeneous steady states as shown in **Figures 4c,h** for $\epsilon = 1.0$. The emergence of multi-chimera death (MCD) state via two cluster chimera death (2CCD) (see **Figures 4d,i** for $\epsilon = 1.12$) is observed upon increasing ϵ further as shown in **Figures 4e,j** for $\epsilon = 1.2$. In the 2CCD state, the oscillators in the cluster edges populate either the upper or the lower branches of the inhomogeneous state randomly and the MCD state is characterized by multiple coherent and incoherent domains of the death states. We may conclude that the imperfect amplitude mediated chimera mediates the transition from traveling wave state to death state.

We further note that the separation of the homogeneous and inhomogeneous oscillations in the imperfect amplitude mediated

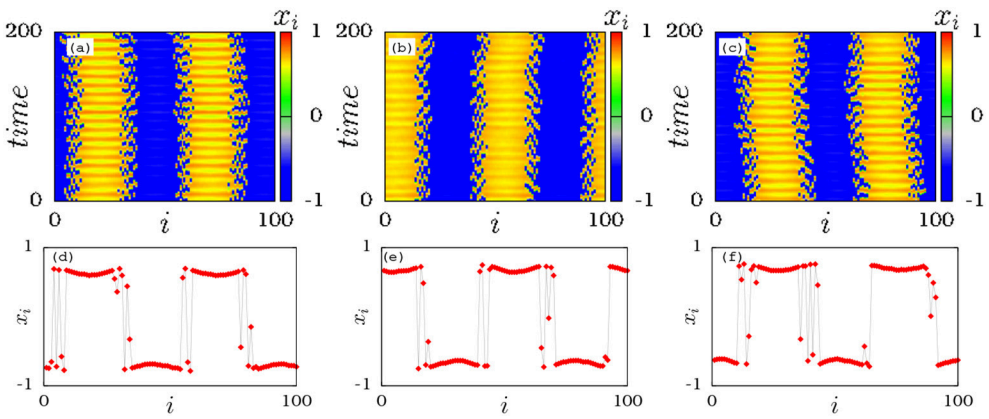

FIGURE 2 | Space-time evolution of amplitude mediated chimera for the distribution of initial states **(a)** between 0 – 1 randomly, **(b)** symmetric cluster, and **(c)** asymmetric clusters. The corresponding snapshots of **(a–c)** are shown in **(d–f)**. Parameters are the same as in **Figure 1**.

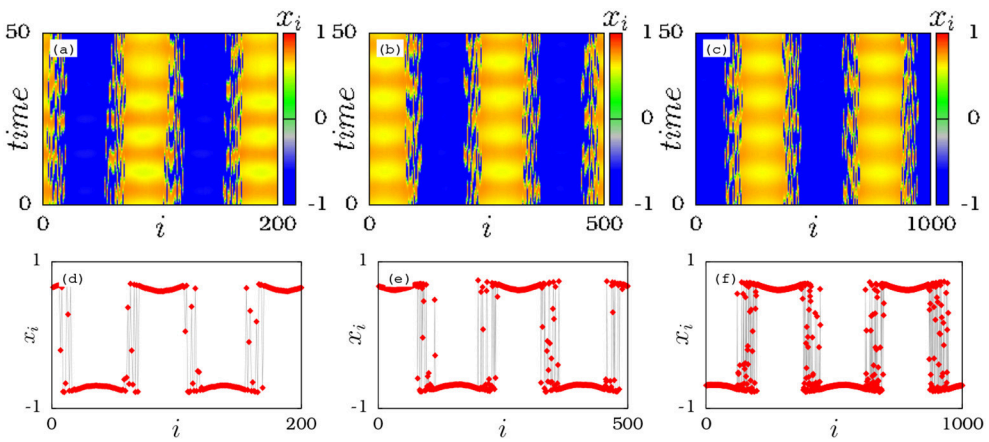

FIGURE 3 | Space-time evolution of amplitude mediated chimera as a function of the size of the network for **(a)** $N = 200$, **(b)** $N = 500$, and **(c)** $N = 1000$. **(d–f)** Correspond to the snapshots in **(a–c)**. Other parameters are the same as in **Figure 1**.

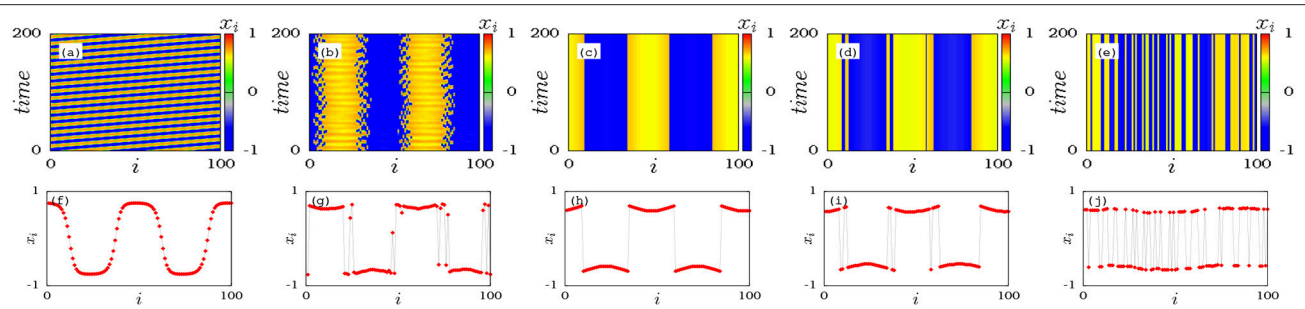

FIGURE 4 | Dynamical behavior of the coupled Stuart-Landau oscillators as a function of coupling strength ϵ for the coupling range $r = 0.4$. Space-time plots of **(a)** Traveling wave (TW) state for $\epsilon = 0.7$, **(b)** imperfect amplitude mediated chimera (IAMC) for $\epsilon = 0.9$, **(c)** two cluster oscillation death (2COD) for $\epsilon = 1.0$, **(d)** two cluster chimera death (2CCD) for $\epsilon = 1.12$ and **(e)** multi-chimera death (MCD) state for $\epsilon = 1.2$. The corresponding snapshots are shown in the lower panel **(f–j)**, respectively. Parameters: $r = 0.4$, $\omega = 1.0$, $\lambda = 1.0$, and $N = 100$.

chimera state is impossible for a large time interval since these states swing in time alternately in a random fashion. In order to overcome this difficulty, we have considered the evolution of the oscillators constituting the imperfect amplitude mediated chimera in a short time interval as in **Figure 5a**, which depicts the time evolution of distinct oscillators in the time interval 0

to 500, where the oscillators x_{20} and x_{45} are the representative oscillators from the inhomogeneous group whereas x_4 is the representative oscillator from the homogeneous group. The phase space dynamics of the representative oscillators are shown in **Figure 5b**. It is evident from the figures that the oscillator from the incoherent group x_4 ($i = 4$) oscillates about the origin quasi-periodically while the oscillators from the coherent group, x_{20} ($i = 20$) and x_{45} ($i = 45$), oscillate in the upper and lower branches of the inhomogeneous state with smaller amplitudes, respectively. In addition, to distinguish the homogeneous and inhomogeneous states, we have calculated the finite-time average of the variable y_i by dividing the total time (T_{tol}) into p bins of equal size $q = \frac{T_{tol}}{p}$ (in this case $T_{tol} = 500$, which we have divided into 5 bins of equal size $q = 100$, see **Figure 5a**). Then the center of mass for the finite-time average of the variable can be estimated by using the formula $< y_{i_{(av)}} > = \int_{\beta_1}^{\beta_2} \frac{y_i(t)dt}{q}$, where $\beta_1 = q(p-1)+1$ and $\beta_2 = pq$. Here p is the number of bins and q is the finite-time period of the oscillations. The average value of the state variable $< y_{i_{(av)}} >$ has been calculated for the homogeneous and inhomogeneous oscillations in **Figure 5**, which takes nonzero value for inhomogeneous oscillations (denoted by squares in **Figure 5b**) and nearly null value for the homogeneous oscillations (represented by a diamond in **Figure 5b**).

In addition, the above dynamical transition is also analyzed by estimating the average number of inhomogeneous oscillators. In the traveling wave (TW) state, all the oscillators oscillate homogeneously about the origin whereas some of the oscillators take nonzero center of mass values in the amplitude mediated chimera state constituting the inhomogeneous state. Thus the coherent oscillators in the inhomogeneous state oscillate with small amplitudes with nonzero value of the finite-time average whereas the incoherent oscillators in the homogeneous states oscillate with large amplitudes and null value of the finite-time average. The nonzero value of the finite-time average of the (individual) oscillators indicate that all the oscillators are in the inhomogeneous states, i.e., death states. The strength of inhomogeneous oscillators among the total population in a dynamical state can be found from the following relation,

$$K = 1 - \frac{\sum_{i=1}^{N} H_{y_i}}{N}, \quad H_{y_i} = \Theta(\delta - < y_{i_{(av)}} >), \tag{2}$$

where δ is a predefined threshold value and $\Theta(.)$ is the Heaviside step function. The strength of inhomogeneous oscillators (K) shows null value for the traveling wave state and unity for the death state. The value of K lying between $0 < K < 1$ corresponds to the amplitude mediated chimera state. To understand the transition among the observed dynamical states, we have plotted the strength of inhomogeneous oscillators (K) in the network as a function of the coupling strength ϵ for two distinct coupling ranges $r = 0.2$ and $r = 0.4$ (which have been earlier traced along the lines L_1 and L_2 in **Figure 7**) in **Figures 6A,B**, respectively. It is evident from the figures that the transition takes place from traveling wave to cluster oscillation death via amplitude mediated chimera state. Shaded region corresponds to the imperfect amplitude mediated chimera which constitutes the intermediate state between the traveling wave and the coherent death states.

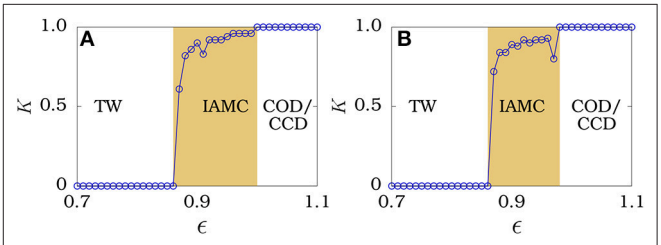

FIGURE 6 | Strength of inhomogeneous oscillators in a network as a function of the coupling strength ϵ for coupling ranges **(A)** $r = 0.2$ and **(B)** $r = 0.4$ which have been traced along the lines L_1 and L_2 in **Figure 7**. TW, IAMC, COD/CCD are the traveling wave, imperfect amplitude mediated chimera, cluster oscillation death or cluster chimera death states, respectively. Parameters: $\omega = 1.0$, $\lambda = 1.0$, and $N = 100$.

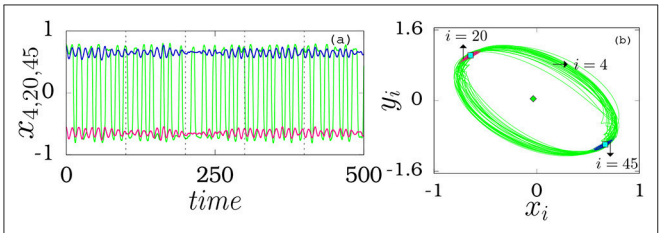

FIGURE 5 | (a) Time series and **(b)** phase portraits of representative oscillators from the homogeneous and inhomogeneous states constituting the imperfect amplitude mediated chimera. The oscillators x_i, $i = 20, 45$ are from the upper and lower branches of the inhomogeneous state. The oscillator $x_j, i = 4$, represents the homogeneous oscillations from the desynchronized group. The corresponding time average of the homogeneous and inhomogeneous oscillations are denoted by diamond and squares in **(b)**. Parameters are the same as in **Figure 1**.

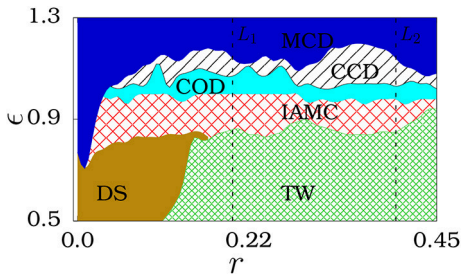

FIGURE 7 | Two parameter plot in (r, ϵ) space. DS, TW, and IAMC represent the desynchronized state, traveling wave state and imperfect amplitude mediated chimera state, respectively. COD, CCD, and MCD denote the cluster oscillation death, cluster chimera death and multi-chimera death states, respectively. Parameters are the same as in **Figure 6**.

5. GLOBAL DYNAMICAL BEHAVIOR IN COUPLED STUART-LANDAU OSCILLATORS

The global dynamical behavior of the nonlocally coupled Stuart-Landau oscillators is shown as a two-parameter phase diagram (see **Figure 7**) in the (r, ϵ) space. For smaller values of the coupling range, there is a transition from desynchronized state to death state via the imperfect amplitude mediated chimera as a function of the coupling strength. On the other hand, for larger values of the coupling range r, the coupled system exhibits transition from the traveling wave state to the death states via imperfect amplitude mediated chimera as a function of the coupling strength. For larger values of the coupling strength, the number of oscillators exhibiting homogeneous large oscillations (constituting incoherent domain of the imperfect amplitude mediated chimera) decreases and finally settles among one of the branches of the inhomogeneous steady state resulting in the coherent oscillation death state in almost the entire coupling range of r. The coherent oscillation death states manifest as a cluster chimera death state and then as a stable multi-chimera death state for further larger values of the coupling strength in the entire coupling range r. We also note here that the structure of the two parameter plot is similar for any other set of initial conditions and that the coexistence of distinct dynamics takes place only near the boundaries due to multistabilities among the dynamical states.

The oscillators in the network segregate into different numbers of clusters as a function of the coupling range r, as shown in **Figure 8**. The system of coupled Stuart-Landau oscillators exhibit more number of clusters for smaller coupling range than that of larger coupling range. Eleven cluster states are observed for coupling range $r = 0.06$ as depicted in **Figure 8a**. Upon increasing the coupling range to $r = 0.14$ and $r = 0.26$, it is observed that the number of clusters decreases to five and three, respectively, as illustrated in **Figures 8b,c**. The number of clusters become two for the coupling range $r = 0.4$ (see **Figure 8d**). It is also evident from the figures that the size of the clusters increases while the number of clusters decreases. It is also found that the number of clusters in the amplitude mediated chimera, cluster oscillation death and cluster chimera death states exponentially decreases with increase in the coupling range r. The number of clusters (n_0) as a function of the coupling range r is depicted in **Figure 9**, which clearly indicates the exponential decrease of the number of clusters. It is also evident from the inset of **Figure 9** that the system obeys a power law relation $n_0 = r^a$ as a function of the nonlocal coupling range r with best fit $a = -0.505$. The open circles in the inset denote numerical data, while the corresponding best fit is shown by solid line (red). It is also noticed that the system exhibits symmetric clusters in the oscillation death state as a function of coupling range.

For any set of initial conditions, including random, symmetric or asymmetric cluster conditions, the system exhibits only symmetric clusters in the death states which are clearly demonstrated through the transient behavior in **Figure 10**. The emergence of symmetric clusters in the oscillation death states from the random distribution of (x_i, y_i) between -1 to $+1$ and 0 to 1 are depicted in **Figures 10a,b**, respectively. The symmetric initial state distribution $((x_j, y_j) = (+1, -1)$ for $j = 1, 2.., \frac{N}{2}$ and $(x_j, y_j) = (-1, +1)$ for $j = \frac{N}{2} + 1, .., N)$ induced symmetric cluster death states is evident from **Figure 10c**. Analogously, the asymmetric distribution of initial states also exhibits symmetric cluster death states which is shown in **Figure 10d**.

6. EFFECT OF NOISE INTENSITY ON AMPLITUDE MEDIATED CHIMERA

The robustness of the imperfect amplitude mediated chimera state is further analyzed in the system (1) by introducing a Gaussian white noise. The system equation with the addition of

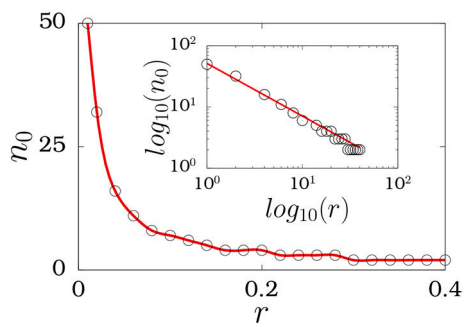

FIGURE 9 | Exponential decay of the number of clusters at $\epsilon = 1.0$ in the inhomogeneous states of cluster oscillation death as a function of the nonlocal coupling range(r). The corresponding power law fit is shown in the inset. The unfilled circles in the inset denote the numerical data and corresponding power law fit is shown by solid line.

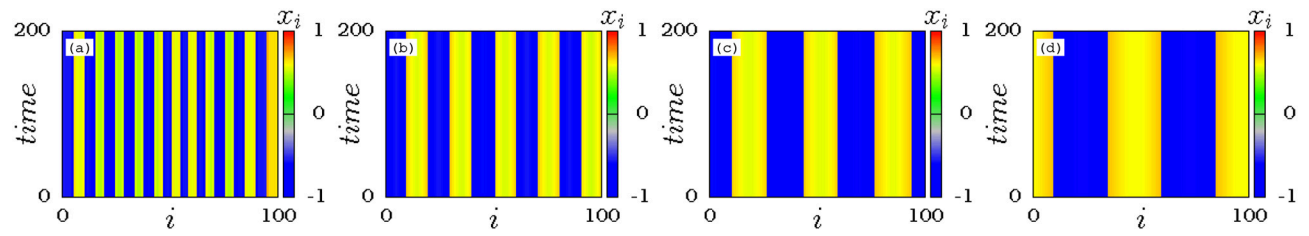

FIGURE 8 | Decreasing number of clusters with increasing value of the coupling range r for the coupling strength $\epsilon = 1.0$: **(a)** 11 clusters for $r = 0.06$, **(b)** 5 clusters for $r = 0.14$, **(c)** 3 clusters for $r = 0.26$ **(d)** 2 clusters for $r = 0.4$. Other parameters $\lambda = 1.0$, $\omega = 1.0$, and $N = 100$.

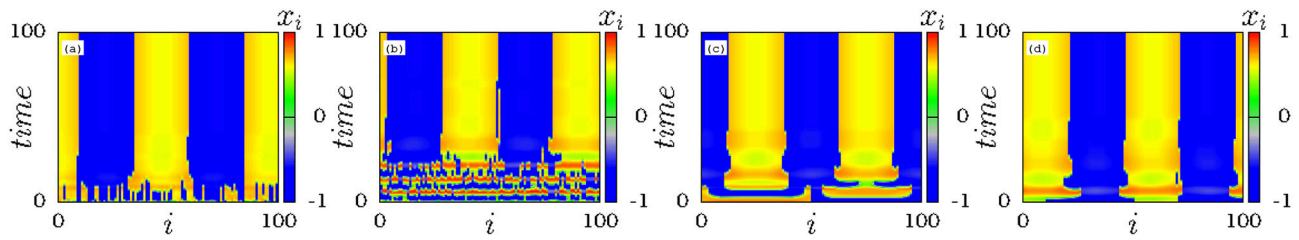

FIGURE 10 | Transient plots for the emergence of symmetric cluster ocillation death states from distict initial states at $r = 0.4$ and $\epsilon = 1.0$. The initial states (x_i, y_i) are distributed **(a)** randomly between -1 to +1, **(b)** randomly between 0 to 1, **(c)** in symmetric cluster, and **(d)** asymmetric cluster conditions. Other parameters are same as in **Figure 8**.

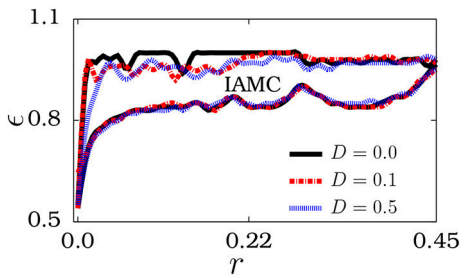

FIGURE 11 | Region of imperfect amplitude mediated chimera (IMAC) states for noise intensities $D = 0.0$ (solid line), $D = 0.1$ (dot-dashed line), and $D = 0.5$ (dotted line).

Gaussian white noise can be expressed as,

$$\dot{x}_i = (\lambda - x_i^2 - y_i^2)x_i - \omega y_i + \frac{\epsilon}{2P}\sum_{k=i-P}^{i+P}(x_k - x_i) + \sqrt{2D}\zeta_i(t),$$
$$\dot{y}_i = (\lambda - x_i^2 - y_i^2)y_i + \omega x_i - \frac{\epsilon}{2P}\sum_{k=i-P}^{i+P}(y_k - y_i), \quad i = 1, 2, ..., N, \tag{3}$$

where $\zeta_i(t) \in R$ is the Gaussian white noise and D is the intensity of noise. Here $\langle \zeta_i(t) \rangle = 0$, $\forall i$, and $\langle \zeta_i(t)\zeta_i(t') \rangle = \delta_{ij}\delta(t - t')$, $\forall i, j$, where δ_{ij} and $\delta(t - t')$ are the Kronecker-delta and delta distribution, respectively. **Figure 11** is plotted for the regions of imperfect amplitude mediated chimera state in the (r, ϵ) space for three different noise intensities, namely $D = 0.0$, $D = 0.1$ and $D = 0.5$ which are denoted by solid, dot-dashed and dotted lines, respectively. It is evident from the figures that the emergence imperfect amplitude mediated chimera even for increasing larger values of noise intensity which confirms their robustness against noise.

7. CONCLUSION

We have investigated the dynamical transitions in a network of nonlocally coupled Stuart-Landau oscillators with combined attractive and repulsive couplings. We found that the competing attractive and repulsive interactions induce imperfect amplitude mediated chimera states. These states are characterized by the oscillators constituting the synchronized and desynchronized groups, which drift randomly between the homogeneous and inhomogeneous states as a function of time. Hence it becomes impossible to determine homogeneous and inhomogeneous groups of oscillators. To overcome this difficulty, we have estimated the finite-time average of each oscillators to distinguish each group. Further, we have distinguished each dynamical state by calculating the strength of the inhomogeneous oscillators in a total population of a network. We found that the observed imperfect amplitude mediated chimera mediates the transition between the oscillatory and oscillation death states and turns out to be the transition route for the cluster oscillation death state. We have also calculated the number of clusters in the oscillation death states as a function of the coupling range. We found that the number of clusters decays exponentially as a function of the coupling range and obeys a power law relation with the nonlocal coupling range.The obtained imperfect amplitude mediated chimera state is robust against various initial states and different sizes of the network. Finally, we also found that the observed imperfect amplitude mediated chimera state is robust against noise by introducing a Gaussian white noise.

AUTHOR CONTRIBUTIONS

VKC formulated the problem in consultation with the other authors and drafted the manuscript. KS carried out the entire study of the work and completed the manuscript. DVS and ML critically read and revised the manuscript. All the authors discussed the results, drew conclusions and edited the manuscript.

ACKNOWLEDGMENTS

KS sincerely thanks the CSIR for a fellowship under SRF Scheme (09/1095(0037)/18-EMR-I). The work of VKC forms part of a research project sponsored by INSA Young Scientist Project under Grant No. SP/YSP/96/2014 and SERB-DST Fast Track scheme for young scientists under Grant No. YSS/2014/000175. DVS is supported by the CSIR EMR Grant No. 03(1400)/17/EMR-II. The work of ML is supported by DST-SERB Distinguished Fellowship.

REFERENCES

1. Pikovsky A, Rosenblum M, Kurths J. *Synchronization: A Universal Concept in Nonlinear Sciences*. Cambridge, UK: Cambridge University Press (2001).
2. Kuramoto Y, Battogtokh D. Coexistence of coherence and incoherence in nonlocally coupled phase oscillators. *Nonlinear Phenom Complex Syst.* (2002) 5:380. Available online at: https://arxiv.org/abs/cond-mat/0210694
3. Schneider I, Kapeller M, Loos S, Zakharova A, Fiedler B, Schöll E. Stable and transient multicluster oscillation death in nonlocally coupled networks. *Phys Rev E* (2015) 92:052915. doi: 10.1103/PhysRevE.92.052915
4. Majhi S, Muruganandam P, Ferreira FF, Ghosh D, Dana SK. Asymmetry in initial cluster size favors symmetry in a network of oscillators. *Chaos* (2018) 28:081101. doi: 10.1063/1.5043588
5. Omelchenko I, Omel'chenko OE, Hövel P, Schöll E. When nonlocal coupling between oscillators becomes stronger: patched synchrony or multichimera states. *Phys Rev Lett.* (2013) 110:224101. doi: 10.1103/PhysRevLett.110.224101
6. Sethia GC, Sen A, Johnston GL. Amplitude-mediated chimera states. *Phys Rev E* (2013) 88:042917. doi: 10.1103/PhysRevE.88.042917
7. Omelchenko I, Maistrenko Y, Hövel P, Schöll E. Loss of coherence in dynamical networks: spatial chaos and chimera states. *Phys Rev Lett.* (2011) 106:234102. doi: 10.1103/PhysRevLett.106.234102
8. Vadivasova TE, Strelkova GI, Bogomolov SA, Anishchenko VS. Correlation analysis of the coherence-incoherence transition in a ring of nonlocally coupled logistic maps. *Chaos* (2016) 26:093108. doi: 10.1063/1.4962647
9. Semenova N, Zakharova A, Schöll E, Anishchenko V. Does hyperbolicity impede emergence of chimera states in networks of nonlocally coupled chaotic oscillators? *Europhys. Lett.* (2015) 112:40002. doi: 10.1209/0295-5075/112/40002
10. Bogomolov SA, Slepnev AV, Strelkova GI, Schöll E, Anishchenko VS. Mechanisms of appearance of amplitude and phase chimera states in ensembles of nonlocally coupled chaotic systems. *Commun Nonlin Sci Numer Simulat.* (2017) 43:25–36. doi: 10.1016/j.cnsns.2016.06.024
11. Gopal R, Chandrasekar VK, Senthilkumar DV, Venkatesan A, Lakshmanan M. Effect of asymmetry parameter on the dynamical states of nonlocally coupled nonlinear oscillators. *Phys Rev E* (2015) 91:062916. doi: 10.1103/PhysRevE.91.062916
12. Hizanidis J, Kanas VG, Bezerianos A, Bountis T. Chimera states in networks of nonlocally coupled Hindmarsh–Rose neuron models. *Int J Bifurcat Chaos* (2014) 24:1450030. doi: 10.1142/S0218127414500308
13. Omelchenko I, Provata A, Hizanidis J, Schöll E, Hövel P. Robustness of chimera states for coupled FitzHugh-Nagumo oscillators. *Phys Rev E* (2015) 91:022917. doi: 10.1103/PhysRevE.91.022917
14. Bastidas VM, Omelchenko I, Zakharova A, Schöll E, Brandes T. Quantum signatures of chimera states. *Phys Rev E* (2015) 92:062924. doi: 10.1103/PhysRevE.92.062924
15. Tsigkri-DeSmedt ND, Hizanidis J, Hövel P, Provata A. Multi-chimera states and transitions in the Leaky Integrate-and-Fire model with nonlocal and hierarchical connectivity. *Eur Phys J* (2016) 225:1149–64. doi: 10.1140/epjst/e2016-02661-4
16. Hizanidis J, Panagakou E, Omelchenko I, Schöll E, Hövel P, Provata A. Chimera states in population dynamics: Networks with fragmented and hierarchical connectivities. *Phys Rev E* (2015) 92:012915. doi: 10.1103/PhysRevE.92.012915
17. Rosin DP, Rontani D, Gauthier DJ. Synchronization of coupled Boolean phase oscillators. *Phys Rev E* (2014) 89:042907. doi: 10.1103/PhysRevE.89.042907
18. Hagerstrom AM, Murphy TE, Roy R, Hövel P, Omelchenko I, Schöll E. Experimental observation of chimeras in coupled-map lattices. *Nat Phys.* (2012) 8:658–61. doi: 10.1038/nphys2372
19. Larger L, Penkovsky B, Maistrenko Y. Virtual chimera states for delayed-feedback systems. *Phys Rev Lett.* (2013) 111:054103. doi: 10.1103/PhysRevLett.111.054103
20. Larger L, Penkovsky B, Maistrenko Y. Laser chimeras as a paradigm for multistable patterns in complex systems. *Nat Commun.* (2015) 6:7752. doi: 10.1038/ncomms8752
21. Tinsley MR, Nkomo S, Showalter K. Chimera and phase-cluster states in populations of coupled chemical oscillators. *Nat Phys.* (2012) 8:662–5. doi: 10.1038/nphys2371
22. Nkomo S, Tinsley MR, Showalter K. Chimera states in populations of nonlocally coupled chemical oscillators. *Phys Rev Lett.* (2013) 110:244102. doi: 10.1103/PhysRevLett.110.244102
23. Wickramasinghe M, Kiss IZ. Spatially organized dynamical states in chemical oscillator networks: synchronization, dynamical differentiation, and chimera patterns. *PLoS ONE* (2013) 8:e80586. doi: 10.1371/journal.pone.0080586
24. Schmidt L, Schönleber K, Krischer K, García-Morales V. Coexistence of synchrony and incoherence in oscillatory media under nonlinear global coupling. *Chaos* (2014) 24:013102. doi: 10.1063/1.4858996
25. Kapitaniak T, Kuzma P, Wojewoda J, Czolczynski K, Maistrenko Y. Imperfect chimera states for coupled pendula. *Sci Rep.* (2014) **4**:6379. doi: 10.1038/srep06379
26. Zakharova A, Kapeller M, Schöll E. Chimera death: symmetry breaking in dynamical networks. *Phys Rev Lett.* (2014) 112:154101. doi: 10.1103/PhysRevLett.112.154101
27. Loos SAM, Claussen JC, Schöll E, Zakharova A. Chimera patterns under the impact of noise. *Phys Rev E* (2016) 93:012209. doi: 10.1103/PhysRevE.93.012209
28. Tumash L, Zakharova A, Lehnert J, Just W, Schöll E. Stability of amplitude chimeras in oscillator networks. *Europhys Lett.* (2017) 117:20001. doi: 10.1209/0295-5075/117/20001
29. Premalatha K, Chandrasekar VK, Senthilvelan M, Lakshmanan M. Stable amplitude chimera states in a network of locally coupled Stuart-Landau oscillators. *Chaos* (2018) 28:033110. doi: 10.1063/1.5006454
30. Sathiyadevi K, Chandrasekar VK, Senthilkumar DV. Stable amplitude chimera in a network of coupled Stuart-Landau oscillators. *Phys Rev E* (2018) 98:032301. doi: 10.1103/PhysRevE.98.032301
31. Sheeba JH, Chandrasekar VK, Lakshmanan M. Chimera and globally clustered chimera: impact of time delay. *Phys Rev E* (2010) 81:046203. doi: 10.1103/PhysRevE.81.046203
32. Bera BK, Ghosh D, Banerjee T. Imperfect traveling chimera states induced by local synaptic gradient coupling. *Phys Rev E* (2016) 94:012215. doi: 10.1103/PhysRevE.94.012215
33. Abrams DM, Mirollo R, Strogatz SH, Wiley DA. Solvable model for chimera states of coupled oscillators. *Phys Rev Lett.* (2008) 101:084103.
34. Buscarino A, Frasca M, Gambuzza LV, Hövel P. Chimera states in time-varying complex networks. *Phys Rev E* (2015) 91:022817. doi: 10.1103/PhysRevE.91.022817
35. Shima Si, Kuramoto Y. Rotating spiral waves with phase-randomized core in nonlocally coupled oscillators. *Phys Rev E* (2004) 69:036213. doi: 10.1103/PhysRevE.69.036213
36. Xie J, Knobloch E, Kao HC. Twisted chimera states and multicore spiral chimera states on a two-dimensional torus. *Phys Rev E* (2015) 92:042921. doi: 10.1103/PhysRevE.92.042921
37. Sethia GC, Sen A. Chimera states: the existence criteria revisited. *Phys Rev Lett.* (2014) 112:144101. doi: 10.1103/PhysRevLett.112.144101
38. Mukherjee R, Sen A. Amplitude mediated chimera states with active and inactive oscillators. *Chaos* (2018) 28:053109. doi: 10.1063/1.5031804
39. Sathiyadevi K, Chandrasekar VK, Senthilkumar DV, Lakshmanan M. Distinct collective states due to trade-off between attractive and repulsive couplings. *Phys Rev E* (2018) 97:032207. doi: 10.1103/PhysRevE.97.032207

40. Mishra A, Hens C, Bose M, Roy PK, Dana SK. Chimeralike states in a network of oscillators under attractive and repulsive global coupling. *Phys Rev E* (2015) 92:062920. doi: 10.1103/PhysRevE.92.062920
41. Frasca M, Bergner A, Kurths J, Fortuna L. Bifurcations in a star-like network of stuart–landau oscillators. *Int J Bifurcat Chaos* (2012) 22:1250173. doi: 10.1142/S0218127412501738
42. Kawaguchi S. Stability gap between off- and on-firing states in a coupled Ginzburg-Landau oscillator neural network. *Prog Theor Phys*. (2000) 104:709–721. doi: 10.1143/PTP.104.709
43. Uchiyama S. Flow version of statistical neurodynamics for oscillator neural networks. *Physica A* (2012) 391:2807–17. doi: 10.1016/j.physa.2011.12.026

Conflict of Interest Statement: The authors declare that the research was conducted in the absence of any commercial or financial relationships that could be construed as a potential conflict of interest.

frontiers in Applied Mathematics and Statistics

ORIGINAL RESEARCH
published: 18 February 2019
doi: 10.3389/fams.2019.00009

Cloning of Chimera States in a Large Short-term Coupled Multiplex Network of Relaxation Oscillators

Aleksei Dmitrichev, Dmitry Shchapin and Vladimir Nekorkin*

Nonlinear dynamics department, Institute of Applied Physics of the Russian Academy of Sciences, Nizhny Novgorod, Russia

A new phenomenon of the chimera states cloning in a large two-layer multiplex network with short-term couplings has been discovered and studied. For certain values of strength and time of multiplex interaction, in the initially disordered layer, a state of chimera is formed with the same characteristics (the same average frequency and amplitude distributions in coherent and incoherent parts, as well as an identical phase distribution in coherent part), as in the chimera which was set in the other layer. The mechanism of the chimera states cloning is examined. It is shown that the cloning is not related with synchronization, but arises from the competition of oscillations in pairs of oscillators from different layers.

Keywords: chimera states, chimera states cloning, dynamical mechanism, bifurcations, relaxation dynamics, multiplex networks

OPEN ACCESS

Edited by:
Anna Zakharova,
Technische Universität Berlin, Germany

Reviewed by:
Jakub Sawicki,
Technische Universität Berlin, Germany
Johanne Hizanidis,
University of Crete, Greece
Vadim S. Anishchenko,
Saratov State University, Russia

****Correspondence:***
Aleksei Dmitrichev
admitry@appl.sci-nnov.ru

Specialty section:
This article was submitted to Dynamical Systems, a section of the journal Frontiers in Applied Mathematics and Statistics

Received: *30 October 2018*
Accepted: *25 January 2019*
Published: *18 February 2019*

Citation:
Dmitrichev A, Shchapin D and Nekorkin V (2019) Cloning of Chimera States in a Large Short-term Coupled Multiplex Network of Relaxation Oscillators. Front. Appl. Math. Stat. 5:9. doi: 10.3389/fams.2019.00009

1. INTRODUCTION

Study of the formation of chimera states, i.e., peculiar types of hybrid states consisting of oscillators with coherent and incoherent behavior is one of the hot problems of the modern non-linear dynamics. To date, the chimera states have been discovered not only in a variety of theoretical papers [1–18], but also in experimental systems of various natures, for example, mechanical [19–22], optical [23, 24], chemical [25–29], and radiotechnical ones [30–33]. Similar states have also been registered in the neural activity of animal brain networks [34, 35]. At present, great attention is paid to studying of interaction of chimera states. The effects of generalized synchronization of chimera states [36], synchronization of chimera states in ensembles with asymmetrical connections [37], synchronization of chimera states in multiplex networks with delays [38], synchronization of chimera states in a two-layer multiplex network with adaptive connections in each layer [39], synchronization of chimera states in modular networks [40, 41], interaction of chimera states with fully coherent or fully incoherent states [42], etc. were explored. Note that in all these works the interaction of chimera states led to the formation of new chimera states (in some cases with synchronous coherent parts) that are different from the pre-existing chimera state. Recently we presented an example [43] of a two-layer multiplex network with seven oscillators in each layer where due to short-term interaction, one more chimera is emerged which is identical to the initial one (excluding the phase distribution of the incoherent part). We called this effect the chimera states cloning. In this article, we generalize the results of Dmitrichev et al. [43] for the case of a multiplex network with an arbitrary dimension of the layer and give a theoretical justification for the cloning effect based on the study of the fast-slow dynamics of the model using the methods of Geometric Singular Perturbation Theory (GPST) [44, 45].

2. MODEL OF MULTIPLEX NETWORK

We consider a two-layer multiplex network with the topology illustrated in **Figure 1A**. Each layer of the network is a ring of locally and linearly coupled relaxational oscillators with phase portrait shown in **Figure 1B**. The dynamics of the network is described by the following system:

$$\begin{aligned}
&\varepsilon\frac{du_j^i}{dt} = f(u_j^i) - v_j^i + d_r(u_{j-1}^i - 2u_j^i + u_{j+1}^i) + d_m(t)(u_j^{i+1} - u_j^i)\\
&\frac{dv_j^i}{dt} = u_j^i,\\
&d_m(t) = \begin{cases} 0, & t \le 0\\ d, & 0 < t \le T_c,\\ 0, & t > T_c, \end{cases}\\
&j = \overline{1,N}, u_{N+1}^i \equiv u_j^i, i = \overline{1,2}, u_j^3 \equiv u_j^1,
\end{aligned} \tag{1}$$

where $f(u) = -u(u^2 - a^2)(u^2 - b^2)(u^2 - c^2)$; the parameters controlling the dynamics of the layers are for definiteness fixed as $a = 0.32, b = 0.79, c = 1.166, \varepsilon = 0.001$, and $d_r = 0.006$; $d > 0$ and $T_c > 0$ are the parameters controlling the strength and the time of inter-layer (multiplex) interaction.

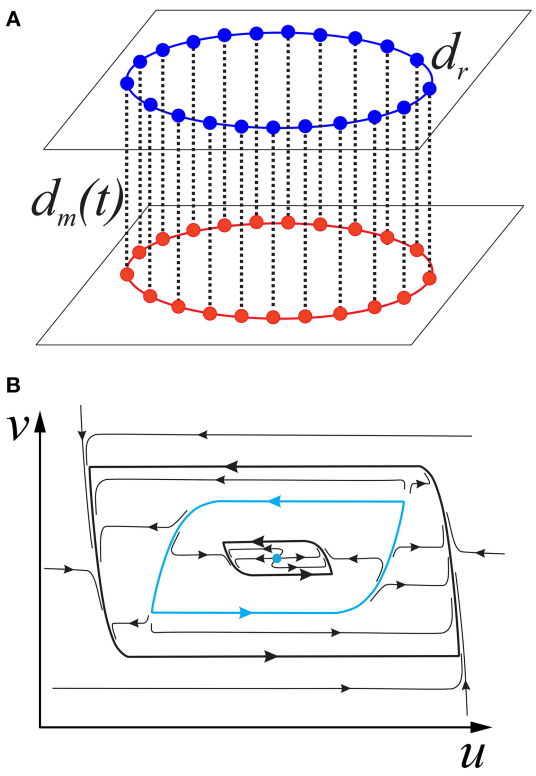

FIGURE 1 | (A) Topology of multiplex network. Red and blue dots depict correspondingly oscillators of first and second layer. Solid and doted lines depict correspondingly intra-layer and (multiplex) inter-layer couplings. **(B)** Qulitative phase portrait of a single oscillator. There exist two stable limit cycles (bold black lines) separated by an unstable limit cycle (bold blue line) and an unstable equilibrium state (bold blue dot) located at the origin.

If the oscillators do not interact with each other, i.e., $d_r = 0$; $d_m(t) \equiv 0$, then the dynamics of each oscillator is described by second-order equation. Two stable limit cycles with "low" and "high" amplitudes exist on the (u, v) phase plane (see **Figure 1B**). The regions of attraction of these cycles are separated by an unstable limit cycle. An unstable equilibrium state is located at the coordinate origin $(u = 0, v = 0)$. Thus, an oscillator can be either in the regime of low-amplitude oscillations with a dimensionless frequency of 0.0039 or, in the case of initial conditions "outside" the unstable cycle, in the regime of high-amplitude oscillations with a dimensionless frequency of 0.0021.

In our previous paper [32] we showed that various chimera states exist in a separate layer of system (1) at the chosen parameters and obtained chimera states at the experimental system consisting of seven bistable self-exciting oscillators with linear couplings. The example of chimera state is presented in **Figure 2A** by black crosses (distribution of instant phases φ, average amplitudes $< A >$, and average frequencies $< \omega >$). Coherent part of the chimera state is formed by first 99 ($j = 1 - 99$) oscillators with high-amplitude oscillations, and incoherent part is formed by oscillators with $j = 101 - 199$ that demonstrate alternately the low- and high-amplitude oscillations. The oscillation frequencies and phases of oscillators were calculated as follows. For definiteness, we consider the jth oscillator in the ith layer. Let $\{t_j^n\}$ be a sequence of time instants at which the output voltage of the oscillator increases and intersects the straight line $u_j^i = 0$; i.e.,

$$t_j^n = \{t : u_j^i(t) = 0, v_j^i(t) > 0\}.$$

Then, the oscillation phase of the jth oscillator at the time t is given by the expression

$$\phi_j = 2\pi\omega_j^n(t - t_j^n) \text{ for } t \in [t_j^n, t_j^{n+1}], \tag{2}$$

and $\omega_j^n = \frac{1}{t_j^n - t_j^{n-1}}$ is the instantaneous oscillation frequency. This definition of the phase is meaningful only if w_j^n are constant or quite close to each other. In the former case, the oscillator undergoes regular oscillations and the phase always varies at the same rate. In the latter case, oscillations can be, in particular, irregular and the phase is a piecewise linear function of the time. Furthermore, the phase introduced in Equation (2) describes the dynamics of only an individual oscillator decoupled from the remaining system. For this reason, to describe the dynamics of the system as a whole, it is more convenient to use the parameter $\varphi_j^k = \phi_j - \phi_k$ describing the oscillation phase of the jth oscillator with respect to oscillations of the reference kth oscillator. If φ_j^k is independent of time, this means the phase matching of oscillations of the kth and jth oscillators. In the general case of interaction between oscillators, instantaneous frequencies and amplitudes are not constant. For this reason, here and below, frequencies and amplitudes are calculated with averaging over a quite long time series

$$< \omega_j >= \frac{1}{n}\Sigma_n\omega_j^n$$

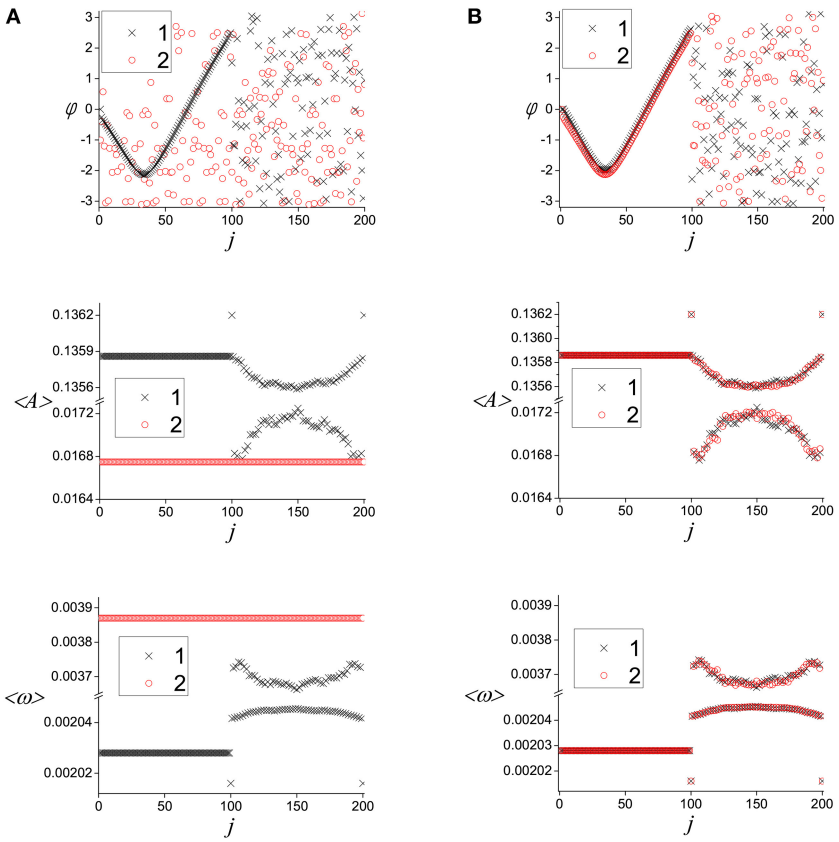

FIGURE 2 | Cloning of chimera state in system (1). Distribution of instant phases φ, average amplitudes $< A >$ and average frequencies $< \omega >$ (from up to bottom) at the initial instant of time **(A)**; after the interaction **(B)**. Indexes "1" (black cross) and "2" (red circle) correspond respectively to the first and second layer states. Parameters values: $a = 0.32, b = 0.79, c = 1.166, \varepsilon = 0.001, d_r = 0.006, d = 0.06, T_C = 1,000$, and $N = 200$.

and

$$< A_j >= \frac{1}{n}\Sigma_n A_j^n,$$

where $A_j^n = \{v_j^i(t) : u_j^i(t) = 0, v_j^i(t) > 0\}$.

Notice that in addition to the coherent and incoherent parts, the chimera state also contains two isolated oscillators at $j = 100$ and $j = 200$. Such solitary states exist due to the bistability of the network oscillators. The explanation of this phenomenon was given in Nekorkin et al. [46]. The bistability leads to formation of amplitude clusters with high- and low-amplitude oscillations and so to an amplitude gap (see the amplitude distribution in **Figure 2A**). The amplitude gap, in turn, causes a frequency gap. Since the magnitudes of gaps are quite large, diffusive coupling between the oscillators leads to emergence of solitary oscillators whose dynamics "smooths out" the dynamics of clusters (amplitude and frequency) having significantly different characteristics.

3. CLONING OF CHIMERA STATES

Let the chimera state exist in the first layer at the initial instant of time when there is no interaction between the layers (black crosses in **Figure 2A**). And the initial conditions in the second layer correspond to the low-amplitude oscillations with random initial phases (red circles in **Figure 2A**). Now if we switch on the interaction between the layers, and then after some time switch the interaction off, then we can obtain a clone of the initial chimera state in the second layer. For certain values of strength and time of multiplex interaction, in the second layer, a chimera state is formed with the same average frequency and amplitude distributions in coherent and incoherent parts, as well as an identical phase distribution in coherent part, as in the chimera which was set in first layer. The example of such cloning for interaction strength $d = 0.06$ and interaction time $T_c = 1,000$ is shown in **Figure 2**. Notice that, by definition, instantaneous phases of the incoherent parts in the chimera state should be random, and integral characteristics, e.g., average frequencies and amplitudes, are of fundamental importance for the incoherent part. For this reason, we believe that the coincidence of the phases of the incoherent parts is not necessary for the cloning of chimera states. Note that the cloning of chimera states occurs with certain initial conditions The role of initial conditions in more detail is discussed in section 4.

Next we show that the cloning effect is structurally stable. To do this, we introduce a reference layer with the index "0."

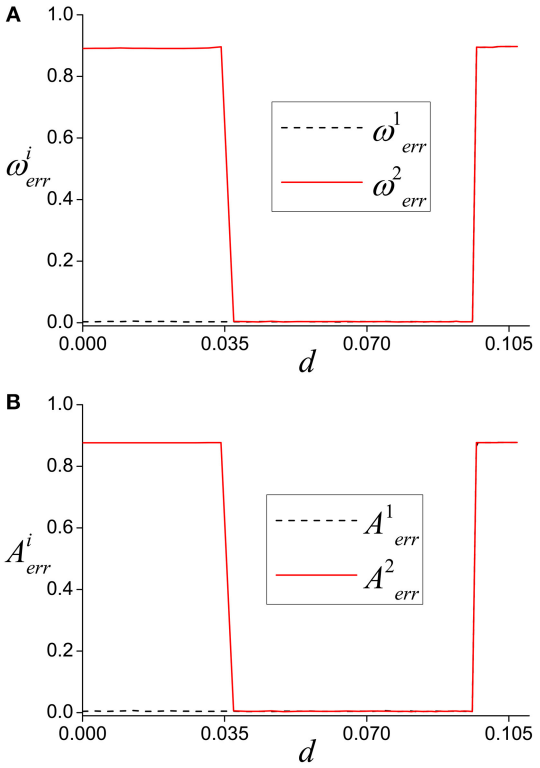

FIGURE 3 | Dependence of the maximum errors between the average frequencies ω^i_{err} **(A)** and amplitudes A^i_{err} **(B)** in the reference chimera state and the states occurring in first (dashed line) and second (solid line) layer. Parameters values: $a = 0.32, b = 0.79, c = 1.166, \varepsilon = 0.001, d_r = 0.006$, and $T_c = 1,000$.

Let us set in the reference layer a chimera state with the same characteristics as the original chimera that we set in the first layer. Then after the interaction of the first and the second layers we compare states formed in those layers with one in the reference layer using the following characteristics:

$$\omega^i_{err} = \max_{1\le j\le N} \left| \frac{< \omega_{i,j} > - < \omega_{0,j} >}{< \omega_{0,j} >} \right|,$$
$$A^i_{err} = \max_{1\le j\le N} \left| \frac{< A_{i,j} > - < A_{0,j} >}{< A_{0,j} >} \right|$$

where $< \omega_{i,j} >$ and $< A_{i,j} >$ are averaged frequencies and amplitudes of the oscillators with the number j of the ith layer; accordingly, $< \omega_{0,j} >$ and $< A_{0,j} >$ are those in the reference layer.

The results of such calculations for $T_c = 1,000$ are presented in **Figure 3**. They indicate that there is an interval of multiplex coupling strength $0.37 \le d \le 0.96$ where the states in all layers have the same averaged characteristics as the reference chimera state. Thus, the cloning occurs in the large enough interval of strength and so the effect is structurally stable.

4. THE CLONING MECHANISM

We showed above that cloning of chimera states takes place when strength of coupling between the elements of the same layer is much smaller than that between the elements of different layers ($d_r << d$, see **Figure 3**). So in the first approximation we can assume that the key role in cloning is played by the dynamics of (multiplex) pairs of elements taken from different layers. Next we consider the dynamics of a pair in more detail. It is described by the following system of equations:

$$\begin{aligned} \varepsilon \frac{du_1}{dt} &= f(u_1) - v_1 + d_m(t)(u_2 - u_1) \\ \varepsilon \frac{du_2}{dt} &= f(u_2) - v_2 + d_m(t)(u_1 - u_2) \\ \frac{dv_1}{dt} &= u_1, \\ \frac{dv_2}{dt} &= u_2, \end{aligned} \tag{3}$$

where $u_1 \equiv u^1_j, u_2 \equiv u^2_j, v_1 \equiv v^1_j, v_2 \equiv v^2_j$.

Notice also that to realize the cloning, initial conditions in non-interacting layers must be formed in a special way. In particular, a chimera state is set in the first layer with coherent part formed by the oscillators, demonstrating high-amplitude oscillations, and incoherent part formed by the oscillators demonstrating alternately low- and high-amplitude oscillations. In the second layer all oscillators are set in the regime of low-amplitude oscillations whose phases are randomly distributed. Moreover, after interaction, the elements of the second layer should switch to the regimes the corresponding elements of the first layer were in initial moment. Thus, we need to consider the evolution of a pair only for two types of initial conditions:

$(\text{I.C.})_1$ An oscillator of the first layer is in the regime of high-amplitude oscillations, while that of the second layer is in the regime of low-amplitude oscillations;

$(\text{I.C.})_2$ The oscillators of both layers are in the regime of low-amplitude oscillations.

4.1. Dynamics of a Pair of Constantly Coupled Oscillators

First, we study dynamics of a pair for the case when interaction between its oscillators is not limited by time. Then we obtain the following system of equations:

$$\begin{aligned} \varepsilon \frac{du_1}{dt} &= f(u_1) - v_1 + d(u_2 - u_1) \\ \varepsilon \frac{du_2}{dt} &= f(u_2) - v_2 + d(u_1 - u_2) \\ \frac{dv_1}{dt} &= u_1, \\ \frac{dv_2}{dt} &= u_2, \end{aligned} \tag{4}$$

Since $0 < \varepsilon \ll 1$, the system (4) belongs to the class of fast-slow systems. Such systems are characterized by the presence of two timescales (or speeds), namely, fast and slow ones. In the result, the trajectories of the systems have epochs of a slow and a fast movements. In our system u_1 and u_2 are fast variables, while

v_1 and v_2 are slow variables. Next to study the dynamics of the system we use GPST theory. According to the GPST, the partition of phase space $\mathbb{R}^4$ of system (4) into trajectories can be established by studying two subsystems. As $\varepsilon \to 0$, the trajectories of system (4) converge during fast epochs to the trajectories of the fast subsystem (or layer equations)

$$\begin{aligned}\frac{du_1}{d\tau} &= f(u_1) - v_1 + d(u_2 - u_1)\\ \frac{du_2}{d\tau} &= f(u_2) - v_2 + d(u_1 - u_2)\\ \frac{dv_1}{d\tau} &= 0,\\ \frac{dv_2}{d\tau} &= 0,\end{aligned} \tag{5}$$

where $t = \varepsilon\tau$. During slow epochs the trajectories of (4) converge to the trajectories of the reduced system (or the slow flow)

$$\begin{aligned}0 &= f(u_1) - v_1 + d(u_2 - u_1)\\ 0 &= f(u_2) - v_2 + d(u_1 - u_2)\\ \frac{dv_1}{dt} &= u_1,\\ \frac{dv_2}{dt} &= u_2,\end{aligned} \tag{6}$$

The goal of GPST is to use the fast and slow subsystems (5) and (6) to understand the dynamics of the full system (4) for $0 < \varepsilon \ll 1$.

4.1.1. Dynamics of the Fast Subsystem

From system (5) one can see that $v_1 = const$ and $v_2 = const$, so they play the role of additional parameters (denote them by v_1^0 and v_2^0 correspondingly). Thus, system (5) can be rewritten in the following gradient form

$$\begin{aligned}\frac{du_1}{d\tau} &= -\frac{\partial G}{\partial u_1}\\ \frac{du_2}{d\tau} &= -\frac{\partial G}{\partial u_2}\end{aligned} \tag{7}$$

where

$$G = -\int_0^{u_1} f(x)dx - \int_0^{u_2} f(x)dx + v_1^0 u_1 + v_2^0 u_2 + \frac{d}{2}(u_1 - u_2)^2.$$

Since

$$\frac{dG}{d\tau} = -(\frac{\partial G}{\partial u_1})^2 - (\frac{\partial G}{\partial u_2})^2,$$

the trajectories of system (7) [and so system (5)], except for equilibrium states, relax to one of the stable equilibrium states. Moreover, since the system is gradient their trajectories relax to the equilibrium states by the fastest way. The number and type of equilibrium states depend on the parameters and may change due to saddle-node bifurcations. For example, for $v_1^0 = v_2^0 = d = 0$ there are 49 equilibrium states, among which there are 16 stable and 9 unstable nodes and 24 saddles. The qualitative phase plane of system (7) in this case is shown in **Figure 4**.

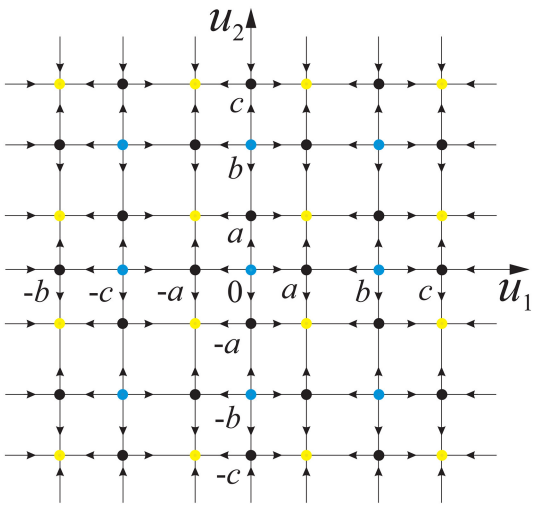

FIGURE 4 | Qualitative phase portrait of fast subsystem (7) for $v_1^0 = v_2^0 = d = 0$, $a = 0.32, b = 0.79$, and $c = 1.166$. The dots mark unstable nodes (blue), stable nodes (yellow), and saddles (black). The lines mark the separatrices of the saddle equilibrium states.

4.1.2. Dynamics of the Reduced Subsystem

The first two algebraic equations in system (6) define a critical manifold $S\{(u_1, u_2, v_1, v_2) \in \mathbb{R}^4 | f(u_i) - v_i + d(u_{i+1} - u_i) = 0, i = 1, 2, u_3 \equiv u_1\}$. Let us rewrite (6) in terms of the fast variables u_1 and u_2 to obtain the slow flow on S. For this, we differentiate algebraic Equation (6) with respect to t and combine the result with the equations for $\dot{v}_1$ and $\dot{v}_2$:

$$\begin{aligned}\left(\frac{df(u_1)}{du_1} - d\right)\frac{du_1}{dt} + d\frac{du_2}{dt} &= u_1\\ \left(\frac{df(u_2)}{du_2} - d\right)\frac{du_2}{dt} + d\frac{du_1}{dt} &= u_2\end{aligned} \tag{8}$$

System (8) is a system of linear inhomogeneous algebraic equations for derivatives $\frac{du_1}{dt}$ and $\frac{du_2}{dt}$. Determinant of its coefficient matrix

$$\Delta = \frac{df(u_1)}{du_1}\frac{df(u_2)}{du_2} - d\left(\frac{df(u_1)}{du_1} + \frac{df(u_2)}{du_2}\right).$$

If $\Delta \neq 0$, then system (8) has the only solution

$$\begin{aligned}\frac{du_1}{dt} &= \frac{1}{\Delta}\left[\frac{df(u_2)}{du_2}u_1 - du_1 - du_2\right]\\ \frac{du_2}{dt} &= \frac{1}{\Delta}\left[\frac{df(u_1)}{du_1}u_2 - du_1 - du_2\right].\end{aligned} \tag{9}$$

Note that in the four-dimensional phase space $\mathbb{R}^4$ of system (4), algebraic equation $\Delta = 0$ and two algebraic equations of system (6) define set $S^\Delta = \cup_j S_j^\Delta$. Any its element, S_j^Δ, defines a curve, where the fast and slow trajectories are stitched. According to GPST, each equilibrium state of fast subsystem (5) [and so (7)] in the phase space $\mathbb{R}^4$ of system (4) corresponds to a submanifold, whose stability with respect to the trajectories of the

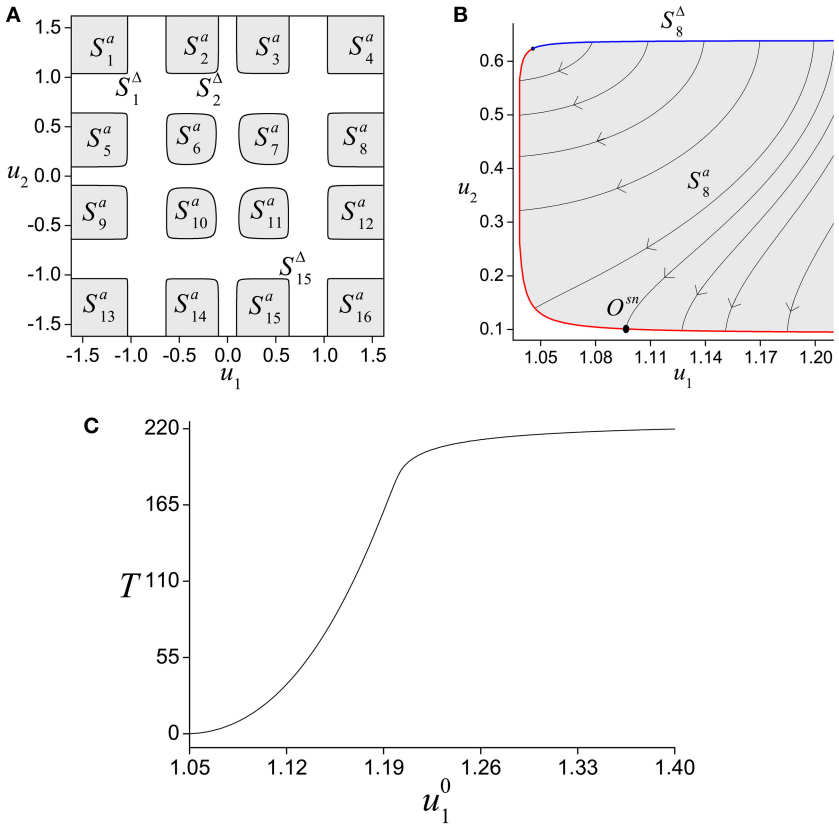

FIGURE 5 | (A) Mutual location of the stable slow submanifolds (S_j^a) of system (5) on the phase plane (u_1, u_2). The boundaries of stable submanifolds (S_j^Δ) defined by the equations $\Delta = 0$. **(B)** Trajectories behavior on slow submanifold S_8^a. **(C)** Dependence of motion time over submanifold S_8^a to its boundary S_8^Δ on the initial conditions. Parameter values: $a = 0.32, b = 0.79, c = 1.166$, and $d = 0.06$.

fast subsystem coincides with the stability of the corresponding equilibrium state. Since the coordinates of the equilibrium states of system (5) depend on two parameters v_1^0 and v_2^0, any such equilibrium state corresponds to a two-dimensional submanifold in the phase space of (4). The boundary of the submanifold is given by one of the curves S_j^Δ. Hence the curves S_j^Δ decompose the critical manifold S into some number of submanifolds of different stability

$$S = S_i^a \cup S_l^\Delta \cup S_k^r \cup S_j^\Delta \cup S_n^{sad},$$

where S_i^a denotes one of the stable submanifolds, S_k^r are the unstable submanifolds, and S_n^{sad} are the saddle submanifolds of the slow flow. Note that $\Delta > 0$ on submanifolds S_i^a and S_k^r, $\Delta < 0$ on submanifolds S_n^{sad} and $\Delta = 0$ on submanifolds S_l^Δ. The number of these submanifolds depends on the parameter d. For example, **Figure 5A** for $d = 0.06$ on the phase plane (u_1, u_2) depicts submanifolds $S_i^a, i = \overline{1,16}$, corresponding to stable nodes O_j^a of the fast subsystem and curves S_l^Δ.

Since the system (4) on submanifolds S_i^a has no equilibrium states and limit cycles, any trajectory starting on the submanifolds eventually leave them. For example, **Figure 5B** shows the behavior of trajectories on S_8^a starting on entering part of its boundary S_8^Δ (blue line) and going till the exit part of the boundary (red line). Note that, the time the trajectories stay on S_i^a varies depending on the initial conditions. The dependence for trajectories on S_8^a is shown in **Figure 5C**. Note that the dependence is a monotonically increasing function asymptotically tending to the value $T \approx 220$.

4.1.3. Dynamics of System (4) for Initial Conditions (I.C.)$_1$

Let us study the dynamics of system (4) for initial conditions (I.C.)$_1$. Note, the dynamics of system (4) is formed by the alternating dynamics of fast and slow epochs, which results in a "stitched" trajectory.

4.1.3.1. Slow epoch of motion

The initial conditions (I.C.)$_1$ corresponds to one of the stable submanifolds of slow motions $S_5^a, S_8^a, S_9^a, S_{12}^a$ (see **Figure 5A**). First let the initial conditions belong to S_8^a. The motions on S_8^a are defined by system (9). Since $\Delta > 0$ on S_8^a, we can de-singularize the slow flow near S_8^Δ by rescaling time with the factor Δ. This

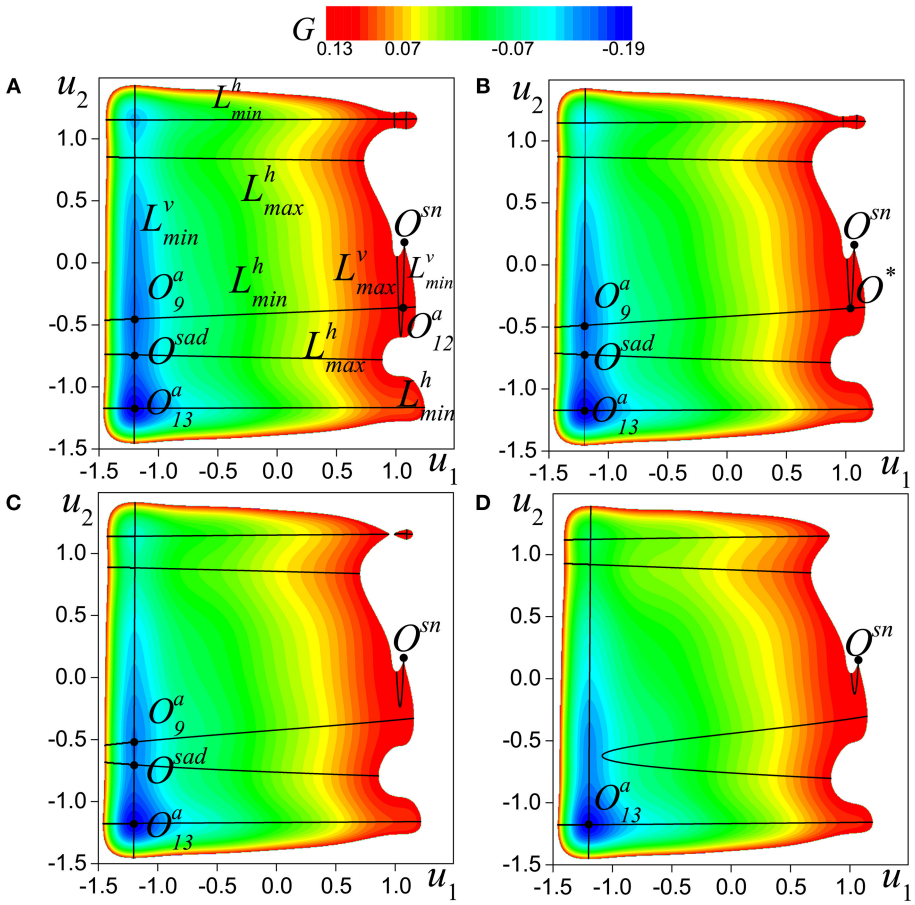

FIGURE 6 | A part of level map of the function $G(u_1, u_2)$ taken at the saddle-node equilibrium state $O^{sn}(u_1^0, u_2^0)$ of the boundary S_8^a [i.e., when $v_1^0 = f(u_1^0)$ and $v_2^0 = f(u_2^0)$] for **(A)** $d = 0.0075$, $(u_1^0 = 1.07178, u_2^0 = 0.166426)$; **(B)** $d = 0.0115$, $(u_1^0 = 1.07178, u_2^0 = 0.16196)$; **(C)** $d = 0.0150$, $(u_1^0 = 1.07178, u_2^0 = 0.15809)$; **(D)** $d = 0.0225$, $(u_1^0 = 1.07178, u_2^0 = 0.0.14980)$. Levels depicted are below the one of O^{sn} (marked by red color). White color marks region with higher levels of G. Curves L^h_{max}, L^h_{min} (respectively L^v_{max}, L^v_{min}) defined by Equation (14) are minimum and maximum of G on variable u_2 (respectively variable u_1). O^*, O^{sad} are additional saddle-node equilibrium states and O^a_9, O^a_{12}, and O^a_{13} are the node equilibrium states. Parameter values: $a = 0.32, b = 0.79$, and $c = 1.166$.

gives the following system:

$$\begin{aligned} \frac{du_1}{dt_n} &= \frac{df(u_2)}{du_2}u_1 - d(u_1 + u_2) \\ \frac{du_2}{dt_n} &= \frac{df(u_1)}{du_1}u_2 - d(u_1 + u_2), \end{aligned} \tag{10}$$

where $dt = \Delta dt_n$. System (6), and hence system (10), have the only equilibrium point at the origin. Therefore, the trajectories starting on S_8^a leave the submanifold at some points of its boundary S_8^Δ. Let $O^{sn}(u_1 = u_1^0, u_2 = u_2^0) \in S_8^\Delta$ be one of such exit points (see **Figure 5B**). Since the fast and slow trajectories of system (4) are glued together on S_8^Δ, the point O^{sn} is also the equilibrium state of the fast system (5). From this condition we find

$$\begin{aligned} v_1 &= f(u_1^0) + d(u_2^0 - u_1^0) \\ v_2 &= f(u_2^0) + d(u_1^0 - u_2^0). \end{aligned} \tag{11}$$

By using Equation (11) fast system (5) can be rewritten in the form

$$\begin{aligned} \frac{du_1}{d\tau} &= f(u_1) - f(u_1^0) + d(u_2 - u_2^0 - u_1 + u_1^0) \\ \frac{du_2}{d\tau} &= f(u_2) - f(u_2^0) + d(u_1 - u_1^0 - u_2 + u_2^0) \end{aligned} \tag{12}$$

The eigenvalues of the Jacobian matrix of (12) in the point O^{sn} are given by

$$\lambda_1 = 0, \lambda_2 = -2d + \frac{df(u_1)}{du_1}|_{u_1 = u_1^0} + \frac{df(u_2)}{du_2}|_{u_2 = u_2^0} < 0 \tag{13}$$

Because of Equation (13), the point O^{sn} is a saddle-node with an unstable separatrix and a stable nodal branch. Further we show that there are such values of the parameter d that the separatrix $W^u(O^{sn})$ tends to the stable node O^a_{13} as $t \to +\infty$.

4.1.3.2. Fast epoch of motion

Consider the level curves of the function $G(u_1, u_2) = C = const$, satisfying the condition $C \leq C^{sn}$, where $C^{sn} = G(u_1^0, u_2^0)$. Obviously, the curves of the level $\{G(u_1, u_2) = C^{sn}\}$ pass through the saddle-node O^{sn}. In **Figure 6A**, the curve of this level has a maximum value, i.e., the curves of the higher levels are not indicated (white color), and the curves of the level corresponding to the values of the lower levels ($C < C^{sn}$) are marked with different colors. Each color corresponds to the same value of C. Solid black lines in **Figure 6** show the critical lines

$$\begin{aligned}
L^h_{min} &= \{(u_1,u_2) \in R^2 | -f(u_2) + du_2 - du_1 + f(u_2^0) \\
&\quad + d(u_1^0 - u_2^0) = 0, -f'(u_2) + d > 0\} \\
L^h_{max} &= \{(u_1,u_2) \in R^2 | -f(u_2) - du_2 + du_1 + f(u_2^0) \\
&\quad + d(u_1^0 - u_2^0) = 0, -f'(u_2) + d < 0\} \\
L^v_{min} &= \{(u_1,u_2) \in R^2 | -f(u_1) + du_1 - du_2 + f(u_1^0) \\
&\quad + d(u_2^0 - u_1^0) = 0, -f'(u_1) + d > 0\} \\
L^v_{max} &= \{(u_1,u_2) \in R^2 | -f(u_1) + du_1 - du_2 + f(u_1^0) \\
&\quad + d(u_2^0 - u_1^0) = 0, -f'(u_1) + d < 0\}. \qquad (14)
\end{aligned}$$

At the points of these lines the following conditions are satisfied:

$$\begin{aligned}
&\frac{\partial G}{\partial u_2} = 0, \quad \frac{\partial^2 G}{\partial u_2^2} > 0, \quad \text{if } (u_1,u_2) \in L^h_{min} \\
&\frac{\partial G}{\partial u_2} = 0, \quad \frac{\partial^2 G}{\partial u_2^2} < 0, \quad \text{if } (u_1,u_2) \in L^h_{max} \\
&\frac{\partial G}{\partial u_1} = 0, \quad \frac{\partial^2 G}{\partial u_1^2} > 0, \quad \text{if } (u_1,u_2) \in L^v_{min} \\
&\frac{\partial G}{\partial u_1} = 0, \quad \frac{\partial^2 G}{\partial u_2^1} < 0, \quad \text{if } (u_1,u_2) \in L^v_{max}. \qquad (15)
\end{aligned}$$

Consider the asymptotic behavior of the separatrix of the saddle-node O^{sn}. Taking into account Equation (8), the location of the level curves of the function $\{G(u_1, u_2) = C^{sn}\}$ and lines (14), we establish that for the parameter value $d = 0.0075$ (**Figure 6A**) the separatrix $W^u(O^{sn})$ asymptotically tends to the equilibrium state O^a_{12}. Without changing the coordinates of the point O^{sn}, we increase the value of the parameter $d = 0.0115$ (**Figure 6B**). For this value of the parameter d the lines $L^h_{min}, L^v_{max}, L^v_{min}$ merge at one point, a saddle-node bifurcation of equilibrium states occurs, and a new equilibrium state O^* appear (see **Figure 6B**). With the further increase in the parameter, the equilibrium state O^* disappears, and following the arrangement of lines (14) and the level curves of the function G, we find that in this case the separatrix $W^u(O^{sn})$ tends to the node O^a_9 (**Figure 6C**). A further increase in the parameter d leads to the merging of the lines $L^h_{min}, L^h_{max}, L^v_{min}$ ($d = 0.020909 = d^*$). This corresponds to the merging of the node O^a_9 and the saddle O^{sad} (**Figure 6C**) and emerging of the saddle-node equilibrium state. For $d > d^*$, this equilibrium state disappears, and the separatrix $W^u(O^{sn})$ tends to the equilibrium state O^a_{13} (**Figure 6D**). It is clear that d^* depends on the coordinates of the point O^{sn}.

To describe such possible transitions, we introduced the distance R on the plane (u_1, u_2) of system (9) from the origin to

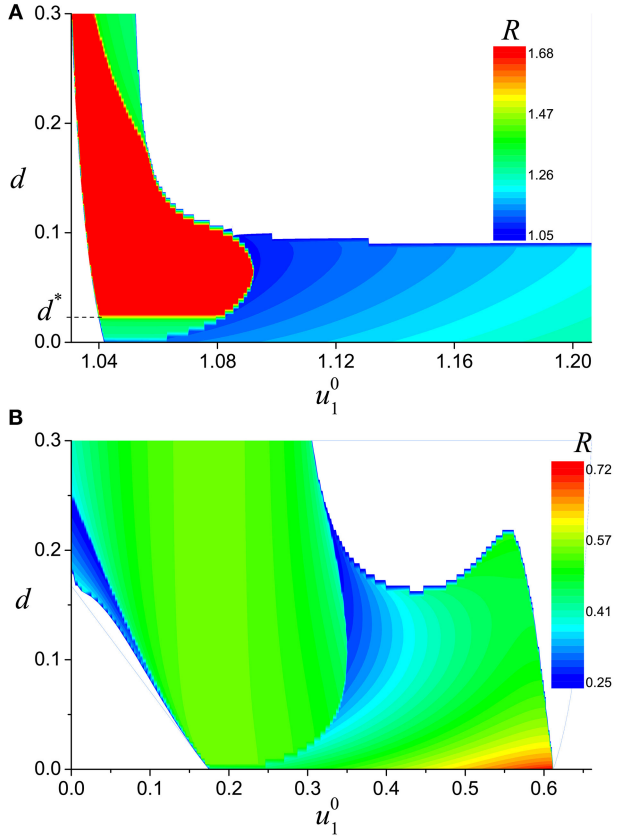

FIGURE 7 | The partition of (u_1^0, d) - parameter plane into areas corresponding to different transitions [along the trajectories of the fast system (7)] from the border of submanifold **(A)** S^a_8 **(B)** S^a_8. R is the distance from the origin of slow subsystem phase plane (u_1, u_2) to a next stable submanifold. The red color in **(A)** marks the region where the next manifold is S^a_{13}. Non-white colors in **(B)** mark the region where the next manifold is only one of S^a_6, S^a_7, S^a_{10}, S^a_{11}. Parameters values: $a = 0.32, b = 0.79, c = 1.166$, and $d = 0.06$.

S^a_i. Note that the largest value of R corresponds to the points of the submanifolds S^a_1, S^a_{13}, S^a_4, and S^a_{16}.

Figure 7A depicts the results of analyzing the behavior of the separatrix $W^u(O^{sn})$ for different values of u_1^0 belonging to the line of escape $(u_1^0, u_2^0) \in S^\Delta_8$ with the submanifold S^a_8 (see **Figure 5A**). For the values of u_1^0, d from the region marked by red color, the separatrix $W^u(O^{sn})$ of any of the saddle-nodes in the fast system (5) asymptotically tends to the stable node O^a_{13}. Since in the phase space $\mathbb{R}^4$ the equilibrium state corresponds to a stable manifold S^a_{13}, high-amplitude oscillations are established in both elements in the system (4). Note that the trajectories of the submanifold S^a_9 of the slow system (10) have a similar behavior. Since the function $\frac{\partial f}{\partial u}$ is even, system (10) does not change when converting $(u_1, u_2) \to (-u_1, -u_2)$. Thus, transitions from S^a_9 to S^a_{16} exist in $\mathbb{R}^4$, and high-amplitude oscillations are established in system (4). The initial conditions found by us do not exhaust the entire set of initial conditions under which the oscillation amplitude changes from low to high in the second oscillator.

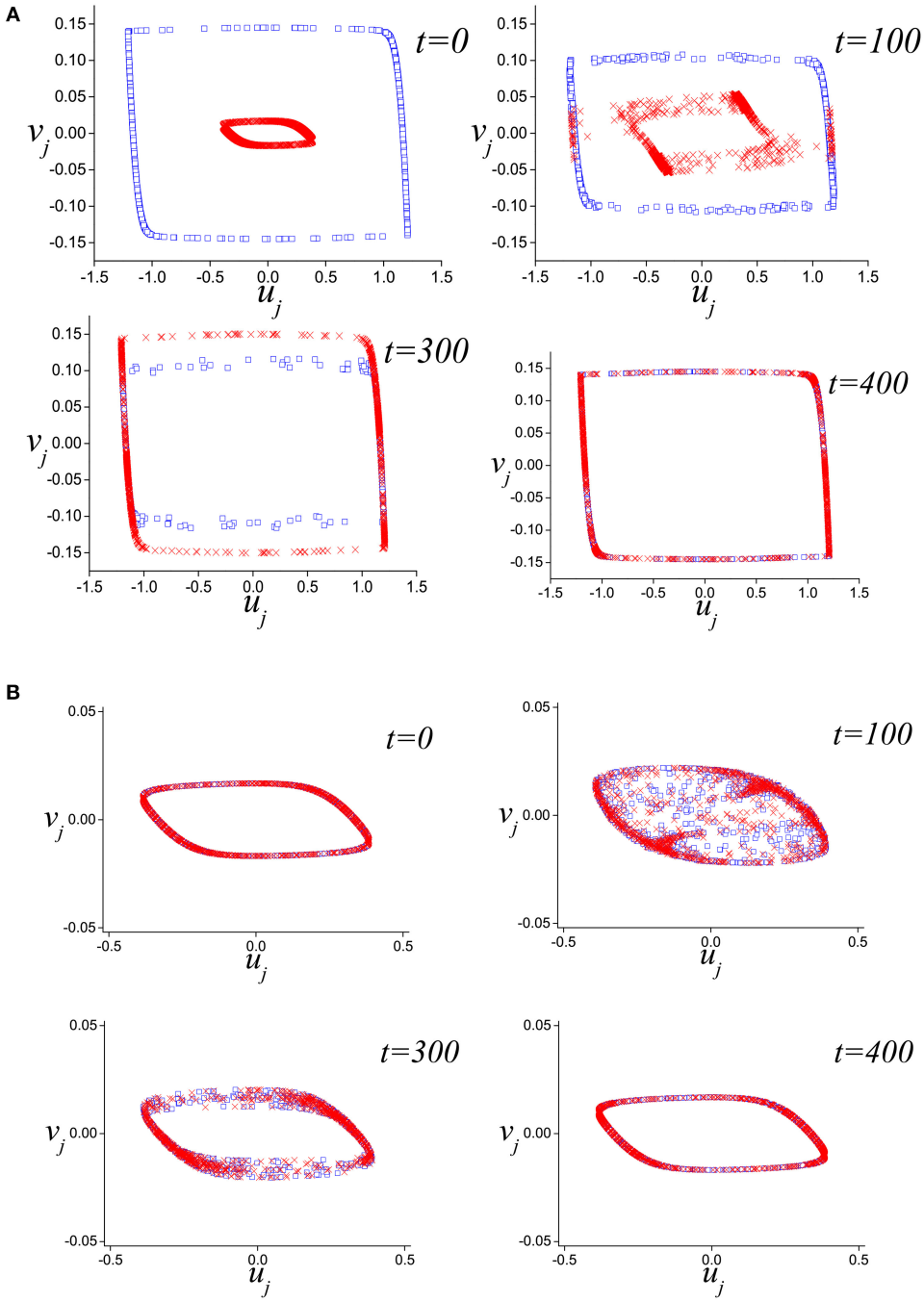

FIGURE 8 | Temporal snapshots of the pair of short-term coupled elements [system (3)] for 1,000 initial conditions such as **(A)** $(I.C.)_1$; **(B)** $(I.C.)_2$. Parameters values: $a = 0.32, b = 0.79, c = 1.166, \varepsilon = 0.001, d = 0.06$, and $T_C = 300$.

4.1.4. Dynamics of System (4) for Initial Conditions $(I.C.)_2$

Let us study the dynamics of system (4) for initial conditions $(I.C.)_2$. These conditions correspond to one of the stable submanifolds of slow motions S_6^a, S_7^a, S_{10}^a, and S_{11}^a. Similar to the case of $(I.C.)_1$ we have analyzed the behavior of the trajectories leaving the submanifolds. **Figure 7B** depicts the transitions of trajectories starting from the points at the boundary S_7^Δ of submanifold S_7^a obtained for different strength of coupling d. One can see that there are no transitions to submanifolds corresponding to high-amplitude oscillations. We have established that such behavior is also typical for other submanifolds, namely S_6^a, S_{10}^a, and S_{11}^a.

4.2. Dynamics of a Pair of Short-term Coupled Oscillators

So far, we have considered the dynamics of system (4) without any restrictions on the interaction time. However, in the initial model, the layers interact only during the time T_c. We numerically investigated the dynamics of system (3). For the initial conditions such as $(\text{I.C.})_1$, **Figure 8A** shows the behavior of 1,000 pair of oscillators, or in other words, 1,000 different initial conditions $(\text{I.C.})_1$ type, interacting during $T_c = 300$ and $d = 0.06$. For all initial conditions, after some transition process, high-amplitude oscillations are established in the interacting pairs. **Figure 8B** illustrates competition of oscillations in the pairs in the case of initial conditions such as $(\text{I.C.})_2$ type. Here, interaction of the pairs does not lead to high-amplitude oscillations, and the regime of low-amplitude oscillations persists.

The occurrence of high-amplitude oscillations for the initial conditions $(\text{I.C.})_1$ depends on the values of the parameters T_c and d. We examine this dependence numerically and the results are presented in **Figure 9**. The color gradation on the plane (d, T_c) shows the dependence of the probability of establishing high-amplitude oscillations. The area highlighted in black corresponds to the establishment of high-amplitude oscillations from any initial conditions. The area highlighted in shades of gray corresponds to the establishment of high-amplitude oscillations from only some initial conditions. And finally the area marked in white corresponds to those values of the parameters for which high-amplitude oscillations are not established at all. Note that there are threshold values for both parameters d and T_c. The existence of threshold value for d has already been discussed above. The presence of threshold value for T_c is associated with the motion time T over stable submanifolds (see **Figure 6C**). Note that the value of the critical value T_c is determined by the dynamics of both oscillators and it is not related to the periods of high and low oscillations of the isolated oscillator.

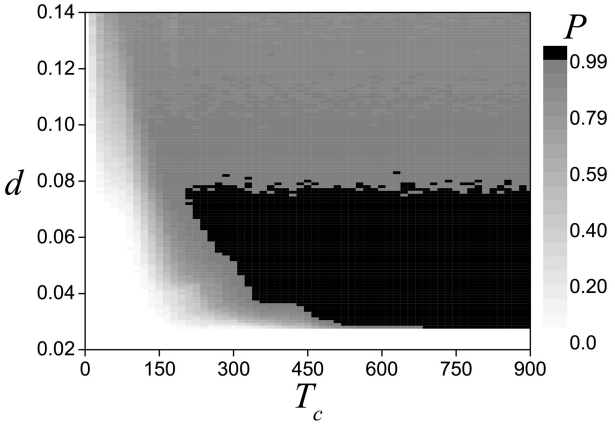

FIGURE 9 | Dependence of establishing probability of high-amplitude oscillations in the pair of short-term coupled elements [system (3)] for initial conditions such as $(I.C.)_1$ on the parameters (d, T_C). Parameters values: $a = 0.32, b = 0.79, c = 1.166$, and $\varepsilon = 0.001$.

4.3. Dynamics of the Multiplex Network

Thus, it has been established that in the case of initial conditions $(\text{I.C.})_1$, there are values of the parameters d and T_c corresponding to the emergence of high-amplitude oscillations in the pairs of interacting oscillators belonging to the different layers. On the other hand, it has been shown that in the case of initial conditions $(\text{I.C.})_2$, when the oscillators belonging to the different layers do not change their initial regimes after the interaction and keep demonstrating low-amplitude oscillations.

Now let us consider the dynamics of multiplex network (1) based on the findings of the previous subsections. It can be divided into two main stages.

(a) In the time interval $0 < t < T_c$, oscillators of different layers interact with each other through inter-layer couplings with strengths, d_c, greatly exceeding those of the diffusive intra-layer couplings, d_r. Therefore, in this stage the main contribution to the dynamics of the system due to the dynamics of the interacting pairs. We have established that as a result of this dynamics, the pairs of oscillators with high-amplitude oscillations are formed in (1) from the initial conditions $(\text{I.C.})_1$. On the other hand, the pairs of oscillators with low-amplitude oscillations are formed in (1) from the initial conditions $(\text{I.C.})_2$. This means that the average amplitude distribution in the first layer does not change, while that of the second layer becomes the same as in the first one.

(b) For $t > T_c$, there are no inter-layer couplings, and the oscillators interact only through diffusive intra-layer ones. Under the influence of these couplings, the neighboring oscillators with similar amplitudes become phase-locked with each other at some average frequency and form the coherent part of the chimera state. The neighboring oscillators with different amplitudes do not become phase-locked with other oscillators and form the incoherent part of the chimera state with distinguished bell-shaped distributions of average frequencies and amplitudes. Thus, the same chimera state is formed in the second layer as in the first one. Note that a finite interaction time is required to stop the competition of oscillations of pairs of oscillators. Otherwise, new complex states arise in the layers and they differ from the initial chimera.

5. CONCLUSIONS

In a large two-layer multiplex network with short-term couplings, a new phenomenon of the chimera states cloning, has been discovered and studied. Each layer of the system has a ring topology and consists of relaxation oscillators having two stable limit cycles on their phase planes. The oscillators inside the layers interact through diffusive couplings, while those of different layers interact by means of multiplex couplings. When the chimera state existing in one of the layers interacts for a while with oscillations of the other layer having a random distribution of phases, the same chimera state appears in the latter layer. Note that the time of occurrence of the chimera state in the second layer is less than the minimal partial oscillation period. We have found that the phenomenon is not related with synchronization of oscillations existing in the layers, but instead is determined

by the competition of high- and low-amplitude oscillations. Using GPST, we showed that competition of oscillations in each (multiplex) pair of oscillators in the multiplex network is controlled by switching four-dimensional slow-fast dynamics. We have analytically established the initial conditions leading to the trajectories in phase space which start from stable "competitive" submanifolds of slow motions and then transit to stable "winner" submanifolds. The "competitive" submanifold corresponds to the case where oscillations in different layers have different (low and high) oscillation amplitudes. The "winner" submanifold corresponds to the case where oscillations in different layers have high amplitudes. Transitions between stable submanifolds occur along the trajectories of a two-dimensional fast subsystem. The given initial conditions belong to the basin of attraction of both the initial chimera state and the clone. We found that strength, as well as time of multiplex interaction, play a crucial role in the existence of the cloning effect of chimera states. A chimera clone is formed with 100% probability if the strength and time of multiplex interaction exceed certain threshold values. Below these threshold values a chimera clone occurs with a certain probability. Note that the effect of chimera state cloning does not depend on the choice of boundary conditions, since the dynamics of pairs of oscillators plays a crucial role in its existence. We hope also that the cloning effect is not specific to considered model and exists in other models, since the conditions necessary for it to take place are fairly general.

AUTHOR CONTRIBUTIONS

VN and AD conceived the original ideas. VN supervised the project. AD performed the numerical computations. VN, AD, and DS wrote the manuscript.

FUNDING

This work was supported by the Russian Foundation for Basic Research (Project Nos. 18-29-10040 and 18-02-00406).

REFERENCES

1. Kuramoto Y. Reduction methods applied to non-locally coupled oscillator systems. In: Hogan J, Champneys A, Krauskopf B, Bernardo M, Wilson E, Osinga H, et al., editors. *Nonlinear Dynamics and Chaos: Where Do We Go From Here?* Bristol; Philadelphia, PA: Institute of Physics Publishing (2003). p. 209–27.
2. Kuramoto Y, Battogtokh D. Coexistence of Coherence and Incoherence in Nonlocally Coupled Phase Oscillators. *Nonlinear Phenomena Complex Syst*. (2002) **5**:380–5. Available online at: http://www.j-npcs.org/abstracts/vol2002/v5no4/v5no4p380.html
3. Abrams D, Strogatz S. Chimera states for coupled oscillators. *Phys Rev Lett*. (2004) **93**:174102. doi: 10.1103/PhysRevLett.93.174102
4. Abrams D, Mirollo R, Strogatz S, Wiley D. Solvable model for chimera states of coupled oscillators. *Phys Rev Lett*. (2008) **93**:084103. doi: 10.1103/PhysRevLett.101.084103
5. Nekorkin V, Voronin M, Velarde M. Clusters in an assembly of globally coupled bistable oscillators. *Eur Phys J B Condens Matter Complex Syst*. (1999) **9**:533–43.
6. Bordyugov G, Pikovsky A, Rosenblum M. Self-emerging and turbulent chimeras in oscillator chains. *Phys Rev E* (2010) **82**:035205. doi: 10.1103/PhysRevE.82.035205
7. Martens EA. Bistable chimera attractors on a triangular network of oscillator populations. *Phys Rev E* (2010) **82**:016216. doi: 10.1103/PhysRevE.82.016216
8. Omelchenko I, Maistrenko Y, Hövel P, Schöll E. Loss of coherence in dynamical networks: spatial chaos and chimera states. *Phys Rev Lett.* (2011) **106**:234102. doi: 10.1103/PhysRevLett.106.234102
9. Sethia GC, Sen A, Johnston GL. Amplitude-mediated chimera states. *Phys Rev E* (2013) **88**:042917. doi: 10.1103/PhysRevE.88.042917
10. Yeldesbay A, Pikovsky A, Rosenblum M. Chimeralike states in an ensemble of globally coupled oscillators. *Phys Rev Lett*. (2014) **112**:144103. doi: 10.1103/PhysRevLett.112.144103
11. Zakharova A, Kapeller M, Schöll E. Chimera death: symmetry breaking in dynamical networks. *Phys Rev Lett*. (2014) **112**:154101. doi: 10.1103/PhysRevLett.112.154101
12. Laing CR. Chimeras in networks with purely local coupling. *Phys Rev E* (2015) **92**:050904. doi: 10.1103/PhysRevE.92.050904
13. Loos SAM, Claussen JC, Schöll E, Zakharova A. Chimera patterns under the impact of noise. *Phys Rev E* (2016) **93**:012209. doi: 10.1103/PhysRevE.93.012209
14. Semenova N, Zakharova A, Anishchenko V, Schöll E. Coherence-resonance chimeras in a network of excitable elements. *Phys Rev Lett*. (2016) **117**:014102. doi: 10.1103/PhysRevLett.117.014102
15. Schöll E. Synchronization patterns and chimera states in complex networks: interplay of topology and dynamics. *Eur Phys J Spec Top*. (2016) **225**:891–919. doi: 10.1140/epjst/e2016-02646-3
16. Semenova NI, Strelkova GI, Anishchenko VS, Zakharova A. Temporal intermittency and the lifetime of chimera states in ensembles of nonlocally coupled chaotic oscillators. *Chaos* (2017) **27**:061102. doi: 10.1063/1.4985143
17. Shepelev IA, Vadivasova TE, Bukh AV, Strelkova GI, Anishchenko VS. New type of chimera structures in a ring of bistable FitzHugh–Nagumo oscillators with nonlocal interaction. *Phys Lett A* (2017) **381**:1398–404. doi: 10.1016/j.physleta.2017.02.034
18. Maistrenko Y, Brezetsky S, Jaros P, Levchenko R, Kapitaniak T. Smallest chimera states. *Phys Rev E* (2017) **95**:010203. doi: 10.1103/PhysRevE.95.010203
19. Martens EA, Thutupalli S, Fourrière A, Hallatschek O. Chimera states in mechanical oscillator networks. *Proc Natl Acad Sci USA*. (2013) **109**:10563–7. doi: 10.1073/pnas.1302880110
20. Kapitaniak T, Kuzma P, Wojewoda J, Czolczynski K, Maistrenko Y. Imperfect chimera states for coupled pendula. *Sci Rep*. (2014) **4**:6379. doi: 10.1038/srep06379
21. Wojewoda J, Czolczynski K, Maistrenko Y, Kapitaniak T. The smallest chimera state for coupled pendula. *Sci. Rep*. (2016) **6**:34329. doi: 10.1038/srep34329
22. Dudkowski D, Grabski J, Wojewoda J, Perlikowski P, Maistrenko Y, Kapitaniak T. Experimental multistable states for small network of coupled pendula. *Sci. Rep*. (2016) **6**:29833. doi: 10.1038/srep29833
23. Hagerstrom AM, Murphy TE, Roy R, Hövel P, Omelchenko I, Schöll E. Experimental observation of chimeras in coupled-map lattices. *Nat Phys*. (2012) **8**:658–61. doi: 10.1038/nphys2372
24. Larger L, Penkovsky B, Maistrenko Y. Laser chimeras as a paradigm for multistable patterns in complex systems. *Nat Commun*. (2015) **6**:7752. doi: 10.1038/ncomms8752
25. Tinsley MR, Nkomo S, Showalter K. Chimera and phase-cluster states in populations of coupled chemical oscillators. *Nat Phys*. (2012) **8**:662–5. doi: 10.1038/nphys2371
26. Schmidt L, Schönleber K, Krischer K, García-Morales V. Coexistence of synchrony and incoherence in oscillatory media under nonlinear global coupling. *Chaos* (2014) **24**:013102. doi: 10.1063/1.4858996
27. Wickramasinghe M, Kiss IZ. Spatially organized dynamical states in chemical oscillator networks: synchronization, dynamical differentiation, and chimera patterns. *PLoS ONE* **8**:e80586. doi: 10.1371/journal.pone.0080586

28. Wickramasinghe M, Kiss IZ. Spatially organized partial synchronization through the chimera mechanism in a network of electrochemical reactions. *Phys Chem Chem Phys*. (2014) **16**:18360–9. doi: 10.1039/C4CP02249A
29. Smart AG. Exotic chimera dynamics glimpsed in experiments. *Phys Today* (2012) **65**:17–9. doi: 10.1063/PT.3.1738
30. Larger L, Penkovsky B, Maistrenko Y. Virtual chimera states for delayed-feedback systems. *Phys Rev Lett*. (2013) **111**:054103. doi: 10.1103/PhysRevLett.111.054103
31. Gambuzza LV, Buscarino A, Chessari S, Fortuna L, Meucci R, Frasca M. Experimental investigation of chimera states with quiescent and synchronous domains in coupled electronic oscillators. *Phys Rev E* (2014) **90**:032905. doi: 10.1103/PhysRevE.90.032905
32. Shchapin DS, Dmitrichev AS, Nekorkin VI. Chimera states in an ensemble of linearly locally coupled bistable oscillators. *JETP Lett*. (2017) **106**:617–21. doi: 10.1134/S0021364017210111
33. Hizanidis J, Lazarides N, Tsironis GP. Robust chimera states in SQUID metamaterials with local interactions. *Phys Rev E* (2016) **94**:032219. doi: 10.1103/PhysRevE.94.032219
34. Mukhametov LM, Supin AY, Polyakova IG. Interhemispheric asymmetry of the electroencephalographic sleep patterns in dolphins. *Brain Res*. (1977) **134**:581–4. doi: 10.1016/0006-8993(77)90835-6
35. Lyamin OI, Manger PR, Ridgway SH, Mukhametov LM, Siegel JM. Cetacean sleep: an unusual form of mammalian sleep. *Neurosci Biobehav Rev*. (2008) **32**:1451–84. doi: 10.1016/j.neubiorev.2008.05.023
36. Andrzejak RG, Ruzzene G, Malvestio I. Generalized synchronization between chimera states. *Chaos* (2017) **27**:053114. doi: 10.1063/1.4983841
37. Tian C, Bi H, Zhang X, Guan S, Liu Z. Asymmetric couplings enhance the transition from chimera state to synchronization. *Phys Rev E* (2017) **96**:052209. doi: 10.1103/PhysRevE.96.052209
38. Majhi S, Perc M, Ghosh D. Chimera states in a multilayer network of coupled and uncoupled neurons. *Chaos* (2017) **27**:073109. doi: 10.1063/1.4993836
39. Kasatkin DV, Nekorkin VI. Synchronization of chimera states in a multiplex system of phase oscillators with adaptive couplings. *Chaos* (2018) **28**:093115. doi: 10.1063/1.5031681
40. Hizanidis J, Kouvaris NE, Zamora-López G, Díaz-Guilera A, Antonopoulos CG. Chimera-like states in modular neural networks. *Sci Rep*. (2016) **6**:19845. doi: 10.1038/srep19845
41. Ujjwal SR, Punetha N, Ramaswamy R. Phase oscillators in modular networks: the effect of nonlocal coupling. *Phys Rev E* (2016) **93**:012207. doi: 10.1103/PhysRevE.93.012207
42. Maksimenko VA, Makarov VV, Bera BK, Ghosh D, Dana SK, Goremyko MV, et al. Excitation and suppression of chimera states by multiplexing. *Phys Rev E* (2016) **94**:052205. doi: 10.1103/PhysRevE.94.052205
43. Dmitrichev AS, Shchapin DS, Nekorkin VI. Cloning of chimera states in a multiplex network of two-frequency oscillators with linear local couplings. *JETP Lett*. (2018) **108**:543–47. doi: 10.1134/S0021364018200079
44. Fenichel N. Geometric singular perturbation theory for ordinary differential equations. *J Different Equat*. (1979) **31**:53–98. doi: 10.1016/0022-0396(79)90152-9
45. Mishchenko EF, Rozov NK. *Differntial Equations With Small Parameters and Relaxation Oscillations*. New York, NY: Plenum Pres (1980).
46. Nekorkin VI, Makarov VA, Velarde MG. Clustering and phase resetting in a chain of bistable nonisochronous oscillators. *Phys Rev E* (1998) **58**:5742–7. doi: 10.1103/PhysRevE.58.5742

Conflict of Interest Statement: The authors declare that the research was conducted in the absence of any commercial or financial relationships that could be construed as a potential conflict of interest.

frontiers in Applied Mathematics and Statistics

ORIGINAL RESEARCH
published: 24 April 2019
doi: 10.3389/fams.2019.00019

Chimeras in Multiplex Networks: Interplay of Inter- and Intra-Layer Delays

Jakub Sawicki[1]*, *Saptarshi Ghosh*[2], *Sarika Jalan*[2] and *Anna Zakharova*[1]

[1] Institut für Theoretische Physik, Technische Universität Berlin, Berlin, Germany, [2] Complex Systems Lab, Discipline of Physics, Indian Institute of Technology Indore, Indore, India

Time delay in complex networks with multiple interacting layers gives rise to special dynamics. We study the scenarios of time delay induced patterns in a three-layer network of FitzHugh-Nagumo oscillators. The topology of each layer is given by a nonlocally coupled ring. For appropriate values of the time delay in the couplings between the nodes, we find chimera states, i.e., hybrid spatio-temporal patterns characterized by coexisting domains with incoherent and coherent dynamics. In particular, we focus on the interplay of time delay in the intra-layer and inter-layer coupling term. In the parameter plane of the two delay times we find regions where chimera states are observed alternating with coherent dynamics. Moreover, in the presence of time delay we detect full and relay inter-layer synchronization.

Keywords: chimera states, multiplex networks, FitzHugh-Nagumo oscillator, time delay, relay synchronization

OPEN ACCESS

Edited by:
Jun Ma,
Lanzhou University of Technology, China

Reviewed by:
Tanmoy Banerjee, University of Burdwan, India
Carlo Laing, College of Sciences, Massey University, New Zealand
V. K. Chandrasekar, SASTRA University, India

***Correspondence:**
Jakub Sawicki
zergon@gmx.net

Specialty section:
This article was submitted to Dynamical Systems, a section of the journal Frontiers in Applied Mathematics and Statistics

Received: *10 January 2019*
Accepted: *28 March 2019*
Published: *24 April 2019*

Citation:
Sawicki J, Ghosh S, Jalan S and Zakharova A (2019) Chimeras in Multiplex Networks: Interplay of Inter- and Intra-Layer Delays. Front. Appl. Math. Stat. 5:19. doi: 10.3389/fams.2019.00019

1. INTRODUCTION

During the early eighteenth century, Leonhard Euler published a paper on The Seven Bridges of Königsberg providing a mathematical background on vertices and edges [1]. Later on, it became the cornerstone of the field of network science. Network science presents a unique platform to study various complex real-world systems by analyzing the interactions between its constituent entities and collectively investigating its behaviors [2–4]. A recent addition to the network science is the multiplex framework which incorporates multiple types of interactions among nodes by representing them in different layers [5, 6]. For example, the neurons in the brain form different groups consisting of the same neurons but interacting in different ways (chemical interaction or electrical synapses) to perform different tasks [7, 8]. Multiplex framework divides these neuronal groups into different layers based on their functionalities [9]. Similarly, transportation networks, communication networks, social networks and a lot of other real-world networks can be represented in a multiplex framework to understand their structural and dynamical features in a better fashion [10].

Recently, various synchronization scenarios have been investigated in multilayer structures, including remote and relay synchronization [11–14]. Moreover, it has been shown that multiplexing can be used to control spatio-temporal patterns in networks [15–18]. The advantage of control schemes based on multiplexing is that they allow to achieve the desired state in a certain layer without manipulating its parameters, and they can work for weak inter-layer coupling. For example, it has been found that weak multiplexing can induce coherence resonance [19] as well as chimera states [18] in neural networks.

Chimera state is a peculiar partial synchronization pattern that refers to a hybrid dynamics where coherence and incoherence emerge simultaneously in a network of identical oscillators [20–22]. Since its inception [23, 24], chimera state has attracted massive interest from the nonlinear community for both its significance in understanding complex spatiotemporal patterns and its probable applicabilities in various fields, especially in neuroscience [25]. Here we study the role of the interplay of intra- and inter-layer time delays for the emergence of chimera states in a multi(tri)plex network. Time delays represent an essential factor in real-world networks due to the finite speed of information propagating through channels connecting the nodes. They play a crucial role in determining the dynamical behavior of a complex system [26–32]. Time delays have been shown to heavily influence the parameter range for which chimera states appear for both single and multiplex networks [14, 15, 33–35]. Moreover, recently a scheme has been proposed for engineering chimera states using suitably placed heterogeneous delays [36]. In the present work we demonstrate that just the variation of delay values in the intra- and inter-layer edges can lead to various dynamical states and allows for control of spatio-temporal patterns.

2. THE MODEL

We study a multiplex network with three layers (triplex) as shown in **Figure 1**. Every single layer represents a ring of N identical FitzHugh-Nagumo (FHN) oscillators with non-local (intra-layer) topology. The outer layers $i = 1$ and $i = 3$ are coupled with the middle layer $i = 2$, so that it acts as a relay layer. There is no direct connection between layers 1 and 3 (so-called ordinal coupling).

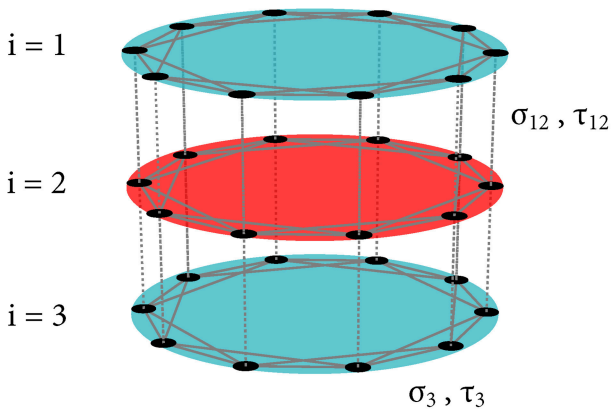

FIGURE 1 | Triplex network with ordinal coupling: The middle layer $i = 2$ (red) acts as relay layer between the two outer layers $i = 1, 3$ (blue). Black dots indicate the nodes, solid lines represent the intra-layer connections, and dashed lines denote the inter-layer links. The intra-layer coupling is characterized by the strength σ_i and time delay τ_i, and the inter-layer coupling is characterized by the strength σ_{ij} and time delay τ_{ij}. For example, in layer 3 the intra-layer coupling strength is given by σ_3 and the intra-layer time delay is τ_3. Similarly, for the layers 1 and 2 the inter-layer coupling strength is given by σ_{12} and the inter-layer time delay is τ_{12}.

Our system is described by the following equations:

$$\dot{\boldsymbol{x}}_k^i(t) = \boldsymbol{F}(\boldsymbol{x}_k^i(t)) + \frac{\sigma_i}{2R_i}\sum_{l=k-R_i}^{k+R_i}\boldsymbol{H}[\boldsymbol{x}_l^i(t-\tau_i) - \boldsymbol{x}_k^i(t)] + \sum_{j=1}^{3}\sigma_{ij}\boldsymbol{H}[\boldsymbol{x}_k^j(t-\tau_{ij}) - \boldsymbol{x}_k^i(t)], \quad (1)$$

where $\boldsymbol{x} = (u, v)^T \in \mathbb{R}^2$, $k \in \{1, ..., N\}$, $i \in \{1, ..., 3\}$ with all indices modulo N, describe the set of activator (u) and inhibitor (v) variables. The intra-layer delay time is τ_i and the inter-layer delay time is τ_{ij}. The coupling radius in layer i is given by R_i. The local dynamics of each oscillator is given by

$$\boldsymbol{F}(\boldsymbol{x}) = \begin{pmatrix} \varepsilon^{-1}(u - \frac{u^3}{3} - v) \\ u + a \end{pmatrix}, \quad (2)$$

where $\varepsilon = 0.05$ is the parameter characterizing the time scale separation. The FHN oscillator exhibits either oscillatory ($|a| < 1$) or excitable ($|a| > 1$) behavior depending on the threshold parameter a. In this work we focus on the oscillatory regime ($a = 0.5$). The parameter σ_i stands for the coupling

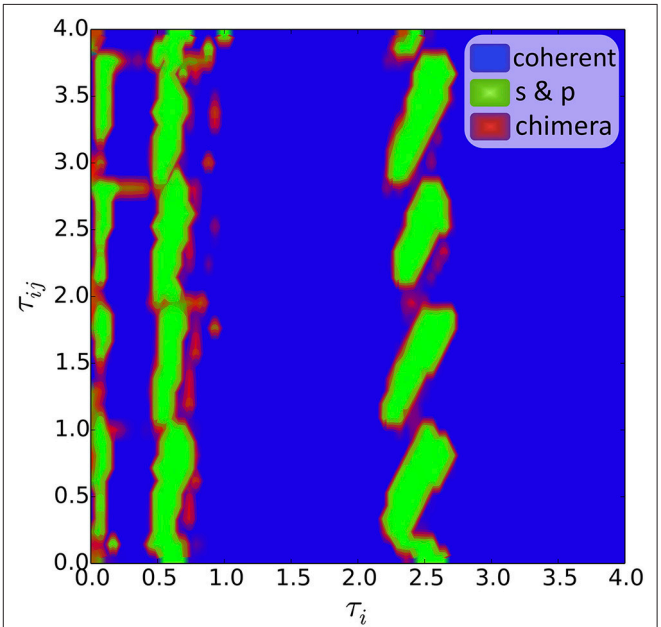

FIGURE 2 | Dynamical regimes in the parameter plane of intra-layer coupling delay $\tau_i \equiv \tau_1 = \tau_2 = \tau_3$ and inter-layer coupling delay $\tau_{ij} \equiv \tau_{12} = \tau_{23}$: "salt & pepper" states (green islands) occur in the region of coherent states (blue region) as traveling waves, cluster or synchronized states. At the border between these two regimes chimera states can be found (red color). We distinguish between the different regions on the one hand, by analyzing the mean phase velocity and a snapshot of variables u_k, on the other hand, by means of the Laplacian distance measure [39]. The boundaries of these regions are fitted linearly after the (τ_i, τ_{ij}) plane has been sampled in steps $\Delta\tau_i = 0.05$ and $\Delta\tau_{ij} = 0.1$. For all simulations of Equation (1) random initial conditions are taken. Parameters are chosen as $\varepsilon = 0.05$, $a = 0.5$, $\sigma_i = 0.2$, $\sigma_{ij} = 0.05$, $N = 500$, $R_i = 170$, $\phi = \frac{\pi}{2} - 0.1$, and $i, j = 1, 2, 3$.

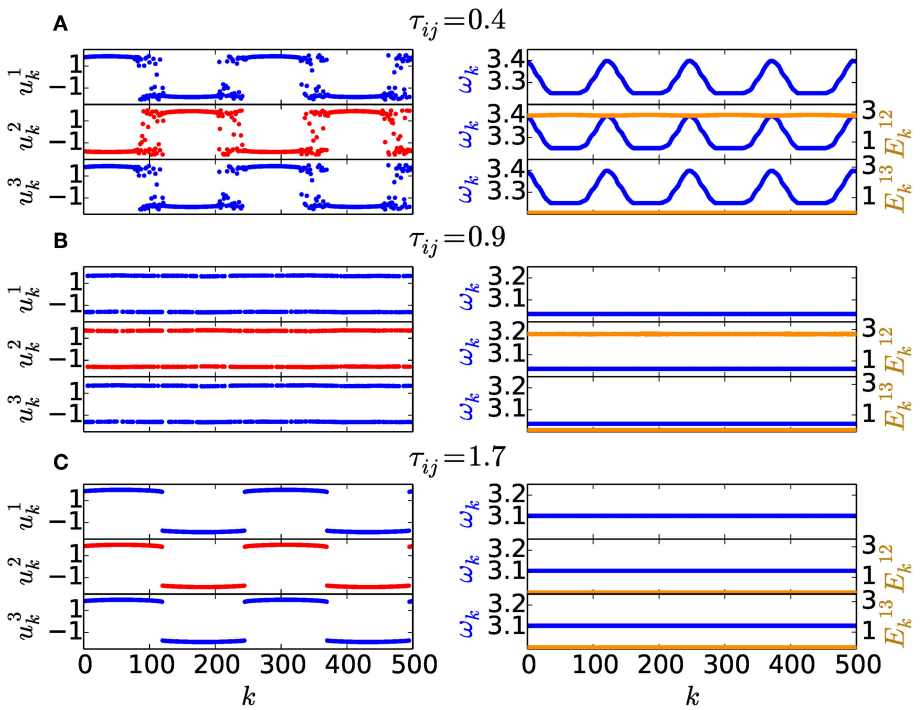

FIGURE 3 | Dynamics in all three layers for different values of the inter-layer delay time τ_{ij}: **(A)** Chimera state for $\tau_{ij} = 0.4$, **(B)** "salt & pepper" state for $\tau_{ij} = 0.9$, **(C)** coherent state (cluster state) for $\tau_{ij} = 1.7$. The intra-layer delay time is fixed at $\tau_i = 0.8$. The left column displays snapshots of variables u_k^j for the layers $i = 1, 2, 3$, while the right column illustrates the mean phase velocity profile ω_k (dark blue) for the individual layers and the local inter-layer synchronization error E_k^{ij} (light yellow). Other parameters as in **Figure 2**.

strength inside the layer (intra-layer coupling), and σ_{ij} is the inter-layer coupling. For an ordinal inter-layer coupling with constant row sum we set $\sigma_{12} = \sigma_{23}$, which yields the inter-layer coupling matrix

$$\boldsymbol{\sigma} = \begin{pmatrix} 0 & \sigma_{12} & 0 \\ \frac{\sigma_{12}}{2} & 0 & \frac{\sigma_{23}}{2} \\ 0 & \sigma_{23} & 0 \end{pmatrix} \tag{3}$$

The connections between the nodes are given by the diffusive coupling with the following coupling matrix

$$\boldsymbol{H} = \begin{pmatrix} \varepsilon^{-1}\cos\phi & \varepsilon^{-1}\sin\phi \\ -\sin\phi & \cos\phi \end{pmatrix} \tag{4}$$

and coupling phase $\phi = \frac{\pi}{2} - 0.1$ [37]. This coupling configuration (i.e., predominantly activator-inhibitor cross-coupling) is similar to a phase-lag of approximately $\pi/2$ in the Kuramoto model that ensures the occurrence of chimera states [37].

3. INTERPLAY OF TIME DELAYS

Chimera states are spatio-temporal patterns where incoherent and coherent domains coexist in space. For certain values of coupling strength σ_i and coupling radius R_i one can detect them in the ith layer [37]. Recently, the phenomenon of relay synchronization of chimera states has been studied in a three-layer network of FHN oscillators [38]. In more detail, for varying the coupling delay and strength in the inter-layer connections relay synchronization of chimera states in the outer network layers has been reported. For appropriate parameters the so-called "double" chimeras are possible where the coherent parts of the chimera states are synchronized, whereas the incoherent parts remain desynchronized. Additionally, the transitions between different synchronization scenarios have been studied. Moreover, time delay in the inter-layer coupling has been shown to be a powerful tool for controlling various partial synchronization patterns in the three-layer network [14]. Therefore, by multiplexing and introducing inter-layer time delays it is possible to destroy or induce chimera states. Here we study the interplay of inter- and intra-layer time delay.

To provide an overview of the patterns observed in the network, we calculate the map of regimes in the parameter plane of intra-layer delay time τ_i and inter-layer delay time τ_{ij} (**Figure 2**). The dominating region is the one corresponding to coherent states (blue region in **Figure 2**). On the one hand, we

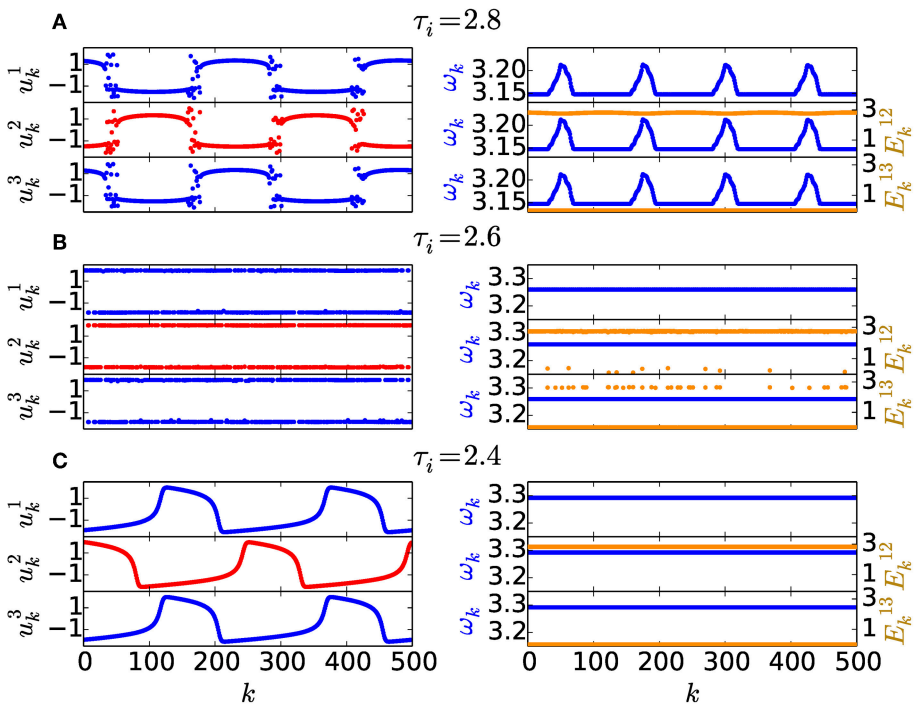

FIGURE 4 | Dynamics in all three layers for different values of the intra-layer delay time τ_i: **(A)** Chimera state for $\tau_i = 2.8$, **(B)** "salt & pepper" state for $\tau_i = 2.6$, **(C)** coherent state (traveling wave) for $\tau_i = 2.4$. The inter-layer delay time is fixed at $\tau_{ij} = 2.6$. The left column displays snapshots of variables u_k^i for the layers $i = 1, 2, 3$, while the right column illustrates the mean phase velocity profile ω_k (dark blue) for the individual layers and the local inter-layer synchronization error E_k^{ij} (light yellow). Other parameters as in **Figure 2**.

detect the in-phase synchronization regime (see **Figure 3C**), on the other hand, we also observe a region of coherent traveling waves (see **Figure 4C**). By varying the delay times we can not only switch between these states, but also adjust the speed of traveling waves. In addition, we can observe *salt and pepper* states (green region in **Figure 2**), where all nodes oscillate with the same phase velocity but they are distributed between states with phase lag π incoherently [40] (see **Figures 3B**, **4B**). The reason for this are strong variations on very short length scales, so that the dynamical patterns have arbitrarily short wavelengths. Besides these two patterns characterized by the same mean phase velocity for all the nodes in the network, we also observe chimera states (red region in **Figure 2**), where the oscillators within each layer show a characteristic arc-shaped mean phase velocity profile. The mean phase velocities of the oscillators are given by $\omega_k = 2\pi S_k/\Delta T, k = 1, ..., N$, where S_k denotes the number of complete rotations performed by the kth oscillator during the time ΔT. The value $\Delta T = 10,000$ is fixed throughout the paper. Because of the delay, the system often exhibits traveling structures. Therefore, the classical arc-shaped profile is transformed into a wider, conical one [41] (see **Figures 3A**, **4A** (right column)). We distinguish between the different regions on the one hand, by analyzing the mean phase velocity and a snapshot of variables u_k, on the other hand, by means of the Laplacian distance measure [39]. The latter identifies strong local curvature in an otherwise smooth spatial profile of $\boldsymbol{x}_k$ by calculating the discrete Laplacian $\|(\boldsymbol{x}_{k+1} - \boldsymbol{x}_k) - (\boldsymbol{x}_k - \boldsymbol{x}_{k-1})\|$ for each k. In case of coherent dynamics we obtain low values (≈ 0) for all k, in case of *salt and pepper* states we get high values (> 2). Chimera states show low and high values for the coherent and incoherent domains, respectively. By taking the mean over all k, we can distinguish between coherent, chimera and "salt & pepper" states. For the numerical integration an Euler integration method is used with a step size $\Delta t = 0.0025$ and a transient time $t_{trans} = 2,000$. All simulations are evaluated then after $\Delta T = 10,000$ as mentioned above.

In many systems with time delays resonance effects can be expected if the delay time is an integer or half-integer multiple of the period in the uncoupled system [42–44]. Regarding the inter-layer delay time τ_{ij} we can observe this effect for half-integer multiples of the period $T = 2.3$ of a uncoupled FHN oscillator (see **Figure 2** for $\tau_i \approx 2.5$). Concerning the intra-layer delay time τ_i we find a resonance effect in the case of integer multiple of the delay. For greater values of the delay times τ_i and τ_{ij} the dynamical regions are becoming curved (see green islands in **Figure 2** at $\tau_i \approx 2.5$). This can be explained by the fact that branches of periodic solutions, which are reappearing for integer multiples of the intrinsic period, are becoming stretched with increasing delay time [41]. In comparison to the almost vertical shape at $\tau_i \approx 0.5$, the green islands at $\tau_i \approx 2.5$ are rotated clockwise by approximate $\pi/8$. The consequence is an overlapping of the delay islands for small intra-layer delay time τ_i, whereas for larger delays the islands become separated.

4. RELAY SYNCHRONIZATION

Networks with multiple layers demonstrate remote synchronization of distant layers via a relay layer. Regarding the inter-layer synchronization, two synchronization mechanisms are conceivable in a triplex network:

- full inter-layer synchronization when synchronization is observed between all the layers and
- relay inter-layer synchronization when synchronization occurs exclusively between the two outer layers.

A useful measure for synchronization between two layers i, j is given by the global inter-layer synchronization error E^{ij} [14, 45]:

$$E^{ij} = \lim_{T\to\infty} \frac{1}{NT} \int_0^T \sum_{k=1}^{N} \left\| \boldsymbol{x}_k^j(t) - \boldsymbol{x}_k^i(t) \right\| \, dt, \tag{5}$$

where $\|\cdot\|$ denotes the Euclidean norm. One can distinguish between the two synchronization mechanisms by measuring the global inter-layer synchronization error between the first and second layer E^{12} and between the first and third layer E^{13}: In the case of full inter-layer synchronization $E^{12} = 0$ as well as $E^{13} = 0$, while in the case of relay inter-layer synchronization $E^{12} \neq 0$ and $E^{13} = 0$.

To provide more insight into the synchronizability of patterns between two layers i, j, the local inter-layer synchronization error in dependence of every single node k can be used [14]:

$$E_k^{ij} = \lim_{T\to\infty} \frac{1}{T} \int_0^T \left\| \boldsymbol{x}_k^j(t) - \boldsymbol{x}_k^i(t) \right\| \, dt. \tag{6}$$

The local inter-layer synchronization error is convenient for detecting the synchronized nodes between two layers. In **Figures 3**, **4** (right column) E_k^{ij} is plotted (light yellow) together with the mean phase velocity (blue): Depending on the delay times τ_i and τ_{ij} we can find full inter-layer synchronization (see **Figure 3C**) as well as relay inter-layer synchronization (see **Figures 3A,B**, **4A,C**). These synchronization scenarios can be found for both coherent and incoherent dynamics. An additional effect is the partial relay synchronization scenario in **Figure 4B**: In all three layers "salt & pepper" dynamics can be observed. The nodes in the outer layers are almost all synchronized, but a small part of them destroys the relay synchronization. On the other hand a few oscillators in the relay layer are synchronized with the outer layers.

5. CONCLUSION

In conclusion, we have studied chimera states in a three-layer network of FitzHugh-Nagumo oscillators, where each layer has a nonlocal coupling topology. Focusing on the role of time delays in the coupling terms and their influence on chimera states, we have performed a numerical study of complex spatio-temporal patterns in the network. In the parameter plane of the intra-layer τ_i and the inter-layer τ_{ij} time delay, we have determined the regions where chimera patterns occur, alternating with regimes of coherent states. A proper choice of time delay allows to achieve the desired state of the network: chimera state or coherent pattern, full or relay inter-layer synchronization.

Combining the delayed interactions with the multiplex framework considered in this work can provide additional insight into the formation of the complex spatio-temporal patterns in real-world systems. Specifically, in brain networks where EEG patterns are recently reported to display chimera-like behavior at the onset of a seizure [46–48]. Inducing the chimera states by tuning the inter- and intra-layer delay values provides us with a powerful tool to control chimera states.

AUTHOR CONTRIBUTIONS

JS did the numerical simulations and the theoretical analysis. AZ supervised the study. All authors designed the study and contributed to the preparation of the manuscript. All the authors have read and approved the final manuscript.

ACKNOWLEDGMENTS

This work was supported by the Deutsche Forschungsgemeinschaft (DFG, German Research Foundation)—Projektnummer—163436311—SFB 910 and by the German Academic Exchange Service (DAAD) and the Department of Science and Technology of India (DST) within the PPP project (INT/FRG/DAAD/P-06/2018).

REFERENCES

1. Euler L. Solutio problematis ad geometriam situs pertinentis. *Comment Acad Sci Petropol.* (1741) **8**:128–40.
2. Albert R, Barabási AL. Statistical mechanics of complex networks. *Rev Mod Phys.* (2002) **74**:47–97. doi: 10.1103/revmodphys.74.47
3. Havlin S, Kenett DY, Ben-Jacob E, Bunde A, Cohen R, Hermann H, et al. Challenges in network science: applications to infrastructures, climate, social systems and economics. *Eur Phys J Spec Top.* (2012) **214**:273–93. doi: 10.1140/epjst/e2012-01695-x
4. Jalan S, Sarkar C, Madhusudanan A, Dwivedi SK. Uncovering randomness and success in society. *PLoS ONE.* (2014) **9**:1–8. doi: 10.1371/journal.pone.0088249
5. Boccaletti S, Bianconi G, Criado R, del Genio CI, Gómez-Gardeñes J, Romance M, et al. The structure and dynamics of multilayer networks. *Phys Rep.* (2014) **544**:1–122. doi: 10.1016/j.physrep.2014.07.001
6. Sarkar C, Yadav A, Jalan S. Multilayer network decoding versatility and trust. *Europhys Lett.* (2016) **113**:18007. doi: 10.1209/0295-5075/113/18007
7. Majhi S, Perc M, Ghosh D. Chimera states in a multilayer network of coupled and uncoupled neurons. *Chaos.* (2017) **27**:073109. doi: 10.1063/1.4993836

8. Buldú JM, Porter MA. Frequency-based brain networks: from a multiplex framework to a full multilayer description. *Netw Neurosci.* (2018) **2**:418–41. doi: 10.1162/netn_a_00033
9. De Domenico M. Multilayer modeling and analysis of human brain networks. *Gigascience.* (2017) **6**:1–8. doi: 10.1093/gigascience/gix004
10. Kivelä M, Arenas A, Barthélemy M, Gleeson JP, Moreno Y, Porter MA. Multilayer networks. *J Complex Netw.* (2014) **2**:203–71. doi: 10.1093/comnet/cnu016
11. Nicosia V, Valencia M, Chavez M, Díaz-Guilera A, Latora V. Remote synchronization reveals network symmetries and functional modules. *Phys Rev Lett.* (2013) **110**:174102. doi: 10.1103/physrevlett.110.174102
12. Ghosh S, Jalan S. Emergence of chimera in multiplex network. *Int J Bifurc Chaos.* (2016) **26**:1650120. doi: 10.1142/s0218127416501200
13. Zhang L, Motter AE, Nishikawa T. Incoherence-mediated remote synchronization. *Phys Rev Lett.* (2017) **118**:174102. doi: 10.1103/physrevlett.118.174102
14. Sawicki J, Omelchenko I, Zakharova A, Schöll E. Delay controls chimera relay synchronization in multiplex networks. *Phys Rev E.* (2018a) **98**:062224. doi: 10.1103/PhysRevE.98.062224
15. Ghosh S, Kumar A, Zakharova A, Jalan S. Birth and death of chimera: interplay of delay and multiplexing. *Europhys Lett.* (2016) **115**:60005. doi: 10.1209/0295-5075/115/60005
16. Ghosh S, Zakharova A, Jalan S. Non-identical multiplexing promotes chimera states. *Chaos Sol Fract.* (2018) **106**:56–60. doi: 10.1016/j.chaos.2017.11.010
17. Jalan S, Singh A. Cluster synchronization in multiplex networks. *Europhys Lett.* (2016) **113**:30002. doi: 10.1209/0295-5075/113/30002
18. Mikhaylenko M, Ramlow L, Jalan S, Zakharova A. Weak multiplexing in neural networks: switching between chimera and solitary states. *Chaos.* (2019) **29**:023122. doi: 10.1063/1.5057418
19. Semenova N, Zakharova A. Weak multiplexing induces coherence resonance. *Chaos.* (2018) **28**:051104. doi: 10.1063/1.5037584
20. Panaggio MJ, Abrams DM. Chimera states: coexistence of coherence and incoherence in networks of coupled oscillators. *Nonlinearity.* (2015) **28**:R67. doi: 10.1088/0951-7715/28/3/r67
21. Schöll E. Synchronization patterns and chimera states in complex networks: interplay of topology and dynamics. *Eur Phys J Spec Top.* (2016) **225**:891–919. doi: 10.1140/epjst/e2016-02646-3
22. Omel'chenko OE. The mathematics behind chimera states. *Nonlinearity* (2018) **31**:R121. doi: 10.1088/1261-6544/aaaa07
23. Kuramoto Y, Battogtokh D. Coexistence of coherence and incoherence in nonlocally coupled phase oscillators. *Nonlin Phen Complex Syst.* (2002) **5**:380–5.
24. Abrams DM, Strogatz SH. Chimera states for coupled oscillators. *Phys Rev Lett.* (2004) **93**:174102. doi: 10.1103/physrevlett.93.174102
25. Majhi S, Bera BK, Ghosh D, Perc M. Chimera states in neuronal networks: a review. *Phys Life Rev.* (2018). doi: 10.1016/j.plrev.2018.09.003. [Epub ahead of print].
26. Ashwin P, Timme M. Unstable attractors: existence and robustness in networks of oscillators with delayed pulse coupling. *Nonlinearity.* (2005) **18**:2035. doi: 10.1088/0951-7715/18/5/009
27. Ahlborn A, Parlitz U. Controlling spatiotemporal chaos using multiple delays. *Phys Rev E.* (2007) **75**:65202. doi: 10.1103/PhysRevE.75.065202
28. Atay FM, (ed.). *Complex Time-Delay Systems*. Understanding Complex Systems. Berlin Heidelberg: Springer (2010).
29. Singh A, Jalan S, Kurths J. Role of delay in the mechanism of cluster formation. *Phys Rev E.* (2013) **87**:030902(R). doi: 10.1103/PhysRevE.87.030902
30. Singh A, Ghosh S, Jalan S, Kurths J. Synchronization in delayed multiplex networks. *Europhys Lett.* (2015) **111**:30010. doi: 10.1209/0295-5075/111/30010
31. Semenov V, Feoktistov A, Vadivasova T, Schöll E, Zakharova A. Time-delayed feedback control of coherence resonance near subcritical Hopf bifurcation: theory versus experiment. *Chaos.* (2015) **25**:033111. doi: 10.1063/1.4915066
32. Masoliver M, Malik N, Schöll E, Zakharova A. Coherence resonance in a network of FitzHugh-Nagumo systems: interplay of noise, time-delay and topology. *Chaos.* (2017) **27**:101102. doi: 10.1063/1.5003237
33. Semenov V, Zakharova A, Maistrenko Y, Schöll E. Delayed-feedback chimera states: forced multiclusters and stochastic resonance. *Europhys Lett.* (2016) **115**:10005. doi: 10.1209/0295-5075/115/10005
34. Gjurchinovski A, Schöll E, Zakharova A. Control of amplitude chimeras by time delay in dynamical networks. *Phys Rev E.* (2017) **95**:042218. doi: 10.1103/physreve.95.042218
35. Zakharova A, Semenova N, Anishchenko VS, Schöll E. Time-delayed feedback control of coherence resonance chimeras. *Chaos.* (2017) **27**:114320. doi: 10.1063/1.5008385
36. Ghosh S, Jalan S. Engineering chimera patterns in networks using heterogeneous delays. *Chaos.* (2018) **28**:071103. doi: 10.1063/1.5042133
37. Omelchenko I, Omel'chenko OE, Hövel P, Schöll E. When nonlocal coupling between oscillators becomes stronger: patched synchrony or multichimera states. *Phys Rev Lett.* (2013) **110**:224101. doi: 10.1103/physrevlett.110.224101
38. Sawicki J, Omelchenko I, Zakharova A, Schöll E. Synchronization scenarios of chimeras in multiplex networks. *Eur Phys J Spec Top.* (2018b) **227**:1161. doi: 10.1140/epjst/e2018-800039-y
39. Kemeth FP, Haugland SW, Schmidt L, Kevrekidis YG, Krischer K. A classification scheme for chimera states. *Chaos.* (2016) **26**:094815. doi: 10.1063/1.4959804
40. Bachmair CA, Schöll E. Nonlocal control of pulse propagation in excitable media. *Eur Phys J B.* (2014) **87**:276. doi: 10.1140/epjb/e2014-50339-2
41. Sawicki J, Omelchenko I, Zakharova A, Schöll E. Delay-induced chimeras in neural networks with fractal topology. *Eur Phys J B.* (2019) **92**:54. doi: 10.1140/epjb/e2019-90309-6
42. Hövel P, Schöll E. Control of unstable steady states by time-delayed feedback methods. *Phys Rev E.* (2005) **72**:046203. doi: 10.1103/PhysRevE.72.046203
43. Yanchuk S, Wolfrum M, Hövel P, Schöll E. Control of unstable steady states by long delay feedback. *Phys Rev E.* (2006) **74**:026201. doi: 10.1103/PhysRevE.74.026201
44. Geffert PM, Zakharova A, Vüllings A, Just W, Schöll E. Modulating coherence resonance in non-excitable systems by time-delayed feedback. *Eur Phys J B.* (2014) **87**:291. doi: 10.1140/epjb/e2014-50541-2
45. Leyva I, Sendiña-Nadal I, Sevilla-Escoboza R, Vera-Avila VP, Chholak P, Boccaletti S. Relay synchronization in multiplex networks. *Sci Rep.* (2018) **8**:8629. doi: 10.1038/s41598-018-26945-w
46. Rothkegel A, Lehnertz K. Irregular macroscopic dynamics due to chimera states in small-world networks of pulse-coupled oscillators. *New J Phys.* (2014) **16**:055006. doi: 10.1088/1367-2630/16/5/055006
47. Andrzejak RG, Rummel C, Mormann F, Schindler K. All together now: analogies between chimera state collapses and epileptic seizures. *Sci Rep.* (2016) **6**:23000. doi: 10.1038/srep23000
48. Chouzouris T, Omelchenko I, Zakharova A, Hlinka J, Jiruska P, Schöll E. Chimera states in brain networks: empirical neural vs. modular fractal connectivity. *Chaos.* (2018) **28**:045112. doi: 10.1063/1.5009812

Conflict of Interest Statement: The authors declare that the research was conducted in the absence of any commercial or financial relationships that could be construed as a potential conflict of interest.

frontiers in Applied Mathematics and Statistics

ORIGINAL RESEARCH
published: 30 January 2019
doi: 10.3389/fams.2018.00067

Control of Chimera States in Multilayer Networks

Iryna Omelchenko, Tobias Hülser, Anna Zakharova and Eckehard Schöll*

Institut für Theoretische Physik, Technische Universität Berlin, Berlin, Germany

Chimera states are intriguing complex spatio-temporal patterns of coexisting coherent and incoherent domains. They can often be observed in networks with non-local coupling topology, where each element interacts with its neighbors within a fixed range. In small-size non-locally coupled networks, chimera states usually exhibit short lifetimes and erratic drifting of the spatial position of the incoherent domain. This problem can be solved with a tweezer feedback control which can stabilize and fix the position of chimera states. We analyse the action of the tweezer control in two-layer networks, where each layer is a small non-locally coupled ring of Van der Pol oscillators. We demonstrate that tweezer control, applied to only one layer, successfully stabilizes chimera patterns in the other, uncontrolled layer, even in the case of non-identical layers. These results might be useful for applications in multilayer networks, where one of the layers cannot be directly accessed, thus it can be effectively controlled via a neighboring layer.

Keywords: dynamical systems, synchronization, chimera states, multilayer networks, feedback control, Van der Pol oscillators

OPEN ACCESS

Edited by:
Jun Ma,
Lanzhou University of Technology, China

Reviewed by:
Dibakar Ghosh,
Indian Statistical Institute, India
Vesna I. Berec,
University of Belgrade, Serbia

****Correspondence:***
Iryna Omelchenko
omelchenko@itp.tu-berlin.de

Specialty section:
This article was submitted to Dynamical Systems, a section of the journal Frontiers in Applied Mathematics and Statistics

Received: *30 October 2018*
Accepted: *27 December 2018*
Published: *30 January 2019*

Citation:
Omelchenko I, Hülser T, Zakharova A and Schöll E (2019) Control of Chimera States in Multilayer Networks. Front. Appl. Math. Stat. 4:67. doi: 10.3389/fams.2018.00067

1. INTRODUCTION

Networks of coupled oscillators are an intensively studied topic in non-linear science, they have a wide range of applications in physics, biology, chemistry, technology, and social sciences. Special interest has been paid to synchronization and partial synchronization of oscillators, including *chimera states* which are characterized by a hybrid nature of coexisting spatially coherent and incoherent domains [1–7]. Theoretical studies of chimera states have considered a wide range of networks with different local dynamics and a variety of regular and irregular coupling topologies: rings of phase oscillators with non-local coupling [8–12], interacting globally coupled populations of phase oscillators [13, 14], non-locally coupled maps [15, 16], oscillators with phase-amplitude dynamics [17–21], neural oscillators [22–26], two- and three-dimensional lattices of oscillators [27–31], networks with adaptive topologies [32, 33], fractal complex topologies [34–38], oscillators with local or global interaction [39–42], and networks with multiple layers[43–47]. Experimentally, chimera states were demonstrated in optical [48] and chemical [49, 50] systems, as well as in mechanical [51], electronic [52, 53], optoelectronic [54, 55], electrochemical [56, 57] oscillator systems, and Boolean networks [58]. Possible analytical insights and bifurcation analysis of chimera states have been obtained in the continuum limit, which explains the behavior of very large ensembles of coupled oscillators [59–63]. In contrast, lab experiments are commonly performed with small-size networks, where chimera states are more difficult to observe [64–67].

Ring networks with non-local coupling, where each element interacts with its neighbors within a certain range, are a prominent example of a topology allowing for the observation of chimera states. However, the size of the network is essential. In small-size rings of non-locally coupled oscillators, chimera states are often short-living chaotic transients, which eventually collapse to the synchronized state. Their mean lifetime decreases rapidly with decreasing system size [10]. In addition to this, chimera states exhibit a chaotic spatial motion of the position of the coherent and incoherent domains, which is more pronounced with decreasing of the system size [68]. These two effects are weakly noticeable in large networks, but they strongly impede the observation of chimera states in small systems. Only in some special cases beyond simple non-local topologies, chimera states can be observed. For instance, when phase interaction involves higher order harmonics [69, 70], or oscillators are organized in globally coupled interacting subpopulations, the observation of stable chimeras that are not transients is possible in small phase oscillator networks [64, 70].

Control of non-linear systems is an important topic in applied complex systems science [71]. Some control techniques, which allow to stabilize chimera patterns in non-locally coupled oscillator networks, have been proposed recently. The lifetime of amplitude chimeras can be greatly enhanced by time-delayed coupling [72]. For Kuramoto phase oscillators the lifetime of chimera states can be extended by proportional feedback control based on the measurement of the global order parameter [73]. The spatial position of the coherent and incoherent domains of the chimera states can be fixed by a feedback loop inducing a state-dependent asymmetry of the coupling topology [74], defined by a finite difference derivative for a local mean field. Moreover, in one-dimensional arrays of identical oscillators, a self-feedback control applied to a subpopulation of the array can be used for the stabilization of the spatial positions of the coherent and incoherent domains of the chimeras [75]. Recently, we introduced a *tweezer control* scheme for stabilization of chimera states [76] in small-size non-locally coupled networks. This control scheme consists of two parts, symmetric and asymmetric, and effectively stabilizes chimera states in small networks of oscillators exhibiting both phase and amplitude dynamics. Note, that in contrast to pure phase oscillators, a simple analytical study for the continuum limit ($N \to \infty$) is not possible for non-linear phase-amplitude oscillators, therefore we concentrated mainly on the numerical stability analysis. In small networks of Van der Pol and FitzHugh-Nagumo oscillators, we demonstrated that tweezer control allows for stabilization of variable chimera patterns with different sizes of coherent domains [77].

Current research in the field of complex systems is moving beyond simple network structures to more complicated, realistic topologies. One of them are multilayer networks, which find a wide range of applications in nature and technology, such as neuronal and genetic networks, social networks, power grids, transportation networks [78–91]. Recent studies have been focused on various synchronization scenarios in multilayer structures, including remote and relay synchronization [92–94]. Moreover, it has been reported that multiplexing can be used to control spatio-temporal patterns in networks [86, 88, 95]. The advantage of control schemes based on multiplexing is that they allow to achieve the desired state in a certain layer without manipulating its parameters, and they can work for weak inter-layer coupling. For example, it has been shown that weak multiplexing can induce coherence resonance [96] as well as chimera states and solitary states [95] in neural networks. However, multiplexing has not been previously combined with tweezer control.

In many real multi-layer networks some of the layers cannot be easily accessed. An urgent issue, therefore, is the question whether it is possible to control or stabilize spatio-temporal patterns in one layer of the network by applying control to the other layer. We aim to answer this question by an analysis of a simple two-layer network of Van der Pol oscillators. We demonstrate that chimera states which are not observable in small isolated networks, can be efficiently stabilized by the combined action of multiplexing and tweezer control.

2. TWEEZER CONTROL IN TWO-LAYER NETWORK OF VAN DER POL OSCILLATORS

We consider a network of $2N$ coupled Van der Pol oscillators, organized in two layers, each of which contains N oscillators, with non-local ring topology within each layer:

$$\begin{aligned}\ddot{x}_k^{(i)} &= (\varepsilon - (x_k^{(i)})^2)\dot{x}_k^{(i)} - x_k^{(i)} \\ &+ \frac{1}{R_i}\sum_{j=1}^{R_i}\left[a_-^{(i)}(x_{k-j}^{(i)} - x_k^{(i)}) + b_-^{(i)}(\dot{x}_{k-j}^{(i)} - \dot{x}_k^{(i)})\right] \\ &+ \frac{1}{R_i}\sum_{j=1}^{R_i}\left[a_+^{(i)}(x_{k+j}^{(i)} - x_k^{(i)}) + b_+^{(i)}(\dot{x}_{k+j}^{(i)} - \dot{x}_k^{(i)})\right] \\ &+ \left[a_{inter}(x_k^{(3-i)} - x_k^{(i)}) + b_{inter}(\dot{x}_k^{(3-i)} - \dot{x}_k^{(i)})\right], \qquad (1)\end{aligned}$$

where $x_k^{(i)} \in \mathbb{R}$, $i = 1, 2$ denotes the layer number, $k = 1, ..., N$ is the oscillator index within each layer. The scalar parameter $\varepsilon > 0$ determines the internal dynamics of the individual elements. For small ε the oscillation of a single element is sinusoidal, while for large ε it is a strongly non-linear relaxation oscillation. Each element is coupled with R_i nearest neighbors to the left and to the right, we assume that the oscillators within the layers are arranged on a ring (i.e., periodic boundary conditions). The coupling term inside each layer consists of two parts: the coupling constants with respect to position and velocity to the left and to the right are denoted as $a_-^{(i)}$, $a_+^{(i)}$ and $b_-^{(i)}$, $b_+^{(i)}$, respectively. Such a coupling scheme can be associated with biological [97, 98] and technological applications [99]. Interaction between the layers consists of one-to-one bidirectional connections between the corresponding pairs of oscillators $x_k^{(1)}$ and $x_k^{(2)}$, with inter-layer coupling strength a_{inter} and b_{inter}. **Figure 1** shows schematically the topology of the considered network: both layers consist of non-locally coupled rings of oscillators, corresponding pairs of oscillators in each layer are connected by inter-layer links shown

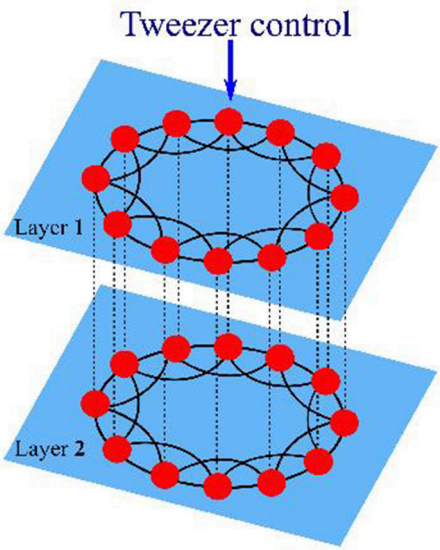

FIGURE 1 | Schematic structure of the two layer networks: red dots denote the oscillators, blue planes correspond to the two layers. Solid lines show intra-layer couplings, dashed lines represent pairwise inter-layer couplings between the oscillators. Tweezer control is applied to layer 1.

by dashed lines. This network structure can also be referred to as a *multiplex*, since only one-to-one inter-layer connections between the layers exist.

For the sake of simplicity we assume

$$a_-^{(i)} = a_+^{(i)} = a^{(i)}, \qquad b_-^{(i)} = a^{(i)}\sigma_-^{(i)}, \qquad b_+^{(i)} = a^{(i)}\sigma_+^{(i)}, \quad (2)$$

with rescaled coupling parameters $a^{(i)}$, $\sigma_-^{(i)}$, and $\sigma_+^{(i)}$.

In order to introduce the tweezer control [76], we define two complex order parameters within each network layer i

$$Z_1^{(i)}(t) = \frac{1}{[N/2]} \sum_{k=1}^{[N/2]} e^{i\phi_k^{(i)}(t)} \quad (3)$$

$$Z_2^{(i)}(t) = \frac{1}{[N/2]} \sum_{k=1}^{[N/2]} e^{i\phi_{N-k+1}^{(i)}(t)}, \quad (4)$$

where $\phi_k^{(i)}(t)$ is the geometric phase of the k-th oscillator computed from

$$e^{i\phi_k^{(i)}(t)} = \left((x_k^{(i)})^2(t) + (\dot{x}_k^{(i)})^2(t)\right)^{-1/2} \left(x_k^{(i)}(t) + \mathrm{i}\dot{x}_k^{(i)}(t)\right). \quad (5)$$

The tweezer feedback control [76] for the non-locally coupled ring of oscillators is defined as

$$\sigma_\pm^{(i)} = K_\mathrm{s}\left(1 - \frac{1}{2}|Z_1^{(i)} + Z_2^{(i)}|\right) \pm K_\mathrm{a}(|Z_1^{(i)}| - |Z_2^{(i)}|). \quad (6)$$

The control term has two parts referred to as *symmetric* and *asymmetric* controls, with corresponding control gains K_s and K_a.

The idea of the symmetric proportional control was suggested for phase oscillators in Sieber et al. [73]. It is defined as a feedback loop between coupling parameters $\sigma_\pm^{(i)}$ and the global Kuramoto order parameter of the oscillators within one layer $|Z_\mathrm{s}^{(i)}| = \frac{|Z_1^{(i)}+Z_2^{(i)}|}{2}$. This feedback loop aims to suppress the collapse of small-size chimera states and extend their lifetime.

The asymmetric control part is realized as a second feedback loop between coupling parameters $\sigma_\pm^{(i)}$ and the difference $Z_\mathrm{a}^{(i)} = |Z_1^{(i)}| - |Z_2^{(i)}|$. It indicates a relative spatial shift of the chimera's incoherent domain with respect to the center of the oscillator array $1, ..., N$. If the incoherent domain of the chimera state is shifted toward larger indices ($|Z_1^{(i)}| > |Z_2^{(i)}|$), then the difference is positive, and as a result $\sigma_+^{(i)} > \sigma_-^{(i)}$. In the opposite case, when the incoherent domain of the chimera state is shifted toward smaller indices ($|Z_1^{(i)}| < |Z_2^{(i)}|$), we will obtain $\sigma_+^{(i)} < \sigma_-^{(i)}$. A discrepancy between $\sigma_+^{(i)}$ and $\sigma_-^{(i)}$ introduces asymmetry in the coupling term, and induces the counterbalancing lateral motion of a chimera state toward dynamically preferable centered position.

In Omelchenko et al. [76, 77] we have demonstrated the effective action of the tweezer control in small rings of non-locally coupled Van der Pol and FitzHugh-Nagumo oscillators. When both the symmetric and asymmetric parts of the control are acting (the control gains K_s and the K_a are positive), a stable chimera state can be observed in the system. When we switch off the asymmetric part of the control, $K_\mathrm{a} = 0$, and keep a positive symmetric gain $K_\mathrm{s} > 0$, the chimera state starts to drift on the ring. Its motion becomes stronger for decreasing system size. To switch off both parts of the control, we keep $\sigma_+^{(i)}$ and $\sigma_-^{(i)}$ constant, and after a short transient time the chimera state collapses to the completely synchronized state.

In the present work, the tweezer control acts in the first layer of our network (1) only, while in the second layer the coupling strength is constant. We will compare patterns obtained in both layers in a network of relatively small size. The characteristic signature of a chimera state is a pronounced difference of the average frequencies for oscillators belonging to the coherent and incoherent domains, respectively. The oscillators from the coherent domain are phase-locked having equal frequencies, while the oscillators from the incoherent domain have different average frequencies which typically form an arc-like profile. The mean phase velocities are obtained as

$$\omega_k^{(i)}(t) = \frac{1}{T_0}\int_0^{T_0} \dot{\phi}_k^{(i)}(t-t')dt', \quad k = 1, \ldots, N, i = 1, 2, \quad (7)$$

averaged over the time window T_0. To visualize the temporal dynamics of the oscillators we plot their mean phase velocities defined by Equation (7) with $T_0 = 50$ for each layer. Throughout this work in our numerical simulations we use random initial conditions.

Figure 2 shows the mean phase velocities for a two-layer network of Van der Pol oscillators with $N = 48$ oscillators within each layer, coupled to their $R_1 = R_2 = 16$ nearest neighbors. Such an intermediate coupling range is the prerequisite of the

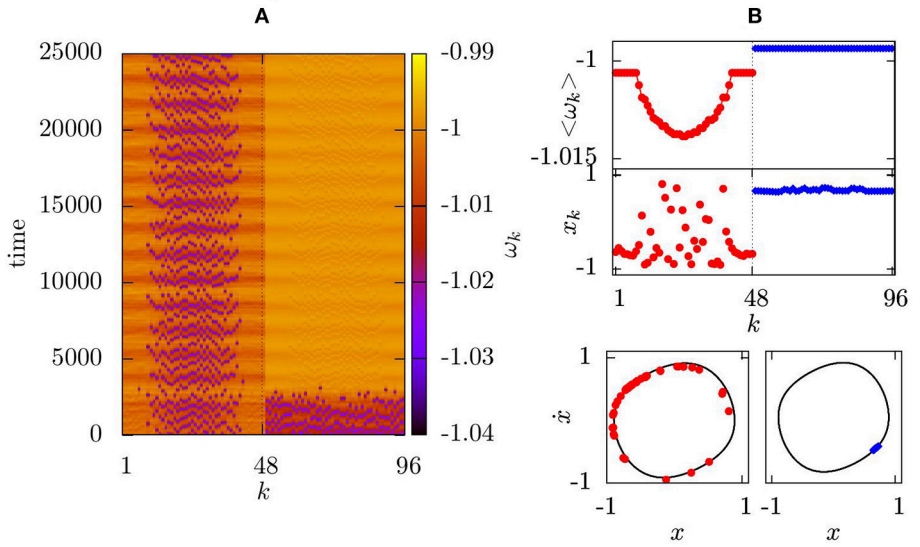

FIGURE 2 | Mean phase velocities for a two-layer system of $N = 48$ oscillators in each layer with $R_1 = R_2 = 16$, $\varepsilon = 0.2$, $a^{(1)} = a^{(2)} = 0.02$, $a_{inter} = 0.002$, $b_{inter} = 0.001$. Layer 1 is controlled with $K_a = 2$, $K_s = 0.5$, layer 2 is uncontrolled with $b_-^{(2)} = b_+^{(2)} = 0.0027$. Oscillators $k = 1...48$ represent the first layer, $k = 49...96$ the second layer; **(A)** space-time plot; **(B)** mean phase velocity profile averaged over 25,000 time units for the first layer (red dots) and the second layer (blue diamonds) (top panel); snapshot of variables x_k (middle panel) and snapshot in the $(x_k; \dot{x}_k)$ phase space at t =25,000 (bottom panel).

existence of chimera patterns in non-locally coupled rings. In our earlier work [21] we have demonstrated analytically that in the ring of non-locally coupled Van der Pol oscillators the ratio of the coupling constants of position and velocity (in our case $a_\pm^{(i)}$ and $b_\pm^{(i)}$) can be associated with the phase lag parameter for a reduced phase oscillator network. In order to observe chimera states, the coupling constant of position should be chosen larger than the coupling constant of velocity. In the following, we will use this property for both intra- and inter-layer couplings. As a first step, we consider very weak inter-layer coupling with constants $a_{inter} = 0.002$, $b_{inter} = 0.001$ approximately ten times smaller than intra-layer coupling strengths. **Figure 2A** shows, that in this case the intra-layer coupling dominates, and the two layers perform different dynamics: in the first layer we observe a stable chimera state due to the action of the tweezer control, while in the second, uncontrolled layer after short transient time all oscillators synchronize. **Figure 2B** shows the mean phase velocities of the oscillators averaged over large time interval T_0 =25,000 (upper panel). In the first layer the typical arc-shape profile is formed (shown red), which is one of the prominent features of chimera states. In the second layer, all oscillators are frequency-locked (shown blue). The middle panel demonstrates snapshots for both layers at fixed time, and the bottom panel depicts the same snapshots in the phase space, where the limit cycle of one uncoupled Van der Pol unit is shown in black. The oscillators from the incoherent domain of the chimera state are scattered around this limit cycle.

With increasing inter-layer coupling strength, we observe successful stabilization of the chimera state in the second layer shown in **Figure 3** for $a_{inter} = 0.011$, $b_{inter} = 0.0025$. Due to the fact that our layers are identical, the mean phase velocities profiles have the same shape, and coherent/incoherent domains of chimera states are synchronized spatially in both layers. **Figure 4** presents a diagram in the parameter plane of inter- and intra-layer coupling constants. When the interlayer coupling is too weak, chimera states in the second layer can not be stabilized (blue region). In the red region synchronization of both layers, and thus successful control of the chimera state in the second layer via multiplexing is observed. In the thin hatched region our numerical evidence shows a sensitive dependence on the initial conditions. However, system (1) has numerous parameters which should also be fixed appropriately. For instance, the control gains K_s and K_a can influence the shape of the controlled chimera pattern and the size of its coherent domain [77]. Moreover, in the examples demonstrated in the present manuscript, the non-linearity parameter ε of the individual Van der Pol oscillator is chosen to be small, corresponding to sinusoidal oscillations. The tweezer control acts successfully also in the case of relaxation oscillations when ε is large [76].

Figure 5 demonstrates the behavior of chimera patterns within two layers under the action of each part of the control (6) separately. When the asymmetric part is deactivated, $K_a = 0$, the lifetime of the chimera state is still extended, but it starts to drift, as shown in **Figure 5A**. The coherent and incoherent domains of the chimera state in the second layer drift along with the chimera in the controlled layer. Thus, extending of lifetime without position control in both layers is possible as well. When we stop to control the lifetime of chimeras, by keeping the coupling coefficients constant in the first layer, after some transient time we observe simultaneous chimera collapse in both layers as depicted in **Figure 5B**.

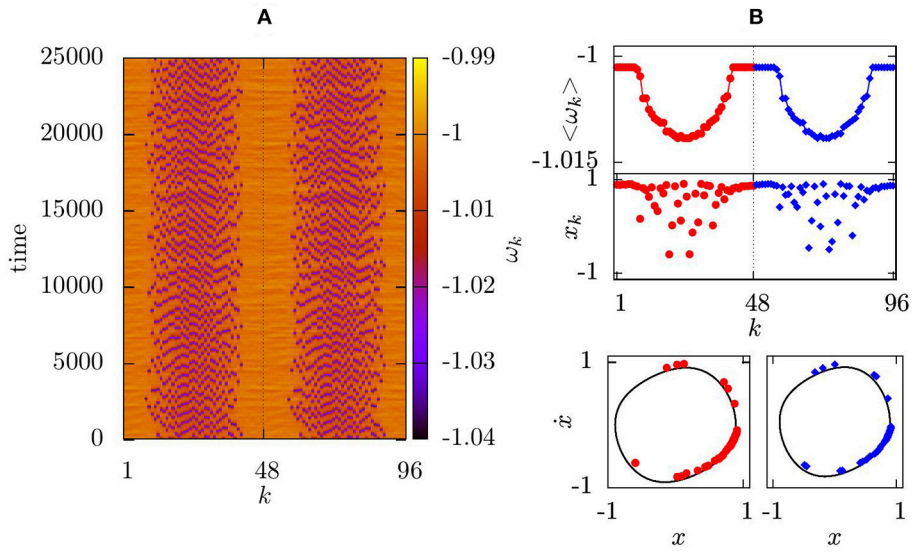

FIGURE 3 | Same as **Figure 2** for a_{inter} =0.011, b_{inter} = 0.0025.

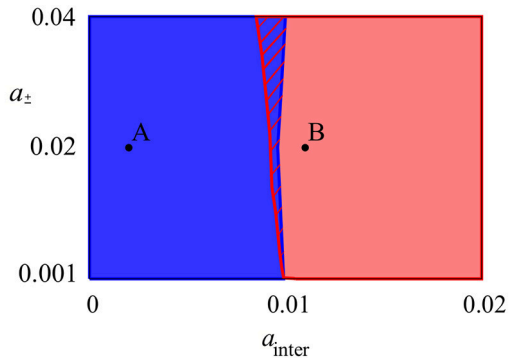

FIGURE 4 | Diagram in the plane of inter-layer a_{inter} and intra-layer a coupling constants for a two-layer system of $N = 48$ oscillators in each layer with $R_1 = R_2 = 16$. The red region corresponds to the successful stabilization of chimera states in both layers, the blue region depicts chimera collapse in the uncontrolled layer. In the hatched region only part of the numerical realizations indicated successful control. Points A and B denote parameter values corresponding to **Figures 2** and **3**, respectively. Other parameters as in **Figure 2**.

Hence, the combination of tweezer control and multiplexing allows for efficient control of chimera states in multiple layers, with the control applied directly to only one layer.

3. ROBUSTNESS OF THE TWEEZER CONTROL IN TWO-LAYER NETWORKS

In real-world networks non-identical layers are more common. Therefore, the analysis of the robustness of the tweezer control in two-layer networks is an important issue. In the following we will consider the topological inhomogeneity of the layers in the network by introducing a coupling range mismatch $R_1 \neq R_2$. In non-locally coupled rings the coupling range is one of the essential parameters for the observation of chimera states. An intermediate coupling range is usually favorable, while too small or too large numbers of coupled neighbors prevent the formation of chimera states. Furthermore, within intermediate values, smaller coupling ranges can cause multiple coherent and incoherent domains of the chimera state. Thus, considering different coupling ranges in two layers will result in competitive patterns formed in each layer. As before, the tweezer control acts only in the first layer of our network.

Figure 6 depicts the stabilization of chimera states in system (1) with $N = 48$ oscillators in each layer, and slightly inhomogeneous topologies with coupling ranges $R_1 = 16$ and $R_2 = 18$. After a short transient time, the interplay of the tweezer control and inter-layer coupling results in the successful spatial alignment of the coherent and incoherent domains, and their mean phase velocity profiles have similar shapes as well, as shown in **Figure 6B**.

As a next step, we increase the layer mismatch and choose $R_1 = 16$, $R_2 = 12$. In the isolated case, the second layer would exhibit a chimera state with multiple incoherent domains [21], which collapses to the completely synchronized state. **Figure 7** demonstrates that by controlling the first layer, we successfully suppress the collapse, and synchronize the chimera states in both layers. However, due to the bidirectional inter-layer interaction, the dynamics of the second layer has indeed an influence on the first one. The chimera states shown in **Figure 7** have larger incoherent domains induced by the smaller coupling range in the second layer. It is worth to note that to stabilize their position, the asymmetric control gain had to be increased ($K_a = 6$). We have shown numerically that we can stabilize the chimera states

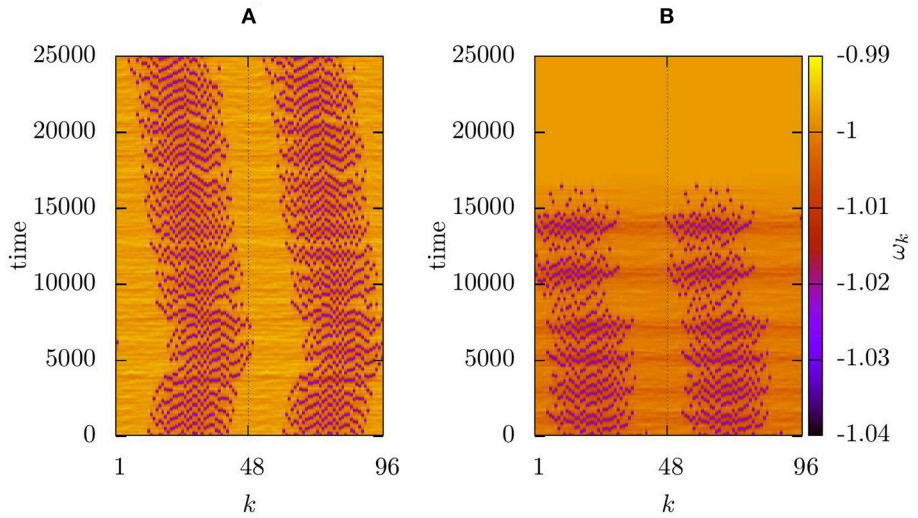

FIGURE 5 | Space-time plot of the mean phase velocities for a two-layer network with one part of the control switched off; **(A)** drifting chimera state in both layers with $K_a = 0$; **(B)** collapse of the uncontrolled chimera state in both layers, with constant coupling coefficients $\sigma_{\pm}^{(1)} = 0.14$. Other parameters as in **Figure 3**.

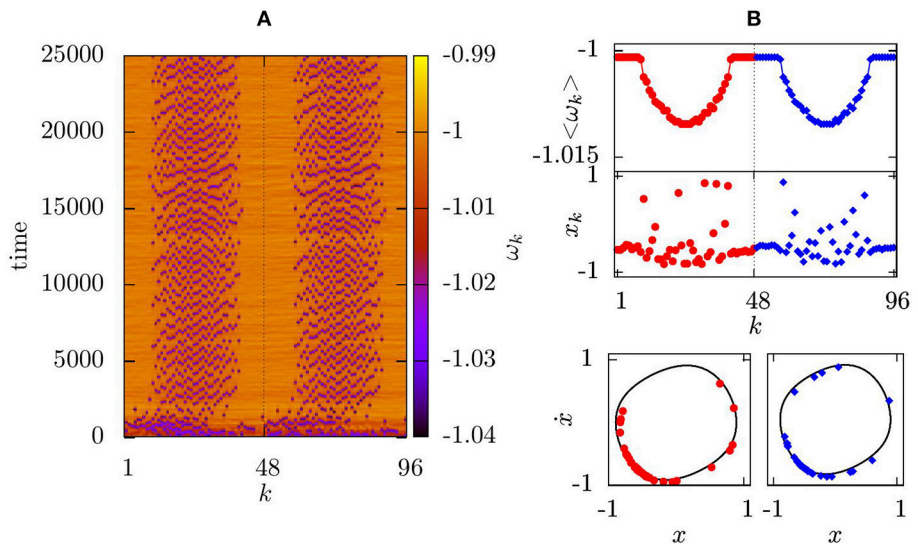

FIGURE 6 | Mean phase velocities for a two-layer system of $N = 48$ oscillators in the layers and non-identical coupling ranges: $R_1 = 16$, $R_2 = 18$, other parameters:$\varepsilon = 0.2$, $a^{(1)} = a^{(2)} = 0.02$, $a_{inter} = 0.009$, $b_{inter} = 0.0023$, $K_a = 2$, $K_s = 0.5$, $b_{-}^{(2)} = b_{+}^{(2)} = 0.0027$. Oscillators $k = 1...48$ represent the first layer, $k = 49...96$ the second layer; **(A)** space-time plot; **(B)** mean phase velocity profile averaged over 25,000 time units for the first layer (red dots) and the second layer (blue diamonds) (top panel); snapshot of variables x_k (middle panel) and snapshot in the $(x_k; \dot{x}_k)$ phase space at t =25,000 (bottom panel).

in two layers for an even larger topology mismatch, however, the coupling parameters and control gains had to be tuned.

4. CONCLUSION

In the present manuscript, we have demonstrated that the combination of the tweezer control for chimera states and multiplexing allows for successful stabilization of chimera states in both layers of two-layer networks of Van der Pol oscillators. Considering a ring topology with non-local interaction between the oscillators within each layer, and one-to-one connections between the corresponding oscillators from the two layers, we have focused on networks of relatively small size, where chimera states are usually hard to observe. Tweezer control, consisting of two parts, extends the lifetime of chimera states, and fixes their spatial position on the ring.

In two-layer networks we have applied the tweezer control to one layer only, and have shown that for sufficiently strong inter-layer coupling the action of the control is transferred to

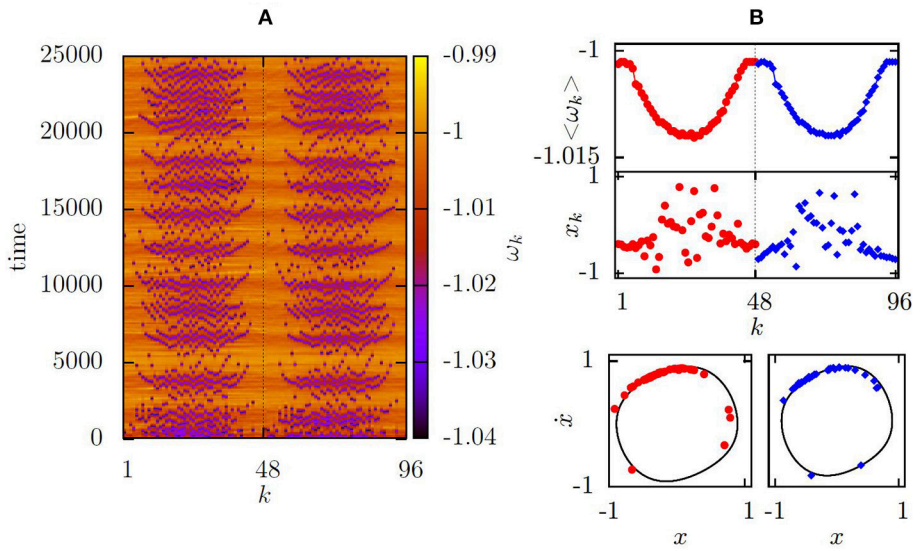

FIGURE 7 | Same as **Figure 6** with $R_1 = 16$, $R_2 = 12$, and $K_a = 6$.

the second layer, where the lifetime of the chimera state is increased and its spatial position if fixed. Without the inter-layer connections, or if their strength is too weak, after a short transient time the chimera state collapses and all oscillators in the second layer synchronize.

We have demonstrated that the combination of tweezer control and multiplexing is robust with respect to the topological inhomogeneity of the layers, and chimera states can be successfully stabilized even in the case of large coupling range mismatch between the layers. Previously, we have demonstrated that tweezer control acts efficiently in non-locally coupled rings consisting of inhomogeneous oscillators [76], therefore the stabilization of chimera states in the two-layer networks with inhomogeneous nodes is plausible as well.

Our results can be useful in real multilayer networks, where the access to some layers is not possible, but there is need to control spatio-temporal patterns. Combination of tweezer control and multiplexing appears to be a powerful and robust tool to solve this problem even for small networks with inhomogeneous layers.

AUTHOR CONTRIBUTIONS

IO, AZ, and ES designed and supervised the study and carried out the analytical work. TH provided numerical simulations and constructed the figures. All authors discussed the results and contributed to writing the manuscript.

FUNDING

Funded by the Deutsche Forschungsgemeinschaft (DFG, German Research Foundation)–Projektnummer 163436311–SFB 910.

REFERENCES

1. Abrams DM, Strogatz SH. Chimera states for coupled oscillators. *Phys Rev Lett.* (2004) **93**:174102. doi: 10.1103/physrevlett.93.174102
2. Kuramoto Y, Battogtokh D. Coexistence of coherence and incoherence in nonlocally coupled phase oscillators. *Nonlinear Phenomena Complex Syst.* (2002) **5**:380–5.
3. Shima S, Kuramoto Y. Rotating spiral waves with phase-randomized core in nonlocally coupled oscillators. *Phys Rev E* (2004) **69**:036213. doi: 10.1103/physreve.69.036213
4. Laing CR. The dynamics of chimera states in heterogeneous Kuramoto networks. *Physica D* (2009) **238**:1569–88. doi: 10.1016/j.physd.2009.04.012
5. Motter AE. Nonlinear dynamics: spontaneous synchrony breaking. *Nat Phys.* (2010) **6**:164–5. doi: 10.1038/nphys1609
6. Panaggio MJ, Abrams DM. Chimera states: coexistence of coherence and incoherence in networks of coupled oscillators. *Nonlinearity* (2015) **28**:R67. doi: 10.1088/0951-7715/28/3/r67
7. Schöll E. Synchronization patterns and chimera states in complex networks: interplay of topology and dynamics. *Eur Phys J Spec Top.* (2016) **225**:891–919. doi: 10.1140/epjst/e2016-02646-3
8. Sakaguchi H. Instability of synchronized motion in nonlocally coupled neural oscillators. *Phys Rev E* (2006) **73**:031907. doi: 10.1103/physreve.73.031907
9. Wolfrum M, Omel'chenko OE, Yanchuk S, Maistrenko Y. Spectral properties of chimera states. *Chaos* (2011) **21**:013112. doi: 10.1063/1.3563579
10. Wolfrum, M, Omel'chenko OE. Chimera states are chaotic transients. *Phys Rev E* (2011) **84**:015201. doi: 10.1103/physreve.84.015201
11. Omel'chenko OE, Wolfrum M, Yanchuk S, Maistrenko Y, Sudakov O. Stationary patterns of coherence and incoherence in two-dimensional arrays of non-locally-coupled phase oscillators. *Phys Rev E* (2012) **85**:036210. doi: 10.1103/physreve.85.036210

12. Wolfrum M, Omel'chenko OE, Sieber J. Regular and irregular patterns of self-localized excitation in arrays of coupled phase oscillators. *Chaos* (2015) **25**:053113. doi: 10.1063/1.4921297
13. Martens EA, Laing CR, Strogatz SH. Solvable model of spiral wave chimeras. *Phys Rev Lett.* (2010) **104**:044101. doi: 10.1103/physrevlett.104.044101
14. Martens EA. Chimeras in a network of three oscillator populations with varying network topology. *Chaos* (2010) **20**:043122. doi: 10.1063/1.3499502
15. Omelchenko I, Maistrenko Y, Hövel P, Schöll E. Loss of coherence in dynamical networks: spatial chaos and chimera states. *Phys Rev Lett.* (2011) **106**:234102. doi: 10.1103/physrevlett.106.234102
16. Omelchenko I, Riemenschneider B, Hövel P, Maistrenko Y, Schöll E. Transition from spatial coherence to incoherence in coupled chaotic systems. *Phys Rev E* (2012) **85**:026212. doi: 10.1103/physreve.85.026212
17. Sethia GC, Sen A, Atay FM. Clustered chimera states in delay-coupled oscillator systems. *Phys Rev Lett.* (2008) **100**:144102. doi: 10.1103/physrevlett.100.144102
18. Sethia GC, Sen A, Johnston GL. Amplitude-mediated chimera states. *Phys Rev E.* (2013) **88**:042917. doi: 10.1063/1.5031804
19. Sethia GC, Sen A. Chimera states: the existence criteria revisited. *Phys Rev Lett.* (2014) **112**:144101. doi: 10.1103/physrevlett.112.144101
20. Zakharova A, Kapeller M, Schöll E. Chimera death: symmetry breaking in dynamical networks. *Phys Rev Lett.* (2014) **112**:154101. doi: 10.1103/physrevlett.112.154101
21. Omelchenko I, Zakharova A, Hövel P, Siebert J, Schöll E. Nonlinearity of local dynamics promotes multi-chimeras. *Chaos* (2015) **25**:083104. doi: 10.1063/1.4927829
22. Omelchenko I, Omel'chenko OE, Hövel P, Schöll E. When nonlocal coupling between oscillators becomes stronger: patched synchrony or multichimera states. *Phys Rev Lett.* (2013) **110**:224101. doi: 10.1103/physrevlett.110.224101
23. Omelchenko I, Provata A, Hizanidis J, Schöll E, Hövel P. Robustness of chimera states for coupled FitzHugh-Nagumo oscillators. *Phys Rev E* (2015) **91**:022917. doi: 10.1103/physreve.91.022917
24. Hizanidis J, Kanas V, Bezerianos A, Bountis T. Chimera states in networks of nonlocally coupled Hindmarsh-Rose neuron models. *Int J Bifurcation Chaos* (2014) **24**:1450030. doi: 10.1142/s0218127414500308
25. Laing CR. Derivation of a neural field model from a network of theta neurons. *Phys Rev E* (2014) **90**:010901. doi: 10.1103/physreve.90.010901
26. Hizanidis J, Panagakou E, Omelchenko I, Schöll E, Hövel P, Provata A. Chimera states in population dynamics: networks with fragmented and hierarchical connectivities. *Phys Rev E* (2015) **92**:012915. doi: 10.1103/physreve.92.012915
27. Panaggio MJ, Abrams DM. Chimera states on a flat torus. *Phys Rev Lett.* (2013) **110**:094102. doi: 10.1103/PhysRevLett.110.094102
28. Xie J, Knobloch E, Kao HC. Multicluster and traveling chimera states in nonlocal phase-coupled oscillators. *Phys Rev E* (2014) **90**:022919. doi: 10.1103/physreve.90.022919
29. Maistrenko Y, Vasylenko A, Sudakov O, Levchenko R, Maistrenko VL. Cascades of multi-headed chimera states for coupled phase oscillators. *Int J Bifur Chaos* (2014) **24**:1440014. doi: 10.1142/S0218127414400148
30. Maistrenko Y, Sudakov O, Osiv O, Maistrenko VL. Chimera states in three dimensions. *New J Phys.* (2015) **17**:073037. doi: 10.1088/1367-2630/17/7/073037
31. Panaggio MJ, Abrams DM. Chimera states on the surface of a sphere. *Phys Rev E* (2015) **91**:022909. doi: 10.1103/physreve.91.022909
32. Kasatkin DV, Yanchuk S, Schöll E, Nekorkin VI. Self-organized emergence of multi-layer structure and chimera states in dynamical networks with adaptive couplings. *Phys Rev E* (2017) **96**:062211. doi: 10.1103/physreve.96.062211
33. Bera BK, Majhi S, Ghosh D, Perc M. Chimera states: effects of different coupling topologies. *Europhys Lett.* (2017) **118**:10001. doi: 10.1209/0295-5075/118/10001
34. Ulonska S, Omelchenko I, Zakharova A, Schöll E. Chimera states in networks of Van der Pol oscillators with hierarchical connectivities. *Chaos* (2016) **26**:094825. doi: 10.1063/1.4962913
35. Sawicki J, Omelchenko I, Zakharova A, Schöll E. Chimera states in complex networks: interplay of fractal topology and delay. *Eur Phys J Spec Top.* (2017) **226**:1883–92. doi: 10.1140/epjst/e2017-70036-8
36. Tsigkri-DeSmedt ND, Hizanidis J, Schöll E, Hövel P, Provata A. Chimeras in leaky integrate-and-fire neural networks: effects of reflecting connectivities. *Eur Phys J. B* (2017) **90**:139. doi: 10.1140/epjb/e2017-80162-0
37. zur Bonsen A, Omelchenko I, Zakharova A, Schöll E. Chimera states in networks of logistic maps with hierarchical connectivities. *Eur Phys J B* (2018) **91**:65. doi: 10.1140/epjb/e2018-80630-y
38. Chouzouris T, Omelchenko I, Zakharova A, Hlinka J, Jiruska P, Schöll E. Chimera states in brain networks: empirical neural vs. modular fractal connectivity. *Chaos* (2018) **28**:045112. doi: 10.1063/1.5009812
39. Yeldesbay A, Pikovsky A, Rosenblum M. Chimeralike states in an ensemble of globally coupled oscillators. *Phys Rev Lett.* (2014) **112**:144103. doi: 10.1103/physrevlett.112.144103
40. Schmidt L, Krischer, K. Clustering as a prerequisite for chimera states in globally coupled systems. *Phys Rev Lett.* (2015) **114**:034101. doi: 10.1103/PhysRevLett.114.034101
41. Laing CR. Chimeras in networks with purely local coupling. *Phys Rev E* (2015) **92**:050904. doi: 10.1103/PhysRevE.92.050904
42. Olmi S, Martens EA, Thutupalli S, Torcini A. Intermittent chaotic chimeras for coupled rotators. *Phys Rev E* (2015) **92**:030901. doi: 10.1103/physreve.92.030901
43. Bogomolov S, Slepnev A, Strelkova G, Schöll E, Anishchenko VS. Mechanisms of appearance of amplitude and phase chimera states in a ring of nonlocally coupled chaotic systems. *Commun Nonlinear Sci Numer Simul.* (2017) **43**:25. doi: 10.1016/j.cnsns.2016.06.024
44. Semenova N, Zakharova A, Anishchenko VS, Schöll E. Coherence-resonance chimeras in a network of excitable elements. *Phys Rev Lett.* (2016) **117**:014102. doi: 10.1103/PhysRevLett.117.014102
45. Kundu S, Majhi S, Bera BK, Ghosh D, Lakshmanan M. Chimera states in two-dimensional networks of locally coupled oscillators. *Phys Rev E* (2018) **97**:022201. doi: 10.1103/PhysRevE.97.022201
46. Majhi S, Ghosh D. Alternating chimeras in networks of ephaptically coupled bursting neurons. *Chaos* (2018) **28**:083113. doi: 10.1063/1.5022612
47. Majhi S, Bera BK, Ghosh D, Perc M. Chimera states in neuronal networks: a review. *Phys Life Rev.* (2018). doi: 10.1016/j.plrev.2018.09.003
48. Hagerstrom AM, Murphy TE, Roy R, Hövel P, Omelchenko I, Schöll E. Experimental observation of chimeras in coupled-map lattices. *Nat Phys.* (2012) **8**:658–61. doi: 10.1038/nphys2372
49. Tinsley MR, Nkomo S,Showalter K. Chimera and phase cluster states in populations of coupled chemical oscillators. *Nat Phys.* (2012) **8**:662–5. doi: 10.1038/nphys2371
50. Nkomo S, Tinsley MR, Showalter K. Chimera states in populations of nonlocally coupled chemical oscillators. *Phys Rev Lett.* (2013) **110**:244102. doi: 10.1103/physrevlett.110.244102
51. Martens EA, Thutupalli S, Fourriere A, Hallatschek O. Chimera states in mechanical oscillator networks. *Proc Natl Acad Sci USA.* (2013) **110**:10563. doi: 10.1073/pnas.1302880110
52. Larger L, Penkovsky B, Maistrenko Y. Virtual chimera states for delayed-feedback systems. *Phys Rev Lett.* (2013) **111**:054103. doi: 10.1103/physrevlett.111.054103
53. Gambuzza LV, Buscarino A, Chessari S, Fortuna L, Meucci R, Frasca M. Experimental investigation of chimera states with quiescent and synchronous domains in coupled electronic oscillators. *Phys Rev E* (2014) **90**:032905. doi: 10.1103/physreve.90.032905
54. Larger L, Penkovsky B, Maistrenko Y. Laser chimeras as a paradigm for multistable patterns in complex systems. *Nat Commun.* (2015) **6**:7752. doi: 10.1038/ncomms8752
55. Brunner D, Penkovsky B, Levchenko R, Schöll E, Larger L, Maistrenko Y. Two-dimensional spatiotemporal complexity in dual-delayed nonlinear feedback systems: chimeras and dissipative solitons. *Chaos* (2018) **28**:103106. doi: 10.1063/1.5043391
56. Wickramasinghe M, Kiss IZ. Spatially organized dynamical states in chemical oscillator networks: Synchronization, dynamical differentiation, and chimera patterns. *PLoS ONE* (2013) **8**:e80586. doi: 10.1371/journal.pone.0080586
57. Schmidt L, Schönleber K, Krischer K, García-Morales V. Coexistence of synchrony and incoherence in oscillatory media under nonlinear

global coupling. *Chaos* (2014) **24**:013102. doi: 10.1063/1.4858996
58. Rosin DP, Rontani D, Haynes N, Schöll E, Gauthier DJ. Transient scaling and resurgence of chimera states in coupled Boolean phase oscillators. *Phys Rev E* (2014) **90**:030902. doi: 10.1103/physreve.90.030902
59. Ott E, Antonsen TM. Low dimensional behavior of large systems of globally coupled oscillators. *Chaos* (2008) **18**:037113. doi: 10.1063/1.2930766
60. Ott E, Antonsen TM. Long time evolution of phase oscillator systems. *Chaos* (2009) **19**:023117. doi: 10.1063/1.3136851
61. Omel'chenko OE. Coherence-incoherence patterns in a ring of non-locally coupled phase oscillators. *Nonlinearity* (2013) **26**:2469. doi: 10.1088/0951-7715/26/9/2469/meta
62. Pazó D, Montbrió E. Low-dimensional dynamics of populations of pulse-coupled oscillators. *Phys Rev X* (2014) **4**:011009. doi: 10.1103/physrevx.4.011009
63. Omel'chenko OE. The mathematics behind chimera states. *Nonlinearity* (2018) **31**:R121. doi: 10.1088/1261-6544/aaaa07
64. Ashwin P, Burylko O. Weak chimeras in minimal networks of coupled phase oscillators. *Chaos* (2015) **25**:013106. doi: 10.1063/1.4905197
65. Panaggio MJ, Abrams DM, Ashwin P, Laing CR. Chimera states in networks of phase oscillators: the case of two small populations. *Phys Rev E* (2016) **93**:012218. doi: 10.1103/physreve.93.012218
66. Böhm F, Zakharova A, Schöll E, Lüdge K. Amplitude-phase coupling drives chimera states in globally coupled laser networks. *Phys Rev E* (2015) **91**:040901. doi: 10.1103/physreve.91.040901
67. Hart JD, Bansal K, Murphy TE, Roy R. Experimental observation of chimera and cluster states in a minimal globally coupled network. *Chaos* (2016) **26**:094801. doi: 10.1063/1.4953662
68. Omel'chenko OE, Wolfrum M, Maistrenko Y. Chimera states as chaotic spatiotemporal patterns. *Phys Rev E* (2010) **81**:065201. doi: 10.1103/physreve.81.065201
69. Suda Y, Okuda K. Persistent chimera states in nonlocally coupled phase oscillators. *Phys Rev E* (2015) **92**:060901. doi: 10.1103/physreve.92.060901
70. Bick C. Heteroclinic switching between chimeras. *Phys Rev E* (2018) **97**:050201. doi: 10.1103/physreve.97.050201
71. Schöll E, Klapp SHL, Hövel P. *Control of Self-organizing Nonlinear Systems*. Berlin: Springer (2016).
72. Gjurchinovski A, Schöll E, Zakharova, A. Control of amplitude chimeras by time delay in dynamical networks. *Phys Rev E* (2017) **95**:042218. doi: 10.1103/physreve.95.042218
73. Sieber J, Omel'chenko OE, Wolfrum M. Controlling unstable chaos: stabilizing chimera states by feedback. *Phys Rev Lett.* (2014) **112**:054102. doi: 10.1103/physrevlett.112.054102
74. Bick C, Martens EA. Controlling chimeras. *New J Phys.* (2015) **17**:033030. doi: 10.1088/1367-2630/17/3/033030
75. Bera BK, Ghosh D, Parmananda P, Osipov GV, Dana SK. Coexisting synchronous and asynchronous states in locally coupled array of oscillators by partial self-feedback control. *Chaos*(2017) **27**:073108. doi: 10.1063/1.4993459
76. Omelchenko I, Omel'chenko OE, Zakharova A, Wolfrum M, Schöll E. Tweezers for chimeras in small networks. *Phys Rev Lett.* (2016) **116**:114101. doi: 10.1103/physrevlett.116.114101
77. Omelchenko I, Omel'chenko OE, Zakharova A, Schöll E. Optimal design of tweezer control for chimera states. *Phys Rev E* (2018) **97**:012216. doi: 10.1103/PhysRevE.97.012216
78. De Domenico M, Solé-Ribalta A, Cozzo E, Kivelä M, Moreno Y, Porter MA, et al. Mathematical formulation of multilayer networks. *Phys Rev X* (2013) **3**:041022. doi: 10.1103/PhysRevX.3.041022
79. Kivelä M, Arenas A, Barthélemy M, Gleeson JP, Moreno Y, Porter MA. Multilayer networks. *J Complex Netw.* (2014) **2**:203–71. doi: 10.1093/comnet/cnu016
80. Kleineberg KK, Boguñá M, Serrano, M. Á, Papadopoulos F. Hidden geometric correlations in real multiplex networks. *Nat Phys.* (2016) **12**:1076–81. doi: 10.1038/nphys3812
81. Maksimenko VA, Makarov VV, Bera BK, Ghosh D, Dana SK, Goremyko MV, et al. Excitation and suppression of chimera states by multiplexing. *Phys Rev E* (2016) **94**:052205. doi: 10.1103/physreve.94.052205
82. De Domenico M. Multilayer modeling and analysis of human brain networks. *Gigascience* (2017) **6**:1–8. doi: 10.1093/gigascience/gix004
83. Battiston F, Nicosia V, Chavez M, Latora V. Multilayer motif analysis of brain networks. *Chaos* (2017) **27**:047404. doi: 10.1063/1.4979282
84. Goremyko MV, Maksimenko VA, Makarov VV, Ghosh D, Bera B, Dana SK, et al. Interaction of chimera states in a multilayered network of nonlocally coupled oscillators. *Technol Phys Lett.* (2017) **43**:712–5. doi: 10.1134/s1063785017080077
85. Majhi S, Perc M, Ghosh D. Chimera states in a multilayer network of coupled and uncoupled neurons. *Chaos* (2017) **27**:073109. doi: 10.1063/1.4993836
86. Ghosh S, Kumar A, Zakharova A, Jalan S. Birth and death of chimera: interplay of delay and multiplexing. *Europhys Lett.* (2016) **115**:60005. doi: 10.1209/0295-5075/115/60005
87. Leyva I, Sendiña-Nadal I, Sevilla-Escoboza R, Vera-Avila VP, Chholak P, Boccaletti S. Relay synchronization in multiplex networks. *Sci Rep.* (2018) **8**:8629. doi: 10.1038/s41598-018-26945-w
88. Ghosh S, Zakharova A, Jalan S. Non-identical multiplexing promotes chimera states. *Chaos Solitons Fractals* (2018) **106**:56–60. doi: 10.1016/j.chaos.2017.11.010
89. Andrzejak RG, Ruzzene G, Malvestio I, Schindler K, Schöll E, Zakharova A. Mean field phase synchronization between chimera states. *Chaos* (2018) **28**:091101. doi: 10.1063/1.5049750
90. Sawicki J, Omelchenko I, Zakharova A, Schöll E. Synchronization scenarios of chimeras in multiplex networks. *Eur Phys J Spec Top.* (2018) **227**:1161. doi: 10.1140/epjst/e2018-800039-y
91. Carpi LC, Schieber TA, Pardalos PM, Marfany G, Masoller C, Díaz-Guilera A, et al. Assessing diversity in multiplex networks. *arXiv:1805.12350* (2018).
92. Nicosia V, Valencia M, Chavez M, Díaz-Guilera A, Latora V. Remote synchronization reveals network symmetries and functional modules. *Phys Rev Lett.* (2013) **110**:174102. doi: 10.1103/physrevlett.110.174102
93. Zhang L, Motter AE, Nishikawa T. Incoherence-mediated remote synchronization. *Phys Rev Lett.* (2017) **118**:174102. doi: 10.1103/physrevlett.118.174102
94. Sawicki J, Omelchenko I, Zakharova A, Schöll E. Delay controls chimera relay synchronization in multiplex networks. *Phys Rev E* (2018) **98**:062224. doi: 10.1103/PhysRevE.98.062224
95. Mikhaylenko M, Ramlow L, Jalan S, Zakharova A. Weak multiplexing in neural networks: switching between chimera and solitary states. *arXiv:1809.07148* (2018).
96. Semenova N, Zakharova, A. Weak multiplexing induces coherence resonance. *Chaos* (2018) **28**:051104. doi: 10.1063/1.5037584
97. Low LA, Reinhall PG, Storti DW. An investigation of coupled van der Pol oscillators. *J Vib Acoust.* (2003) **125**:162–9. doi: 10.1115/1.1553469
98. Low LA, Reinhall PG, Storti DW, Goldman EB. Coupled van der Pol oscillators as a simplified model for generation of neural patterns for jellyfish locomotion. *Struct Control Health Monit.* (2006) **13**:417–29. doi: 10.1002/stc.133
99. Storti DW, Reinhall PG. Phase-locked mode stability for coupled van der Pol oscillators. *J Vib Acoust.* (2000) **122**:318. doi: 10.1115/1.1302314

Conflict of Interest Statement: The authors declare that the research was conducted in the absence of any commercial or financial relationships that could be construed as a potential conflict of interest.

frontiers in Applied Mathematics and Statistics

ORIGINAL RESEARCH
published: 19 June 2019
doi: 10.3389/fams.2019.00031

Chimera States on a Ring of Strongly Coupled Relaxation Oscillators

Julian Rode[1,2†], *Jan Frederik Totz*[2*], *Enrico Fengler*[2†] *and Harald Engel*[2†]

[1] *Center for Information Services and High Performance Computing, Technische Universität Dresden, Dresden, Germany,*
[2] *Institute for Theoretical Physics, Technische Universität Berlin, Berlin, Germany*

Weakly coupled oscillators can exhibit seemingly incongruous synchronization patterns comprised of coherent and incoherent spatial domains known as chimera states. However, the weak coupling approximation is invalid when the characteristic phase response curve of an oscillator does not scale linearly with the coupling strength and instead changes its shape. In chemical experiments with photo-coupled relaxation oscillators, we find that beyond weak coupling chimera patterns consist of different coexisting cluster states. Numerical modeling reveals that the observed cluster states result from a phase-dependent excitability that is also commonly observed in neural tissue and cardiac pacemaker cells.

Keywords: pattern formation, synchronization, chimera state, nonlocal coupling, networks, chemical oscillators

OPEN ACCESS

Edited by:
Anna Zakharova,
Technische Universität Berlin,
Germany

Reviewed by:
Tatyana Vadivasova,
Saratov State University, Russia
Zigen Song,
Shanghai Ocean University, China
M. Lakshmanan,
Bharathidasan University, India

***Correspondence:**
Jan Frederik Totz
jantotz@itp.tu-berlin.de
orcid.org/0000-0003-4961-1630

†Julian Rode
orcid.org/0000-0001-5185-2199
Enrico Fengler
orcid.org/0000-0002-6338-7834
Harald Engel
orcid.org/0000-0003-3680-9496

Specialty section:
This article was submitted to Dynamical Systems, a section of the journal Frontiers in Applied Mathematics and Statistics

Received: *20 January 2019*
Accepted: *28 May 2019*
Published: *19 June 2019*

Citation:
Rode J, Totz JF, Fengler E and Engel H (2019) Chimera States on a Ring of Strongly Coupled Relaxation Oscillators. Front. Appl. Math. Stat. 5:31. doi: 10.3389/fams.2019.00031

1. INTRODUCTION

In populations of coupled nonlinear oscillators synchronization [1] and macroscopic non-equilibrium pattern formation [2] are intrinsically linked. In 2002, studying synchronization in a system of nonlocally coupled phase oscillators, Kuramoto and co-workers discovered a symmetry-broken solution comprised of in-phase synchronized and desynchronized oscillatory domains [3, 4]. This state, which was later named chimera state due to its incongruous composition, triggered an increasing number of studies on partial synchronization in populations of coupled nonlinear oscillators [5, 6]. The existence of chimera states on ring topologies has been verified in experiments with chemical and electrochemical oscillators [7, 8], electronic units [9, 10], laser systems [11, 12] and hydrodynamically coupled colloids [13]. They are thought to play an important role in neurological disorders [14] and new metamaterials [15].

Intuitively, chimera states exist due to the nonlocal coupling term, which does not depend on the state of a single local element, but takes into account the spatially extended pattern. Both dynamically distinct domains modulate the coupling term to maintain themselves, respectively. A spatial domain with high coherence results in a large feedback signal that supports high coherence. Conversely a domain with a low coherence leads to a small feedback signal that obstructs high coherence. Together this reinforces the respective coexisting, but incongruous spatiotemporal dynamics [4].

Many studies on coupled oscillators utilize the paradigmatic Kuramoto phase oscillator model due to its simplicity and analytical tractability [16, 17]. Our goal in this paper is to go beyond the weak coupling oscillators and describe chimera patterns on a ring of strongly coupled oscillators, which are based on chemical laboratory experiments. The commonly employed weak-coupling limit in oscillator networks is defined as the lowest order of a systematic perturbation expansion in a smallness parameter ϵ, reducing dynamics of coupled limit-cycle oscillators to pure phase dynamics. This reduction is possible, if the decay of amplitude disturbances, quantified by the transversal Lyapunov exponent, is much faster than the decay of phase disturbances.

A clear definition of a strong coupling limit is not so obvious and the focus of current research on coupled oscillators [18, 19]. A coupling scheme that implies substantial changes in the oscillator frequencies, cannot be viewed as weak. One possibility to differentiate between weak and strong coupling is to measure the phase response curve (PRC) of an oscillator [20]. It quantifies how much the phase ϕ, that parametrizes the oscillation cycle, is advanced or delayed in response to an external perturbation. Small perturbations representative of weak coupling lead to a continuous phase response curve $Q(\phi)$. Strong coupling perturbations evoke a non-smooth, discontinuous PRC exhibiting a finite jump, for example. Moreover, the PRC under weak-coupling scales linearly with the perturbation amplitude A, while under strong coupling the amplitude scaling turns out to be nonlinear: $Q(\phi; \lambda A) \neq \lambda \times Q(\phi; A)$ with $\lambda \in \mathbb{R}$.

2. MODELS

The dynamics on an arbitrary finite network of N interacting Kuramoto phase oscillators are described by

$$\frac{d\phi_i}{dt} = \omega_i + \sum_{j=1}^{N} W_{ij} \sin(\phi_j - \phi_i - \alpha)\,. \tag{1}$$

The state of the i-th oscillator is given by a scalar time-dependent phase variable $\phi_i(t)$, that repeatedly cycles through values from 0 to 2π. The interaction with other nodes in the network effectively modulates the natural angular frequency ω_i. The modulation strength is encoded in the weighted adjacency matrix W_{ij} and a 2π-periodic interaction function of the phase difference $\phi_j - \phi_i$.

The weighted adjacency matrix W_{ij} can encode any network connectivity. Additionally each link can have its own individual weight. In this paper we focus on global coupling given by $W_{ij} = K/N\,(1 - \delta_{ij})$, where δ_{ij} is the Kronecker delta, and rings with nonlocal coupling given by $W_{ij} = K \exp(||i-j||/\kappa)$. In both cases K is the coupling strength. For global coupling, the weights are normalized by the number of nodes N. In the nonlocally coupled system, the weights between nonlocal neighbors decay exponentially with a characteristic range of κ according to their distance on the ring network.

The simplest choice for the interaction function is the first Fourier mode. Given a vanishing phase frustration parameter $\alpha = 0$, if the neighboring node j is ahead in phase, node i will accelerate and conversely if neighbor j lags behind, then node i will decelerate. In the case of identical natural frequencies this interaction eventually leads to exact in-phase alignment. For $\alpha \neq 0$, the contribution by the interaction function does not vanish for in-phase alignment, which effectively impedes in-phase synchronization.

Remarkably, all dissipative systems with oscillatory dynamics can be reduced to a Kuramoto phase model with an appropriate interaction function under the assumption that the coupling between oscillators is weak [21]. As discussed above the most important consequence is that the resultant phase change $\Delta\phi$ due to a perturbation scales linearly with the perturbation amplitude. However, for strongly coupled oscillators this condition can be violated, when the total effect of multiple perturbations is not equal to the linear superposition of the individual effects.

We illustrate one possible realization of this case and its real-world relevance with experimentally well-accessible chemical relaxation oscillators [22–24], that show qualitatively identical behavior to biological nerve and heart cells [25–31]. The oscillators are based on the Belousov-Zhabotinsky reaction and their dynamics are well-captured in the two-component non-dimensionalized Zhabotinsky-Buchholtz-Kiyatkin-Epstein (ZBKE) model [23, 32, 33]:

$$\begin{aligned}
\dot{u}_i &= \frac{1}{\epsilon_1}\left(I_i - u_i(1+u_i) - \frac{u_i-\mu}{u_i+\mu}\left(\beta + q_i\frac{\alpha v_i}{\epsilon_3+1-v_i}\right) \right.\\
&\qquad \left. + \gamma\epsilon_2 w_{ss,i}^2 + (1-v_i)w_{ss,i} \right),\\
\dot{v}_i &= 2I_i + (1-v_i)w_{ss,i} - \frac{\alpha v_i}{\epsilon_3+1-v_i}\,,\\
w_{ss,i}(u_i,v_i) &= \frac{1}{4\gamma\epsilon_2}\left(\sqrt{16\gamma u_i\epsilon_2 + v_i^2 - 2v_i + 1} + v_i - 1\right),\\
I_i(t) &= I_0 + \sum_{j=1}^{N} W_{ij}\Big[\, v_j(t-\tau) - v_i(t) \,\Big].
\end{aligned} \tag{2}$$

The oscillation takes place in the dimensionless concentrations of u (bromous acid, $HBrO_2$) and v (oxidized form of the ruthenium-tris-dimethylene-bipyridine catalyst, $Ru(dmbpy)_3^{3+}$). The latter can be measured spectrophotometrically via fluorescence light in an experiment [23]. The parameters $\epsilon_1, \epsilon_2, \epsilon_3, \alpha, \beta, \gamma, \mu, q$ depend on reaction rates and initial reagent concentrations. The dimensionless steady-state concentration w_{ss} (bromous acid radical $HBrO_2^+$) adapts adiabatically. The interaction between oscillators is mediated by individual light application I_i via a spatial light modulator that influences the production rates of u and v. For comparability with the Kuramoto model Equation (1), here the interaction is chosen to depend linearly on the difference of the oxidized catalyst concentrations $v_j - v_i$. To allow for phase frustration in limit cycle oscillators, instead of a phase frustration parameter α Equation (1) we utilize a time delay: $v_j(t-\tau) - v_i(t)$ [5]. Only for $\tau = 0$ in-phase synchronization is possible, whereas $\tau \neq 0$ obstructs it. The weighted adjacency matrix W_{ij} in the coupling term encodes the network connectivity and can be freely chosen as discussed above. Due to the dissipative nature of both models, we employ the explicit Euler method with a fixed time step Δt for numerical simulation [34].

To get intuition for the dynamics of the ZBKE model (Equation 2), we present the u-v phase plane of a single oscillator in **Figure 1A**. It features an unstable fixed point inside a stable limit cycle that resulted from a Hopf bifurcation with a consecutive canard explosion [35]. The phase space structure with the cubic shape of the u-nullcline (continuous) and its single intersection with the v-nullcline (dashed) resembles the FitzHugh-Nagumo model for neuronal oscillations [36]. However, the ZBKE phase plane is plotted in logarithmic scale and thus there are only single fast and slow domains on the right and left branch of the limit cycle, respectively. This is further

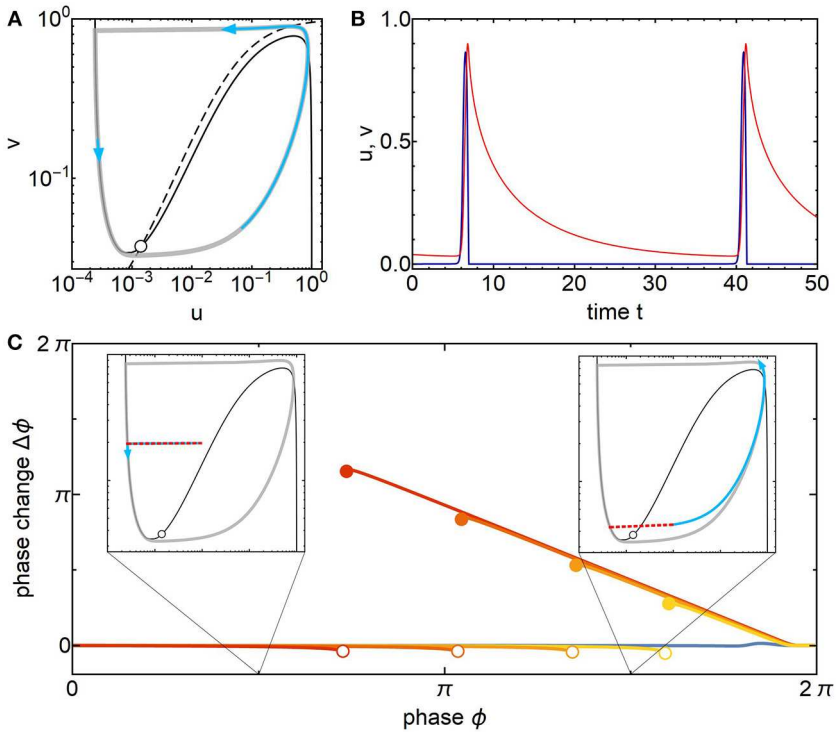

FIGURE 1 | Relaxation oscillator dynamics of the ZBKE model **(A)** Logarithmically-scaled phase plane consisting of unstable fixed point (empty dot) at the intersection of u- and v-nullclines (continuous, dashed black lines) surrounded by stable limit cycle (gray). Two example trajectories (blue) lasting 3 dimensionless time units illustrate fast and slow dynamics along the limit cycle. **(B)** Time series of u, v variables (blue, red) exhibit time scale separation that is characteristic for a relaxation oscillation. **(C)** Phase response curves for different perturbation amplitudes (red to yellow: $I_p = \{1, 1/2, 1/4, 1/8\} \times 10^{-3}$, blue: $I_p = 10^{-5}$). Insets show perturbation (red dashed) and perturbed phase plane trajectories (blue) in phase space underlying the measured phase change $\Delta\phi$. Parameters: $\epsilon_1 = 0.11$, $\epsilon_2 = 1.7 \times 10^{-5}$, $\epsilon_3 = 1.6 \times 10^{-3}$, $\alpha = 0.1$, $\beta = 1.7 \times 10^{-5}$, $\gamma = 1.2$, $\mu = 2.4 \times 10^{-4}$, $q = 0.7$, $I_0 = 5.25 \times 10^{-4}$, natural frequency $\omega_0 = 0.177$, time step $\Delta t = 2 \times 10^{-4}$.

reflected in the consecutive switches between fast rise and slow decay of the v variable (**Figure 1B**).

To gain insight into the synchronization properties of a set of such oscillators, we measure the corresponding phase response curve $Q(\phi)$. In **Figure 1C** we choose an additive perturbation, $(u, v) \mapsto (u+\epsilon_1^{-1} I_p, v+2I_p)$, where I_p is the perturbation strength. This perturbation imitates a short application of light intensity in the experiment.

In contrast to commonly employed smooth phase response curves [20] our PRC exhibits two distinguishing features (**Figure 1**): First, there is a jump-discontinuity between an initial flat interval, during which the oscillator is insensitive to a perturbation, $\Delta\phi = 0$, and a second interval, which is well approximated by $\Delta\phi = 2\pi - \phi$. Secondly, the perturbation strength does not linearly scale the amplitude of the PRC, but instead changes the position of the jump point ϕ^* and thus the shape, $Q(\phi; \lambda A) \neq \lambda \times Q(\phi; A)$. Overall the PRC is well captured by:

$$Q(\phi; I_p) = \begin{cases} 0 & , \phi < \phi^*(I_p) \\ 2\pi - \phi & , \phi \geq \phi^*(I_p) \end{cases} . \tag{3}$$

These features are incompatible with the commonly employed weak coupling approximation. The reason is that the perturbation amplitudes are large and our system exhibits phase-sensitive excitability [37]: During the refractory window at early phases, a perturbation of fixed amplitude fails to push the state across the u-nullcline, but it succeeds during the vulnerable window at later phases and induces a new oscillation cycle immediately (insets **Figure 1C**). Consequently the position of the jump point $\phi^*(I_p)$ in the PRC for a certain perturbation strength I_p can be predicted by the distance between the left branch of the limit cycle and the unstable branch of the u-nullcline. Note that for weak perturbations the PRC qualitatively changes its shape and scales linearly with the perturbation amplitude, as expected.

In **Figure 2** we highlight the contrasting synchronization behavior of strongly coupled oscillators (Equation 2) by direct comparison with Kuramoto phase oscillators (Equation 1), which are weakly coupled by definition. It is well known that in an all-to-all coupled network heterogeneous Kuramoto phase oscillators synchronize beyond a critical coupling strength [16]. The Kuramoto order parameter,

$$R = \frac{1}{N} \left| \sum_{j=1}^{N} e^{\mathrm{i}\phi_j} \right| , \tag{4}$$

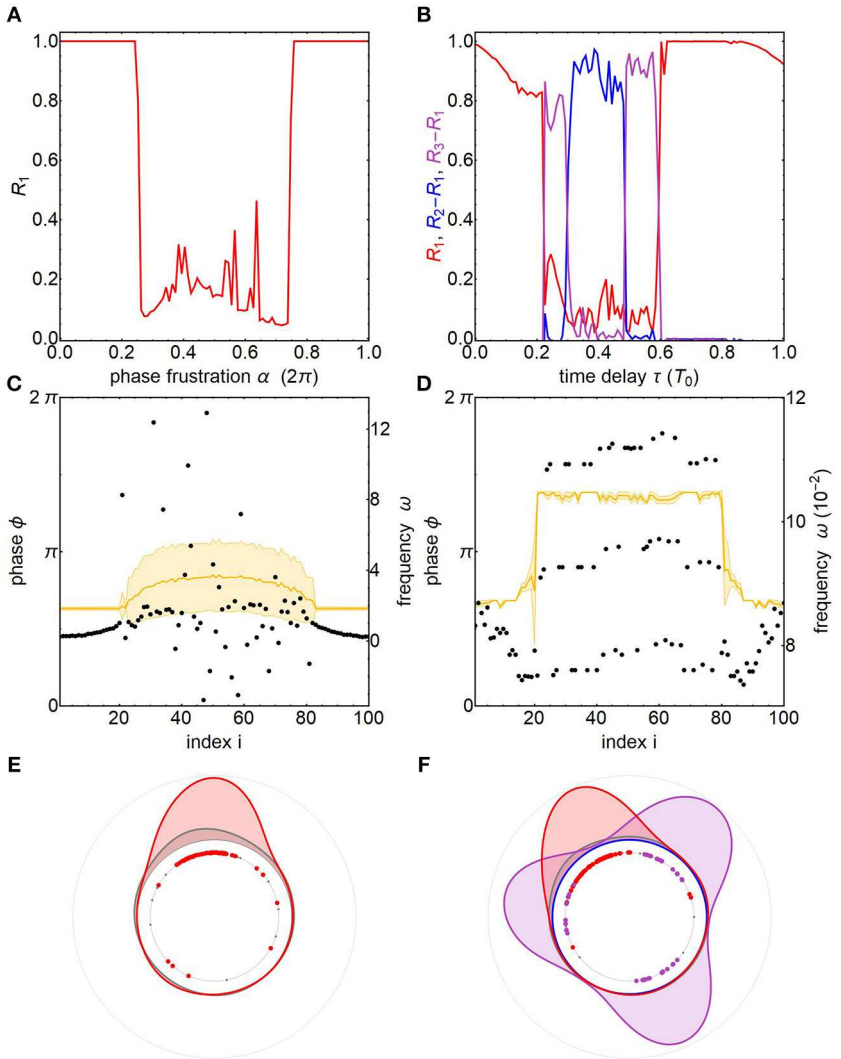

FIGURE 2 | Comparison of chimera states in weakly and strongly coupled oscillators on a ring. Left column: Kuramoto phase oscillators (Equation 1), Right column: ZBKE relaxation oscillators (Equation 2). **(A,B)** Collective dynamics in a globally coupled network quantified by Kuramoto order parameters as a function of synchronization frustration (α, τ) exhibiting in-phase synchronization, incoherence and d-clusters with $d \in \{2, 3\}$. Parameters for phase (ZBKE) oscillators: $K = 50$, $\Delta t = 5 \times 10^{-3}$ ($K = 4 \times 10^{-5}$, $\Delta t = 2 \times 10^{-4}$). **(C,D)** Collective dynamics on a nonlocally coupled ring network consisting of dynamic modes found in a globally coupled network. Snapshots show phases (black) and frequencies (yellow). Parameters for phase (ZBKE) oscillators: $K = 0.1$, $\kappa = 35$, $\alpha = 1.457$ ($K = 7.93 \times 10^{-4}$, $\kappa = 2$, $\tau = 8.67$, $q \in [0.69, 0.71]$). **(E,F)** Smoothed distributions of in-phase (red), 3-cluster (purple) and incoherent (gray) oscillator populations on the phase circle. Parameters: $N = 100$. Others as in **Figure 1** .

quantifies the level of phase synchronization. It ranges from 0 for evenly balanced phase distributions, that include incoherent and cluster states, to 1 for coherent states where all phases narrowly align together. Inclusion of an additive phase frustration parameter in the interaction function of the Kuramoto model, $\sin(\phi_j - \phi_i - \alpha)$, allows for tuning the interactions between oscillators from attractive to repulsive, leading, respectively to phase alignment for $\alpha \in [0, \pi/2[\cup]3\pi/2, 2\pi[$ or conversely to frequency detuning for $\alpha \in [\pi/2, 3\pi/2]$ (**Figure 2A**).

On a ring topology with nonlocal interactions, it is possible for these two distinct collective states to exist simultaneously in neighboring spatial domains realizing a chimera state (**Figure 2C**). Oscillators 21-79 are not frequency-locked and their phases are spread out. In contrast, oscillators 1–20 and 80–100 are frequency-locked and their phases align together. They exhibit an average frequency that is smaller than their mean natural frequency, because the phase frustration α for $\Delta\phi = 0$ does not get compensated.

This phase pattern is furthermore illustrated with a smoothed polar histogram of the oscillator population (**Figure 2E**). To differentiate between the populations we employ a localized version of the Kuramoto order parameter that measures the phase coherence in a spatially-bounded interval $[i - \ell, i + \ell]$

around oscillator i:

$$r_i = \frac{1}{2\ell+1}\left|\sum_{j=i-\ell}^{i+\ell} e^{\mathrm{i}\phi_j}\right| . \quad (5)$$

While oscillators in the coherent population, identified by $r_i \geq 0.7$, coalesce to the same phase, incoherent oscillators with $r_i < 0.7$ are more evenly spread out over the phase circle. The distribution of the incoherent population also exhibits a minor peak that is slightly ahead in phase of the coherent population due to intermittent phase-locking.

In comparison, the strongly coupled oscillators feature coherent and apparently incoherent states in an all-to-all network (**Figure 2B**). On closer inspection the incoherent state is revealed to be a d-cluster with $d \in \{2, 3\}$ as quantified by $R_d - R_1$ with the d-cluster Kuramoto order parameter [38]

$$R_d = \frac{1}{N}\left|\sum_{j=1}^{N} e^{\mathrm{i}d\phi_j}\right| . \quad (6)$$

For $d = 3$ it maps phases of $0, 2\pi/3, 4\pi/3$ and 2π onto the same value due to the $2\pi/d$-periodicity of the complex exponential. Note that R_d also approaches unity for 1-cluster states, which are also known as coherent in-phase synchronization states. To distinguish d-cluster states from 1-cluster states, we use the difference $R_d - R_1$.

On the nonlocally coupled ring network we again observe coexistence of the collective states from the all-to-all network. However, for the strongly coupled ZBKE oscillators these are 1-cluster and 3-cluster states (**Figure 2D**). Apart from the state shown, we also observed coexisting 1 and 2-cluster states as well as 2 and 3-cluster states for other coupling parameters. The polar phase histogram (**Figure 2F**) clearly highlights the distinct populations as identified by $r_{d,i}$, which is a localized version of d-cluster Kuramoto order parameter (Equation 6) similar to Equation (5). The coherent oscillators ($r_{1,i} \geq 0.7$) coalesce around the same phase, while the members of the 3-cluster population ($r_{3,i} - r_{1,i} > 0.5$) are found at three distinct locations on the phase circle. Oscillators at the spatial border between both clusters fail to join either of them due to competing perturbations.

We stress that the mechanism for cluster formation in strongly coupled limit cycle oscillators with delay is qualitatively different from Kuramoto phase oscillators with higher harmonics in the interaction function. The number of clusters for strongly coupled oscillators is not determined by the number of harmonics in the interaction function [21], but instead by the size of the refractory window in relation to the time delay τ in the coupling. The role of time delay is illustrated for a 2-cluster state in **Figure 3**.

In a globally coupled network starting from uniformly random phases, oscillators will join either of two clusters, depending on whether they are initially in their refractory window or not. Once the two clusters establish themselves, they stabilize each other via delayed perturbations (**Figure 3A**) that are sharply localized in time due to the peaked waveform of the v variable (**Figure 1B**). Even though the network is globally coupled, this perturbation does not affect the population that emits it, because its oscillators are still in their refractory window (**Figure 3B**). Only the subsequent perturbation from the second cluster induces a new firing event in the first cluster, because it arrives in the vulnerable window. Consequently the period of an oscillator is $T_2 = 2\delta$, where $\delta = \tau + \Delta t_{\mathrm{peak}}$ that accounts for the transmission delay and the time required for a peak in $v(t)$ to rise ($\Delta t_{\mathrm{peak}} \approx 1$). Utilizing the PRC, we find that a necessary condition for the appearance of a 2-cluster is that the period T_2 exceeds the refractory window given by the jump discontinuity point $t^* = \phi^*/\omega_0$. Note that this can be generalized to d-clusters with $d \geq 1$, whose periods follow $T_d = \delta \times d/\Delta d$, where $\Delta d < d$ is the number of omitted clusters during one spike transmission. It turns out that for weaker coupling strength K, and hence larger refractory windows, cluster states with larger d are possible. This opens the possibility of chimera states, which are comprised of spatial domains exhibiting various d-cluster states [33, 39].

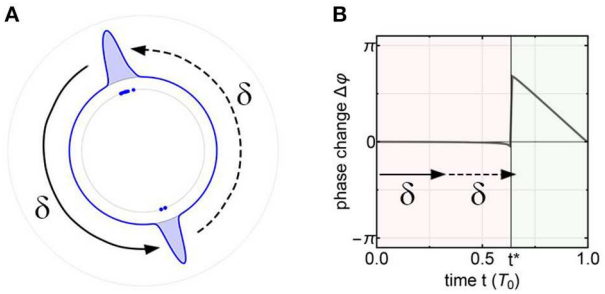

FIGURE 3 | Cluster state mechanism. **(A)** The smoothed polar histogram shows two antiphasic subpopulations in a globally coupled network. They perturb each other a time δ after they have been perturbed themselves, respectively. Parameters: $N = 100$, $K = 1.4 \times 10^{-4}$, $\tau = 8.67$. Other parameters as in **Figure 2**. **(B)** The 2-cluster state emerges if the perturbation from the other cluster arrives in the vulnerable window (green) given by the jump point t* in the PRC.

3. EXPERIMENTS

To demonstrate the real-world viability of the chimera state in strongly coupled relaxation oscillators, we utilize a large reservoir of more than 2,000 chemical micro-oscillators that are coupled via light illumination [23, 33, 39]. From this reservoir we select $N = 100$ oscillators with a narrow natural frequency distribution ($\omega_0 = 0.07 \pm 0.01$ Hz). Starting from random initial conditions we observe the development of a two-headed chimera state consisting of two in-phase synchronized domains separated by noisy cluster states (**Figures 4A,B**). Similar multi-headed chimera states were previously only observed in laser systems [11, 12]. Due to the inherent heterogeneity in periods and phase response behavior [40], the oscillators in the clusters show a larger phase spread than in simulations with homogeneous oscillators. Stronger heterogeneity can furthermore lead to phase switchers [41], which prevent the formation of stationary clusters, resulting in an apparently incoherent domain.

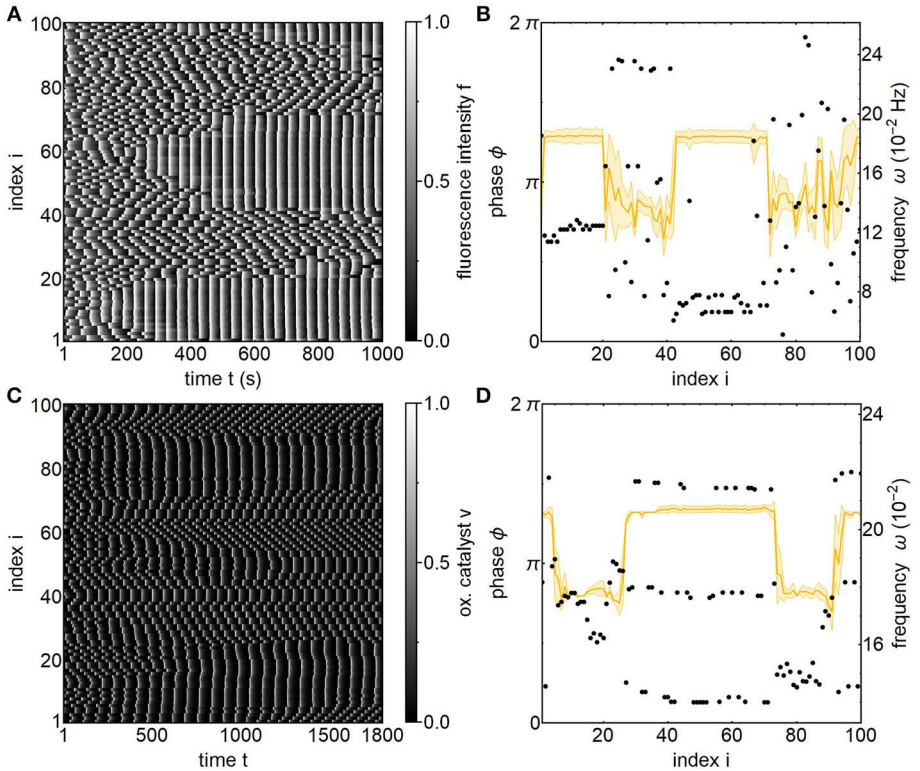

FIGURE 4 | Two-headed chimera state. **(A)** Experimental space-time plot of the fluorescence intensities of $N = 100$ nonlocally photo-coupled chemical oscillators exhibiting a two-headed chimera state. **(B)** Snapshot of instantaneous phases and time-averaged frequencies at time $t = 586\,\mathrm{s}$ revealing two in-phase synchronized and two noisy cluster domains. Parameters: $K = 0.1$, $\kappa = 3.3$, $\tau = 32\,\mathrm{s}$, $T_0 = 86 \pm 12\,\mathrm{s}$, $[H_2SO_4]_0 = 0.77\,\mathrm{M}$, $[NaBrO_3]_0 = 0.51\,\mathrm{M}$, [malonic acid]$_0 = 0.16\,\mathrm{M}$, catalyst load: 2.5×10^{-5} mol Rudmbipy$_3^{3+}$/g resin. **(C)** Numerical space-time plot of the oxidized catalyst v. **(D)** Snapshot of instantaneous phases and time-averaged frequencies at time $t = 1,362$ revealing two in-phase synchronized and two noisy cluster domains. Parameters: $K = 2.98 \times 10^{-4}$, $\kappa = 4$, $\tau = 8.67$. Other parameters as in **Figure 1**.

We stress that the chimera state with strongly coupled oscillators does not require special initial conditions as in the case with phase oscillators [42]. The space-time plot of the observed fluorescence intensities emitted by the oscillators shows the spontaneous formation of the first coherent head ($i \in [8, 18]$) in an environment of incoherent oscillators after only 3 periods. The second head ($i \in [52, 63]$) nucleates at the opposite side of the ring network after 7 periods. After their formation the coherent heads grow over 8 periods until they encompass about 30 oscillators. Upon reaching this extent, their size fluctuates, but their position is fixed on the ring. A snapshot of the phases and frequencies at $t = 586\,\mathrm{s}$ shows the coherent domains and the clusters with equal phase differences between their constituent subgroups. Even though both coherent heads are respectively in-phase synchronized and move at the same frequency, there is a phase-lag between them. Since in a d-cluster domain, all oscillators are phase-locked they all exhibit the same frequency depending on the number of clusters d. Thus, the frequency distribution of a chimera state consisting of different d-clusters shows distinct noisy flat plateaus for each cluster. This is in contrast to chimera states in Kuramoto phase oscillators, where the frequency distribution exhibits a flat plateau for synchronized oscillators and a large band of frequencies for desynchronized oscillators.

Corresponding numerical simulations (**Figures 4C,D**) successfully reproduce the two-headed chimera state. In contrast to the experiments, the space-time plot shows a different route to a two-head chimera. At the beginning more than two coherent domains form, but over time they merge together or breakup into a 3-cluster state until only two coherent heads remain. The simulations also highlight that the phase distribution, here consisting of coherent and 3-cluster domains, is not enough to fully characterize the state. The snapshot in **Figure 4D** shows that the 3-cluster domains have a larger frequency than the coherent domains, whereas the experiments shows the opposite relationship.

Within established classification schemes put forward by Kemeth et al. [43] and Gopal et al. [44], our states can be identified as two-headed static chimera states based on the spatial correlation measure $g_0(t)$ and strength of incoherence $SI(t)$ with a discontinuity measure $\eta = 2$.

4. CONCLUSIONS

We analyzed the collective behavior of strongly coupled limit cycle oscillators through simulations and experiments. Under strong perturbations the characteristic phase response curve develops a jump-discontinuity, whose position depends on the perturbation amplitude. This behavior is directly rooted in the phase-dependent excitability of the oscillator (**Figure 1**) and is found commonly in nature [25–31].

We further numerically elucidated the differences between chimera states in Kuramoto phase oscillators and ZBKE relaxation oscillators as exemplary cases for weak and strong coupling. The coherence-incoherence chimera states emerging in the case of weakly coupled Kuramoto phase oscillators are replaced with chimera states consisting of coexisting domains of coherence and *d*-clusters for strongly coupled relaxation oscillators (**Figure 2**). The cluster states can be identified using generalized Kuramoto order parameters [38] and their formation can be understood in an all-to-all network with the help of the phase response curve (**Figure 3**). Ultimately we verified our predictions and their real-world robustness in an experimental setup with photo-coupled chemical oscillators and observed a two-headed chimera state that consisted of two coherent domains and two 3-cluster states (**Figure 4**). In the future it would be interesting to apply previously developed control schemes[45–47] in the experiment to dictate the position, drift speed and lifetime of the observed multi-headed chimera state as well as investigate the role of noise [48] and multi-layer interaction [49].

Besides resulting in chimera states of different nature, the strongly coupled oscillators also highlight the connection between collective states in global and nonlocal networks. Our results suggest that beyond incoherence-coherence patterns, chimera states can be viewed as time-dependent pattern with distinct spatial domains, whose behavior is inherited from the various dynamical modes during global coupling of the underlying dynamical units.

AUTHOR'S NOTE

The simulation codes for oscillators in globally and nonlocally coupled networks are available at: https://github.com/bzjan/Coupled_Oscillators_Solver.

AUTHOR CONTRIBUTIONS

JT and JR built the set-up and performed experiments. JT and HE designed the study and wrote the paper. The simulations were carried out by JT, JR, and EF. All authors discussed the results and commented on the manuscript.

FUNDING

This work was supported by the Deutsche Forschungsgemeinschaft (grants GRK 1558 and SFB 910 to JT, JR, EF, and HE).

ACKNOWLEDGMENTS

The authors thank J. Six and F. Sielaff from TU Berlin physics department's precision mechanical workshop for preparing the acrylic glass plates with micrometer-sized cavities that hold the micro-oscillators, U. Künkel for assistance in the laboratory.

REFERENCES

1. Pikovsky A, Rosenblum M, Kurths J. *Synchronization: A Universal Concept in Nonlinear Sciences*. Cambridge University Press (2001). doi: 10.1017/cbo9780511755743
2. Cross MC, Hohenberg PC. Pattern formation outside of equilibrium. *Rev Mod Phys*. (1993) **65**:851–1112. doi: 10.1103/RevModPhys.65.851
3. Kuramoto Y. Reduction methods applied to non-locally coupled oscillator systems. In: *Nonlinear Dynamics and Chaos: Where Do We Go from Here?* CRC Press (2002). p. 209–27. Available online at: https://www.taylorfrancis.com/books/9781420033830/chapters/10.1201/9781420033830-11 (accessed January 20, 2019).
4. Kuramoto Y, Shima S. Rotating spirals without phase singularity in reaction-diffusion systems. *Prog Theor Phys Suppl*. (2003) **150**:115–25. doi: 10.1143/PTPS.150.115
5. Panaggio MJ, Abrams DM. Chimera states: coexistence of coherence and incoherence in networks of coupled oscillators. *Nonlinearity*. (2015) **28**:R67. doi: 10.1088/0951-7715/28/3/R67
6. Schöll E. Synchronization patterns and chimera states in complex networks: interplay of topology and dynamics. *Eur Phys J Spec Top*. (2016) **225**:891–919. doi: 10.1140/epjst/e2016-02646-3
7. Nkomo S, Tinsley MR, Showalter K. Chimera states in populations of nonlocally coupled chemical oscillators. *Phys Rev Lett*. (2013) **110**:244102. doi: 10.1103/PhysRevLett.110.244102
8. Wickramasinghe M, Kiss IZ. Spatially organized partial synchronization through the chimera mechanism in a network of electrochemical reactions. *Phys Chem Chem Phys*. (2014) **16**:18360–9. doi: 10.1039/C4CP02249A
9. Rosin DP, Rontani D, Haynes ND, Schöll E, Gauthier DJ. Transient scaling and resurgence of chimera states in networks of boolean phase oscillators. *Phys Rev E*. (2014) **90**:030902. doi: 10.1103/PhysRevE.90.030902
10. English LQ, Zampetaki A, Kevrekidis PG, Skowronski K, Fritz CB, Abdoulkary S. Analysis and observation of moving domain fronts in a ring of coupled electronic self-oscillators. *Chaos*. (2017) **27**:103125. doi: 10.1063/1.5009088
11. Hagerstrom AM, Murphy TE, Roy R, Hövel P, Omelchenko I, Schöll E. Experimental observation of chimeras in coupled-map lattices. *Nat Phys*. (2012) **8**:658–61. doi: 10.1038/nphys2372
12. Larger L, Penkovsky B, Maistrenko Y. Laser chimeras as a paradigm for multistable patterns in complex systems. *Nat Commun*. (2015) **6**:7752. doi: 10.1038/ncomms8752
13. Brumley DR, Bruot N, Kotar J, Goldstein RE, Cicuta P, Polin M. Long-range interactions, wobbles, and phase defects in chains of model cilia. *Phys Rev Fluids*. (2016) **1**:081201. doi: 10.1103/PhysRevFluids.1.081201
14. Majhi S, Bera BK, Ghosh D, Perc M. Chimera states in neuronal networks: a review. *Phys Life Rev*. (2019) **28**:100–21. doi: 10.1016/j.plrev.2018.09.003
15. Lazarides N, Tsironis GP. Superconducting metamaterials. *Phys Rep*. (2018) **752**:1–67. doi: 10.1016/j.physrep.2018.06.005
16. Kuramoto Y. *Chemical Oscillations, Waves, and Turbulence*. Vol. 19. Springer (1984). Available online at: http://dx.doi.org/10.1007/978-3-642-69689-3.
17. Acebrón JA, Bonilla LL, Pérez Vicente CJ, Ritort F, Spigler R. The kuramoto model: a simple paradigm for synchronization phenomena. *Rev Mod Phys*. (2005) **77**:137–85. doi: 10.1103/RevModPhys.77.137

18. Wilson D, Ermentrout B. Greater accuracy and broadened applicability of phase reduction using isostable coordinates. *J Math Biol*. (2018) **76**:37–66. doi: 10.1007/s00285-017-1141-6
19. Rosenblum M, Pikovsky A. Numerical phase reduction beyond the first order approximation. *Chaos*. (2019) **29**:011105. doi: 10.1063/1.5079617
20. Winfree AT. *The Geometry of Biological Time*. 2nd ed. Springer (2001). Available online at: http://dx.doi.org/10.1007/978-1-4757-3484-3.
21. Kiss IZ. Synchronization engineering. *Curr Opin Chem Eng*. (2018) **21**:1–9. doi: 10.1016/j.coche.2018.02.006
22. Totz JF, Snari R, Yengi D, Tinsley MR, Engel H, Showalter K. Phase-lag synchronization in networks of coupled chemical oscillators. *Phys Rev E*. (2015) **92**:022819. doi: 10.1103/PhysRevE.92.022819
23. Totz JF, Rode J, Tinsley MR, Showalter K, Engel H. Spiral wave chimera states in large populations of coupled chemical oscillators. *Nat Phys*. (2018) **14**:282–5. doi: 10.1038/s41567-017-0005-8
24. Wilson D, Faramarzi S, Moehlis J, Tinsley MR, Showalter K. Synchronization of heterogeneous oscillator populations in response to weak and strong coupling. *Chaos*. (2018) **28**:123114. doi: 10.1063/1.5049475
25. Jalife J, Moe GK. Effect of electrotonic potentials on pacemaker activity of canine purkinje fibers in relation to parasystole. *Circ Res*. (1976) **39**:801–8. doi: 10.1161/01.RES.39.6.801
26. Johnson CH, Hastings JW. Circadian phototransduction: phase resetting and frequency of the circadian Clock of gonyaulax cells in red light. *J Biol Rhythms*. (1989) **4**:417–37. doi: 10.1177/074873048900400403
27. Prinz AA, Thirumalai V, Marder E. The functional consequences of changes in the strength and duration of synaptic inputs to oscillatory neurons. *J Neurosci*. (2003) **23**:943–54. doi: 10.1523/JNEUROSCI.23-03-00943.2003
28. Russell DF. Respiratory pattern generation in adult lampreys (lampetra fluviatilis): interneurons and burst resetting. *J Comp Physiol*. (1986) **158**:91–102. doi: 10.1007/BF00614523
29. Anumonwo JM, Delmar M, Vinet A, Michaels DC, Jalife J. Phase resetting and entrainment of pacemaker activity in single sinus nodal cells. *Circ Res*. (1991) **68**:1138–53. doi: 10.1161/01.RES.68.4.1138
30. Wessel R. *In vitro* study of phase resetting and phase locking in a time-comparison circuit in the electric fish, eigenmannia. *Biophys J*. (1995) **69**:1880–90. doi: 10.1016/S0006-3495(95)80058-5
31. Nabi A, Stigen T, Moehlis J, Netoff T. Minimum energy control for *in vitro* neurons. *J Neural Eng*. (2013) **10**:036005. doi: 10.1088/1741-2560/10/3/036005
32. Zhabotinsky AM, Buchholtz F, Kiyatkin AB, Epstein IR. Oscillations and waves in metal-ion-catalyzed bromate oscillating reactions in highly oxidized states. *J Phys Chem*. (1993) **97**:7578–84. doi: 10.1021/j100131a030
33. Totz JF. *Synchronization and Waves in Active Media*. Springer International Publishing (2019). doi: 10.1007/978-3-030-11057-4
34. Press WH, Teukolsky SA, Vetterling WT, Flannery BP. *Numerical Recipes: The Art of Scientific Computing*. 3rd ed. Cambridge University Press (2007). Available online at: http://www.cambridge.org/de/academic/subjects/mathematics/numerical-recipes/numerical-recipes-art-scientific-computing-3rd-edition?format=HB&utm_source=shortlink&utm_medium=shortlink&utm_campaign=numericalrecipes (accessed January 20, 2019).
35. Bertram R, Rubin JE. Multi-timescale systems and fast-slow analysis. *Math Biosci*. (2017) **287**:105–21. doi: 10.1016/j.mbs.2016.07.003
36. Izhikevich EM. *Dynamical Systems in Neuroscience*. MIT Press (2007). doi: 10.7551/mitpress/2526.001.0001
37. Franović I, Omel'chenko OE, Wolfrum M. Phase-sensitive excitability of a limit cycle. *Chaos*. (2018) **28**:071105. doi: 10.1063/1.5045179
38. Daido H. Order function and macroscopic mutual entrainment in uniformly coupled limit-cycle oscillators. *Prog Theor Phys*. (1992) **88**:1213–18. doi: 10.1143/PTP.88.1213
39. Rode J. *Synchronization in heterogeneous networks-from phase to relaxation oscillators* (M.Sc. Thesis). TU Berlin, Berlin, Germany (2016).
40. Pazó D, Montbrió E, Gallego R. The winfree model with heterogeneous phase-response curves: analytical results. *arXiv:arxiv.org/abs/1809.09456* (2018).
41. Taylor AF, Kapetanopoulos P, Whitaker BJ, Toth R, Bull L, Tinsley MR. Clusters and switchers in globally coupled photochemical oscillators. *Phys Rev Lett*. (2008) **100**:214101. doi: 10.1103/PhysRevLett.100.214101
42. Abrams DM, Strogatz SH. Chimera states in a ring of nonlocally coupled oscillators. *Int J Bifurcat Chaos*. (2006) **16**:21–37. doi: 10.1142/S0218127406014551
43. Kemeth FP, Haugland SW, Schmidt L, Kevrekidis IG, Krischer K. A classification scheme for chimera states. *Chaos*. (2016) **26**:094815. doi: 10.1063/1.4959804
44. Gopal R, Chandrasekar VK, Venkatesan A, Lakshmanan M. Observation and characterization of chimera states in coupled dynamical systems with nonlocal coupling. *Phys Rev E*. (2014) **89**:052914. doi: 10.1103/PhysRevE.89.052914
45. Bick C, Martens EA. Controlling chimeras. *New J Phys*. (2015) **17**:033030. doi: 10.1088/1367-2630/17/3/033030
46. Omelchenko I, Omel'chenko OE, Zakharova A, Wolfrum M, Schöll E. Tweezers for chimeras in small networks. *Phys Rev Lett*. (2016) **116**:114101. doi: 10.1103/PhysRevLett.116.114101
47. Isele T, Hizanidis J, Provata A, Hövel P. Controlling chimera states: the influence of excitable units. *Phys Rev E*. (2016) **93**:022217. doi: 10.1103/PhysRevE.93.022217
48. Semenova N, Zakharova A, Anishchenko V, Schöll E. Coherence-resonance chimeras in a network of excitable elements. *Phys Rev Lett*. (2016) **117**:014102. doi: 10.1103/PhysRevLett.117.014102
49. Sawicki J, Omelchenko I, Zakharova A, Schöll E. Synchronization scenarios of chimeras in multiplex networks. *Eur Phys J Spec Top*. (2018) **227**:1161–71. doi: 10.1140/epjst/e2018-800039-y

Conflict of Interest Statement: The authors declare that the research was conducted in the absence of any commercial or financial relationships that could be construed as a potential conflict of interest.

frontiers in Applied Mathematics and Statistics

ORIGINAL RESEARCH
published: 31 July 2019
doi: 10.3389/fams.2019.00038

Weak Chimeras in Modular Electrochemical Oscillator Networks

Jorge Luis Ocampo-Espindola[1], *Christian Bick*[2] *and István Z. Kiss*[1]*

[1] *Department of Chemistry, Saint Louis University, St. Louis, MO, United States,* [2] *Centre for Systems Dynamics and Control and Department of Mathematics, University of Exeter, Exeter, United Kingdom*

We investigate the formation of weak chimera states in modular networks of electrochemical oscillations during the electrodissulution of nickel in sulfuric acid. In experiment and simulation, we consider two globally coupled populations of highly non-linear oscillators which are weakly coupled through a collective resistance. Without cross coupling, the system exhibits bistability between a one- and a two-cluster state, whose frequencies are distinct. For weak cross coupling and initial conditions for the one- and two-cluster states for populations 1 and 2, respectively, weak chimera dynamics are generated. The weak chimera state exhibits localized frequency synchrony: The oscillators in each population are frequency-synchronized while the two populations are not. The chimera state is very robust: The behavior is maintained for hundreds of cycles for the rather heterogeneous natural frequencies of the oscillators. The experimental results are confirmed with numerical simulations of a kinetic model for the chemical process. The features of the chimera states are compared to other previously observed chimeras with oscillators close to Hopf bifurcation, coupled with parallel resistances and capacitances or with a non-linear delayed feedback. The experimentally observed synchronization patterns could provide a mechanism for generation of chimeras in biological systems, where robust response is essential.

Keywords: chimera, network, oscillation, synchronization, clustering

OPEN ACCESS

Edited by:
Ralph G. Andrzejak, Universitat Pompeu Fabra, Spain

Reviewed by:
Jan Frederik Totz, Massachusetts Institute of Technology, United States
Tanmoy Banerjee, University of Burdwan, India

***Correspondence:**
István Z. Kiss
izkiss@slu.edu

Specialty section:
This article was submitted to Dynamical Systems, a section of the journal Frontiers in Applied Mathematics and Statistics

Received: *15 December 2018*
Accepted: *15 July 2019*
Published: *31 July 2019*

Citation:
Ocampo-Espindola JL, Bick C and Kiss IZ (2019) Weak Chimeras in Modular Electrochemical Oscillator Networks. Front. Appl. Math. Stat. 5:38. doi: 10.3389/fams.2019.00038

INTRODUCTION

Synchronization of oscillatory chemical reactions is an important dynamical phenomenon with relevance to many physical and biological processes [1]. Early studies focused on the dynamics of continuous, stirred tank reactors (CSTRs) where coupling is through active or passive mass transfer, or by electrical means [2–6]. Different types of interactions were able to induce different synchronization patterns, e.g., in-phase, anti-phase, and out-of-phase entrainment. The CSTR technology however is difficult to scale up to a large population of reactors [7, 8]. Belousov-Zhabotinsky (BZ) microdroplets [9, 10], beads [11, 12], microwell arrays [13], and nanodroplets [14] provide ways to study synchronization of populations. In oscillatory electrochemical systems, electrode arrays can be applied to investigate coupled systems, up to about 100 oscillators [15]. Globally coupled electrochemical oscillators indeed showed a variety of synchrony patterns with various levels of coherence, including full synchrony [16] and other stable [17] and intermittent [18] cluster states.

Understanding what coupling properties—topology, delay, symmetry, and non-linearity—influence synchronization in dynamical models [1, 19] provides guidelines for the design of experiments. In particular, phase-model-based predictions turned out to be useful for identification

of synchronization patterns in experiments [17, 18]. While the importance of phase models in interpreting synchronization structures was emphasized in early studies [5], some reluctance remained among chemists to adopt phase models in the theoretical description of chemical reactions due to their simplified nature [20]. Only one angular variable, the phase, is used to uniquely identify the state of the chemical reactions. However, oscillatory chemical reactions typically require at least two chemical species [20]. While phase descriptions can be rigorously justified for weak interaction [21], the full range of interactions in chemical systems include strong and highly non-linear coupling. Hence, pure phase model description should be used with care. Nonetheless, many dynamical phenomena, e.g., clustering [17], desynchronization [22, 23], and slow switching [18] were interpreted and designed using phase model approaches.

Chimeras, synchrony patterns with coexisting domains of coherence and incoherence in networks of identical oscillators, have attracted a tremendous amount of attention in the last decades [24, 25]. They were originally reported by Kuramoto and Battogtokh in rings of non-locally coupled oscillators where the coupling strength depends on the distance between oscillators [26]. These traditional chimeras have been studied theoretically in the continuum limit of infinitely many oscillators [26, 27]. By contrast, the concept of a "weak chimera" [28, 29] provides a rigorous characterization of chimeras in networks of finitely many oscillators and capture features of the chimeras originally described by Kuramoto and Battogtokh: Weak chimeras in networks of identical oscillators are characterized by localized frequency synchrony, i.e., there are oscillators that are synchronized in frequency and others which have distinct frequencies.

The theoretically predicted chimera states challenged the fundamental understanding of the non-linear dynamics of chemical reactions and the experimental techniques that enabled the construction of networks of coupled chemical reactions. Can we design networks and choose experimental conditions favorable for the chimera state?

As the theory of chimera states is quickly growing [24, 25], developments of experimental and data analysis techniques were also needed to identify and classify partially synchronized states as chimera states [30]. The BZ bead system with optical feedback technique is a promising approach that can generate various types of chimera patterns in different configurations [31–34]. In electrochemistry, non-linear electrical coupling during silicon dissolution generates localized patterns that possess many features similar to chimeras [35–40]. The beating mercury drop system also showed that while homogeneous coupling generates rather synchronized states, inhomogeneous coupling results in partial synchronization similar to a chimera [41]. Current oscillations of nickel electrodissolution, in the transpassive dissolution region, on electrode arrays exhibit a wide range synchronization patterns [15]. Oscillation occurs due to the hidden negative differential resistance of the electrodissolution process [42]. Two different types of chimeras were identified [43–45]. On a ring with long-range interaction, a short-lived synchrony pattern, similar to the traditional chimera was found [44, 45]. When non-linear coupling was generated with a computer feedback, weak chimeras [28, 29, 46] were obtained with a four-oscillator network, where two pairs of elements were locked in-phase and anti-phase configurations with distinct frequencies [43].

In this paper, we report the occurrence of weak chimera states in a modular network of electrochemical oscillators with the electrodissolution of nickel in sulfuric acid. First, for comparison with previous results, an overview is given on the characteristics of chimera states in the nickel electrodissolution system [43–45]. In these previous experiments, the chimera state was observed either in a device [44, 45] with relatively short life-time, or in a computer feedback system [43] with long life-time. Here we seek long life-time chimeras in a device. Numerical simulations are performed to explore parameter space and identify experimental conditions for which weak chimera states can be observed with strongly non-linear oscillators in the presence of linear (or difference) coupling through the electrode potential. Finally, experiments are performed to show the existence of the weak chimeras in the electrochemical system.

MATERIALS AND METHODS

Figure 1 shows the experimental setup and the three different network topologies. Each approach uses different techniques to generate favorable experimental conditions for the chimera state.

Ring Network With Non-local Coupling

A standard three-electrode electrochemical cell for the ring network with non-local coupling [44] is shown in **Figure 1A**. This approach used an electrode array, in which the electrode pairs are coupled by parallel resistance/capacitance circuit elements. An array of nickel wires (only two are shown in the figure) were used as the working electrode. A Hg/Hg_2SO_4 saturated K_2SO_4 is the reference, and a platinum rod is the counter electrode. The electrodes were immersed in a 3 M H_2SO_4 solution. The cell temperature was maintained at 10°C by a circulating bath. The working electrode array has 1 mm diameter wires, embedded in epoxy, with a spacing of 2 mm. With this large spacing the potential drop in the electrolyte is sufficiently small (about 0.1 mV), so that without the presence of additional coupling, the oscillations do not show synchronization [16]. The working electrodes were connected to a potentiostat through an external resistance (R_{ind}) for each wire. The potentiostat sets the constant circuit potential, and the currents, measured from the potential drops across the individual resistances, were digitized using a National Instrument PCI 6255 data acquisition board at a rate of 200 Hz (Note that each wire has the same circuit potential in this configuration).

The properties of individual oscillations for a wire of a given diameter can be changed by the circuit potential (V), the attached total external resistance, the concentration of the sulfuric acid, and the temperature. Once the properties of the individual oscillators are set, the wires in the electrode arrays can be coupled externally for a given topology. As shown in the bottom panel of **Figure 1A**, the network topology consists of 20 nodes with 140 links. Each node is an oscillatory nickel

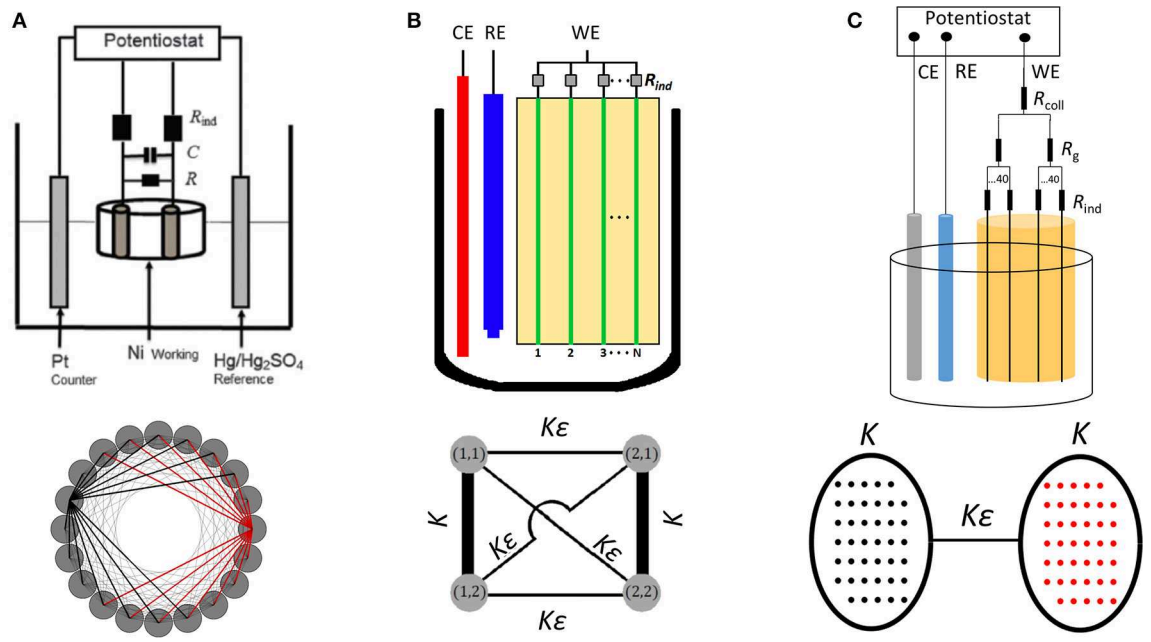

FIGURE 1 | Schematics of the experimental setups (top) for the different types of network topologies (bottom). **(A)** Non-local ring network with 20 nodes and 140 links. R_{ind}: individual resistance. C: capacitance. R: cross resistance. **(B)** Weakly non-linear oscillator and highly non-linear delayed feedback in two pairs of oscillators with weak cross-coupling. CE: Counter electrode. RE: Reference electrode. WE: Working electrode. K: coupling strength. ε: cross coupling factor. N: number of oscillators in a general configuration. **(C)** Highly non-linear oscillators and linear interactions in two populations of electrodes with weak, global cross coupling. R_{coll}: collective resistance. R_g: group resistance.

electrodissolution reaction, which takes place on the surface of the electrode. The links of the network are established through a coupling resistance R [45] and capacitance C. To induce some delay in the coupling current a capacitor in parallel was added to each coupling resistor [47]. In the network, each node is coupled to seven of its nearest neighbors of the ring network in both directions.

Network With Spatially Distributed Non-linear Delayed Feedback

The experimental setup with non-linear feedback shown in **Figure 1B** [43]. The system consisted of four oscillators divided into two populations with stronger coupling in the populations and a weaker coupling between them (**Figure 1B** bottom). The oscillators are coupled through linear and quadratic delayed feedback. The same electrode array can be used as with the non-local ring network. (To further eliminate coupling through the electrolyte, the electrodes had 3 mm spacing.) A multichannel potentiostat (ACM Instruments Gill IK64) was used. The potential $V_{\sigma,k}(t)$ of the wire k in population $\sigma \in \{1, 2\}$ with respect Hg/Hg_2SO_4 sat K_2SO_4 reference electrode, was set with a multichannel potentiostat interfaced with a real-time Labview controller. The electrode potentials $E_{\sigma,k}(t)$ of the four wires were converted using the currents $(I_{\sigma,k}(t))$: $E_{\sigma,k}(t) = V_{\sigma,k}(t) - I_{\sigma,k}(t)R_{ind}$, with $R_{ind} = 1$ kOhm. The electrode potentials were adjusted for offset with, $E_{\sigma,k} = E_{\sigma,k} - o$, where o is the time averaged electrode potential (The quantity o was measured before the experiments, for a timeframe of about 100 oscillations). The circuit potential of each wire is adjusted by the feedback using the equation:

$$V_{\sigma,k}(t) = V_0 + K \sum_{\kappa,\, j\in\{1,\,2\}} K_{\kappa\sigma} h(\overline{E}_{\kappa,j}(t-\tau)) \tag{1}$$

where $K_{\kappa\sigma}$ determines the network topology, K is the total feedback gain, τ is the global delay, and

$$\begin{aligned} h\left(\overline{E}_{\kappa,j}(t)\right) &= k_1\left[\overline{E}_{\kappa,j}(t) - \overline{E}_{\kappa,j}(t-\tau_{Ex})\right] \\ &\quad + k_2\left[\overline{E}_{\kappa,j}(t)^2 + \overline{E}_{\kappa,j}(t-\tau_{Ex})^2\right] \end{aligned} \tag{2}$$

is the feedback. For each population, $K_{11} = K_{22} = 1$. Coupling between the population is set to $K_{12} = K_{21} = \varepsilon$, where ε is the cross-coupling factor. The linear and quadratic feedback gains, k_1 and k_2, respectively, are applied to induce the required dynamics. The delay τ_{Ex} was set to be equal to half of the period of the uncoupled oscillators. See [43] for more details on the choice of the parameters k_1, k_2, and τ_{Ex}. $V_0 = 1,160$ mV and the natural frequency (i.e., the frequency of the oscillation without coupling) was about 0.45 Hz. In a typical experiment of about 500 oscillations, the natural frequency change is about 2–3 mHz.

Modular Network

Figure 1C shows the experimental setup for a modular network consisting of coupled oscillator populations. In the bottom

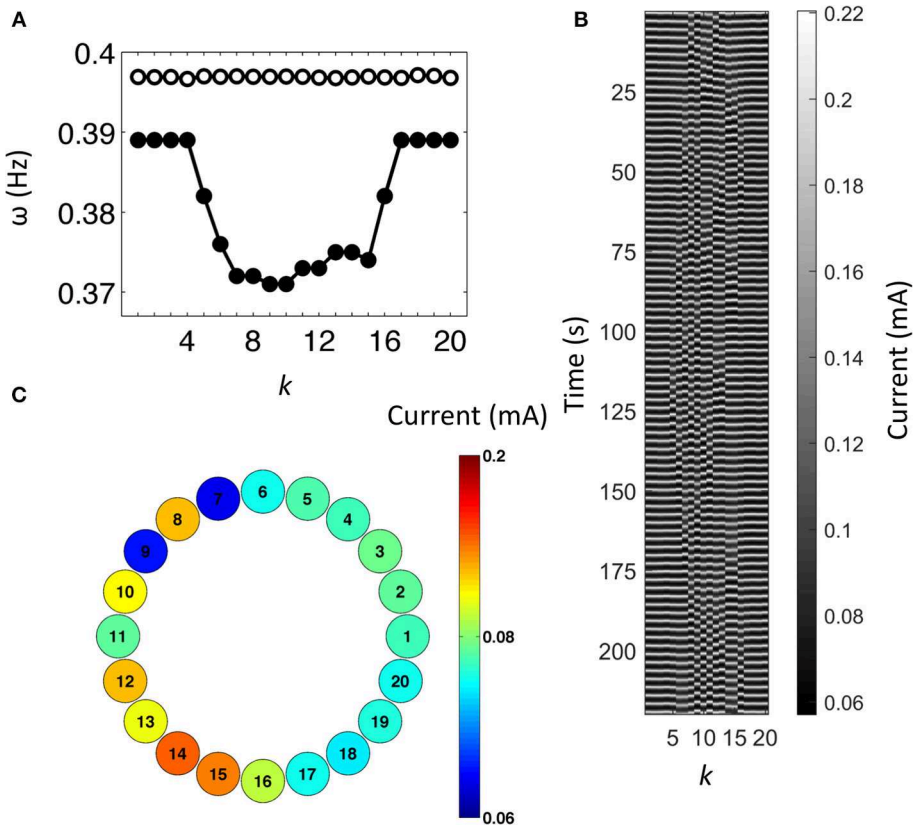

FIGURE 2 | Experimental traditional chimera state in a non-locally coupled regular network. **(A)** Frequency of the oscillators. Open circles: natural frequency. Solid circles: frequency with coupling. **(B)** Space-time plot of the current in gray scale. **(C)** Snapshot of the current of the electrodes. $V = 1{,}094$ mV, $R_{\text{ind}} = 1$ kOhm, $R = 499$ kOhm, $C = 4.7$ μF.

of **Figure 1C** a schematic of the network topology is shown: A total of 80 oscillators are divided into two populations of 40. The same working electrode array, reference and counter electrodes, and electrolyte was used as with the feedback experiment above. The cell was connected to a single channel potentiostat (ACM Instruments, Gill AC), and an individual resistance (R_{ind}) was added to each electrode. Additionally, two group resistances (R_{g}) and a collective resistance (R_{coll}) were used to generate the intra- and inter-population coupling, respectively.

RESULTS AND DISCUSSIONS

To put our results in context, we start out with reviewing the chimera states observed earlier with non-local ring network (section Chimera State with Non-local Ring Network Close to Hopf Bifurcation) and weak chimeras with non-linear feedback (section Weak Chimera with Non-linear Feedback). In section Weak Chimera in Modular Networks with Strongly Non-linear Oscillators, new results are presented in a modular network of highly non-linear oscillators coupled through differences in the electrode potentials.

Chimera State With Non-local Ring Network Close to Hopf Bifurcation

Here we considered oscillations in the experimental system that occur close to Hopf bifurcation [48]. Normally, the natural frequency of the oscillations has a range of about 16 mHz and frequency of 0.4 Hz [45]. To ensure nearly identical oscillators, the range of the natural frequencies was carefully tuned to fall below 0.5 mHz by small changes of the individual resistances, as shown in **Figure 2A**. Coupling through resistors corresponds to a Kuramoto-model-like behavior (i.e., with nearly sinusoidal phase interaction function) [47]. When coupling is through capacitance, the coupling signal is delayed with a phase of about $\pi/2$ [47]. A combination of resistive and capacitive coupling was applied such that the coupling parallel RC circuit had a time constant 2.35 s, which approximately matches the oscillation period of 2.5 s [45]. Such coupling, in our experiments, ensured that the oscillations synchronized at relatively weak strengths, with a delay sufficient for the chimera states to arise. As the coupling was turned on, the population split into a domain of synchronized (electrodes 1–4, 17–20) and desynchronized (electrodes 5–16) elements, as shown in **Figure 2B**. The frequency of the synchronized elements is 0.389 Hz and the desynchronized elements have lower frequencies (**Figure 2A**).

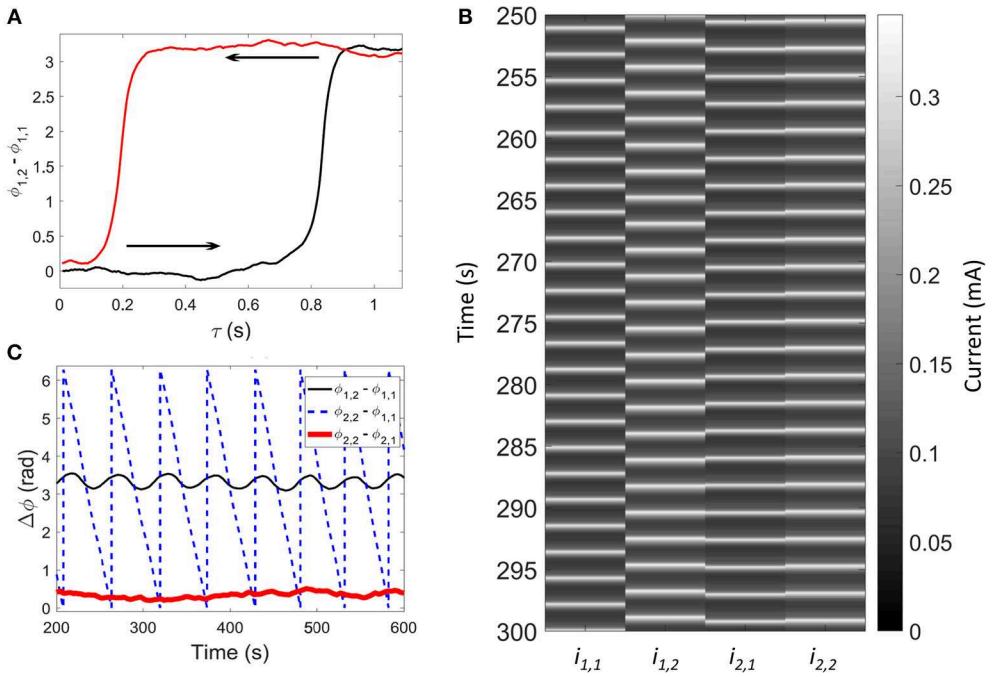

FIGURE 3 | Experimental weak chimera state with non-linear feedback. **(A)** Hysteresis between the in-phase and anti-phase synchronization, as a function of the global coupling delay, τ; black line: forward sweep; red line: backward sweep. **(B,C)** Weak chimera state with $\tau = 0.51$ s and $\varepsilon = 0.1$. **(B)** Space time plot of the current of the four oscillators. **(C)** Time series of the phase difference within population 1 (black thin line $\varphi_{1,2} - \varphi_{1,1}$), population 2 (red thick line, $\varphi_{2,2} - \varphi_{2,1}$), and for two elements between the populations (blue dashed line, $\varphi_{2,2} - \varphi_{1,1}$). Feedback parameters: $K = 0.52$, $k_1 = 0.22$, $k_2 = 2.0$ 1/V.

Additionally, these frequencies form a semi-circle as a function of the position of the elements. This distribution was predicted theoretically for the chimera state [26]. Note that for this chimera state some oscillators are synchronized in frequency, while others are not. **Figure 2C** shows a snapshot of the currents. The elements 1–4 and 17–20 have very similar values and the desynchronized elements have a broader distribution. This chimera state has a limited lifetime of about 80–100 oscillations. This lifetime is in accordance with theoretical predictions [49] and numerical simulations with experiment-based phase models [45] describing the chemical process. The observations thus show that the experimentally observed dynamical state is similar to the traditional Kuramoto chimera state, induced by non-local interactions in a ring topology [49]. Later efforts were focused on characterizing the impact of oscillator heterogeneity (i.e., "remnant" chimeras obtained without adjustments of natural frequencies) [45], and increasing the lifetime of the chimera states with a more non-linear system [43].

Weak Chimera With Non-linear Feedback

Weak chimeras can arise in modular oscillator networks consisting of multiple populations with stronger coupling within populations and weaker coupling between different populations [28]. In a phase model, with a pair of oscillators, bistability between an in-phase, and an anti-phase solution with distinct frequencies can be observed. Under such conditions, a chimera state forms in a network of two pairs of two oscillators, where one of the two strongly coupled oscillator pairs exhibit in-phase, the other anti-phase state. The two synchronized pairs of oscillators have different frequencies, resulting in a weak chimera [29].

We used a synchronization engineering [18] technique to design a combination of first and second order feedbacks to induce a dynamics that represents the desired phase model. When this feedback is applied to two oscillators [43], there is region global delay τ with bistability between in-phase and anti-phase synchronization (see **Figure 3A**). For $\tau = 0$ s, the electrodes are in-phase synchronized; increasing the value until $\tau \approx 0.8$ s the dynamics shift to anti-phase synchronization. Now, when we started from anti-phase synchronization and the global delay was decreased, there was a critical point where the dynamics shifted back into in-phase synchronization at about 0.2 s. Consequently, there is a region from $\tau \approx 0.2$ s to $\tau \approx 0.8$ s in which both states can exist and are stable. A delay of $\tau \approx 0.51$ s was chose for investigation of the chimera state.

As shown in **Figure 3B**, in the four-oscillator network with weak cross coupling ($\varepsilon = 0.1$), population 1 is in anti-phase while population 2 is in-phase synchronized [43]. The phase difference between elements are shown in **Figure 3C**. For elements in the same population, the phase difference remains nearly the same (in- or anti-phase), but the phase difference between one element in population 1 and population 2 is growing. This state thus represents a weak chimera. With the weak chimera, the in- and anti-phase populations can remain desynchronized even in the presence of the cross coupling. Note that the oscillations of the

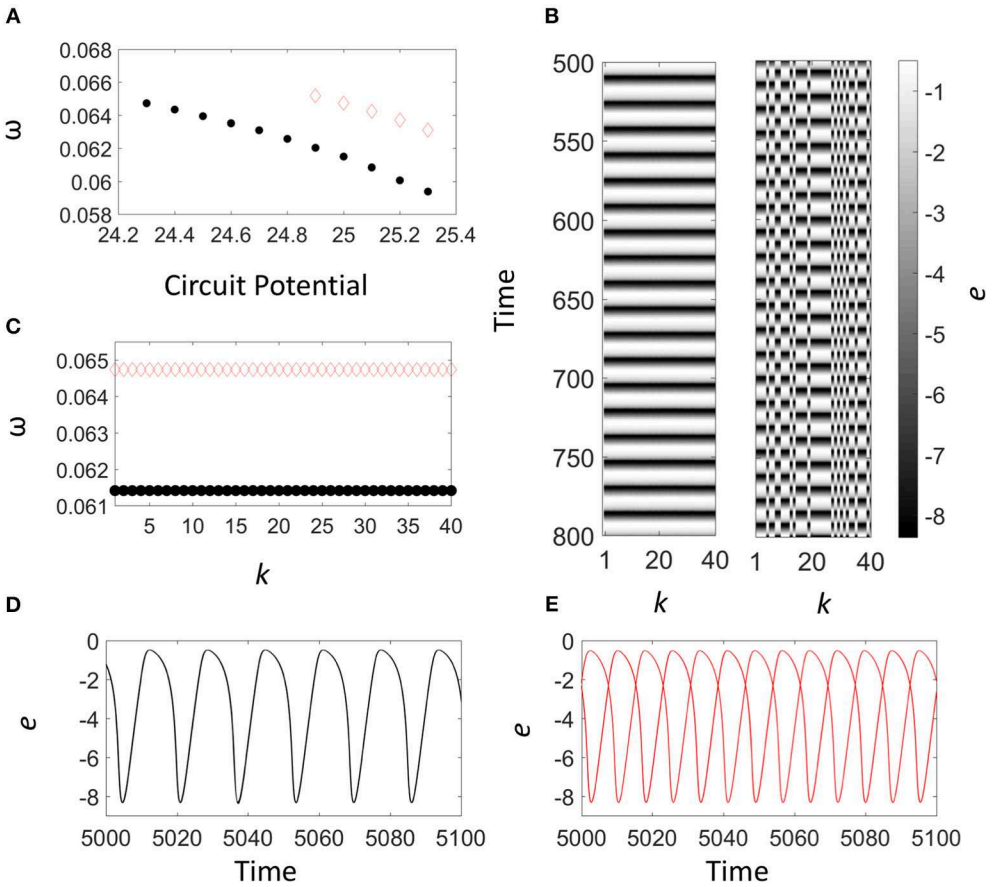

FIGURE 4 | Numerical simulation: Cluster formation with global coupling ($K = 2 \times 10^{-4}$). **(A)** Frequency of the one- (black solid circles) and the two-cluster states (red empty diamonds) as a function of the circuit potential, V. **(B)** Space time plot of the electrode potential for the one- and the two-cluster states. **(C)** Frequency of the elements in the one- (black solid circles) and two-cluster (red empty diamonds) states. **(D,E)** Time series of the electrode potentials for the elements in the one- (black line) and two-cluster (red line) states. In panels **(B–D)**, $V = 25.0$.

phase difference for the anti-phase pair arise due to the presence of coupling from the two nearly in phase oscillators in the other populations. These oscillators speed up and slow down the anti-phase pair (due to their weak cross coupling) as their phase difference drifts apart [43].

Weak Chimera in Modular Networks With Strongly Non-linear Oscillators

We now consider networks of two coupled populations with a larger number of oscillators per population and inherent non-linearities through the phase response curve and the oscillators' waveforms. For a phase description, these properties lead to non-sinusoidal phase interaction, which can give multistability between in-phase synchrony and other cluster states with global coupling [17, 50, 51]. This suggests that weak chimeras can occur for coupled populations. In contrast to the setup in the previous section, the coupling is not mediated by a computer but through a resistance, i.e., the electrode potential difference between the electrodes results in a coupling current that can induce chemical changes [47]. First, we demonstrate the approach with model simulations, and then confirm the findings in experiments.

Numerical Simulations

We used the kinetic scheme proposed by Haim et al. [52] of nickel electrodissolution to model the behavior of a single electrode. The model was written for two variables, the dimensionless electrode potential e and the total surface coverage of the nickel oxide and hydroxide θ. For 40 electrodes coupled through a combination of individual (R_{ind}) and global (collective) (R_{coll}) resistance, the charge and mass balance equations are the following [53]:

$$\frac{de_i}{dt} = \frac{V - e_i}{R} - J_F(e_i, \theta_i) + K\sum_{j=1}^{40}(e_j - e_i) \quad (3)$$

$$\Gamma_i \frac{d\theta_i}{dt} = \frac{\exp(0.5e_i)}{1 + C_h \exp(e_i)}(1 - \theta_i) - \frac{bC_h \exp(2e_i)\,\theta_i}{cC_h + \exp(e_i)} \quad (4)$$

where $i = 1, \ldots, 40$, V is the dimensionless circuit potential, $R = 20$ is the dimensionless individual total resistance, $J_F(e, \theta)$ is the

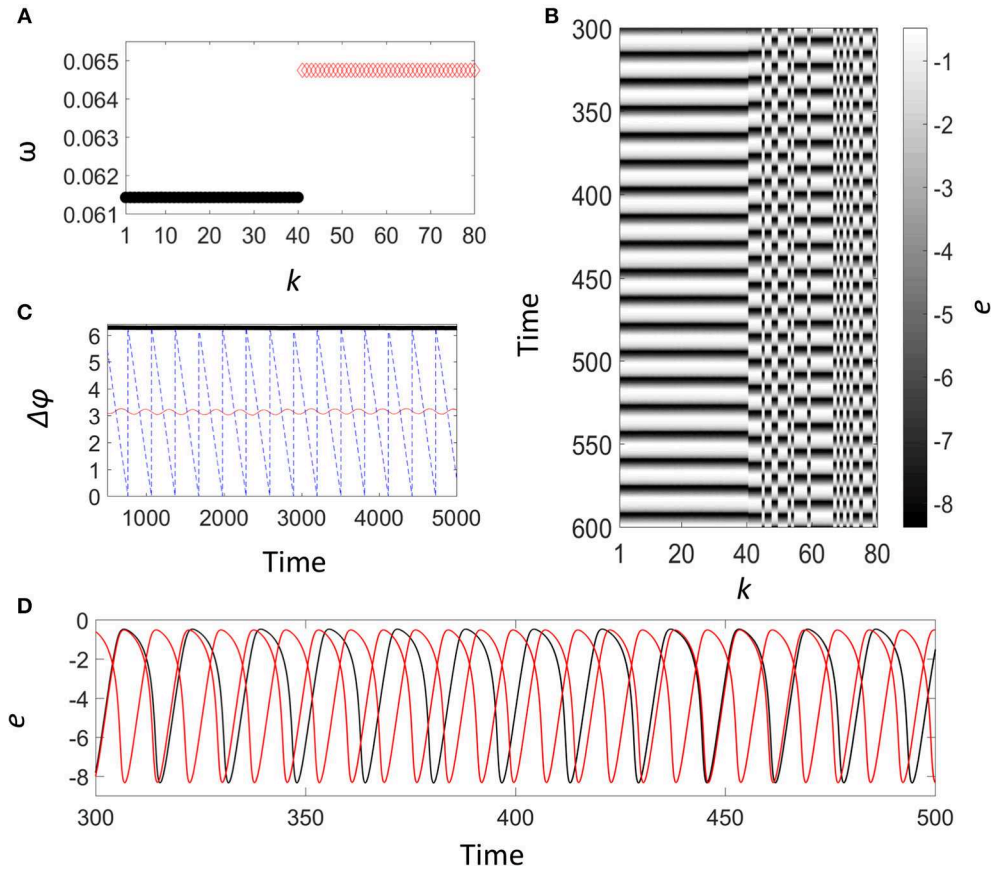

FIGURE 5 | Numerical simulation: Weak chimera state in the modular network with weak cross coupling. $V = 25$, $K = 2 \times 10^{-4}$ and $\varepsilon = 0.05$. **(A)** Frequency of elements (population 1: black solid circles; population 2: red open diamonds). **(B)** Space time plot of the electrode potential. Population 1: $k = 1,\ldots,40$. Population 2: $k = 41,\ldots,80$. **(C)** Phase difference between two elements in population one, (black thick line $\varphi_1 - \varphi_2$), populations 2 red thin line, ($\varphi_{41} - \varphi_{45}$), and between populations (blue dashed, $\varphi_1 - \varphi_{41}$). **(D)** Time series of the electrode potential for the chimera state; population 1: black line, populations 2: red line.

Faraday current density calculated by the equation

$$J_F(e,\,\theta) = \left[\frac{C_h \exp(0.5e)}{1 + C_h \exp(e)} + a \exp(e)\right](1-\theta)\,, \qquad (5)$$

and Γ_i is the surface capacity. Γ_i were randomly chosen between 9.999×10^{-3} and 10.001×10^{-3} for simulating the heterogeneities of the different natural frequencies of the oscillators [54]. Moreover, $C_h = 1600$, a = 0.3, b = 6×10^{-5} and c = 0.001 are kinetic parameters. The global coupling occurs through the electrode potential equation (last term in Equation 3). K is the global coupling strength, $K = R_c/(R_{ind}R)$ and $R = R_{ind} + 40R_c$ [53]. Equation 3 is the charge balance: Current can be generated by charging the electrical double layer, the charge transfer electrochemical reactions (Faradayic current), and through coupling to the electrode potentials of the other wires. Nickel electrodissolution and water electrolysis are the two major chemical steps that contribute to the Faradayic current density in Equation 5 [52]. The oxide layer, whose coverage is given by Equation 4, blocks parts of the electrode from dissolution and water electrolysis. Without coupling ($K = 0$), Equations (3–5) exhibit a supercritical Hopf bifurcation at $V = 10.2$. The numerical simulations are performed at somewhat elevated circuit potentials ($V > 24$), where the oscillations exhibit non-linear waveforms.

Figure 4A shows the frequency of the synchronized oscillations as a function of the circuit potential (V) with $K = 2 \times 10^{-4}$ for the one- and two-cluster states for $24.3 \leq V \leq 25.3$. At low V, only the one-cluster state exists. For $24.9 \leq V \leq 25.3$ there is bistability between the one- and two-cluster states. Note the frequencies of both the one- and the two-cluster states decrease with increasing the potential and that the two-cluster states have slightly larger frequencies. In previous study [17], a phase model analysis was performed, which showed that very close to a Hopf bifurcation the phase coupling function exhibits only first harmonic components, and thus only one-cluster state is possible with positive coupling. The two-cluster state arises because of the presence of higher harmonics in the phase coupling function, which are induced by higher harmonics in both the infinitesimal phase response function and the oscillation waveform [17]. These non-linearities have been interpreted with higher-order correction terms of the amplitude equations close to a Hopf bifurcation [55],

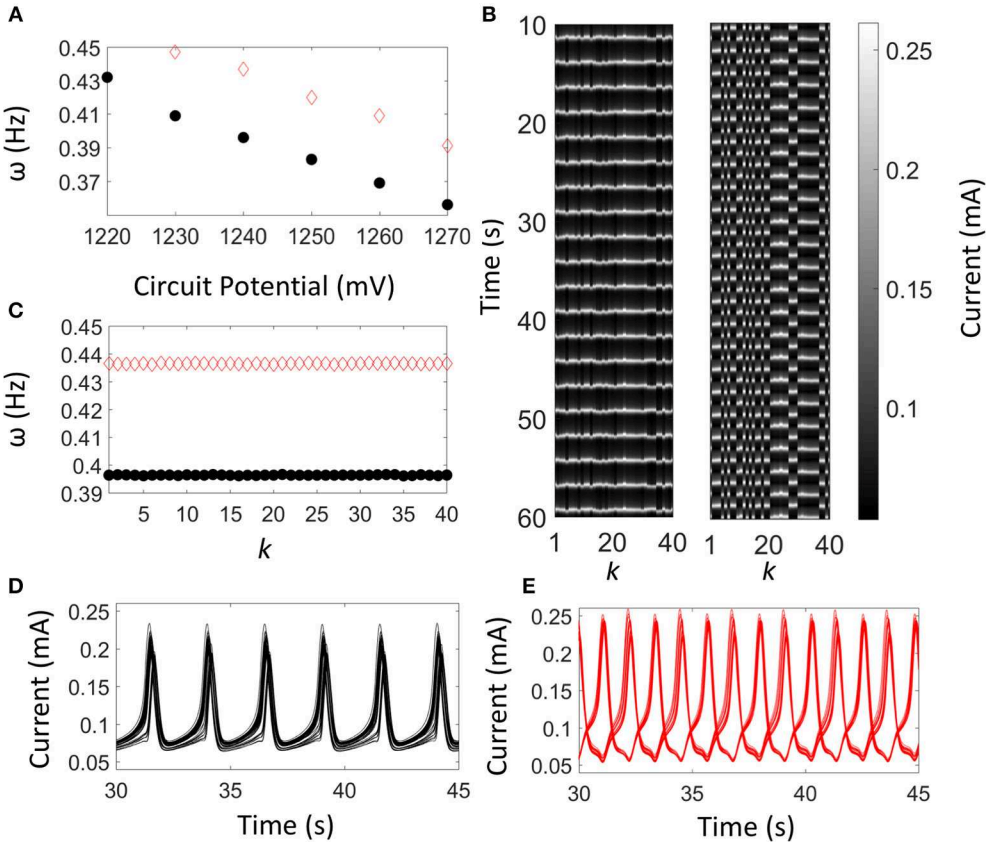

FIGURE 6 | Experiments: Cluster formation with global coupling. **(A)** Frequency of the one- (black solid circles) and the two-cluster state (red empty diamonds) as a function of the circuit potential, V. The one cluster state was obtained by increasing the circuit potential from $V = 1.100$ V. The two-cluster state can be obtained by increasing the circuit potential past $V = 1,270$ mV, where the one-cluster state breaks up, and decreasing V. **(B)** Space time plot of the current for the one- and two-cluster states. **(C)** Frequency of the elements in the one- (black solid circles) and two-cluster (red empty diamonds) states. **(D,E)** Time series of the current of the elements in the one- (black line) and two-cluster (red line) states. $R_{ind} = 600$ Ohm, $R_g = 10$ Ohm, $R_{coll} = 0$ Ohm, $K = 16.7$ μS. In panels **(B–E)**, $V = 1,240$ mV.

or with integrate-and-fire type models with a refractory period [56].

The behavior at $V = 25.0$ of the one- and the two-cluster states are shown in **Figures 4B–E**. In the one-cluster state, the electrode potentials (**Figure 4D**) follow the same variations. In the two-cluster state (**Figure 4E**), there are two groups of 20 elements that are in nearly anti-phase configuration. Note that in contrast to previous studies [43–45], the waveforms are not very harmonic and exhibit a moderate relaxation character.

The space time plot for the one- and two-cluster state (the left and right panel, respectively) are shown in **Figure 4B**. The one cluster exhibits uniform oscillations, while in the two-cluster state there are two groups in an approximate anti-phase configuration (Note that in the two clusters the configurations depend on initial conditions. Here we consider initial conditions opposite of the limit cycle, randomized in space). The frequencies of the elements are shown in **Figure 4C**. The two-cluster state has about 5% higher frequency ($\omega = 0.06474$) than the one cluster ($\omega = 0.06142$) state, with frequency difference $\Delta\omega = 3.32 \times 10^{-3}$. Because there is bistability between the one-cluster and the two-cluster states with differing frequency, the conditions may favor the formation of weak chimera states in networks. We note that oscillator heterogeneity was added to the model to better represent the experimental scenario. The same bistability also occurs for uniform populations (i.e., with $\Gamma_i = 0.01$ for all oscillators).

As a simple modular network obtained from the globally coupled oscillator populations, we introduce some cross coupling between two populations. For the electrode potential, the equations are:

$$\frac{de_l}{dt} = \frac{V - e_l}{R} - J_F\left(e_l, \theta_l\right) + K\sum_{j=1}^{40}(e_j - e_l) + \varepsilon K \sum_{k=41}^{80}(e_k - e_l)$$
$$l = 1, 2, \ldots, 40 \quad (6)$$

$$\frac{de_i}{dt} = \frac{V - e_i}{R} - J_F\left(e_i, \theta_i\right) + \varepsilon K\sum_{j=1}^{40}\left(e_j - e_i\right) + K \sum_{k=41}^{80}\left(e_k - e_i\right)$$
$$i = 41, 42, \ldots, 80 \quad (7)$$

(The equations for surface coverages are the same, i.e., Equation 4). There is a strong global coupling within the

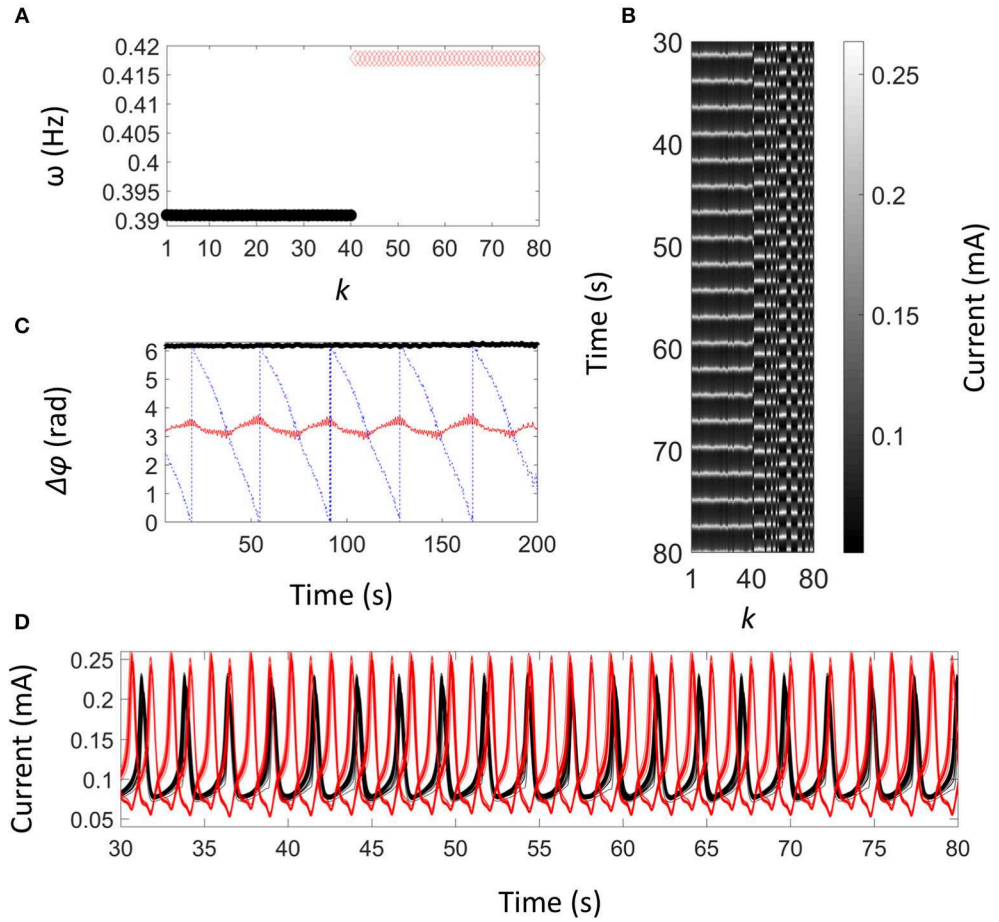

FIGURE 7 | Experiments: Weak chimera state in modular network with weak cross coupling. **(A)** Frequency of elements (population 1: black solid circles; population 2: red open diamonds). **(B)** Space time plot of the current oscillations. Population 1: $k = 1,\ldots,40$. Population 2: $k = 41,\ldots,80$. **(C)** Phase difference between two elements in population one (black thick line $\varphi_1 - \varphi_2$), populations 2 red thin line ($\varphi_{41} - \varphi_{45}$), and between populations (blue dashed, $\varphi_1 - \varphi_{41}$). **(D)** Time series of the currents of the elements in the chimera state; population 1: black line, population 2: red line. $V = 1{,}250$ mV, $R_{\text{ind}} = 580$ Ohm, $R_{\text{g}} = 9$ Ohm, $R_{\text{coll}} = 0.5$ Ohm, $K = 17.0$ μS, $\varepsilon = 0.03$.

populations, K, and weak global cross coupling between the populations εK, where ε is the cross-coupling factor ($0 \leq \varepsilon \leq 1$).

With $\varepsilon = 0.05$ with initial conditions corresponding to the one (or two)-cluster states for all the oscillators, the expected one (or two) cluster state was obtained. **Figure 5** shows the behavior with $\varepsilon = 0.05$ from initial conditions for population 1 (elements 1–40) with in-phase, and population 2 (elements 41–80) with conditions opposite of the limit-cycle randomized in space (Other parameters are the same as in **Figure 4**). **Figure 5A** shows the frequency of the elements. The two-cluster still has about 5% higher frequency ($\omega = 0.06485$) than the one-cluster ($\omega = 0.06157$) but the frequency difference is slightly lower than that without coupling, $\Delta\omega = 3.28 \times 10^{-3}$. The grayscale plot (**Figure 5B**) shows that the first forty elements (population 1) exhibit uniform oscillations while the elements 41–80 (population 2) form two clusters in anti-phase configurations. As shown in **Figure 5C**, the phase difference of the elements in the one-cluster state remains constant, approximately 2π (or zero), while in the two-cluster the phase difference between two elements in different clusters has small amplitude oscillations around π. For a pair of elements in different populations, we observed a phase drifting behavior, further confirming the chimera state. The presence of the desynchronized behavior between the populations could also be seen in the times series data of the electrode potentials (**Figure 5D**). Under these conditions, the presence of the chimera state is a unique behavior of the network interactions. With global coupling ($\varepsilon = 1.0$), the chimera state disappears: With initial conditions similar to the chimera state in **Figure 5** we obtained a one-cluster, in-phase synchronized state.

Experiments

Without coupling, the oscillators exhibit slight heterogeneity, and the natural frequencies have a standard deviation of about 14 mHz. To confirm the weak chimera state, we performed a set of experiments following the guidelines developed in the

simulations. First, we used only population 1 (40 electrodes), and coupled them globally (i.e., $R_{coll} = 0\,\text{Ohm}$, $R_g = 10$ Ohm in **Figure 1C**). With $K = 16.7\ \mu\text{S}$, the frequencies of the elements in the one- and two-cluster states are shown in **Figure 6**. For $V \leq 1,220\,\text{mV}$, only the one-cluster state is stable. The frequencies decrease with increasing circuit potential. For $1,230\,\text{mV} \leq V \leq 1,270\,\text{mV}$ a two-cluster state was also found (This two-cluster state can be obtained by increasing the circuit potential past $V = 1,270\,\text{mV}$, where the one-cluster state breaks up, and decreasing the potential). Thus, in this region, there is bistability between the one- and two-cluster states and, similar to the simulations, the two-cluster state has slightly larger frequency than the one-cluster state. Note that the occurrence of such bistability between one- and two-cluster states was predicted by experiment-based phase models [17].

As an example of the behavior observed in this region, the dynamics is shown at $V = 1,240\,\text{mV}$. The time series data for the one- and two-cluster states also confirm that this state was found with oscillation waveform of relaxation character (see **Figures 6D,E**). The grayscale plots (**Figure 6B**) show the one- (left) and two-cluster states (right). The elements in the one-cluster state oscillate nearly uniformly, while those in the two-cluster states form two groups, oscillating in anti-phase. The two-cluster state forms an almost balanced configuration with 18 and 22 elements in each cluster. As in the simulation, the two-cluster state has a higher frequency ($\omega = 0.437$ Hz) than the one-cluster ($\omega = 0.396$ Hz); the frequency increase is about 10% with a frequency difference of 41 mHz (see **Figure 6C**).

Now we consider the modular network with two populations of 40 electrodes. The oscillators in each population are coupled with R_g. As shown in **Figure 1C**, the two populations are coupled through a collective resistance R_{coll}. The resistance R_{coll} induces global coupling between every electrode pair, with coupling strength $K_{coll} = R_{coll}/[\left(R_{ind} + 40R_g\right) R_{eq}]$, where $R_{eq} = R_{ind} + 40R_g + 80R_{coll}$. The group resistance induces coupling only within a population, i.e., $K_g = R_g/[R_{ind}(R_{ind} + 40R_g)]$. The total coupling thus $K = K_g + K_{coll}$, and $\varepsilon = K_g/K$.

Figure 7A shows the frequency of the one- and two-cluster states in the network configuration with $K = 17\mu S$ and $\varepsilon = 0.03$. In this set of experiments, the frequency of the one- and the two-cluster states with $\varepsilon = 0$ was 0.384 Hz and 0.413 Hz, respectively; the frequency difference was 29 mHz with the two-cluster state having about 8% higher frequency than the one-cluster state. With $\varepsilon = 0.03$, the frequency difference between the populations decreased to 27 mHz; the frequency of the two-cluster state (0.418 Hz) was about 7% higher than that of the one-cluster state (0.391 Hz). The grayscale plot (**Figure 7B**) of the chimera state shows that the first forty elements (population 1) are in-phase synchronized and elements 41–80 (population 2) form two clusters, in anti-phase configuration, with 17 and 23 elements in each cluster. The phase differences are shown in **Figure 7C**. The elements in population 1 are nearly in-phase with a phase difference close to 2π (or zero). The clusters in the two-cluster population are approximately in anti-phase; the phase difference shows the characteristics small amplitude oscillations around π (The high frequency modulation on top of the slow oscillation is due to in-cycle fluctuation of the phase; averaged phase models cannot explain such fluctuations). Finally, elements in between population 1 and 2 exhibit phase drifting. The lack of frequency synchrony can also be seen in the current time series in **Figure 7D**.

We also performed a long-term experiment to check for the robustness of the chimera state. The chimera state was stable for about 1,000 cycles, after which a one-cluster state was observed. In this parameter region, the system parameters exhibit a slow drift toward the Hopf bifurcation point. One explanation for the loss of the chimera state is that during this slow drift the oscillations become less non-linear for the chimera state to occur as the parameters leave the region where bistability is present.

We also confirmed that by increasing the coupling strength, the chimera state breaks down. While for $\varepsilon = 0.1$ stable chimera state occurs, with $\varepsilon = 0.2$ (with similar coupling strengths and initial conditions) only in-phase behavior can be observed in the experiments.

CONCLUSIONS

Robust weak chimera states were observed in a modular network of two populations of globally coupled electrochemical oscillators with simple resistive cross coupling between populations that is sufficiently weak ($\varepsilon < 0.2$). There are important differences in the observed chimera states compared to those in our previous studies [43–45]. A ring network of electrochemical oscillators, close to Hopf bifurcation, showed chimera state with long-range interactions [44, 45]. This chimera state was not very robust in the sense that even small heterogeneities destroyed the behavior, and only chimera "remnants" occurred. From an engineering perspective, even the relatively small system size (20 electrodes) required large number (140) of coupling resistors and capacitances. In addition, the chimera state only occurred as a transient behavior, for about 80–100 cycles. In the weak chimera state reported here, global coupling within and between the modules can be induced with one resistance each; this design greatly simplifies the experimental setup. Because the chimera state is very robust it does not require adjustment of natural frequencies, and the chimera state is sustained for many hundreds of cycles.

In identifying the experimental conditions for the chimera state, we relied on our previous study [43], where two populations of weakly non-linear oscillators were coupled with a strongly non-linear feedback mechanism. However, here we assumed that the same type of non-linearities can be obtained with linear (difference) coupling of highly non-linear oscillators. Such conditions ($1,230\,\text{mV} \leq V \leq 1,270\,\text{mV}$) were found far from the Hopf bifurcation ($V \approx 1.10\,\text{V}$) in the electrochemical system. While the parameter region favorable for the chimera state is relatively small (40 mV) compared to the region of oscillations ($\sim$200 mV), we note that we focused here on weak chimeras of a particular type with one- and two-cluster states with distinct frequencies. Weak chimeras could also occur with other initial conditions (e.g., with balanced and unbalanced two-cluster states) and parameter regions with other types of

desynchronized clusters, e.g., two- and three-cluster states; see also Bick et al. [29].

Similar weak chimera states could be observed in many other chemical systems. For example, other electrochemical systems and the BZ reaction can generate rich variety of clusters, in particular, when the sign of the coupling strength can also be varied (e.g., excitatory and inhibitory coupling) [31, 39]. The weak chimera state could contribute to exploring chimeras in robust biological systems, e.g., circadian clocks [57], and dynamical diseases [58]; see also [59] for a recent review. Along these lines, we showed that an integrate-and-fire neuron model, with refractory period can generate bistability between cluster states in globally coupled populations [56]. Other possible biological system could include the oscillatory glycolysis, where highly non-linear feedback mechanisms are common [60].

AUTHOR CONTRIBUTIONS

IK and CB conceived the presented idea. CB encouraged IK and JO-E to investigate the weak chimeras in modular networks. IK and JO-E planned the experiments and the numerical simulations. JO-E performed the experiments and numerical simulations, and processed the data. JO-E took the lead in writing the manuscript. IK and CB revised the manuscript. IK supervised the project. All authors provided critical feedback and helped shape the research, analysis, and manuscript.

FUNDING

IK acknowledges support from National Science Foundation CHE-1465013 grant.

REFERENCES

1. Pikovsky AS, Rosenblum MG, Kurths J. *Synchronization: A Universal Concept in Non-Linear Sciences*. Cambridge: Cambridge University Press (2001). doi: 10.1017/CBO9780511755743
2. Marek M, Stuchl I. Synchronization in two interacting oscillatory systems. *Biophys Chem*. (1975) **3**:241–8. doi: 10.1016/0301-4622(75)80016-0
3. Crowley MF, Field RJ. Electrically coupled Belousov-Zhabotinskii oscillators. 1. Experiments and simulations. *J Phys Chem*. (1986) **90**:1907–15. doi: 10.1021/j100400a033
4. Crowley MF, Epstein IR. Experimental and theoretical studies of a coupled chemical oscillator: phase death, multistability and in-phase and out-of-phase entrainment. *J Phys Chem*. (1989) **93**:2496–502. doi: 10.1021/j100343a052
5. Fujii H, Sawada Y. Phase-difference locking of coupled oscillating chemical systems. *J Chem Phys*. (1978) **69**:3830–2. doi: 10.1063/1.437048
6. Nakajima K, Sawada Y. Experimental studies on the weak coupling of oscillatory chemical reaction systems. *J Chem Phys*. (1980) **72**:2231–4. doi: 10.1063/1.439466
7. Booth V, Erneux T, Laplante J-P. Experimental and numerical study of weakly coupled bistable chemical reactors. *J Phys Chem*. (1994) **98**:6537–40. doi: 10.1021/j100077a019
8. Dechert G, Zeyer K, Lebender D, Schneider F. Recognition of phase patterns in a chemical reactor network. *J Phys Chem*. (1996) **100**:19043–8. doi: 10.1021/jp9616066
9. Toiya M, Vanag VK, Epstein IR. Diffusively coupled chemical oscillators in a microfluidic assembly. *Angew Chem Int Ed*. (2008) **47**:7753–5. doi: 10.1002/anie.200802339
10. Toiya M, Gonzalez-Ochoa HO, Vanag VK, Fraden S, Epstein IR. Synchronization of chemical micro-oscillators. *J Phys Chem Lett*. (2010) **1**:1241–6. doi: 10.1021/jz100238u
11. Taylor AF, Tinsley MR, Wang F, Huang ZY, Showalter K. Dynamical quorum sensing and synchronization in large populations of chemical oscillators. *Science*. (2009) **323**:614–7. doi: 10.1126/science.1166253
12. Taylor AF, Tinsley MR, Wang F, Showalter K. Phase clusters in large populations of chemical oscillators. *Angew Chem Int Edit*. (2011) **50**:10161–4. doi: 10.1002/anie.201008248
13. Okano T, Miyakawa K. Feedback-controlled dynamics in a two-dimensional array of active elements. *Phys Rev E*. (2009) **80**:026215. doi: 10.1103/PhysRevE.80.026215
14. Vanag VK, Epstein IR. Pattern formation in a tunable medium: the Belousov-Zhabotinskii reaction in an aerosol OT microemulsion. *Phys Rev Lett*. (2001) **87**:228301. doi: 10.1103/PhysRevLett.87.228301
15. Wickramasinghe M, Kiss IZ. *Synchronization of Electrochemical Oscillators. Engineering of Chemical Complexity*. New Jersey: Wolrd Scientific (2013). p. 215–36. doi: 10.1142/9789814390460_0011
16. Kiss IZ, Zhai Y, Hudson JL. Emerging coherence in a population of chemical oscillators. *Science*. (2002) **296**:1676–8. doi: 10.1126/science.1070757
17. Kiss IZ, Zhai YM, Hudson JL. Predicting mutual entrainment of oscillators with experiment-based phase models. *Phys Rev Lett*. (2005) **94**:248301. doi: 10.1103/PhysRevLett.94.248301
18. Kiss IZ, Rusin CG, Kori H, Hudson JL. Engineering complex dynamical structures: sequential patterns and desynchronization. *Science*. (2007) **316**:1886–9. doi: 10.1126/science.1140858
19. Manrubia SC, Mikhailov AS, Zanette DH. *Emergence of Dynamical Order: Synchronization Phenomena in Complex Systems*. Singapore: World Scientific. (2004). doi: 10.1142/9789812562463
20. Epstein IR, Pojman JA. *An Introduction to Non-Linear Chemical Dynamics: Oscillations, Waves, Patterns, and Chaos*. Oxford: Oxford University Press (1998).
21. Nakao H. Phase reduction approach to synchronisation of non-linear oscillators. *Contemp Phys*. (2016) **57**:188–214. doi: 10.1080/00107514.2015.1094987
22. Zhai YM, Kiss IZ, Kori H, Hudson JL. Desynchronization and clustering with pulse stimulations of coupled electrochemical relaxation oscillators. *Physica D*. (2010) **239**:848–56. doi: 10.1016/j.physd.2009.06.004
23. Zhai Y, Kiss IZ, Hudson JL. Control of complex dynamics with time-delayed feedback in populations of chemical oscillators: desynchronization and clustering. *Ind Eng Chem Res*. (2008) **47**:3502–14. doi: 10.1021/ie0708632
24. Panaggio MJ, Abrams DM. Chimera states: co-existence of coherence and incoherence in networks of coupled oscillators. *Nonlinearity*. (2015) **28**:R67–87. doi: 10.1088/0951-7715/28/3/R67
25. Omel'Chenko OE. The mathematics behind chimera states. *Nonlinearity*. (2018) **31**:R121–64. doi: 10.1088/1361-6544/aaaa07
26. Battogtokh D, Kuramoto Y. Coexistence of coherence and incoherence. *Nonlin Phenom Complex Syst*. (2002) 5:380–5.
27. Abrams DM, Strogatz SH. Chimera states for coupled oscillators. *Phys Rev Lett*. (2004) **93**:174102. doi: 10.1103/PhysRevLett.93.174102
28. Ashwin P, Burylko O. Weak chimeras in minimal networks of coupled phase oscillators. *Chaos*. (2015) **25**:013106. doi: 10.1063/1.4905197
29. Bick C, Ashwin P. Chaotic weak chimeras and their persistence in coupled populations of phase oscillators. *Nonlinearity*. (2016) **29**:1468–86. doi: 10.1088/0951-7715/29/5/1468
30. Kemeth FP, Haugland SW, Schmidt L, Kevrekidis IG, Krischer K. A classification scheme for chimera states. *Chaos*. (2016) **26**:094815. doi: 10.1063/1.4959804
31. Tinsley MR, Nkomo S, Showalter K. Chimera and phase-cluster states in populations of coupled chemical oscillators. *Nat Phys*. (2012) **8**:662–5. doi: 10.1038/nphys2371
32. Nkomo S, Tinsley MR, Showalter K. Chimera states in populations of non-locally coupled chemical oscillators. *Phys Rev Lett*. (2013) **110**:244102. doi: 10.1103/PhysRevLett.110.244102
33. Nkomo S, Tinsley MR, Showalter K. Chimera and chimera-like states in populations of non-locally coupled homogeneous and heterogeneous chemical oscillators. *Chaos*. (2016) **26**:094826. doi: 10.1063/1.4962631

34. Totz JF, Rode J, Tinsley MR, Showalter K, Engel H. Spiral wave chimera states in large populations of coupled chemical oscillators. *Nat Phys*. (2018) **14**:282–5. doi: 10.1038/s41567-017-0005-8
35. Haugland SW, Schmidt L, Krischer K. Self-organized alternating chimera states in oscillatory media. *Sci Rep*. (2015) **5**:9883. doi: 10.1038/srep09883
36. Kemeth FP, Haugland SW, Krischer K. Symmetries of chimera states. *Phys Rev Lett*. (2018) **120**:214101. doi: 10.1103/PhysRevLett.120.214101
37. Schmidt L, Krischer K. Clustering as a prerequisite for chimera states in globally coupled systems. *Phys Rev Lett*. (2015) **114**:034101. doi: 10.1103/PhysRevLett.114.034101
38. Schmidt L, Krischer K. Chimeras in globally coupled oscillatory systems: from ensembles of oscillators to spatially continuous media. *Chaos*. (2015) **25**:064401. doi: 10.1063/1.4921727
39. Schmidt L, Schönleber K, Krischer K, García-Morales V. Coexistence of synchrony and incoherence in oscillatory media under non-linear global coupling. *Chaos*. (2014) **24**:013102. doi: 10.1063/1.4858996
40. Schönleber K, Zensen C, Heinrich A, Krischer K. Pattern formation during the oscillatory photoelectrodissolution of n-type silicon: turbulence, clusters and chimeras. *New J Phys*. (2014) **16**:063024. doi: 10.1088/1367-2630/16/6/063024
41. Kumar P, Verma DK, Parmananda P. Partially synchronized states in an ensemble of chemo-mechanical oscillators. *Phys Lett A*. (2017) **381**:2337–43. doi: 10.1016/j.physleta.2017.05.032
42. Koper MTM. Oscillations and complex dynamical bifurcations in electrochemical systems *Adv Chem Phys*. (1996) **92**:161–298. doi: 10.1002/9780470141519.ch2
43. Bick C, Sebek M, Kiss IZ. Robust weak chimeras in oscillator networks with delayed linear and quadratic interactions. *Phys Rev Lett*. (2017) **119**:168301. doi: 10.1103/PhysRevLett.119.168301
44. Wickramasinghe M, Kiss IZ. Spatially organized dynamical states in chemical oscillator networks: synchronization, dynamical differentiation, and chimera patterns. *PLoS ONE*. (2013) **8**:e80586. doi: 10.1371/journal.pone.0080586
45. Wickramasinghe M, Kiss IZ. Spatially organized partial synchronization through the chimera mechanism in a network of electrochemical reactions. *Phys Chem Chem Phys*. (2014) **16**:18360–9. doi: 10.1039/C4CP02249A
46. Thoubaan M, Ashwin P. Existence and stability of chimera states in a minimal system of phase oscillators. *Chaos*. (2018) **28**:103121. doi: 10.1063/1.5044750
47. Wickramasinghe M, Kiss IZ. Synchronization of electrochemical oscillators with differential coupling. *Phys Rev E*. (2013) **88**:062911. doi: 10.1103/PhysRevE.88.062911
48. Kiss IZ, Kazsu Z, Gáspár V. Tracking unstable steady states and periodic orbits of oscillatory and chaotic electrochemical systems using delayed feedback control. *Chaos*. (2006) **16**:033109. doi: 10.1063/1.2219702
49. Wolfrum M, Omel'chenko OE. Chimera states are chaotic transients. *Phys Rev E*. (2011) **84**:015201. doi: 10.1103/PhysRevE.84.015201
50. Ashwin P, Swift JW. The dynamics of n weakly coupled identical oscillators. *J Non-lin Sci*. (1992) **2**:69–108. doi: 10.1007/BF02429852
51. Okuda K. Variety and generality of clustering in globally coupled oscillators. *Physica D*. (1993) **63**:424–36. doi: 10.1016/0167-2789(93)90121-G
52. Haim D, Lev O, Pismen LM, Sheintuch M. Modeling periodic and chaotic dynamics in anodic nickel dissolution. *J Phys Chem*. (1992) **96**:2676–81. doi: 10.1021/j100185a051
53. Zhai Y, Kiss IZ, Hudson J. Emerging coherence of oscillating chemical reactions on arrays: experiments and simulations. *Ind Eng Chem Res*. (2004) **43**:315–26. doi: 10.1021/ie030164z
54. Kiss IZ, Wang W, Hudson JL. Experiments on arrays of globally coupled periodic electrochemical oscillators. *J Phys Chem B*. (1999) **103**:11433–44. doi: 10.1021/jp992471h
55. Kori H, Kuramoto Y, Jain S, Kiss IZ, Hudson JL. Clustering in globally coupled oscillators near a Hopf bifurcation: theory and experiments. *Phys Rev E*. (2014) **89**:062906. doi: 10.1103/PhysRevE.89.062906
56. Kori H, Kiss IZ, Jain S, Hudson JL. Partial synchronization of relaxation oscillators with repulsive coupling in autocatalytic integrate-and-fire model and electrochemical experiments. *Chaos*. (2018) **28**:045111. doi: 10.1063/1.5022497
57. Rattenborg NC, Amlaner CJ, Lima SL. Behavioral, neurophysiological and evolutionary perspectives on unihemispheric sleep. *Neurosci Biobehav Rev*. (2000) **24**:817–42. doi: 10.1016/S0149-7634(00)00039-7
58. Andrzejak RG, Rummel C, Mormann F, Schindler K. All together now: analogies between chimera state collapses and epileptic seizures. *Sci Rep*. (2016) **6**:23000. doi: 10.1038/srep23000
59. Bick C, Goodfellow M, Laing CR, Martens EA. Understanding the dynamics of biological and neural oscillator networks through mean-field reductions: a review. *eprint arXiv:190205307*. (2019).
60. Dhumpa R, Truong TM, Wang X, Bertram R, Roper MG. Negative feedback synchronizes islets of langerhans. *Biophys J*. (2014) **106**:2275–82. doi: 10.1016/j.bpj.2014.04.015

Conflict of Interest Statement: The authors declare that the research was conducted in the absence of any commercial or financial relationships that could be construed as a potential conflict of interest.

frontiers in Applied Mathematics and Statistics

ORIGINAL RESEARCH
published: 24 October 2019
doi: 10.3389/fams.2019.00052

Synchronization Patterns in Modular Neuronal Networks: A Case Study of *C. elegans*

Armin Pournaki[1,2], *Leon Merfort*[1,3], *Jorge Ruiz*[1,4], *Nikos E. Kouvaris*[5,6], *Philipp Hövel*[1,4,7]* *and Johanne Hizanidis*[8]

[1] *Institute of Theoretical Physics, Technische Universität Berlin, Berlin, Germany,* [2] *Max Planck Institute for Mathematics in the Sciences, Leipzig, Germany,* [3] *Potsdam Institute for Climate Impact Research, Potsdam, Germany,* [4] *Bernstein Center for Computational Neuroscience Berlin, Humboldt-Universität zu Berlin, Berlin, Germany,* [5] *Department of Mathematics, Namur Institute for Complex Systems (naXys), University of Namur, Namur, Belgium,* [6] *DRIBIA Data Research S.L., Barcelona, Spain,* [7] *School of Mathematical Sciences, University College Cork, Cork, Ireland,* [8] *Department of Physics, University of Crete, Herakleio, Greece*

We investigate synchronization patterns and chimera-like states in the modular multilayer topology of the connectome of *Caenorhabditis elegans*. In the special case of a designed network with two layers, one with electrical intra-community links and one with chemical inter-community links, chimera-like states are known to exist. Aiming at a more biological approach based on the actual connectivity data, we consider a network consisting of two synaptic (electrical and chemical) and one extrasynaptic (wireless) layers. Analyzing the structure and properties of this layered network using Multilayer-Louvain community detection, we identify modules whose nodes are more strongly coupled with each other than with the rest of the network. Based on this topology, we study the dynamics of coupled Hindmarsh-Rose neurons. Emerging synchronization patterns are quantified using the pairwise Euclidean distances between the values of all oscillators, locally within each community and globally across the network. We find a tendency of the wireless coupling to moderate the average coherence of the system: for stronger wireless coupling, the levels of synchronization decrease both locally and globally, and chimera-like states are not favored. By introducing an alternative method to define meaningful communities based on the dynamical correlations of the nodes, we obtain a structure that is dominated by two large communities. This promotes the emergence of chimera-like states and allows to relate the dynamics of the corresponding neurons to biological neuronal functions such as motor activities.

Keywords: synchronization, multilayer network, chimera state, neuronal oscillators, metastability, community detection

OPEN ACCESS

Edited by:
Ralph G. Andrzejak, Universitat Pompeu Fabra, Spain

Reviewed by:
Roberto Barrio, University of Zaragoza, Spain
Syamal Kumar Dana, Jadavpur University, India

***Correspondence:**
Philipp Hövel
philipp.hoevel@ucc.ie

Specialty section:
This article was submitted to Dynamical Systems, a section of the journal Frontiers in Applied Mathematics and Statistics

Received: *15 December 2018*
Accepted: *07 October 2019*
Published: *24 October 2019*

Citation:
Pournaki A, Merfort L, Ruiz J, Kouvaris NE, Hövel P and Hizanidis J (2019) Synchronization Patterns in Modular Neuronal Networks: A Case Study of C. elegans. Front. Appl. Math. Stat. 5:52. doi: 10.3389/fams.2019.00052

1. INTRODUCTION

Synchronization phenomena are widely studied across fields, from classical mechanics [1] to complex dynamical systems [2–5] and music [6, 7]. Surprising phenomena in nature, for instance, the synchronized flashing of fireflies [8] or the unexpected motion of bridges due to the emergence of synchronized walking [9] have sparked the interest in synchronization patterns. However, some more peculiar patterns of synchronization can also be observed in complex systems. These include the surprising coexistence of coherent and incoherent parts of coupled identical oscillators, a hybrid state that became known as *chimera*.

Chimera states were first reported in rings of non-locally and symmetrically coupled identical phase oscillators [10]. Since their discovery, they have been extensively studied both theoretically [11–26] and experimentally [27–31] in a wide range of systems. For recent reviews see references [32–35]. For a long time, chimera states were believed to exist mostly for nonlocal coupling schemes. This consensus was revised when chimeras were found in systems of globally [36–41] and locally coupled oscillators [42–47]. Although these regular topologies often capture the nature of the interaction between the coupled elements, there are many real-world systems where a more complex connectivity description is required. Prominent examples of such systems are biological neuron networks, where synchronization is important for various cognitive functions, and chimera states, in particular, can be used to interpret phenomena such as epileptic seizures [48] and bump states [49, 50].

Previous works on the effect of nontrivial topologies on chimera states have involved scale-free and random networks [51, 52], hierarchical (fractal) schemes [53], modular structures [54], and "reflecting" connectivities [55]. Our aim is to contribute in this direction and take it one step further by considering a multilayer structure. In recent years, the study of multilayer networks has become highly popular owing to their significant relevance in several complex systems [56–58]. In the context of neuronal networks, such a multilayer approach is ideal for addressing the relationship between structure and function, an essential question in theoretical neuroscience [59]. Concerning chimera states, studies on multilayer/multiplex networks are limited and mainly deal with artificial coupling schemes [23, 60–63]. For example, the case of two populations with various coupling schemes has been systematically studied in reference [22]. In the present work, we focus on the possibility to observe chimera-like patterns in a multiplex structure of a real-world system, namely the neuronal network of *Caenorhabditis elegans* (*C. elegans*). Our main focus is to demonstrate the existence and emergence of synchronization patterns in a multilayer network obtained from the connection of this real organism. In short, we will show that chimera-like states can be hard to identify in real-world networks and suggest an alternative approach to dynamically define communities, whose dynamics can be related to biological functions to the involved neurons. The *C. elegans* multilayer connectome is used as a case study, but the proposed approach can be easily generalized to other networks.

The nematode *C. elegans* has been studied for many decades as a standard model organism for many processes of biological interest and beyond [64]. Particularly for neurobiology, the structure and connectivity of its nervous system has been deducted from reconstructions of electron micrographs of serial sections [65, 66]. Its nervous system includes sensory organs in the head and can produce highly plastic behavior, e.g., disassociative and associative learning and memory as response to taste, smell, temperature, touch and slightly to light, even though the nematode has no eyes [67]. A number of molecular mechanisms is involved in learning and memory, mediated through the same neurotransmitters as in humans and every species with a nervous system. In fact, neurons in *C. elegans* are very similar to those of humans, and their synapses are also classified as electrical or chemical.

It has been found that some of *C. elegans*' neurotransmitters, specifically the four monoamines dopamine, octopamine, serotonin and tyramine, act at both neurons and muscles to affect egg laying, pharyngeal pumping, locomotion and learning, or in general, modulate behavior in response to changing environmental cues [68]. Not only in *C. elegans* but also in many animals, one important route of neuromodulation is through monoamine signaling, and it is well known that this extrasynaptic communication is critical to some human brain functions. In both humans and *C. elegans*, many neurons expressing aminergic receptors are not post-synaptic to releasing neurons, indicating that a significant amount of monoamine signaling occurs outside the wired connectome. This defines a wireless connectivity network between neurons [69] for *C. elegans*. In general, this wireless or extrasynaptic communication is known as volume transmission in neuroscience [70–72], and is characterized by three-dimensional signal diffusion in the extracellular fluid, for distances larger than the synaptic cleft. This leads to multiple extracellular pathways connecting intercommunicating cells that are not well characterized from a structural perspective. For further details about our implementation of this network please refer to the Methods 5.1.

In our multilayer approach to modeling the neuronal connectivity of *C. elegans*, the network's nodes represent neurons connected by either electrical, chemical, or wireless pathways, which defines three layers. The electrical network is undirected, while the chemical and wireless networks are directed. Taking a closer look at the three layers' hubs in **Figure 1**, a strong overlap exists between hubs in the electrical and in the chemical network, however not so in the wireless network. This is in agreement with results from Bentley et al. [69], where a multilayer analysis of the three networks delineates topological overlaps between the two synaptic networks and discrepancies between the wireless and the synaptic networks. These topological differences of the different layers can be further explored by the degree distributions depicted in **Figure 1**, where it is clear that all of them present a heavy-tailed degree distribution with a maximum degree/average degree of 40/4 (electrical layer), 53/16 (chemical layer), and 137/15 (wireless layer). Since there are not many monoamine-releasing neurons, we observe many nodes with zero in- and out-degree. Note that the values of the wireless degree distribution need to be interpreted as maximum possible values. The underlying parameters that could lead to an equivalent of link weights are disregarded due to their complexity. Biologically, a source neuron in the wireless network influences a potential target neuron depending on parameters related to the diffusion processes of neurotransmitters throughout the body. Such parameters can be the physical distance between the presynaptic source and the postsynaptic target or the chemical concentration of the released neurotransmitters [70–72].

In order to investigate the synchronization patterns of the neuronal network at hand, we will first investigate the dynamics based on a previous approach from Hizanidis et al. [54]. This modeling approach is then extended to get closer to the biological connectome of *C. elegans*. The synchronization of the network

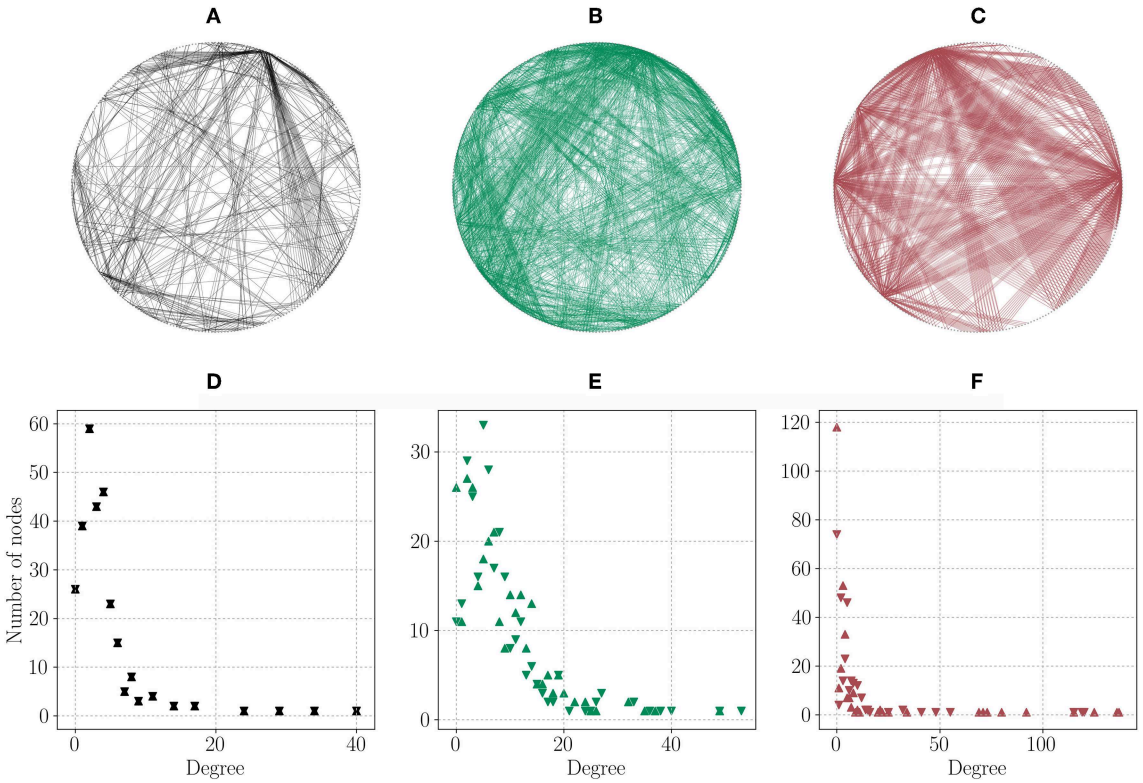

FIGURE 1 | Layers of the *C. elegans* network and their degree distributions. All networks are plotted undirected and in a ring for visualization purposes only, with the same node positions across layers. ▽: in-degree, △: out-degree. **(A)** Electrical sub-network. **(B)** Chemical sub-network. **(C)** Wireless sub-network. **(D)** Electrical layer degree distribution. **(E)** Chemical layer in- and out-degree distribution. **(F)** Wireless layer in- and out-degree distribution.

is computed based on the pairwise Euclidean distances of the dynamical variables of nodes (cf. Methods 5.3 and Kemeth et al. [73]). Furthermore, we introduce an alternative way of finding meaningful communities in the neuronal network and relate the observed synchronization patterns—including chimera-like states – to biological functions of the involved neurons.

2. COUPLING BY DESIGN

Before investigating the *C. elegans* network using the actual connectivity data, we discuss results following the modeling approach of Hizanidis et al. [54], where first, the communities are computed from the aggregated connectome irrespective of the link type. Then, all intra-community links are assigned to the electrical layer and all inter-community links to the chemical layer. In other words, the designed network is modular or multilayer, where the neurons of each module and their intra-community links occupy a different layer. We follow this approach in order to test the applicability of the Euclidean distance method in evaluating the synchronization of the network.

Figure 2 shows the six communities obtained from the Walktrap algorithm [74] applied to the aggregated connectome of *C. elegans*. The resulting topology is exactly the same as in Hizanidis et al. [54]: electrical intra-community links and chemical inter-community connections. Therefore, numerical integration of the coupled Hindmarsh-Rose (Equation 1) using this topology leads to similar time series of the dynamical variable as in Hizanidis et al. [54]. See Methods 5.2 for details on the Hindmarsh-Rose model.

In **Figure 3**, the level of synchronization of every community γ_1 to γ_6, the global level of synchronization γ of the whole network, the chimera-like index χ_γ as well as the metastability index λ_γ are shown for a large range of electrical and chemical couplings. Note that the global level of synchronization γ is computed from the pairwise Euclidean distances of the three dimensional coordinates defined by the dynamical parameters p, q and n, between any pair of nodes in the network (cf. Methods 5.3). Thus, γ, in contrast to χ_γ and λ_γ is independent of the community structure.

It can be seen that for an electrical coupling strength of $g_{\mathrm{el}} = 0.4$ and no chemical coupling ($g_{\mathrm{ch}} = 0$) the chimera-like index based on Euclidean distances attains a value of $\chi_\gamma \approx 0.25$. Furthermore, the metastability index for these coupling strengths $\lambda_\gamma \approx 0.12$ is only half as large as the chimera-like index. This serves as justification why we may call the state a "chimera-like" state, in contrast to a "metastable" state where the metastability index prevails.

Figure 4A depicts a space-time plot of the p-variable of the Hindmarsh-Rose model, which corresponds to the membrane

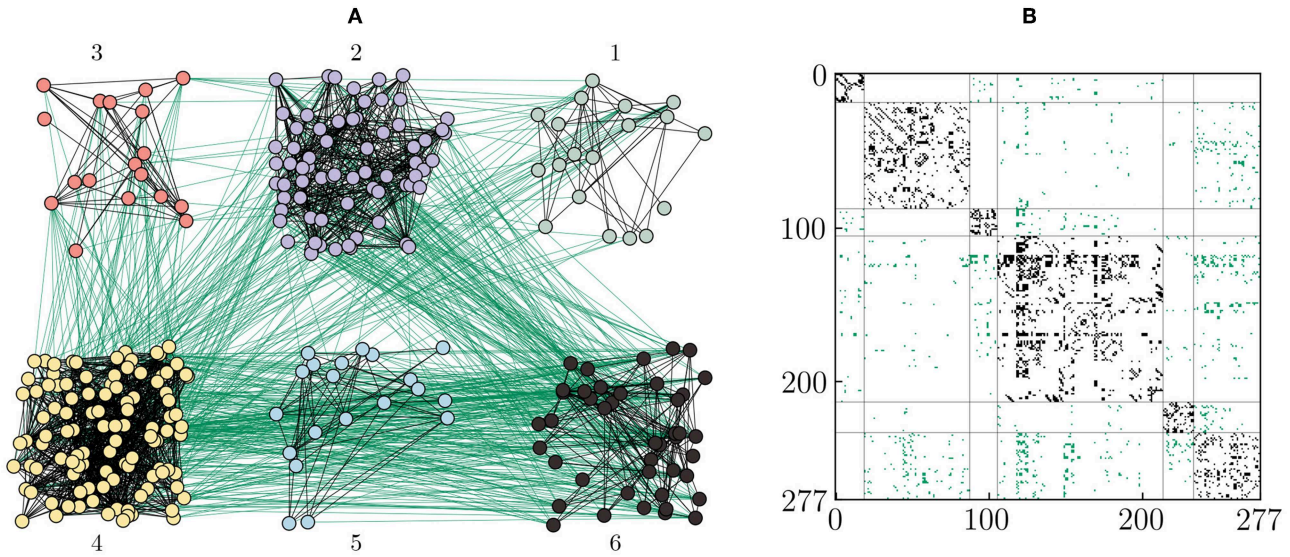

FIGURE 2 | Topology of the artificial *C. elegans* network. The network of 277 neurons is divided into 6 communities of different sizes using the Walktrap algorithm. **(A)** Neurons are colored according to their community [1: gray (19 neurons), 2: violet (69 neurons), 3: red (18 neurons), 4: yellow (108 neurons), 5: blue (20 neurons), 6: black (43 neurons)]. Electrical and chemical connections are shown as black and green lines, respectively. In this approach, electrical junctions exist only within every communities, whereas chemical synapses span only across communities. **(B)** The adjacency matrix with electrical (black) and chemical (green) edges, where the axes represent the node indices. The vertical and horizontal lines divides the matrix in the ordered communities (1 to 6), from left to right in the horizontal axis, and from up to down in the vertical axis, respectively.

potential (cf. Methods 5.2) for disconnected communities with high electrical (intra-community) coupling. One can see that every community operates in the synchronized regime. For smaller electrical coupling, **Figure 4B** shows the space-time plot of the p-variable with a pattern of mixed synchrony that resembles a chimera-like state, that is, varying synchronization across communities. This state is achieved for $g_{\mathrm{el}} = 0.4$ and $g_{\mathrm{ch}} = 0$, that is, that communities are not connected. It can be seen that especially the nodes in the larger communities 2 and 4 are much more synchronized than the nodes in the small communities. The chimera-like index is still large in a close neighborhood of this point (cf. **Figure 3**). However, when the chemical coupling is increased, the intra-community synchronization weakens and inhibits the emergence of chimera-like states. In summary, different levels of synchronization can be achieved by means of reducing the inter-community coupling strength. This raises to the hypothesis that, when observing the designed model, the main driver of chimera-like behavior is in fact the relative size of the communities, since larger communities do not need a high intra-community coupling strength to reach a high level of synchronization. **Figure 4C** shows the mean order parameter depending on the size of the community. As expected, the order parameter grows with the number of nodes in the community. While the mean order parameter of the three small communities (1, 3, and 5) is always below 0.6, the largest community reaches a value of $\gamma_4 \approx 0.95$.

The actual size of the community affects the order parameter only in an indirect way. What seems to be more important is the higher mean degree of nodes in the larger communities. In **Figure 4D**, it can be seen that there is a strong correlation between the number of nodes and the mean node degree of each community. In other words, since the nodes in large communities have more neighbors than the nodes in small communities, it is easier for them to synchronize. Note that this does not imply causality between node degree and level of synchronization. To corroborate this, more general investigations, e.g., on randomized versions of the network would be insightful. For our purpose however, it suffices to know that different community sizes influence the level of synchronization significantly.

3. COUPLING BY BIOLOGY

In order to investigate the synchronization of the *C. elegans* network even further, a third layer is added to the graph, representing the monoamine connections (wireless network). Furthermore, the assumptions about electrical and chemical synapses made in Hizanidis et al. [54] related to intra- and inter-connectivity are dropped, and the three-layer neuronal network is created using the actual connectivity data of the three synapse types (see Methods 5.1). In this section, we present two approaches to finding communities in this biological multilayer network.

3.1. Communities Based on Topology

The communities are first evaluated using a Multilayer-Louvain community detection algorithm (see Methods 5.4), which yields 8 communities instead of 6 as in the aggregated case discussed in the previous section (cf. **Figure 2**). **Figure 5** gives an overview of the partition at hand. The adjacency matrices (**Figures 5A–C**) highlight clear differences between the edge types: while the

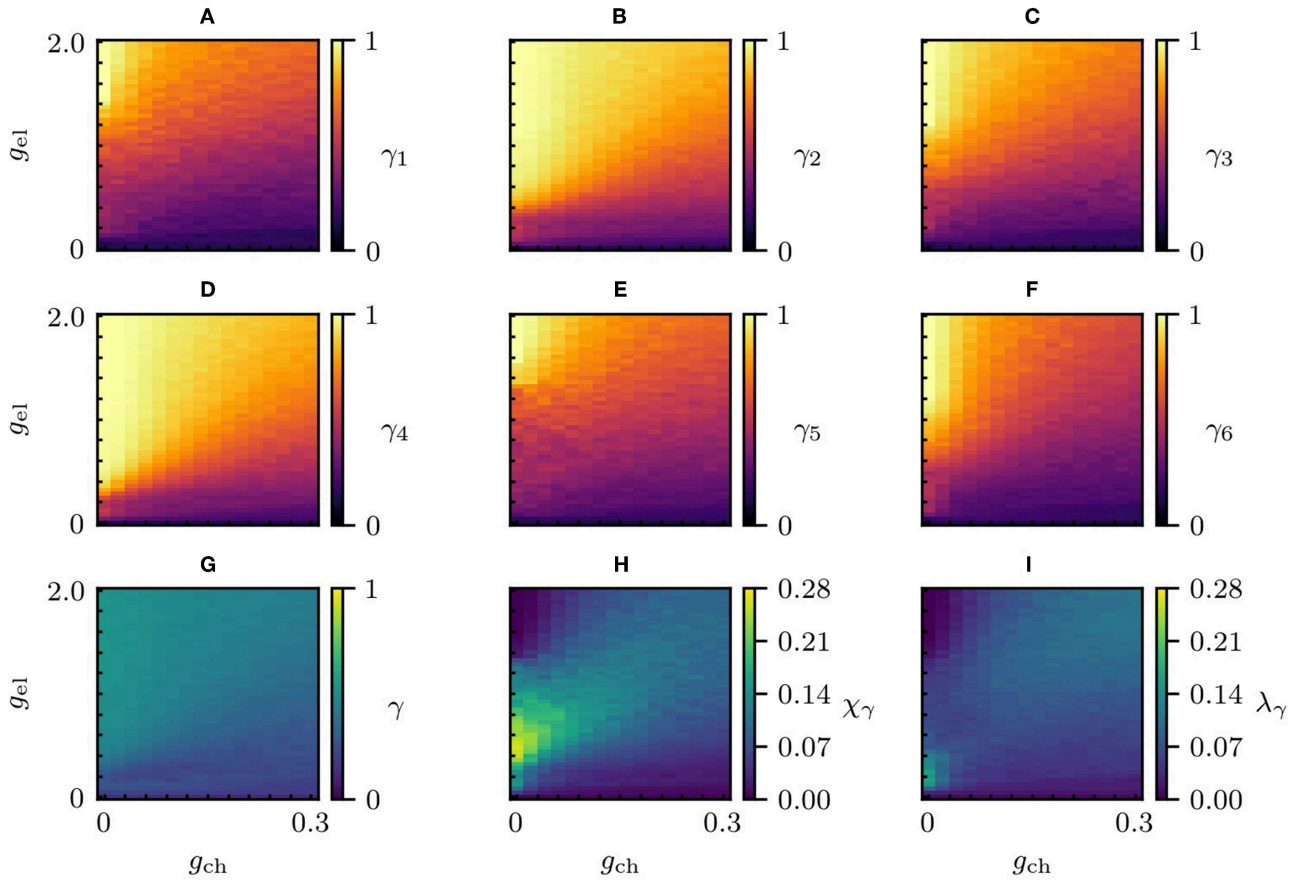

FIGURE 3 | Synchronization parameter scans of the designed network. Changes in the community dynamical properties and global dynamical properties as the electric and chemical coupling strengths vary. **(A–F)** Level of synchronization of each community, γ_1 to γ_6. **(G)** The global level of synchronization γ of the whole network. **(H)** The chimera-like index χ_γ. **(I)** The metastability index λ_γ. System parameters: $a = 1$, $b = 3$, $c = 1$, $d = 5$, $s = 4$, $p_0 = -1.6$, $I_{ext} = 3.25$, $r = 0.005$, $V_{syn} = 2$ and $g_{wl} = 0$.

wireless network, presenting few intra-community links, is distributed almost randomly across the network, the chemical layer for instance strongly reflects the underlying community structure in the adjacency matrix. Since chemical connections make up most of the edges in the network, the algorithm optimized the community partition mainly based on the chemical layer. Comparing this partition to the one in **Figure 2**, one can observe that the clear separation between edge types into intra- and inter-community edges is not achieved when using the biological connectome without assumptions.

The unclear separation of edge types in the partition shows its effects when analyzing the dynamics of the system using the Hindmarsh-Rose equations (see Methods 5.2). **Figure 6** shows the parameter scans for the global level of synchronization γ, the chimera-like index χ_γ and the metastability index λ_γ for two different wireless coupling strengths. For the level of synchronization γ_1 to γ_8 within the individual communities (see **Figures S1, S2**). First of all, the global level of synchronization of the system is highly reduced when using the real connectome, which can be explained by the previously mentioned edge distribution. Since the electrical layer synchronized the nodes within communities in the designed partition, the inter-community coupling could easily be tuned using the chemical coupling strength. Therefore, a clear chimera-like region could be observed in the parameter scans in **Figure 3**. In the case of the real connectome, it is not possible to tune intra- and intercommunity coupling separately, since all edge types are distributed across and within communities.

Even though the parameters used to identify chimera-like states (γ, χ_γ, and λ_γ) are significantly lower than in the model by design, the timeseries of the neuron membrane potential p in **Figure 7** suggest that the system adopts three different synchronization patterns, depending on the dynamical coupling strengths g_{wl}, g_{el} and g_{ch}. The corresponding coupling strengths and synchronization parameters are noted in **Table 1**. **Figures 7A–C** show the evolution of p for $g_{wl} = 0.0$, and **Figures 7D–F** show p for $g_{wl} = 0.2$. One observes that for high electrical coupling strengths (**Figures 7A,D**), the system is synchronized, meaning that most of the nodes follow the same periods of bursting (green) and quiescent (blue) states. However,

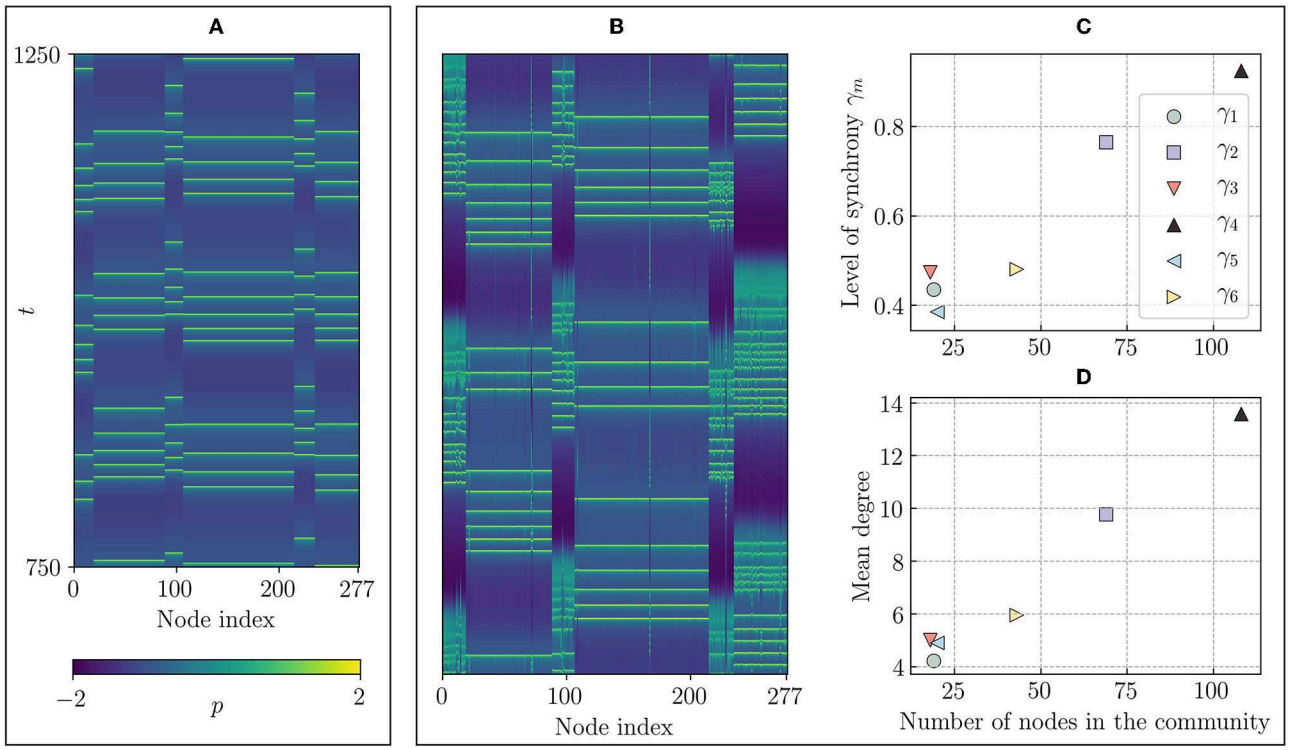

FIGURE 4 | Space-time plots of the designed network. **(A)** Time series of the p-variables for a state in which every community is internally synchronized. The nodes are ordered as in **Figure 2** with communities 1 to 6 from left to right. This state is achieved for $g_{el} = 1.76$, $g_{ch} = 0$. Keeping the chemical coupling at $g_{ch} = 0$ and decreasing the electrical coupling to $g_{el} = 0.4$ leads to the timeseries in panel **(B)**, with the same color code and time scales as before, where the large communities (2 and 4) are more synchronized than the smaller communities. We call this a chimera-like state. **(C)** Level of synchronization γ_m and **(D)** mean degree of each community ($m = 1, \ldots, 6$), vs. the size of the community, respectively, indicating a strong correlation between size and order. Parameters as in **Figure 3**.

one can see singular nodes that fall out of the synchronized pattern (especially in communities 1 to 3), which correspond to the nodes that are not electrically coupled. **Figures 7C,F** depict the system in the desynchronized regime, where one cannot distinguish any clear pattern of synchronization. The desynchronization becomes higher when the wireless coupling strength is increased. In **Figure 7B**, the system seems to exhibit chimera-like behavior at first glance. However, the chimera-like index for this coupling parameter set is very small (see **Table 1**). Even though community 3 seems less synchronized, one can read from the synchronization parameters (cf. **Figure S1**) that in fact all communities present very low synchronization. This behavior does not change significantly when adding wireless coupling (cf. **Figure 7E**).

Using the Multilayer-Louvain community detection approach to partition the network, one observes a system expressing different synchronization patterns depending on the interplay of the coupling strengths of the three layers. However, even though these patterns are visible in the evolution of the p-variable (**Figure 7**), the topological community partition cannot reflect these patterns in the parameter scans (**Figure 6**). Therefore, the question about the meaning of community detection can be raised. The following section proposes an alternative way of detecting communities in multilayer networks, which is not based on the topology or link distribution, but on the correlation of nodes with respect to their dynamic variable p.

3.2. Communities Based on Dynamics

In the previous section it was shown that the Multilayer-Louvain partition already leads to significant differences in the synchronization behavior of the distinct communities. Yet, as this barely becomes apparent in the chimera-like index, we investigated an alternative approach of finding communities, based on dynamical correlations between the time series of the p-variable. The heuristic algorithm leading to the correlation-based partition is described in detail in Methods 5.5. It is worth mentioning that this algorithm only changes the partition of the network, it does not change the nodes' dynamics when compared to section 3.1, as the underlying graph itself remains untouched. However, the synchronization measures (i.e. γ_m, χ_γ, and λ_γ, see Methods 5.3) do intrinsically depend on the particular partition.

Figure 8 shows that the correlation-based partition strongly differs from the partition found with the Multilayer-Louvain algorithm. The most striking difference is the stronger heterogeneity among inter-community links in the correlation-based partition. The outgoing and incoming links between communities are relatively evenly distributed in the topology-based Multilayer-Louvain partition. In the correlation-based

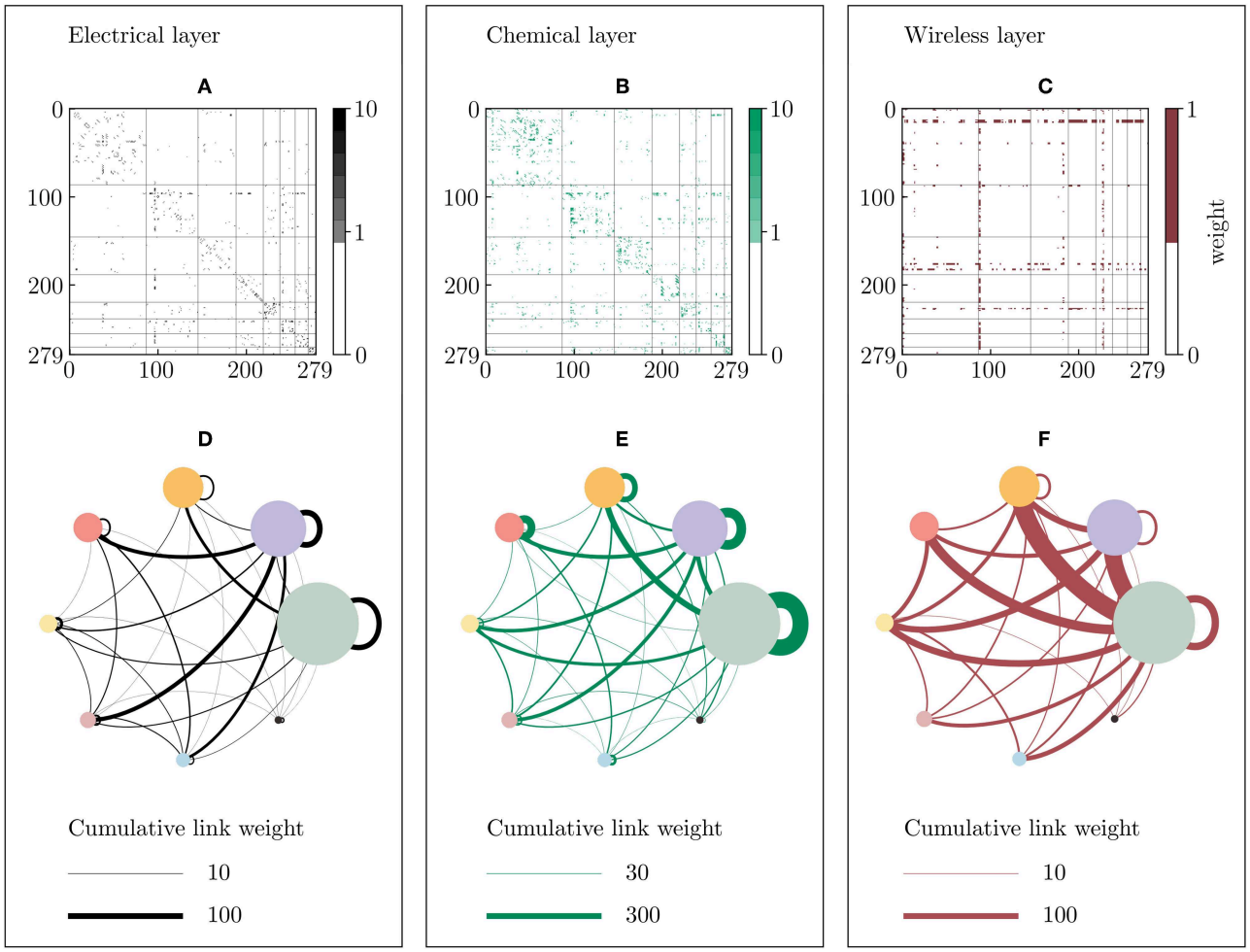

FIGURE 5 | Communities of the Multilayer-Louvain *C. elegans* network. The network is divided into 8 communities of different size using the Multilayer implementation of the Louvain algorithm (see Methods 5.4). **(A–C)** Weighted adjacency matrices of the electrical (black), chemical (green) and wireless (red) networks, where the axes represent the node indices. The vertical and horizontal lines divides the matrix in the counter-clockwise ordered communities, from left to right in the horizontal axis, and from up to down in the vertical axis, respectively. Note that the maximum depicted weight is set to 10 in both the electrical and chemical layers for visualization reasons, even though few higher weights exist. **(D–F)** Inter- and intra-community coupling of the three layers, where colored circles represent communities [1: gray (87 neurons), 2: violet (59 neurons), 3: orange (43 neurons), 4: red (31 neurons), 5: yellow (19 neurons), 6: pink (17 neurons), 7: blue (15 neurons), 8: black (8 neurons)], and lines represent the cumulative link weight between two or within one community (self-loops).

partition however, the two largest communities (3 and 6) are much stronger connected than the rest of the network. Furthermore, it can be seen that the two smallest communities (5 and 8) present no electrical connection to any other community in the network. In general, the electrical sub-network shows only very few inter-community links compared to the strong intra-community coupling (self-loops) of the two largest communities (3 and 6).

Regarding the dynamical properties, the dynamical correlation-based partition leads to qualitatively similar results as the Multilayer-Louvain partition. Compare **Figures 6** and **9**. In particular, **Figure 9B** clearly shows that the highest values of the chimera-like index χ_γ are still obtained for high electrical couplings and small chemical couplings. Increasing the wireless coupling as in **Figure 9E** reduces the value of χ_γ, similar to what has been observed previously in the dynamical analysis of the Multilayer-Louvain partition. However, the value of the highest chimera-like index ($\chi_\gamma \approx 0.14$, obtained at $g_{\text{el}} = 1.96$ and $g_{\text{ch}} = 0.04$) is significantly higher for the correlation-based partition. Moreover, it is also higher than the corresponding metastability index ($\lambda_\gamma \approx 0.07$). Therefore, we may indeed call the state "chimera-like" [38, 54, 75–78].

The reason for the high chimera-like index can be observed in the space time plots of the p-variables in **Figure 10**. As was mentioned before, the dynamics of single oscillators do not depend on the partition. In order to compare the results from the correlation-based partition with the Multilayer-Louvain partition, we decided to show the time series of p using the same coupling constants as in **Figure 7**. The different ordering of the nodes, though, leads to a significantly higher homogeneity

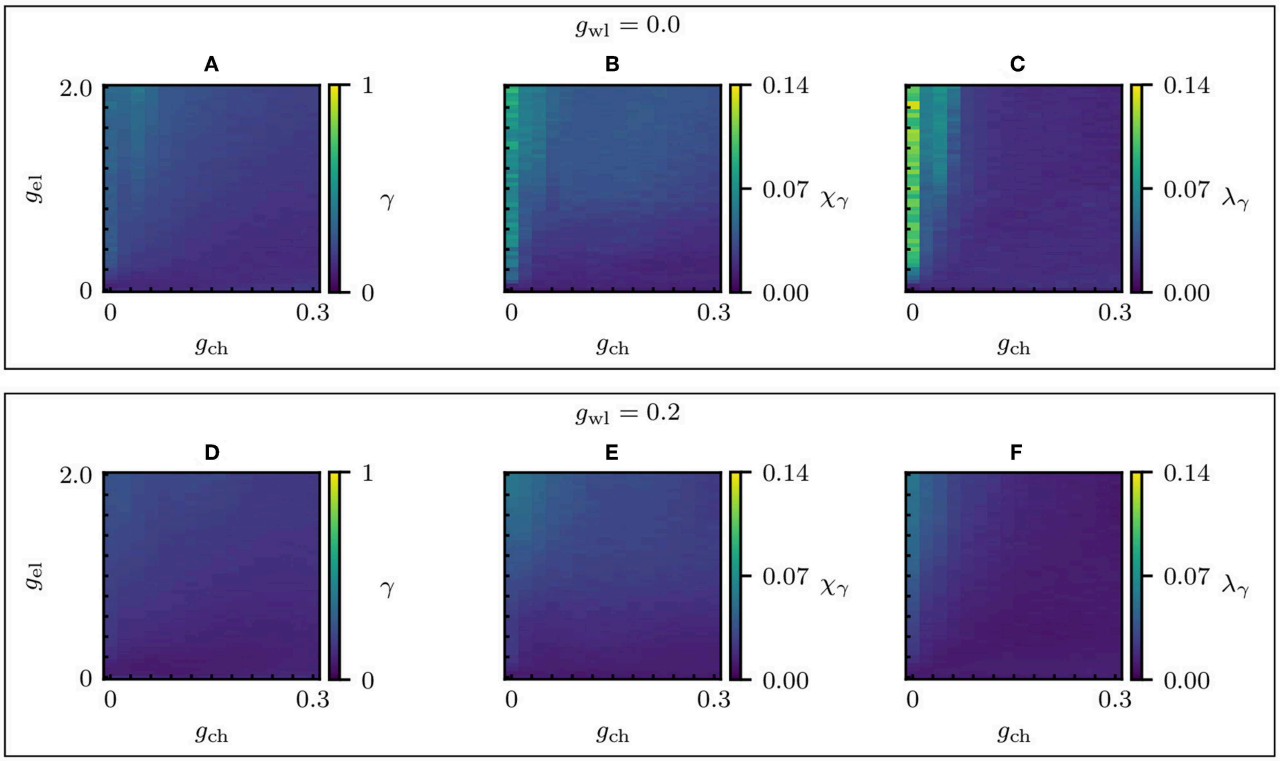

FIGURE 6 | Synchronization parameter scans of the Multilayer-Louvain network. Changes in the global dynamical properties as the electric and chemical coupling strengths vary. **(A–C)** Absence of wireless coupling ($g_{wl} = 0$) for different electrical and chemical couplings: the global level of synchronization of the whole network γ, the chimera-like index χ_γ and the metastability index λ_γ. **(D–F)** γ, χ_γ, and λ_γ for $g_{wl} = 0.2$. The system parameters are the same as in **Figure 3**, except for g_{wl}.

between nodes within one community, which is especially apparent for the largest communities (3 and 6) in **Figures 10A,D**. As a consequence, the respective levels of synchronization ($\gamma_3 \approx 0.40$ and $\gamma_6 \approx 0.67$) are higher than for the other communities, which raises the chimera-like index. The reason for this high level of synchronization is the strong intra-community coupling of the two large communities in the electrical layer, since the electrical coupling strength is the very high in parameter set ($g_{el} = 1.80$).

For time series with small electrical coupling (see **Figures 10C,F**), the communities are not separated as clearly, particularly when wireless coupling is applied to the system, which can be observed in **Figure 10F**. Especially the largest community (3) is much less synchronized, which can be explained by a stronger influence of the chemical and wireless layers, where a high number of intra-community links exist. This demonstrates that the dynamical correlation-based algorithm seems to preferentially sort the network according to the electrical sub-network, as this layer seems to be most important for the overall synchronization of the network. The adjacency matrices in **Figures 8A–C** support this observation: Only the electrical layer shows a large number of intra-community links, whereas the other layers present no clear visible structure. This is again in contrast to the Multilayer-Louvain partition, where the chemical layer also shows a pronounced community structure (see **Figure 5B**).

TABLE 1 | Parameter sets used in **Figure 7**.

	g_{wl}	g_{el}	g_{ch}	γ	χ_γ	λ_γ
7 (A)	0.00	1.80	0.05	0.35	0.05	0.07
7 (B)	0.00	0.50	0.20	0.15	0.02	0.02
7 (C)	0.00	0.10	0.25	0.13	0.02	0.02
7 (D)	0.20	1.80	0.05	0.22	0.04	0.03
7 (E)	0.20	0.50	0.20	0.11	0.02	0.01
7 (F)	0.20	0.10	0.25	0.10	0.01	0.01

In the case of intermediate electrical, chemical coupling and no wireless coupling (see **Figure 10B**), the distinct communities can still be identified, yet the level of synchronization in the large communities does not suffice to reach a high chimera-like index. Adding wireless coupling as shown in **Figure 10E** does not lead to significant changes in the values.

For a full review of the different coupling strengths of to the system that lead to the time series in **Figure 10**, as well as the consequent values of the synchronization parameters γ, χ_γ, and λ_γ, please refer to **Table 2**.

4. DISCUSSION

Interesting synchronization patterns were found using different modeling approaches in the multilayer network of *C. elegans*.

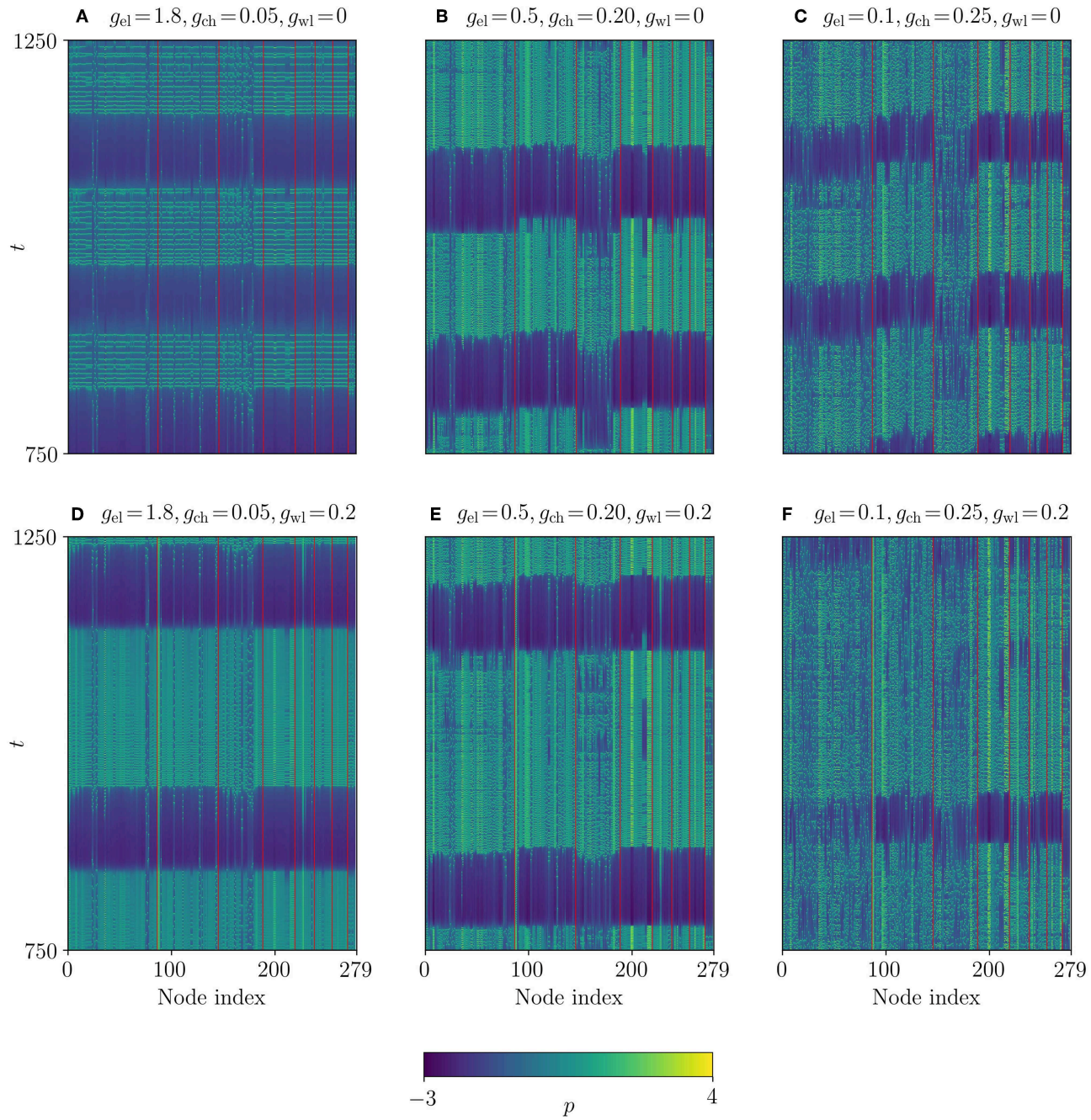

FIGURE 7 | Space-time plots of the Multilayer-Louvain network. The system parameters are the same as in **Figure 3**, except for g_{wl}. **(A–C)** Temporal evolution of the p-variable for different g_{el} and g_{ch} with $g_{wl} = 0$. **(D–F)** Similar plots for $g_{wl} = 0.2$. The values of all coupling strengths are summarized in **Table 1**. Red lines separate different communities.

They were quantified based on the pairwise Euclidean distance between the dynamical variables p, q and n of the underlying Hindmarsh-Rose system (see Methods 5.3).

Following the approach of Hizanidis et al. [54], we first assume purely electrical connections within the communities, and chemical synaptic intercommunity coupling (section 2). This results in a designed coupling scenario, where chimera-like states are clearly visible due to a strong separation of connection types. While the electrical sub-network synchronizes the communities within themselves, the chemical sub-network only allows for connections across communities.

Moving toward a more biologically-inspired modeling (section 3), these synchronization states are more difficult to observe. Since the edge types are not clearly separated

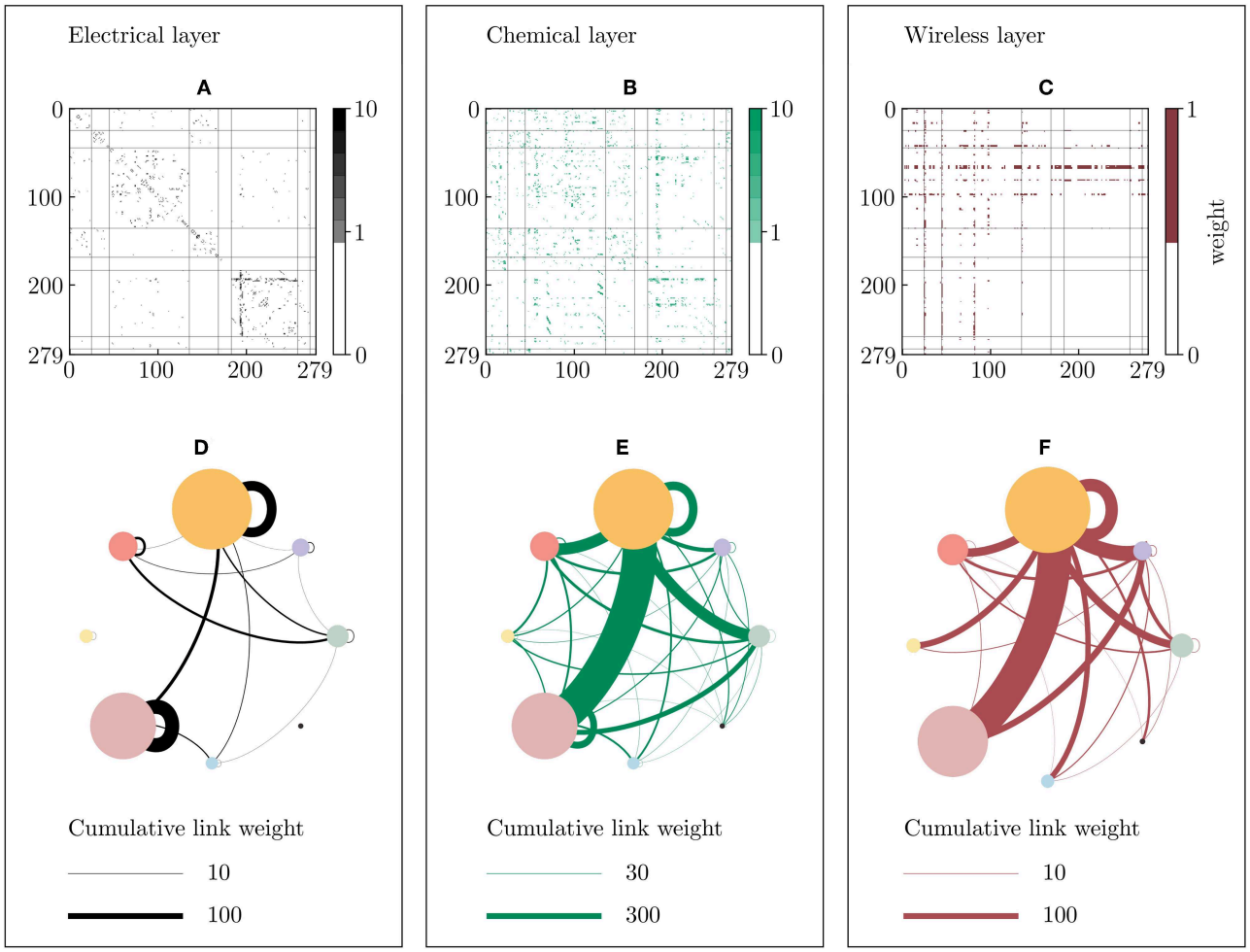

FIGURE 8 | Communities of the dynamical correlation-based *C. elegans* network. The network is divided into 8 communities of different size using the correlation matrices of the *p*-variable from the dynamical equations (see Methods 5.5). **(A–C)** Weighted adjacency matrices of the electrical (black), chemical (green) and wireless (red) sub-network, where the axes represent the nodes indices. The vertical and horizontal lines divides the matrix in the counter-clockwise ordered communities, from left to right in the horizontal axis, and from up to down in the vertical axis, respectively. Note that the maximum depicted weight is set to 10 in both the electrical and chemical layers for visualization reasons, even though few higher weights exist. **(D–F)** Inter- and intra-community coupling of the three layers, where colored circles represent communities [1: gray (25 neurons), 2: violet (20 neurons), 3: orange (91 neurons), 4: red (33 neurons), 5: yellow (15 neurons), 6: pink (75 neurons), 7: blue (14), 8: black (6 neurons)]. Electrical and chemical connections are shown as black and green lines, respectively. Wireless connections are colored in red. In this partition, edges are distributed more clearly than in the partition obtained from the Multilayer-Louvain approach in **Figure 5**.

anymore and it is therefore impossible to tune intra- and intercommunity coupling separately, the nodes within one community cannot synchronize as easily. This is especially the case when partitioning the network with the Multilayer-Louvain algorithm: the synchronization patterns are visible in the time series (see **Figure 7**), but the synchronization indices are very low (see **Figure 6**).

We also discussed an alternative way to identify correlated clusters in the network, namely to sort nodes in communities according to the Pearson correlation matrix of the *p*-variable (see Methods 5.5). In this case, the community structure is dominated by two large communities with a high amount of electrical self-loops (see **Figure 8**) that present a strong synchronization (see **Figure 10**). There are two small communities that share no electrical links to the rest of the network and therefore scarcely synchronize with nodes from the other communities. This promotes the emergence of chimera-like states. Further insights on the dynamical correlation-based partition can be obtained by investigating the neuronal functions of the nodes. In **Table 3**, one can see that the highly synchronized communities (3 and 6) contain 75% of the motor neurons of the system. The synchronization of motor neurons under varied coupling strengths is in harmony with experimental findings, for example in rats [79].

In this context, a question could be raised regarding the multilayer nature of the studied network. Since the three layers do not share the same number of neurons (only 253 of the 279 neurons are connected by electrical gap junctions), a certain

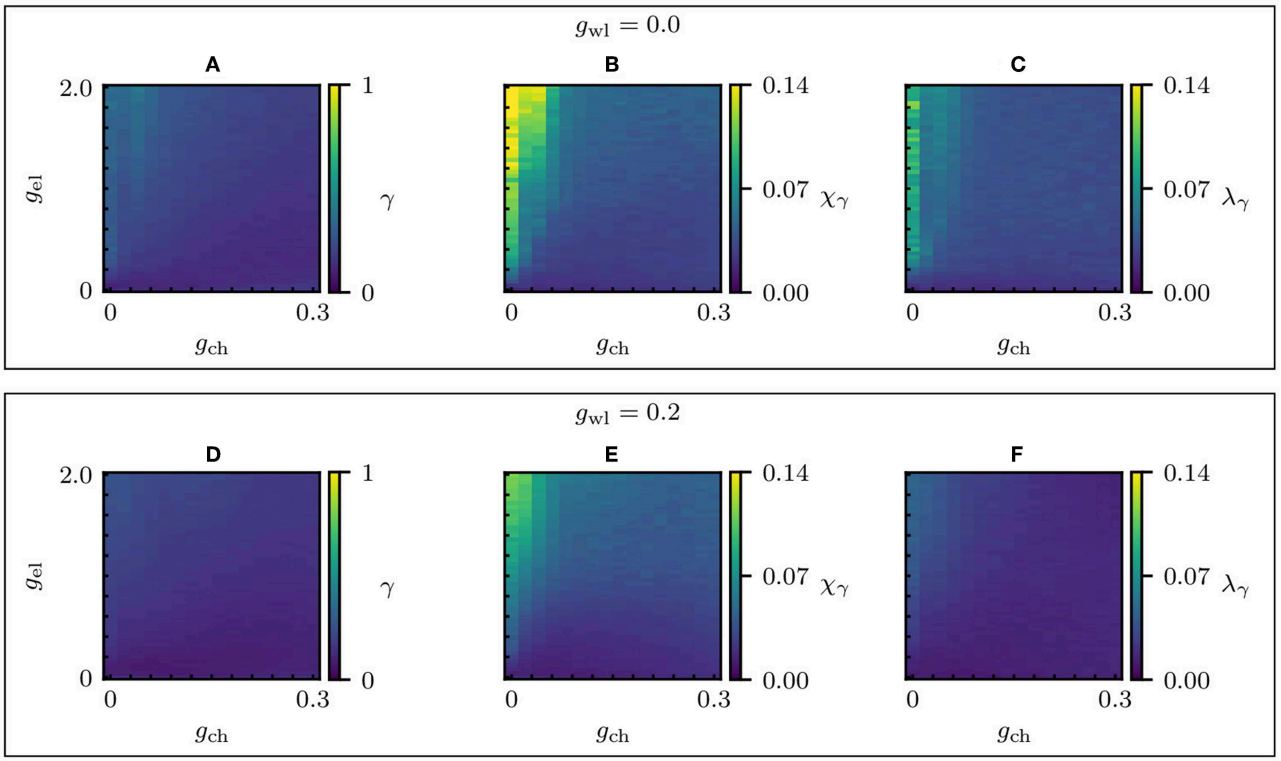

FIGURE 9 | Synchronization parameter scans of the dynamical correlation-based network. Changes in the global dynamical properties as the electric and chemical coupling strengths vary. **(A–C)** Absence of wireless coupling ($g_{wl} = 0$) for different electrical and chemical couplings: the global level of synchronization of the whole network γ, the chimera-like index χ_γ and the metastability index λ_γ. **(D–F)** γ, χ_γ, and λ_γ for $g_{wl} = 0.2$. The system parameters are the same as in **Figure 3**, except for g_{wl}. Refer to **Figures S3, S4** for the parameter scans including γ_l.

group of nodes are prone to remain desynchronized for certain combinations of g_{el}, g_{ch} and g_{wl}. However, the strong biological interplay between synapse types is crucial to the understanding of the neuronal network as an entity [80, 81]. Therefore, the connectome should be modeled as a multilayer network.

Keep in mind that the studied three-layer network contains information only about the electrical, chemical and monoamine connections. Another layer could be added for the neuropeptide wireless network, which was not included since many neuropeptide receptors, as well as ligands for many neuropeptide receptors are unknown. Also, the distance over which neuropeptide signaling can occur is uncharacterized for many of them.

Furthermore, concerning the synchronization metric based on Euclidean distances (see section 5.3), the threshold parameter which defines the limit between synchronized and desynchronized nodes has been set to $\delta = 0.01$ as in reference [73]. This value could be adapted to better suit the system and the three-dimensional distances.

This work presents an approach for analyzing the complex biological network of *C. elegans* using metrics of synchronization based on Euclidean distances and a new method of finding clustered nodes by correlating their dynamical variables. The underlying framework can be extended for multiple complex network applications.

5. METHODS

5.1. Datasets

The gap junction and chemical synapse networks of a hermaphrodite *C. elegans* have been obtained in [66], and are available through WormAtlas [82]. The associated adjacency matrices are computed for the electrical and chemical layers, where we omitted the neuromuscular junctions since we are only interested in neuronal interaction. Note that this dataset does not include the 20 pharyngeal neurons. Hence, we work with the somatic giant component of the neuronal network.

The electrical sub-network consists of 253 neurons and 890 synapses or gap junctions from 517 unique neuron pairs (including 3 self-connections). A total of 352 out of 517 neuron pairs have only one synapse between them, while the other 165 pairs show multiple parallel connections, with a maximum value of 23. This means that the respective symmetric (undirected) adjacency matrix has weights varying from 1 to 23 for connected neurons.

The chemical sub-network contains 253 source and 268 target neurons, the union of both sets is composed of 279 neurons, which is the total number of nodes of the modeled *C. elegans* network. There are 6,294 synapses from 2,575 unique source-target neuron pairs. A total of 1,362 out of the 2,575 neuron pairs have only one synapse, while the other 1,211 pairs have multiple

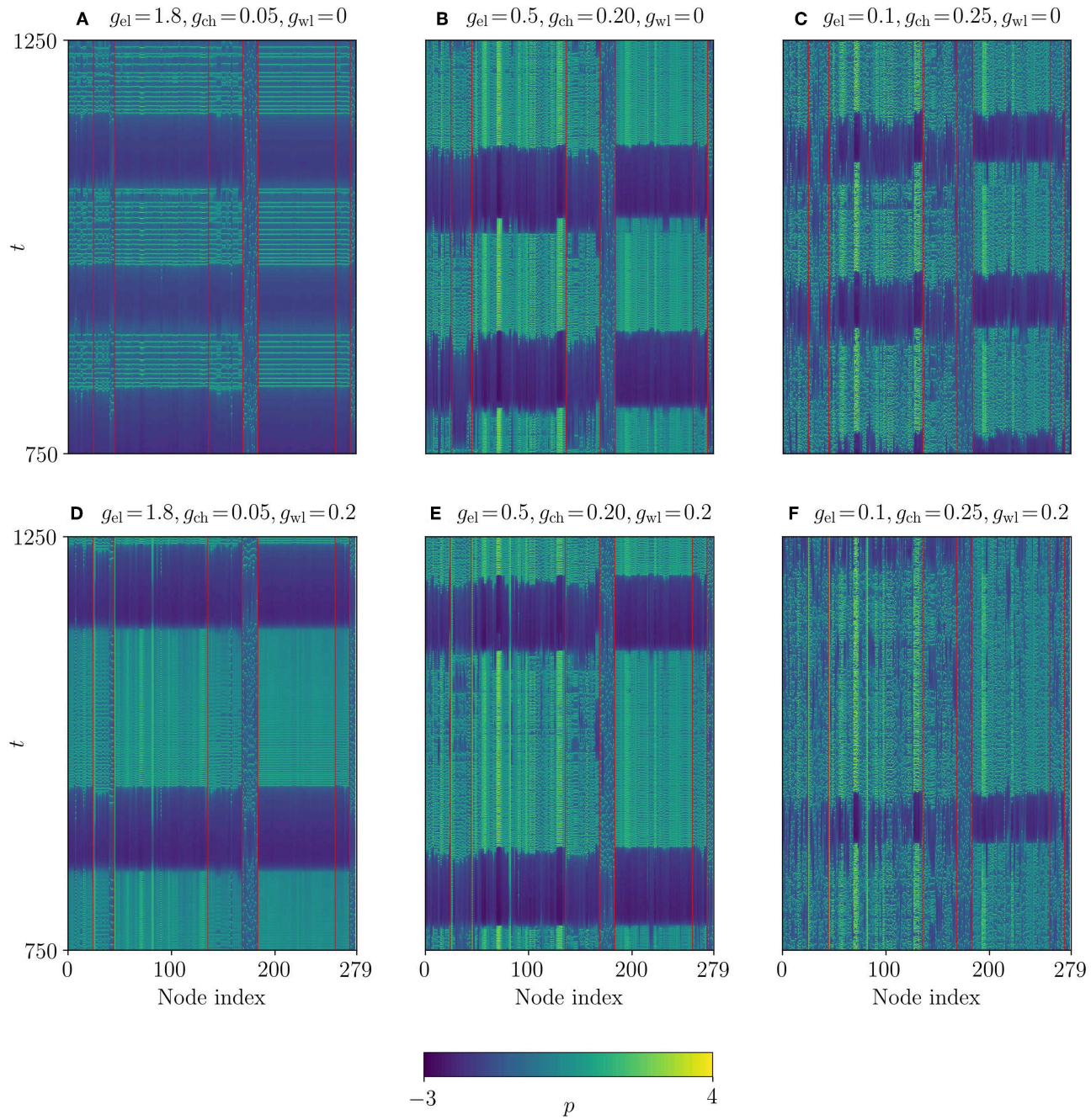

FIGURE 10 | Space-time plots of the dynamical correlation-based network. The system parameters are the same as in **Figure 3**, except for g_{wl}. **(A–C)**. Temporal evolution of the p-variable for different g_{el} and g_{ch} with $g_{wl} = 0$. **(D–F)** Similar plots for $g_{wl} = 0.2$. The values of all coupling strengths are summarized in **Table 2**. Red lines separate different communities. The time series are identical to **Figure 7**, but for a different ordering of nodes.

synaptic connections with a maximum value of 37. Therefore, the associated asymmetric (directed) adjacency matrix has weights varying from 1 to 37 for connected neurons.

The wireless sub-network of this study is restricted to the monoamine network in Bentley et al. [69] and is available in Bentley et al. [83]. Again, the pharyngeal neurons are excluded. This network by itself can be thought of as a directed quadripartite network composed of a source neuron, a neurotransmitter, a receptor and a target neuron. The considered wireless network is composed of 16 source neurons, 4 monoamine neurotransmitters, 16 associated protein receptors and 215 target neurons. As a first approach to the implementation of the wireless connectivity within our dynamical model, we are only interested in an effective connectivity between a source and

TABLE 2 | Parameter sets used in **Figure 10**.

	g_{wl}	g_{el}	g_{ch}	γ	χ_γ	λ_γ
10 (A)	0.00	1.80	0.05	0.35	0.11	0.06
10 (B)	0.00	0.50	0.20	0.15	0.03	0.03
10 (C)	0.00	0.10	0.25	0.13	0.03	0.02
10 (D)	0.20	1.80	0.05	0.22	0.07	0.03
10 (E)	0.20	0.50	0.20	0.11	0.02	0.01
10 (F)	0.20	0.10	0.25	0.10	0.02	0.02

TABLE 3 | Neuron functions of nodes in the dynamical correlation-based partition.

Function \ Community	1	2	3	4	5	6	7	8	All
Interneuron	10	7	32	11	5	16	8	0	89
Motor	7	2	32	7	3	49	6	2	108
Sensory	8	11	27	15	7	10	0	4	82
All	25	20	91	33	15	75	14	6	279

a target neuron. For this purpose, we reduce the quadripartite nature by assigning binary weights to the adjacency matrix: 1, if there is any path between the neurons and 0, if there is no possible connection from a source to a target neuron through any neurotransmitter and matching receptor. The final directed adjacency matrix includes 2,282 edges.

The functional classification of the neurons in three categories (sensory, motor and interneurons) has also been obtained from [66] and manually created based on the dataset in WormAtlas [84]. We excluded the male data, since we only consider the hermaphrodite information. If the description of a particular neuron includes both interneuron and motor characteristics, we choose to describe it as motor neuron, as well as we define amphid neurons to be sensory, following the approach in Varshney et al. [66].

For details relevant to our study on the individual neurons and their characteristics, please refer to the **Table S1**.

5.2. Hindmarsh-Rose Dynamics

We consider a network of neurons locally characterized by Hindmarsh-Rose dynamics [85], a model intended to describe the transition between the stable resting state and the stable limit cycle of neurons. The model was intended for two types of coupling (electrical and chemical), we propose extending it by a third coupling term to account for the wireless connections in the studied network, as described by the following equations:

$$\begin{aligned}
\dot{p}_i &= q_i - a p_i^3 + b p_i^2 - n_i + I_{\text{ext}} + g_{\text{el}} \sum_{j=1}^{N} L_{ij} H(p_j) \\
&\quad - g_{\text{ch}}(p_i - V_{\text{syn}}) \sum_{j=1}^{N} A_{ij}^{\text{ch}} S(p_j), -g_{\text{wl}}(p_i - V_{\text{syn}}) \sum_{j=1}^{N} A_{ij}^{\text{wl}} \tilde{S}(p_j), \\
\dot{q}_i &= c - d p_i^2 - q_i, \\
\dot{n}_i &= r[s(p_i - p_0) - n_i],
\end{aligned} \tag{1}$$

where $i = 1, \ldots, N$ is the neuron index, p_i is the membrane potential of the i-th neuron, q_i is associated with the fast current, either Na^+ or K^+, and n_i with the slow current, for example Ca^{2+}. The parameters of Equation (1) are chosen such that $a = 1$, $b = 3$, $c = 1$, $d = 5$, $s = 4$, $p_0 = -1.6$, and $I_{\text{ext}} = 3.25$, for which the system exhibits a multi-scale chaotic behavior characterized as spike bursting [86]. The parameter r modulates the slow dynamics of the system and is set to 0.005 so that each neuron lies in the chaotic regime in the absence of coupling [54]. For these parameters, the Hindmarsh-Rose model enables the spike-bursting behavior of the membrane potential observed in experiments made with single neurons *in vitro*. We choose random initial conditions in the time series shown and find that changing the initial conditions does not change the long-term synchronization behavior. In our time series analysis, we always remove the transients and average over a long time period. The chaotic behavior of the Hindmarsh-Rose model has been studied in earlier publications with slightly different parameters, which led to the investigation of a plethora of chaotic phenomena using spike-counting techniques [87] and detailed bifurcation analysis [88].

The connectivity structure of the electrical synapses is described in terms of the Laplacian matrix $\mathbf{L}$, whose elements are defined as $L_{ij} = A_{ij}^{\text{el}} - \delta_{ij} k_i^{\text{el}}$, where k_i^{el} is the degree of node i in the electrical layer and $\delta_{ij} = 1$ if $i = j$, $\delta_{ij} = 0$ otherwise. $\mathbf{A}^{\text{el}}$ is the symmetric adjacency matrix whose elements are $A_{ij}^{\text{el}} \neq 0$ if there are electrical synapses connecting the neurons i and j, and $A_{ij}^{\text{el}} = 0$ otherwise. The strength of the electrical coupling is given by the parameter g_{el} and its functionality is governed by the linear function $H(p) = p$.

The connectivity structure of the chemical synapses is described by the adjacency matrix $\mathbf{A}^{\text{ch}}$, whose elements are $A_{ij}^{\text{ch}} \neq 0$ if there are chemical synapses between neurons i and j, and $A_{ij}^{\text{ch}} = 0$ otherwise. The nonlinear chemical coupling is described by the sigmoidal function $S(p) = \{1 + \exp[-\lambda_{\text{syn}}(p - \theta_{\text{syn}})]\}^{-1}$, which acts as a continuous mechanism for the activation and deactivation of the chemical synapses. The associated coupling strength is noted as g_{ch}. For the chosen set of parameters, $|p_i| < 2$ and thus $(p_i - V_{\text{syn}})$ is always negative. Therefore, the chemical coupling is excitatory if $V_{\text{syn}} = 2$. The other parameters are $\theta_{\text{syn}} = -0.25$ and $\lambda_{\text{syn}} = 10$, following references [89, 90].

The wireless connectivity structure is described by the adjacency matrix $\mathbf{A}^{\text{wl}}$. It is also considered nonlinear; however, much slower than the chemical synaptic coupling [69]. Intuitively, the exponential function $S(p)$ in the denominator can be decreased by replacing λ_{syn} with $\tilde{\lambda}_{\text{syn}} \ll \lambda_{\text{syn}}$. We chose $\tilde{\lambda}_{\text{syn}} = 1$, $V_{\text{syn}} = 2$ and $\theta_{\text{syn}} = -0.25$, as for the chemical coupling. Furthermore, the wireless coupling is considered as an additional disrupting signal to the synchronization of the network. It is therefore treated like excitatory chemical synapses.

5.3. Level of Synchronization

We adapt an approach based on Kemeth et al. [73] in order to compute a level of synchronization of the studied network. Instead of considering the local curvature, which is optimized for a ring network, we calculate the pairwise Euclidean distances

between the variables $\{\mathbf{x}_1, \mathbf{x}_2, \ldots, \mathbf{x}_N\}$ at every time step t, with $\mathbf{x}_i = (p_i, q_i, n_i)$. For all t, we obtain a set of all possible distances between a set of N nodes:

$$\hat{D}\mathbf{x}(t) := \{||\mathbf{x}_i(t) - \mathbf{x}_j(t)||\,, \forall\, i,j \in \{1,\ldots,N\}\}\,. \tag{2}$$

Two nodes i and j are now defined to be synchronized if $||\mathbf{x}_i(t) - \mathbf{x}_j(t)|| \leq \delta$ and desynchronized if $||\mathbf{x}_i(t) - \mathbf{x}_j(t)|| > \delta$, where $\delta = 0.01 \cdot D_{\max}$ is a threshold value. The value $D_{\max}$ is the maximum possible Euclidean distance between a pair of nodes:

$$D_{\max} = \sqrt{(\mathbf{x}_{\max} - \mathbf{x}_{\min})^2}, \tag{3}$$

where $\mathbf{x}_{\max} = (p_{\max}, q_{\max}, n_{\max})$ and $\mathbf{x}_{\min} = (p_{\min}, q_{\min}, n_{\min})$ are vectors containing the maximum and minimum values of the dynamical variables for all time steps t and nodes N. Therefore, two nodes are defined to be synchronized at time t if their Euclidean distance does not exceed 1% of the maximum possible distance, which is well defined for every space-time series.

Based on the set of Euclidean distances, we can measure the amount of spatially coherent nodes at each time step t. For this purpose, we consider a different set of distances, containing only those that are smaller than the threshold value δ:

$$\hat{D}_\delta\mathbf{x}(t) := \{||\mathbf{x}_i(t) - \mathbf{x}_j(t)|| < \delta\,, \forall\, i,j \in \{1,\ldots,N\}\}\,. \tag{4}$$

The fraction between the number of distances within the range of the threshold value and the possible number of distances then results in the amount of synchronized node pairs. Note that the number of node pairs grows at a rate of N^2. It is therefore necessary to take the square root of this value, in order to make it comparable across network sizes. We call the resulting value "level of synchronization:"

$$\gamma(t) := \sqrt{\frac{|\hat{D}_\delta\mathbf{x}(t)|}{|\hat{D}\mathbf{x}(t)|}}\,. \tag{5}$$

If $\gamma(t)$ is only computed for a certain community m, it is called $\gamma_m(t)$, representing the level of synchronization of community m at time t. For a network consisting of M communities, it is now possible to compute the chimera-like index:

$$\sigma_\gamma(t) := \frac{1}{M-1}\sum_{m=1}^{M}\left(\gamma_m(t) - \langle\gamma_m(t)\rangle_M\right)^2 \tag{6}$$

at time t as proposed in Shanahan [91] and also used in Hizanidis et al. [54], where $\langle\gamma_m(t)\rangle_M$ denotes the average level of synchronization at time t over all communities m. Thus, the only difference to Shanahan [91] is the application of the Euclidean-distance-based level of synchronization $\gamma(t)$ instead of the Kuramoto order parameter. The temporal mean then defines the time-averaged chimera-like index of the network:

$$\tilde{\chi}_\gamma := \langle\sigma_\gamma(t)\rangle_T\,. \tag{7}$$

Similarly we can compute the metastability index:

$$\sigma_{\mathrm{met},\gamma}(m) := \frac{1}{T-1}\sum_{t=1}^{T}\left(\gamma_m(t) - \langle\gamma_m(t)\rangle_T\right)^2 \tag{8}$$

of community m, where $\langle\gamma_m(t)\rangle_T$ denotes the temporal mean of $\gamma_m(t)$ over all time steps. The average over all communities yields the metastability index of the whole network:

$$\tilde{\lambda}_\gamma = \langle\sigma_{\mathrm{met},\gamma}(m)\rangle_M\,. \tag{9}$$

The subscript γ is utilized to emphasize that these parameters differ from the parameters in Shanahan [91] and Hizanidis et al. [54] in the way the underlying level of synchronization is computed.

In order to compare community partitions with different numbers of communities, it is important to know that the ranges of χ_γ and λ_γ depend on the number of communities M of the studied network. The chimera-like index of a chimera state, where half of the communities is completely synchronized and the other half is desynchronized, becomes:

$$\tilde{\chi}_{\gamma,\max} = \frac{M}{4(M-1)}, \tag{10}$$

since the deviation from the mean is 0.5 for every community. The same considerations lead to a maximum metastability index of:

$$\tilde{\lambda}_{\gamma,\max} = \frac{T}{4(T-1)}, \tag{11}$$

which is approximately 0.25, since the total number of time steps T is large. Hence, we obtain the chimera-like and metastability indices normalized to unity:

$$\chi_\gamma = \frac{\tilde{\chi}_\gamma}{\tilde{\chi}_{\gamma,\max}} \tag{12}$$

and,

$$\lambda_\gamma = \frac{\tilde{\lambda}_\gamma}{\tilde{\lambda}_{\gamma,\max}}. \tag{13}$$

5.4. Multilayer-Louvain Community Detection

The communities discussed in section 3 are computed based on a multiplex Louvain community algorithm [92]. In single-layered graphs, the key to finding communities usually lies in optimizing the modularity function Q [93]:

$$Q = \frac{1}{2m_l}\sum_{i,j=1}^{N}\left[A_{ij} - \frac{k_i k_j}{2m_l}\right]\delta\left(g_i, g_j\right), \tag{14}$$

where A_{ij} is the graph's $N\times N$ adjacency matrix, $m_l = \frac{1}{2}\sum_{i,j=1}^{N} A_{ij}$ is the total link weight in the network, and $k_i = \sum_{j=1}^{N} A_{ij}$ is the weight incident to node i. The weight of a link between i and

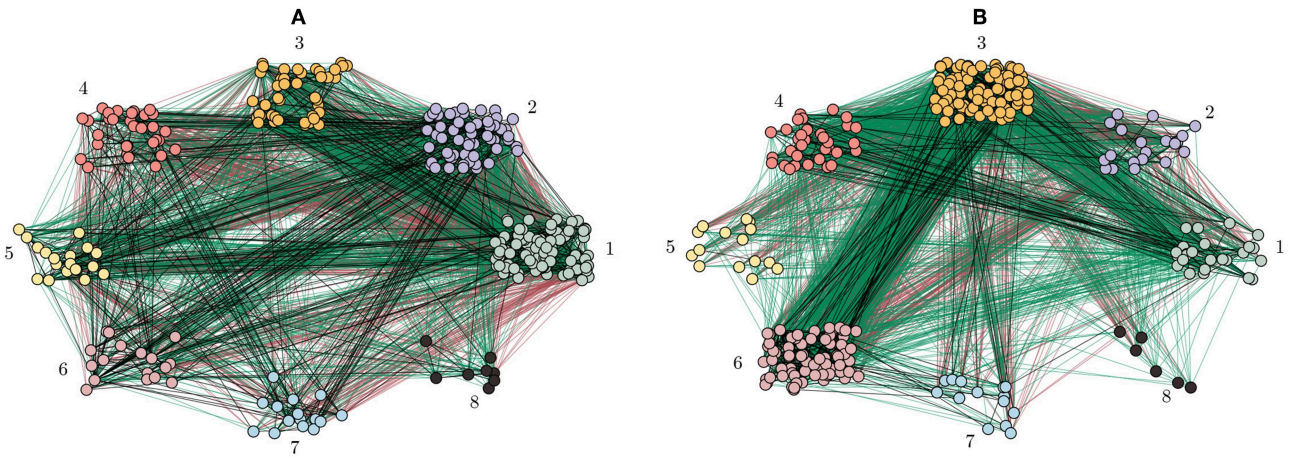

FIGURE 11 | Community partitions of the biological *C. elegans* network. **(A)** The network is divided into 8 communities of different size using the Multilayer-Louvain algorithm (see Methods 5.4). Neurons are colored according to their community as in **Figure 5**. **(B)** The same network is partitioned using the correlation matrix approach (see Methods 5.5). Refer to **Figure 8** for community sizes.

j corresponds to the number of connections between these two nodes (see Methods 5.1). $\delta\left(g_i, g_j\right) = 1$ if nodes i and j are in the same community, and $\delta\left(g_i, g_j\right) = 0$ otherwise. Therefore, the term $A_{ij} - \frac{k_i k_j}{2m_l}$ quantifies how strongly the two nodes will be coupled in the studied network, compared to how strongly they would be coupled in a random network. In the algorithm, the function Q is computed for every pair of nodes iteratively until it reaches a maximum value.

For multilayer networks, the modularity as defined in Equation (14) is not well suited as it does not differentiate if nodes are connected by different layers. In order to extend the modularity to multilayer applications, consider a network with S layers. We define the degree of node j within the same layer as $k_j^{(\sigma)} = \sum_{i=1}^{N} A_{ij}^{(\sigma)}, \sigma = 1, \ldots, S$ with $A_{ij}^{(\sigma)}$ denoting the adjacency matrix in layer σ. The generalized modularity function $Q_{\text{multilayer}}$ for a multilayer network with S layers is defined as [92]:

$$Q_{\text{multilayer}} = \frac{1}{2\mu} \sum_{i,j=1}^{N} \sum_{\sigma=1}^{S} \left[\left(A_{ij}^{(\sigma)} - \frac{k_i^{(\sigma)} k_j^{(\sigma)}}{2m_{l,\sigma}} \right) \delta\left(g_i^{(\sigma)}, g_j^{(\sigma)}\right) \right], \tag{15}$$

where $m_{l,\sigma} = \frac{1}{2} \sum_{j=1}^{N} k_j^{(\sigma)}$ is the total link weight within layer σ, and $\mu = \sum_{\sigma=1}^{S} m_{l,\sigma}$ is used for normalization similar to m_l in Equation (14). Note that in the case of the considered *C. elegans* network, there are no inter-layer connections, since every connection type (electrical, chemical, and wireless) represents an independent sub-network. In this study, we consider 3 layers with $\sigma \in \{\text{el}, \text{ch}, \text{wl}\}$ that are shown by black, red and green link color in **Figures 11A,B** for the multilayer connectome and correlation-based matrix, respectively. However, Equation (15) can be extended to be used for the study of multiplex networks, in which inter-layer connections exist [92].

5.5. Dynamical Correlation Community Detection

We present a heuristic approach to finding meaningful communities based on the dynamics of the system. While previous approaches aimed to find a community structure based on the topology, we propose an algorithm which partitions the network based on the nodes' correlations of the p-variable.

Figure 12 shows a schematic description of the algorithm. In order to gain insight on the synchronization of the time series for each pair of nodes, we compute the Pearson-correlation matrix from the p-time series of all nodes

$$P_{ij} = \frac{\langle [p_i(t) - \langle p \rangle][p_j(t) - \langle p \rangle] \rangle}{\sqrt{\langle p_i(t)^2 \rangle - \langle p \rangle^2} \sqrt{\langle p_j(t)^2 \rangle - \langle p \rangle^2}}. \tag{16}$$

In the hereby created matrix, every entry represents the correlation value of two time series of the two respective nodes (cf. the matrix in **Figure 12**, top left corner).

In order to find a community partition in the correlation matrix, we employ the stochastic block model approach from the *graph_tool* framework [94]. Since this framework does not intrinsically support weights in the network, we created a graph with a discrete number of edges between two distinct nodes that depends on the link weight in the correlation matrix; higher link weight therefore corresponds to a larger number of edges.

For every parameter set (i.e. every combination of the three different coupling strengths g_{el}, g_{ch} and g_{wl}) we obtain one correlation matrix, on which we apply the *graph_tool* algorithm. Note that, for some parameter sets, the algorithm will not find a "reasonable" partition. In particular, some partitions may consist of very small communities with only very few nodes. This is problematic in terms of the level of synchronization γ_m, since one node in a small community m plays a bigger role in the synchronization of this community; this implies stronger fluctuations of γ_m. Therefore, very small communities

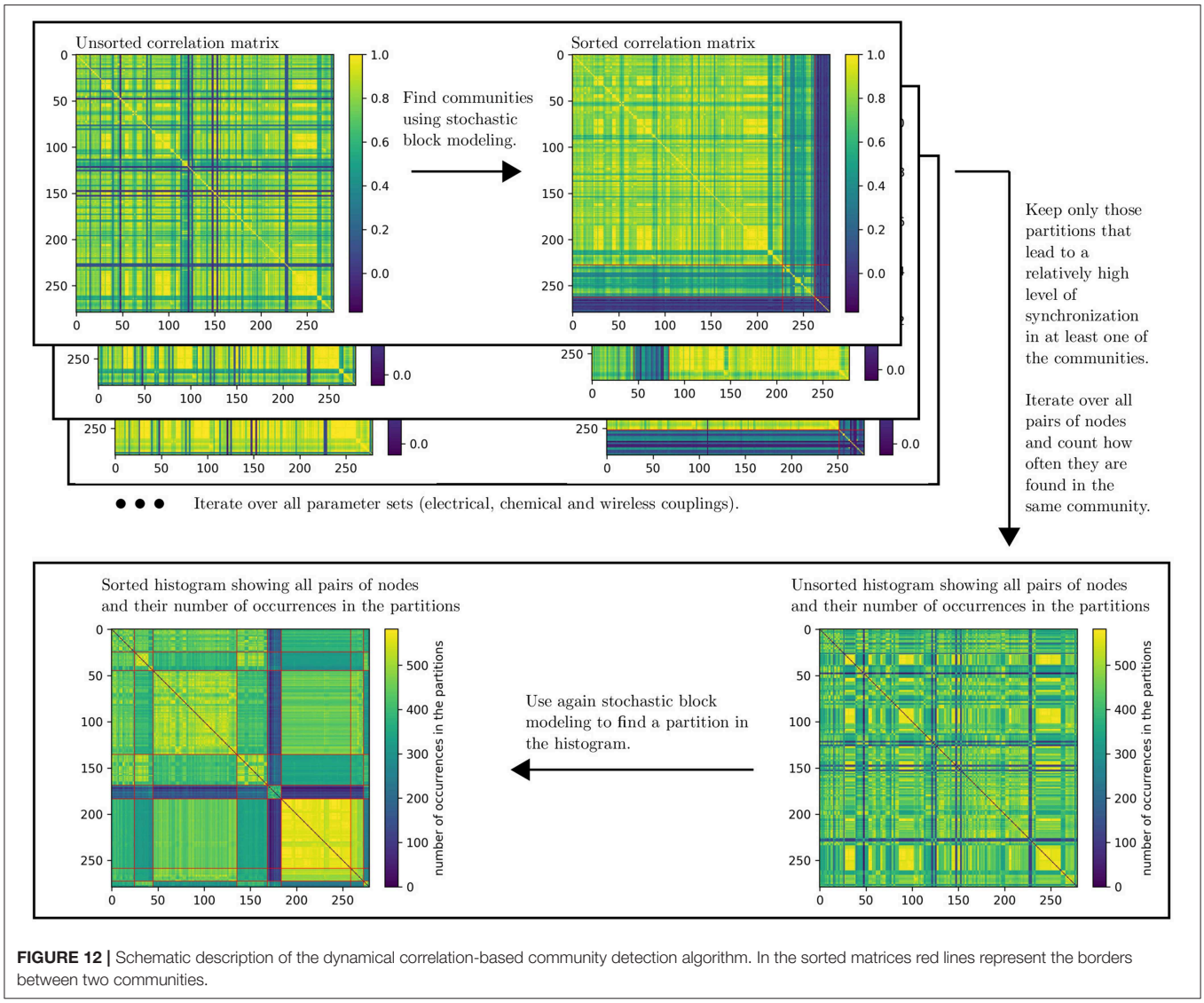

FIGURE 12 | Schematic description of the dynamical correlation-based community detection algorithm. In the sorted matrices red lines represent the borders between two communities.

(especially communities consisting of only two or three nodes) can have a significantly stronger influence on the chimera-like and the metastability index than large communities. This is why we only consider community partitions with at least six nodes per community.

Another constraint applied to the partitions is a lower boundary for the level of synchronization in at least one community. The constraint is needed, because nodes do not synchronize as easily in the system based on the connectivity data (see section 3). However, a highly synchronized community is crucial to finding chimera-like states. The threshold value used to filter out partitions containing low-synchronized communities was set to $\gamma_{\text{thr}} = 0.30$. This is a reasonable compromise between reaching a high level of synchronization in at least one community and still keeping a relatively high number of partitions.

The algorithm finds 582 partitions that satisfy the constraints out of an initial set of $50 \cdot 15 \cdot 7 = 5250$ possible partitions ($g_{\text{el}} \in [0.04, 0.08, ..., 2.00]$, $g_{\text{ch}} \in [0.02, 0.04, ..., 0.30]$ and $g_{\text{wl}} \in [0.00, 0.05, ..., 0.30]$). Subsequently, we iterate over all pairs of nodes (i, j) and count how often they are found in the same community for the 582 partitions. In other words, if a pair of nodes always finds itself in the same community, the counter will be 582, while a pair that is always found in distinct communities will receive a counter of 0. This then leads to a 2-dimensional histogram as can be seen in **Figure 12** in the bottom right corner.

As a final step, this histogram is sorted using the *graph_tool* algorithm in order to find a merged community partition that contains information over a large set of parameter values g_{el}, g_{ch}, and g_{wl}. The resulting sorted histogram is shown in **Figure 12** in the bottom left corner and the network is visualized in **Figure 11B**. There is one community consisting of nodes that almost always find themselves in the same community. This implies that the time series of the corresponding nodes have a high correlation value for almost every parameter

set. All the results from section 3.2 were created using this community partition.

Please note that the proposed algorithm is only *one* possible way of finding partitions based on a system's dynamical behavior. In fact, it invites to further explore the interplay between topology and dynamics.

AUTHOR CONTRIBUTIONS

AP, LM, and JR had the lead analyzing the network data and performing the numerical simulations. All authors designed the study, analyzed the results, and wrote the manuscript.

FUNDING

AP, LM, and PH acknowledge support by *Deutsche Forschungsgemeinschaft* (DFG) under grant no. HO4695/3-1 and within the framework of Collaborative Research Center 910. JR acknowledges support by the German Academic Exchange Service (DAAD) and the Chilean National Commission for Scientific and Technological Research (CONICYT). NK acknowledges financial support by the MOVE-IN Louvain fellowship, co-funded by the Marie Curie Actions of the European Commission. JH acknowledges financial support by the General Secretariat for Research and Technology (GSRT) and the Hellenic Foundation for Research and Innovation (HFRI) (Code: 203).

ACKNOWLEDGMENTS

The authors would like to thank P. Orlowski for technical support.

SUPPLEMENTARY MATERIAL

The Supplementary Material for this article can be found online at: https://www.frontiersin.org/articles/10.3389/fams.2019.00052/full#supplementary-material

REFERENCES

1. Ramirez JP, Olvera LA, Nijmeijer H, Alvarez J. The sympathy of two pendulum clocks: beyond Huygens' observations. *Sci Rep*. (2016) **6**:23580. doi: 10.1038/srep23580
2. Arenas A, Díaz-Guilera A, Kurths J, Moreno Y, Zhou C. Synchronization in complex networks. *Phys Rep*. (2008) **469**:93–153. doi: 10.1016/j.physrep.2008.09.002
3. Kapitaniak M, Czolczynski K, Perlikowski P, Stefanski A, Kapitaniak T. Synchronization of clocks. *Phys Rep*. (2012) **517**:1. doi: 10.1016/j.physrep.2012.03.002
4. Schöll E, Klapp SHL, Hövel P, editors. *Control of Self-organizing Nonlinear Systems*. Berlin: Springer (2016).
5. Boccaletti S, Pisarchik AN, del Genio CI, Amann A. *Synchronization: From Coupled Systems to Complex Networks*. Cambridge: Cambridge University Press (2018).
6. Bader R. *Nonlinearities and Synchronization in Musical Acoustics and Music Psychology*. Berlin; Heidelberg: Springer (2013).
7. Mukherjee S, Palit SK, Banerjee S, Ariffin MRK, Bhattacharya DK. Phase synchronization of instrumental music signals. *Eur Phys J Spec Top*. (2014) **223**:1561–77. doi: 10.1140/epjst/e2014-02145-7
8. Strogatz SH, Stewart I. Coupled oscillators and biological synchronization. *Sci Am*. (1993) **269**:102–9.
9. Eckhardt B, Ott E, Strogatz SH, Abrams DM, McRobie A. Modeling walker synchronization on the Millennium Bridge. *Phys Rev E*. (2007) **75**:021110. doi: 10.1103/PhysRevE.75.021110
10. Kuramoto Y, Battogtokh D. Coexistence of coherence and incoherence in nonlocally coupled phase oscillators. *Nonlin Phen in Complex Sys*. (2002) **5**:380–5. Available online at: http://www.jp.j-npcs.org/abstracts/vol2002/v5no4/v5no4p380.html
11. Abrams DM, Strogatz SH. Chimera states for coupled oscillators. *Phys Rev Lett*. (2004) **93**:174102. doi: 10.1103/PhysRevLett.93.174102
12. Montbrió E, Kurths J, Blasius B. Synchronization of two interacting populations of oscillators. *Phys Rev E*. (2004) **70**:056125. doi: 10.1103/PhysRevE.70.056125
13. Omel'chenko OE, Maistrenko Y, Tass P. Chimera states: the natural link between coherence and incoherence. *Phys Rev Lett*. (2008) **100**:044105. doi: 10.1103/PhysRevLett.100.044105
14. Abrams DM, Mirollo RE, Strogatz SH, Wiley DA. Solvable model for chimera states of coupled oscillators. *Phys Rev Lett*. (2008) **101**:084103. doi: 10.1103/PhysRevLett.101.084103
15. Pikovsky A, Rosenblum MG. Partially integrable dynamics of hierarchical populations of coupled oscillators. *Phys Rev Lett*. (2008) **101**:264103. doi: 10.1103/PhysRevLett.101.264103
16. Martens EA, Laing CR, Strogatz SH. Solvable model of spiral wave chimeras. *Phys Rev Lett*. (2010) **104**:044101. doi: 10.1103/PhysRevLett.104.044101
17. Martens EA. Bistable chimera attractors on a triangular network of oscillator populations. *Phys Rev E*. (2010) **82**:016216. doi: 10.1103/PhysRevE.82.016216
18. Martens EA. Chimeras in a network of three oscillator populations with varying network topology. *Chaos*. (2010) **20**:043122. doi: 10.1063/1.3499502
19. Omelchenko I, Maistrenko Y, Hövel P, Schöll E. Loss of coherence in dynamical networks: spatial chaos and chimera states. *Phys Rev Lett*. (2011) **106**:234102. doi: 10.1103/PhysRevLett.106.234102
20. Omelchenko I, Omel'chenko OE, Hövel P, Schöll E. When nonlocal coupling between oscillators becomes stronger: patched synchrony or multichimera states. *Phys Rev Lett*. (2013) **110**:224101. doi: 10.1103/PhysRevLett.110.224101
21. Hizanidis J, Kanas V, Bezerianos A, Bountis T. Chimera states in networks of nonlocally coupled Hindmarsh-Rose neuron models. *Int J Bifurcation Chaos*. (2014) **24**:1450030. doi: 10.1142/S0218127414500308
22. Martens EA, Bick C, Panaggio MJ. Chimera states in two populations with heterogeneous phase-lag. *Chaos*. (2016) **26**:094819. doi: 10.1063/1.4958930
23. Ghosh S, Zakharova A, Jalan S. Non-identical multiplexing promotes chimera states. *Chaos Solitons Fractals*. (2018) **106**:56–60. doi: 10.1016/j.chaos.2017.11.010
24. Calim A, Hövel P, Ozer M, Uzuntarla M. Chimera states in networks of Type-I morris-lecar neurons. *Phys Rev E*. (2018) **98**:062217. doi: 10.1103/PhysRevE.98.062217
25. Andrzejak RG, Ruzzene G, Malvestio I. Generalized synchronization between chimera states. *Chaos*. (2017) **27**:053114. doi: 10.1063/1.4983841
26. Saha S, Bairagi N, Dana SK. Chimera states in ecological network under weighted mean-field dispersal of species. *Front Appl Math Stat*. (2019) **5**:15. doi: 10.3389/fams.2019.00015
27. Tinsley MR, Nkomo S, Showalter K. Chimera and phase cluster states in populations of coupled chemical oscillators. *Nat Phys*. (2012) **8**:662–5. doi: 10.1038/nphys2371
28. Hagerstrom AM, Murphy TE, Roy R, Hövel P, Omelchenko I, Schöll E. Experimental observation of chimeras in coupled-map lattices. *Nat Phys*. (2012) **8**:658–61. doi: 10.1038/nphys2372
29. Martens EA, Thutupalli S, Fourriere A, Hallatschek O. Chimera states in mechanical oscillator networks. *Proc Natl Acad Sci USA*. (2013) **110**:10563. doi: 10.1073/pnas.1302880110

30. Gambuzza LV, Buscarino A, Chessari S, Fortuna L, Meucci R, Frasca M. Experimental investigation of chimera states with quiescent and synchronous domains in coupled electronic oscillators. *Phys Rev E*. (2014) **90**:032905. doi: 10.1103/PhysRevE.90.032905
31. Totz J, Rode J, Tinsley MR, Showalter K, Engel H. Spiral wave chimera states in large populations of coupled chemical oscillators. *Nat Phys*. (2018) **14**:282–5. doi: 10.1038/s41567-017-0005-8
32. Panaggio MJ, Abrams DM. Chimera states: coexistence of coherence and incoherence in networks of coupled oscillators. *Nonlinearity*. (2015) **28**:R67. doi: 10.1088/0951-7715/28/3/R67
33. Schöll E. Synchronization patterns and chimera states in complex networks: interplay of topology and dynamics. *Eur Phys J Spec Top*. (2016) **225**:891–919. doi: 10.1140/epjst/e2016-02646-3
34. Omel'chenko OE. The mathematics behind chimera states. *Nonlinearity*. (2018) **31**:R121. doi: 10.1088/1361-6544/aaaa07
35. Majhi S, Bera BK, Ghosh D, Perc M. Chimera states in neuronal networks: a review. *Phys Life Rev*. (2019) **26**:100. doi: 10.1016/j.plrev.2018.09.003
36. Schmidt L, Schönleber K, Krischer K, García-Morales V. Coexistence of synchrony and incoherence in oscillatory media under nonlinear global coupling. *Chaos*. (2014) **24**:013102. doi: 10.1063/1.4858996
37. Sethia GC, Sen A. Chimera states: the existence criteria revisited. *Phys Rev Lett*. (2014) **112**:144101. doi: 10.1103/PhysRevLett.112.144101
38. Yeldesbay A, Pikovsky A, Rosenblum M. Chimeralike states in an ensemble of globally coupled oscillators. *Phys Rev Lett*. (2014) **112**:144103. doi: 10.1103/PhysRevLett.112.144103
39. Böhm F, Zakharova A, Schöll E, Lüdge K. Amplitude-phase coupling drives chimera states in globally coupled laser networks. *Phys Rev E*. (2015) **91**:040901. doi: 10.1103/PhysRevE.92.069905
40. Mishra A, Hens C, Bose M, Roy PK, Dana SK. Chimeralike states in a network of oscillators under attractive and repulsive global coupling. *Phys Rev E*. (2015) **92**:062920. doi: 10.1103/PhysRevE.92.062920
41. Mishra A, Saha S, Hens C, Roy PK, Bose M, Louodop P, et al. Coherent libration to coherent rotational dynamics via chimeralike states and clustering in a Josephson junction array. *Phys Rev E*. (2017) **95**:010201. doi: 10.1103/PhysRevE.95.010201
42. Laing CR. Chimeras in networks with purely local coupling. *Phys Rev E*. (2015) **92**:050904. doi: 10.1103/PhysRevE.92.050904
43. Hizanidis J, Lazarides N, Tsironis GP. Robust chimera states in SQUID metamaterials with local interactions. *Phys Rev E*. (2016) **94**:032219. doi: 10.1103/PhysRevE.94.032219
44. Bera BK, Ghosh D. Chimera states in purely local delay-coupled oscillators. *Phys Rev E*. (2016) **93**:052223. doi: 10.1103/PhysRevE.93.052223
45. Clerc MG, Coulibaly S, Ferreira AM, Rojas R. Chimera states in a Duffing oscillators chain coupled to nearest neighbors. *Chaos*. (2018) **28**:083126. doi: 10.1063/1.5025038
46. Bera BK, Ghosh D, Lakshmanan M. Chimera states in bursting neurons. *Phys Rev E*. (2016) **93**:012205. doi: 10.1103/PhysRevE.93.012205
47. Belykh I, de Lange E, Hasler M. Synchronization of bursting neurons: what matters in the network topology. *Phys Rev Lett*. (2005) **94**:188101. doi: 10.1103/PhysRevLett.94.188101
48. Andrzejak RG, Rummel C, Mormann F, Schindler K. All together now: analogies between chimera state collapses and epileptic seizures. *Sci Rep*. (2016) **6**:23000. doi: 10.1038/srep23000
49. Laing CR, Chow CC. Stationary bumps in networks of spiking neurons. *Neural Comput*. (2001) **13**:1473–94. doi: 10.1162/089976601750264974
50. Sakaguchi H. Instability of synchronized motion in nonlocally coupled neural oscillators. *Phys Rev E*. (2006) **73**:031907. doi: 10.1103/PhysRevE.73.031907
51. Laing CR, Rajendran K, Kevrekidis YG. Chimeras in random non-complete networks of phase oscillators. *Chaos*. (2012) **22**:043104. doi: 10.1063/1.3694118
52. Zhu Y, Zheng Z, Yang J. Chimera states on complex networks. *Phys Rev E*. (2014) **89**:022914. doi: 10.1103/PhysRevE.89.022914
53. Omelchenko I, Provata A, Hizanidis J, Schöll E, Hövel P. Robustness of chimera states for coupled FitzHugh-Nagumo oscillators. *Phys Rev E*. (2015) **91**:022917. doi: 10.1103/PhysRevE.91.022917
54. Hizanidis J, Kouvaris NE, Zamora-López G, Díaz-Guilera A, Antonopoulos C. Chimera-like states in modular neural networks. *Sci Rep*. (2016) **6**:19845. doi: 10.1038/srep22314
55. Tsigkri-DeSmedt ND, Hizanidis J, Schöll E, Hövel P, Provata A. Chimeras in leaky integrate-and-fire neural networks: effects of reflecting connectivities. *Eur Phys J B*. (2017) **90**:139. doi: 10.1140/epjb/e2017-80162-0
56. De Domenico M, Solé-Ribalta A, Cozzo E, Kivelä M, Moreno Y, Porter MA, et al. Mathematical formulation of multilayer networks. *Phys Rev X*. (2013) **3**:041022. doi: 10.1103/PhysRevX.3.041022
57. Kivelä M, Arenas A, Barthélemy M, Gleeson JP, Moreno Y, Porter MA. Multilayer networks. *J Complex Networks*. (2014) **2**:203–71. doi: 10.1093/comnet/cnu016
58. Kouvaris NE, Hata S, Díaz-Guilera A. Pattern formation in multiplex networks. *Sci Rep*. (2015) **5**:10840. doi: 10.1038/srep10840
59. Sporns O. Structure and function of complex brain networks. *Dialogues Clin Neurosci*. (2013) **15**:247–62.
60. Ghosh S, Jalan S. Emergence of chimera in multiplex network. *Int J Bifurc Chaos*. (2016) **26**:1650120. doi: 10.1142/S0218127416501200
61. Majhi S, Perc M, Ghosh D. Chimera states in a multilayer network of coupled and uncoupled neurons. *Chaos*. (2017) **27**:073109. doi: 10.1063/1.4993836
62. Kasatkin DV, Nekorkin VI. Synchronization of chimera states in a multiplex system of phase oscillators with adaptive couplings. *Chaos*. (2018) **28**:1054. doi: 10.1063/1.5031681
63. Majhi S, Perc M, Ghosh D. Chimera states in uncoupled neurons induced by a multilayer structure. *Sci Rep*. (2016) **6**:39033. doi: 10.1038/srep39033
64. Yan G, Vértes PE, Towlson EK, Chew YL, Walker JD, Schafer WR, et al. Network control principles predict neuron function in the Caenorhabditis elegans connectome. *Nature*. (2017) **550**:519. doi: 10.1038/nature24056
65. White JG, Southgate E, Thomson JN. The Structure of the nervous system of the nematode Caenorhabditis legans. *Phil Trans R Soc B*. (1986) **314**:1–340.
66. Varshney LR, Chen BL, Paniagua E, Hall DH, Chklovskii DB. Structural properties of the Caenorhabditis elegans neuronal network. *PLOS Comput Biol*. (2011) **7**:e1001066. doi: 10.1371/journal.pcbi.1001066
67. Ardiel EL, Rankin CH. An elegant mind: Learning and memory in Caenorhabditis elegans. *Learn Memory*. (2010) **17**:191–201. doi: 10.1101/lm.960510
68. Chase DL, Koelle MR. *Biogenic Amine Neurotransmitters in C. elegans*. Wormbook (2007). p. 1–15. Available online at: http://www.wormbook.org/chapters/www_monoamines/monoamines.html
69. Bentley B, Branicky R, Barnes CL, Chew YL, Yemini E, Bullmore ET, et al. The multilayer connectome of caenorhabditis elegans. *PLOS Comput Biol*. (2016) **12**:1–31. doi: 10.1371/journal.pcbi.1005283
70. Agnati LF, Zoli M, Strömberg I, Fuxe K. Intercellular communication in the brain: wiring versus volume transmission. *Neuroscience*. (1995) **69**:711–26.
71. Zoli M, Torri C, Ferrari R, Jansson A, Zini I, Fuxe K, et al. The emergence of the volume transmission concept. *Brain Res Rev*. (1998) **26**:136–47.
72. Sykova E. Extrasynaptic volume transmission and diffusion parameters of the extracellular space. *Neuroscience*. (2004) **129**:861–76. doi: 10.1016/j.neuroscience.2004.06.077
73. Kemeth FP, Haugland SW, Schmidt L, Kevrekidis YG, Krischer K. A classification scheme for chimera states. *Chaos*. (2016) **26**:094815. doi: 10.1063/1.4959804
74. Pons P, Latapy M. Computing communities in large networks using random walks. In: *Computer and Information Sciences - ISCIS 2005*. Berlin; Heidelberg: Springer (2005). p. 284–93.
75. Nkomo S, Tinsley MR, Showalter K. Chimera and chimera-like states in populations of nonlocally coupled homogeneous and heterogeneous chemical oscillators. *Chaos*. (2016) **26**:094826. doi: 10.1063/1.4962631
76. Dutta PS, Banerjee T. Spatial coexistence of synchronized oscillation and death: a chimeralike state. *Phys Rev E*. (2015) **92**:042919. doi: 10.1103/PhysRevE.92.042919
77. Hizanidis J, Kouvaris NE, Antonopoulos C. Metastable and chimera-like states in the C. elegans brain network. *Cybernetics Phys*. (2015) **4**:17–20. Available online at: http://repository.essex.ac.uk/18338/
78. Santos MS, Szezech JD, Borges FS, Iarosz KC, Caldas IL, Batista AM, et al. Chimera-like states in a neuronal network model of the cat brain. *Chaos Solit Fractals*. (2017) **101**:86. doi: 10.1016/j.chaos.2017.05.028
79. Tresch MC, Kiehn O. Synchronization of motor neurons during locomotion in the neonatal rat: predictors and mechanisms. *J Neurophysiol*. (2002) **22**:9997–10008. doi: 10.1523/JNEUROSCI.22-22-09997.2002

80. Pereda AE. Electrical synapses and their functional interactions with chemical synapses. *Nat Rev Neurosci*. (2014) **15**:250–63. doi: 10.1038/nrn3708
81. Jabeen S, Thirumalai V. The interplay between electrical and chemical synaptogenesis. *J Neurophysiol*. (2018) 120:1914–22. doi: 10.1152/jn.00398.2018
82. Varshney LR, Chen BL, Paniagua E, Hall DH, Chklovskii DB. *Connectivity Data*. (2011). Available online at: http://www.wormatlas.org/neuronalwiring.html#NeuronalconnectivityII (accessed October 15, 2019).
83. Bentley B, Branicky R, Barnes CL, Chew YL, Yemini E, Bullmore ET, et al. *Edge List MonoAmines*. (2016). Available online at: https://doi.org/10.1371/journal.pcbi.1005283.s004 (accessed October 15, 2019).
84. Altun Z. *Individual Neurons*. (2011). Available online at: http://wormatlas.org/neurons/Individual%20Neurons/Neuronframeset.html.
85. Hindmarsh JL, Rose RM. A model of neuronal bursting using three coupled first order differential equations. *Proc R Soc London Ser B*. (1984) **221**:87.
86. Storace M, Linaro D, de Lange E. The Hindmarsh-Rose neuron model: bifurcation analysis and piecewise-linear approximations. *Chaos*. (2008) **18**:033128. doi: 10.1063/1.2975967
87. Barrio R, Shilnikov A. Parameter-sweeping techniques for temporal dynamics of neuronal systems: case study of Hindmarsh-Rose model. *J Math Neurosc*. (2011) **1**:6. doi: 10.1186/2190-8567-1-6
88. Barrio R, Angeles Martínez M, Serrano S, Shilnikov A. Macro-and micro-chaotic structures in the Hindmarsh-Rose model of bursting neurons. *Chaos*. (2014) **24**:023128. doi: 10.1063/1.4882171
89. Baptista MS, Kakmeni FMM, Grebogi C. Combined effect of chemical and electrical synapses in Hindmarsh-Rose neural networks on synchronization and the rate of information. *Phys Rev E*. (2010) **82**:036203. doi: 10.1103/PhysRevE.82.036203
90. Antonopoulos CG, Srivastava S, Pinto SE, Baptista MS. Do brain networks evolve by maximizing their information flow capacity? *PLOS Comp Bio*. (2015) **11**:e1004372. doi: 10.1371/journal.pcbi.1004372
91. Shanahan M. Metastable chimera states in community-structured oscillator networks. *Chaos*. (2010) **20**:013108. doi: 10.1063/1.3305451
92. Mucha PJ, Richardson T, Macon K, Porter MA, Onnela JP. Community structure in time-dependent, multiscale, and multiplex networks. *Science*. (2010) **328**:876–8. doi: 10.1126/science.1184819
93. Blondel VD, Guillaume JL, Lambiotte R, Lefebvre E. Fast unfolding of communities in large networks. *J Stat Mech*. (2008) **2008**:P10008. doi: 10.1088/1742-5468/2008/10/P10008
94. Peixoto TP. *The Graph-Tool Python Library*. figshare. (2014). Available online at: https://figshare.com/articles/graph_tool/1164194

Conflict of Interest: The authors declare that the research was conducted in the absence of any commercial or financial relationships that could be construed as a potential conflict of interest.

frontiers in Applied Mathematics and Statistics

ORIGINAL RESEARCH
published: 30 July 2019
doi: 10.3389/fams.2019.00035

Chimera States With 2D Deterministic and Random Fractal Connectivity

George Argyropoulos [1,2] *and Astero Provata* [1*]

[1] *Institute of Nanoscience and Nanotechnology, National Center for Scientific Research "Demokritos", Athens, Greece,*
[2] *School of Electrical and Computer Engineering, National Technical University of Athens, Athens, Greece*

We study the formation of chimera states in 2D lattices with hierarchical (fractal) connectivity. The dynamics of the nodes follow the Leaky Integrate-and-Fire model and the connectivity has the form of a deterministic or a random Sierpinski carpet. We provide numerical evidence that for deterministic fractal connectivity and small values of the coupling strength, a hierarchical incoherent spot is produced with internal structure influenced by the fractal connectivity scheme. The spot size is similar to the size of the coupling matrix. Stable spots can be formed for symmetric fractal connectivity, while traveling ones are found when the connectivity matrix is asymmetric with respect to the center. For fractal coupling schemes spiral wave chimeras are produced and curious stable patterns are reported, which present triple coexistence of coherent regions, incoherent domains and traveling waves. In all cases, the coherent domains demonstrate the lowest mean phase velocities ω, the incoherent domains show intermediate ω-velocities, while the traveling waves show the highest ω-values. These findings confirm previous studies on symmetric deterministic hierarchical connectivities and extend here to slanted and random fractals.

Keywords: local synchronization, chimera states, leaky integrate-and-fire model, hierarchical connectivity, deterministic fractals, random fractals

OPEN ACCESS

Edited by:
Anna Zakharova, Technische Universität Berlin, Germany

Reviewed by:
Iryna Omelchenko, Technische Universität Berlin, Germany
Jan Frederik Totz, Massachusetts Institute of Technology, United States
Nadezhda Semenova, Saratov State University, Russia

***Correspondence:**
Astero Provata
a.provata@inn.demokritos.gr

Specialty section:
This article was submitted to Dynamical Systems, a section of the journal Frontiers in Applied Mathematics and Statistics

Received: *09 April 2019*
Accepted: *08 July 2019*
Published: *30 July 2019*

Citation:
Argyropoulos G and Provata A (2019) Chimera States With 2D Deterministic and Random Fractal Connectivity. Front. Appl. Math. Stat. 5:35. doi: 10.3389/fams.2019.00035

1. INTRODUCTION

A Chimera state is characterized by the unexpected coexistence of coherent and incoherent domains in networks of coupled oscillators. Chimera states were first discovered in 2002 in a system of coupled Kuramoto phase oscillators [1, 2] and were further established 2 years later in a seminal work by Abrams and Strogatz [3]. They captivated scientific interest during the past 15 years due to their intriguing structural and dynamical properties and to potential applications in physics [4–7], chemistry [8–10], and biology [11–16]. Although original studies referred to coupled phase oscillators, later works have reported chimera states in coupled FitzHugh-Nagumo, Hindmarsh-Rose, Van der Pol, and Leaky Integrate-and-Fire (LIF) oscillator networks [17–24]. Most recent advances in the general domain of local synchronization are summarized in review articles [25–29].

Previous studies on 2D nonlocal connectivity with periodic, toroidal boundary conditions have demonstrated a variety of chimera patterns. Using the phase oscillator, the FitzHugh Nagumo system or the LIF neuron oscillators chimera patterns emerged in the form of coherent and incoherent single or multiple spots, rings, lines, and grids of spots [19, 30–34]. Some of these

patterns, come as generalizations of the 1D chimera forms to 2D geometry (e.g., spots and stripes), while others are new patterns which do not have an analogy in 1D (e.g., spiral waves).

As early structural studies of the human brain, using Magnetic Resonance Imaging (MRI) techniques and Diffusion Tensor Imaging (DTI) analysis, have captured fractal attributes and self-similarities in the structure of the neuron axons network [35–39], recent numerical studies have introduced fractal, hierarchical connectivity in the simulations of networks of spiking neurons. The use of Cantor-type connectivities in 1D ring networks has demonstrated that the induced chimera states retain some of the fractal features of the Cantor connectivity schemes [18, 21, 40–44]. More recently 2D simulations of chimera states were attempted, using the LIF model with symmetric Sierpinski-carpet connectivity and first evidence was provided that for small values of the coupling strength single asynchronous spots are formed which acquire hierarchical structure, reminiscent of the Sierpinski connectivity matrix [45]. This was a first study, providing evidence of hierarchical chimeras in 2D networks.

In the present study we confirm the presence of hierarchical chimeras for different parameter values (especially for different refractory periods) in 2D LIF networks and we extend our study to slanted fractals and random fractal connectivity schemes. We provide evidence of asymmetric hierarchical chimera states, multiple incoherent spot chimeras with internal hierarchical connectivity which fades away with time, as well as stable patterns where coherent spots, incoherent domains, and traveling waves coexist.

We would like to stress here, that the aim of this study is not to simulate in detail the three-dimensional connectivity of the human brain, based on the MRI recordings. Rather, this research is inspired by the fractal and multifractal analysis of the MRI images, which indicate that the neuron axons are not homogeneously distributed in the brain but they span a subspace with fractal dimension $d_f \approx 2.5$. These fractal attributes have been computed for length scales between [1 and 10 cm] using the box-counting technique [36–38]. The present study aims to address the influence of fractal connectivity (as opposed to the usual non-local connectivity) in the formation of chimera states. Although chimera states with hierarchical connectivity in one-dimensions have been studied in many works [18, 21, 41, 42, 44], the problem of hierarchical connectivity in two-dimensions has not been adequately addressed. To this end, several drastic simplifications were made due mostly to limitations of computational resources: (a) the LIF model is used which is a minimal model addressing the biological neuron activity, (b) only restricted system sizes are considered as will be described in the next section, (c) the connectivity was reduced to a flat fractal kernel, and (d) periodic boundary conditions are considered in order to retain the symmetry of interactions. All these simplifications aim to avoid including too many parameters in the system and to focus on the mechanisms producing hierarchical chimera patterns and 2D spiral wave chimeras.

In the next section we give a brief presentation of the LIF model and its implementation on a 2D network with deterministic and random fractal connectivity. In section 3.1 we present our results when the fractal connectivity is deterministic and symmetric, while the slanted fractal case is presented in section 3.2. Our results on random fractal connectivity are presented in section 4 where we report the finding of spiral wave chimeras and chimeras exhibiting three different coexisting domain types: coherent, incoherent and traveling waves. The conclusions of this study are briefly summarized in the final section 5 and relevant open issues are discussed.

2. THE MODEL AND THE CONNECTIVITY SCHEMES

The LIF model for single neuron dynamics was introduced by Louis Lapicque in 1907 and is in frequent use by computational neuroscientists due to its easy numerical implementation, while it retains the main dynamical features of biological neuron activity [46–48]. In relation to collective neuron dynamics, coupled LIF neurons were shown to produce chimera states under various types of non-local connectivity schemes in 1D [22–24, 41, 49–51], in 2D [19, 45], and in 3D [52].

In this section, we present the LIF coupling scheme in 2D using different fractal connectivity geometries. Namely, after recapitulating the LIF dynamics in 2D for a generic coupling matrix, we introduce the following coupling schemes: (a) symmetric deterministic Sierpinski carpet, (b) slanted deterministic Sierpinski carpet, and (c) random Sierpinski carpet (which is almost always asymmetric). These coupling schemes will be used in sections 3 and 4 for studying local synchronization phenomena.

2.1. The LIF Coupling Scheme

The dynamics describing the temporal evolution of the potential $u_{ij}(t)$ of a neuron having Cartesian coordinates (i, j) is divided in three phases: (i) the integration phase shown below in Equation (1a) characterized by a linear differential equation exhibiting an exponential increase of the membrane potential, (ii) the abrupt resetting phase (Equation 1b) and (iii) a refractory period (Equation 1c). These phases are expressed by the following equations:

$$\frac{du_{ij}(t)}{dt} = \mu - u_{ij}(t) - \frac{1}{N_c}\sum_{kl\in\{N_{ij}\}} \sigma_{ijkl}\left[u_{kl}(t) - u_{ij}(t)\right] \quad (1a)$$

$$\lim_{\epsilon\to 0} u_{ij}(t_r+\epsilon) \to u_{\text{rest}}, \quad \text{when } u_{ij}(t_r) \geq u_{\text{th}}, \ r = 1, 2, \cdots \quad (1b)$$

$$u_{ij}(t) = u_{\text{rest}}, \quad \text{when } t_r \leq t < t_r + T_r, \quad (1c)$$

On the right hand side of Equation (1a), the first two terms correspond to the integration of the potential while the last term accounts for the exchange between neuron (i, j) and other neurons in the network.

The various parameters in Equation (1) have the following interpretation: The variable u_{th} defines the maximum value that the potentials u_{ij} can take, after which the oscillators are reset to their rest potential u_{rest}. The resetting times t_r are counted by

the index $r = 1, 2, \cdots$. μ is the value that the potential of the neuron (i, j) would asymptotically tend to if there was no resetting condition, $u_{\text{th}} < \mu$. T_r is a refractory period after resetting, during which the neuron potential remains at the rest state. N_c is the number of neurons that are connected with the neuron (i, j). These neurons are members of the set $\{N_{ij}\}$.

In the present study we assume that all oscillators are identical, they have identical parameters: $\mu, u_{\text{rest}}, u_{\text{th}}$ and N_c. For simplicity, we also assume that the coupling is linear and every oscillator is linked to all others through a coupling matrix, whose element σ_{ijkl} links oscillators (i, j) and (k, l). The values of the matrix elements may take any value (positive, negative, or zero), depending on the connectivity of the network, but in the current study we restrict the coupling matrix elements to the interval $0 \leq \sigma_{ijkl} \leq 0.3$.

The solution of Equation (1) in the absence of coupling provides the period T_s of the single neuron and the corresponding phase velocity ω_s (the subscript "s" stands for "single", uncoupled neuron), as:

$$T_s = \ln \frac{\mu - u_{\text{rest}}}{\mu - u_{\text{th}}} + T_r, \quad \omega_s = 2\pi / T_s. \tag{2}$$

Although all neurons have the same parameters when uncoupled, coupling induces local and global variations in the period of the individual neurons and the network acquires a distribution of mean phase velocities. This distribution characterizes the collective behavior of the network. The mean phase velocity of all coupled neurons ω_{ij} in a time interval Δt is computed as:

$$\omega_{ij} = \frac{2\pi Z_{ij}(\Delta t)}{\Delta t} \tag{3}$$

where $Z_{ij}(\Delta t)$ is the integer number of full cycles that neuron (i, j) has completed in the time interval Δt, and is computed numerically during the simulations. The relative values of ω are of central importance when studying chimera states, because they differentiate between the coherent and incoherent domains. In the coherent domains all the elements have common mean phase velocities, while the incoherent domains are characterized by a distribution of ω-values [17].

2.2. Connectivity Schemes

In the present study the neuron oscillators are arranged on a 2D lattice-network of size $N \times N$. The three fractals used to construct the connections of the LIF oscillators are Sierpinski carpets, which are flat fractals with Hausdorff dimension $\ln 8 / \ln 3 \approx 1.8928$. The construction of the Sierpinski carpets is recursive and follows three simple algorithms:

- **The deterministic symmetric Sierpinski carpet**: (a) We begin with a square which we subsequently divide into 9 equal smaller squares. (b) We then remove the central square and this concludes the first iteration of the process. (c) We divide each of the remaining 8 squares into 9 equal smaller squares and remove the central one of each group of 9. (d) This concludes the second iteration. (e) The same sequence of dividing and removing can be applied arbitrarily many times to obtain as many spatial scales as required [53, 54]. The connectivity scheme which is produced is shown in **Figure 1A**.
- **The deterministic slanted Sierpinski carpet**: (a) We begin with a square which we subsequently divide into 9 equal smaller squares. (b) We then remove one of the 8 non-central squares and this concludes the first iteration of the process. In **Figure 1B** we have chosen to remove the lower right square. (c) We divide each of the remaining 8 squares into 9 equal smaller squares and remove the same one as in the previous iteration (lower right squares) in each group of 9. (d) This concludes the second iteration. e) The same sequence of dividing and removing can be applied arbitrarily many times to obtain the connectivity scheme depicted in **Figure 1B**.
- **The random Sierpinski carpet**: (a) We begin with a square which we subsequently divide into 9 equal smaller squares. (b) We then remove randomly one of the 9 squares and this concludes the first iteration of the process. In **Figure 1C** we have chosen to remove the central square. (c) We divide each of the remaining 8 squares into 9 equal smaller squares and remove one square at random from each group of 9. (d) This concludes the second iteration. (e) The same sequence of dividing and removing randomly can be applied arbitrarily many times to obtain the connectivity of **Figure 1C**.

The resulting deterministic and random hierarchical pictures are used as connection matrices. Namely, the central node (i, j) of the connectivity scheme is only linked with all black nodes that belong to the Sierpinski carpet surrounding it. The coupling of other nodes is formed by translation of the fractals. To maintain an identical coupling scheme for all nodes we use periodic boundary conditions in both $x-$ and $y-$directions, leading to a torus geometry [45].

In all three cases, symmetric deterministic, slanted deterministic or random hierarchical connectivity, if we denote by $\{N_{ij}\}$ the set of all nonzero cells of the Sierpinski carpet centered around the node (i, j) and denote by (k, l) any arbitrary element of the system, then the coupling matrix elements σ_{ijkl} between nodes (i, j) and (k, l) take the form:

$$\sigma_{ijkl} = \begin{cases} \sigma, & \forall (k, l) \in \{N_{ij}\} \\ 0, & \text{elsewhere} \end{cases} \tag{4}$$

In this study the coupling strength value σ is a positive constant, common for all network connections [45]. As working parameter set we use $\mu = 1$, $u_{\text{th}} = 0.98$, $u_{\text{rest}} = 0$ and $N = 81$, while $N = 243$ in some simulations. All simulations start with random initial conditions. For the system integration the explicit Euler scheme was used with integration step $dt = 10^{-3}$. 4-th order Runge-Kutta was also used as a test and the results were compatible with the Euler scheme. The connectivity pattern was used directly within the Euler scheme and the iteration time was 10^4 time units for all reported simulations. The spatial coupling was performed via direct convolution. Using an MPI parallel implementation of the algorithm on multiple (usually 20–80) CPUs each simulation took on average 8 CPU hours for 10^4 time units. The algorithms are available online[1].

[1] https://github.com/gArgyropoulos/LIF_2D (2019).

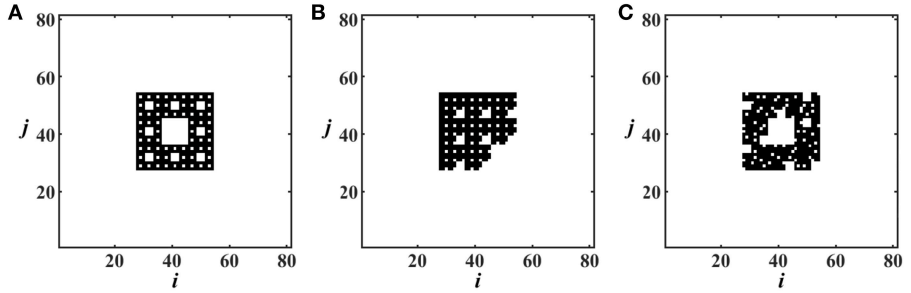

FIGURE 1 | The Sierpinski carpets used as coupling matrices: **(A)** deterministic symmetric Sierpinski connectivity pattern, **(B)** deterministic slanted Sierpinski connectivity pattern and **(C)** random Sierpinski connectivity pattern. In all cases three orders of iteration are used, based on a 3×3 initiation square.

In **Table 1**, we present collectively all the qualitative results we obtained by scanning the parameters, $0.1 \leq \sigma \leq 0.3$ and $0 \leq T_r \leq 2.0$ (in time units). For the 2D LIF scheme (Equation 1), it is relatively easy to find chimera states in the parameter regions reported in **Table 1**. In these regions there is little sensitivity to initial conditions and most initial states end-up in the corresponding chimeras. Only for intermediate parameter values, between domains which support distinct chimera patterns, the different initial conditions may result to different synchronization motifs. Overall, for small σ values we observe spot chimeras many of which present structure reminiscent of the features of the connectivity matrix (see more in section 3). For larger values of σ and T_r more intricate patterns arise such as multiple spots, grids, stripes, spirals and even stable triple combinations of coherent spots, incoherent domains and traveling waves. Details on the particular patterns are given in sections 3, 4 and the **Table 1**.

3. DETERMINISTIC FRACTAL CONNECTIVITY

3.1. Symmetric Coupling

In a previous study, the present authors and T. Kasimatis have used the symmetric coupling of **Figure 1A** to explore the influence of the hierarchical connectivity in the form of 2D chimera patterns [45]. For small positive values of the coupling strength and medium values of the refractory period, $T_r = 0.5$ time units, they report spot chimera patterns with internal structure reminiscent of the connectivity matrix. The chimeras are best visualized in the ω-profiles, when the spots are immobile. For larger values of the coupling strength σ, stripe and grid chimeras were reported which were mostly traveling and, as a result, the hierarchical structure of the chimeras, visible in the ω-profiles, was masked. In such cases one can always resort to using the comoving frame to avoid that the motion of the spot smooths out the ω-structure, but this is outside the scope of the present study.

In the following we present evidence that hierarchical spot chimeras are possible even for $T_r = 0$. In **Figure 2A** we present the u_{ij}-profile for $\sigma = 0.18$ and $T_r = 0$. The internal structure of an asynchronous spot chimera is visible but the hierarchical scheme in **Figure 2B** is not as clear as it was in Argyropoulos et al. [45], where $T_r = 0.5$ time units was used. In this realization the incoherent elements are ordered in stripes parallel to the i-direction. Depending on the initial conditions the stripes appear parallel to the $i-$ or to the $j-$direction, reflecting the square geometry of the connectivity kernel. The grid-formations in Argyropoulos et al. [45] (**Figures 2B**, **3B**, therein) can be viewed as coexistence/superpositions of stripes in both directions.

In **Figure 3** we present the evolution of ω of two elements, one belonging to the coherent domain (**Figure 3A**), and one to the incoherent (**Figure 3B**). The calculations of ω were performed in time windows of $\Delta t = 30$ time units. While in the coherent domains the ω values stabilize mostly around 1.68 (with infrequent excursions to higher values), in the incoherent domains the mean phase velocity alternates between the values $\omega = 1.88$ and $\omega = 1.68$. This apparent bistability may reflect the slight erratic motion of the incoherent domains. Their elements may spent some time participating in the coherent domain and other time in the incoherent and thus bistability is observed in their mean phase velocity.

By increasing the system size it is possible to increase the number of incoherent domains that the system can accommodate (see **Figure 4**). They take the form of spiral wave multichimeras. In the present case, each of the four incoherent domains is the core region of a distinct spiral wave chimera. Around each core there is a rotating phase wave with a large wavelength. Apart from the number of asynchronous cores, larger systems (e.g., 243×243 in the present case) can accommodate incoherent cores with non-homogeneous internal structure, caused (as we believe) by the hierarchical ordering of the connectivity matrix. This is evident mainly in **Figures 4A,B** while in **Figures 4C,D** this internal structure is gradually destroyed due to the tiny erratic motion of the incoherent domains, giving rise to incoherent cores composed of random phases. The filamented structure of the incoherent domains in **Figure 4A** has been also found in 2D coupled phase oscillators [55]. In both cases the filaments are observed in the 4-chimera states and for specific parameter values. In the LIF case with fractal connectivity, these filaments are short-lived and they dissociate passing via a hierarchical phase (see **Figures 4B,C**) into becoming the stable incoherent domains (see **Figure 4D**) of the spiral chimera.

TABLE 1 | Collective presentation of the chimera patterns in the LIF model for σ ranging between (0.1–0.3) and T_r in the interval from 0 to 2.0 time units.

$T_r\sigma$	0.1	0.12	0.14	0.16	0.18	0.2	0.22	0.24	0.26	0.28	0.3
Deterministic Hierarchical Symmetric Coupling											
0	sspot	sspot	sspot	sspot	sspot	sspot	sspot	sspot	sspot	sspot	sspot
0.1	sspot	sspot	sspot	sspot	sspot	sspot	sspot	sspot	hspot	hspot	hspot
0.2	sspot	sspot	sspot	sspot	sspot	sspot	hspot	hspot	spot	s	s
0.3	sspot	sspot	sspot	sspot	sspot	sspot	hspot	spot	s	s	s
0.4	sspot	sspot	sspot	sspot	sspot	hspot	hspot	s	s	s	s
0.5	sspot	sspot	sspot	sspot	sspot	hspot	s	s	s	s	s
0.6	sspot	sspot	sspot	sspot	sspot	hspot	s	s	s	s	s
0.7	sspot	sspot	sspot	sspot	sspot	hspot	s	s	s	s	tr
0.8	sspot	sspot	sspot	sspot	sspot	hspot	s	s	s	s	tr
0.9	sspot	sspot	sspot	sspot	hspot	hspot	s	s	s	tr	stripe
2.0	sspot	sspot	sspot	hspot	tr	stripe	stripe	stripe	tr	mspots	stripe
Deterministic Slanted Hierarchical Coupling											
0	t	t	t	t	t	t	t	t	t	t	s
0.1	t	t	t	t	t	t	t	t	s	s	s
0.2	t	t	t	t	t	t	t	s	s	s	s
0.3	t	t	t	t	t	s	s	s	s	s	s
0.4	t	t	t	t	s	s	s	s	s	s	s
0.5	t	t	t	t	s	s	s	s	s	s	s
0.6	t	t	t	s	s	s	s	s	s	s	s
0.7	t	t	t	s	s	s	s	s	s	s	s
0.8	t	t	t	s	s	s	s	s	s	s	s
0.9	t	t	t	s	s	s	s	s	s	s	s
2.0	t	s	s	s	s	s	s	s	s	s	s
Random Hierarchical Coupling											
0	spot	spot	spot	spot	spot	spot	spot	spot	spot	spot	spot
0.1	spot	spot	spot	spot	spot	spot	spot	spot	spot	spot	spot
0.2	spot	spot	spot	spot	spot	spot	spot	spot	spot	s	s
0.3	spot	spot	spot	spot	spot	spot	spot	s	s	s	s
0.4	spot	spot	spot	spot	spot	spot	spiral	s	s	s	spiral
0.5	spot	spot	spot	spot	spot	spot	spiral	s	s	spiral	s
0.6	spot	spot	spot	spot	spot	spot	spiral	s	s	s	s
0.7	spot	spot	spot	spot	spot	spot	s	s	s	s	s
0.8	spot	spot	spot	spot	spot	s	s	s	s	s	stripe
0.9	spot	spot	spot	spot	spot	s	s	s	s	tr	stripe
2.0	spot	spot	spot	tr	tr	stripe	stripe	tr	syn-spots	syn-spot	s

*The annotation is mostly self explanatory: s, synchronized oscillations; **t**, triangle asymmetric spot; spot, single asynchronous spot; sspot, single asynchronous spot with striped ω-profile (see **Figure 2**); hspot, hierarchical asynchrononous spot; tr, transient; syn-spot, synchronous spots; stripe, stripes; spiral, spiral wave chimera (see **Figure 7**).*

In the 2nd row of **Figure 4**, first the long time ω-profile is presented (**Figure 4E**). As the mean phase velocities change during the transition time, we record here the ω-profile after the four cores have stabilized to their full incoherent state. The ω-histogram in logarithmic scale (**Figure 4F**) demonstrates one very distinct peak at low frequencies which corresponds to the coherent region and one distributed region in higher frequencies, which correspond to the four incoherent spots, collectively. There is no distinctive maximum related to the incoherent cores due to the distributed $\omega-$ values in these regions. In **Figures 4G,H** the temporal evolution of the ω-values in the coherent and the incoherent domains are monitored during the transition period. The incoherent elements are frequently passing from low to high frequencies and thus have higher average ω as compared with the coherent ones, which mostly oscillate with low frequency. The development of this pattern is presented in a short 30 s video included in the **Supplementary Material**[2].

3.2. Slanted Fractal Coupling

In the case of slanted deterministic coupling, with connectivity depicted in **Figure 1B**, chimera patterns are produced which are mostly traveling in the direction of the reflection symmetry axis

[2]Two videos related to **Figures 4**, **7** are added in the **Supplementary Material** (2019).

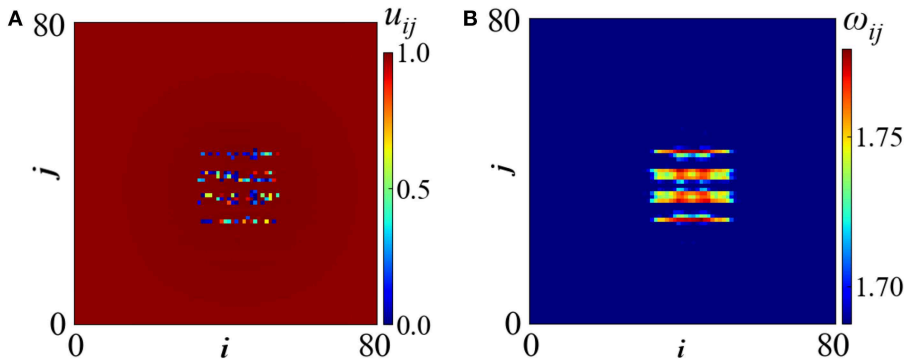

FIGURE 2 | (A) The potential profile and **(B)** the mean phase velocity profile for an asynchronous spot chimera realized for symmetric hierarchical coupling with $\sigma = 0.18$ and $T_r = 0$. Other parameters are $\mu = 1$, $u_{\text{th}} = 0.98$, $u_{\text{rest}} = 0$ and $N = 81$. The simulations start from random initial conditions.

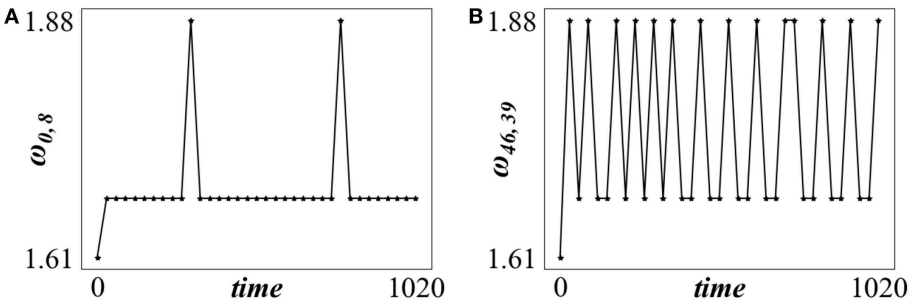

FIGURE 3 | The time evolution of ω for **(A)** element $(i,j) = (0, 8)$ belonging to the coherent domain and **(B)** element $(i,j) = (46, 39)$ belonging to the incoherent domain of **Figure 2**. $\sigma = 0.18$ and $T_r = 0$. Parameters are as in **Figure 2A**.

of the kernel [56]. Because traveling is mostly accompanied by erratic motion, it is difficult to detect the fractality in the ω-profile. **Figure 5** is a rare example of an immobile incoherent spot where a meaningful ω-profile can be calculated. In **Figure 5A** the u_{ij}-profile shows that the form of the chimera is not circular but takes the arrow-like shape of the seeding connectivity, **Figure 1B**. Besides u, also the $\omega-$profile reflects the form of the connectivity matrix, **Figure 5B**.

The external shape of the asymmetric spot, which mimics the perimeter of the oblique connectivity kernel, supports previous results in hierarchical 2D chimeras indicating that, for appropriate choices of (small) coupling strengths, the form of the kernel is mirrored in the ω-profile [45]. Here, the erratic motion of the pattern does not allow the observation of potential hierarchical internal structure in the $\omega-$profile, induced as a result of fractal connectivity schemes as in Argyropoulos et al. [45]. A resolution of this issue involves the use of a comoving frame, but this is outside the scope of the present study.

4. RANDOM FRACTAL CONNECTIVITY

Random connectivity is almost always asymmetric and this is the case we consider here. As a general observation the asymmetry of the connectivity pattern often causes motion of the chimera patterns. As an example, for $\sigma = 0.2$ and $T_r = 0.5$ an erratically traveling incoherent spot is formed, depicted in **Figure 6**. The incoherent spot potential profile, u_{ij}, seems to present some internal structure in the form of irregular vertical stripes (see **Figure 6A**). To make an analogy, we remind of the more regular, stripped structure that was reported in **Figure 2** for deterministic symmetric coupling. Here, the kernel is non-symmetric and this fact together with the motion of the incoherent part makes it difficult to discern any fine details in its $\omega-$profile (see **Figure 6B**). In **Figure 6B** the ω-profile has been calculated in time windows of size $\Delta t = 30$ time units, where the incoherent spot can be considered as almost immobile. As in all cases of traveling patterns, the use of a comoving frame could resolve possible patterns inside the incoherent part of the mean phase velocity profile. Different realizations of the fractal coupling matrix do not affect the number and sizes of the coherent and incoherent domains of the chimera pattern, provided that the fractal dimension and the hierarchical order are retained in the different realizations.

Increasing slightly the coupling strengths while keeping T_r to low values, the patterns become unstable. A typical example is shown in **Figure 7**, where wave domains are shown spiraling around the torus. The four spiraling regions have the form of successive wavefronts with arrow-like shapes [55]. They rotate around coherent cores which are characterized by different wavelengths than the spiraling fronts. This is a new type of spiral chimera composed by coherent waves with two different wave lengths. Even in this case, we observe that the sizes of the spiraling

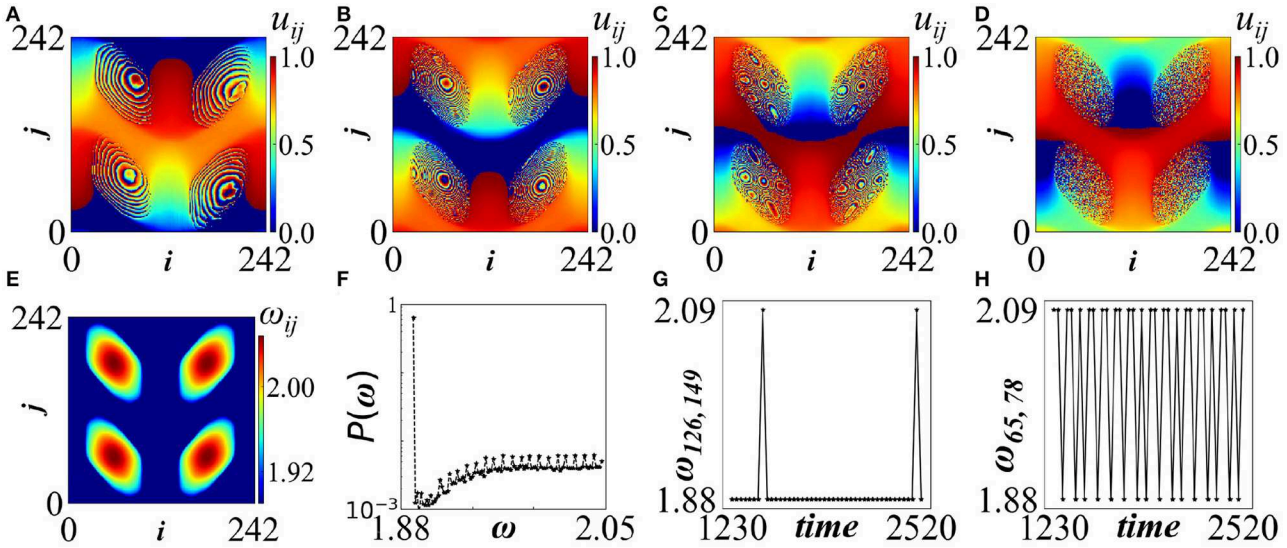

FIGURE 4 | Top row: Spiral wave multichimera state with four incoherent cores in symmetric deterministic connectivity for system size 243 × 243; the potential profiles are depicted at times: **(A)** $t = 1200$, **(B)** $t = 1800$ **(C)** $t = 2700$ and **(D)** $t = 10020$ time units. Bottom row: **(E)** Mean phase velocity profile, **(F)** Typical histogram of mean phase velocities, **(G)** Time evolution of ω on a node contained in the coherent regions and **(H)** Time evolution of ω on a node belonging to one of the incoherent cores. Parameters are $\sigma = 0.25$ and $T_r = 0.5$ and $N = 243$. All other parameters are as in **Figure 2A**. Simulations start from random initial conditions. A related video is included in the **Supplementary Material**.

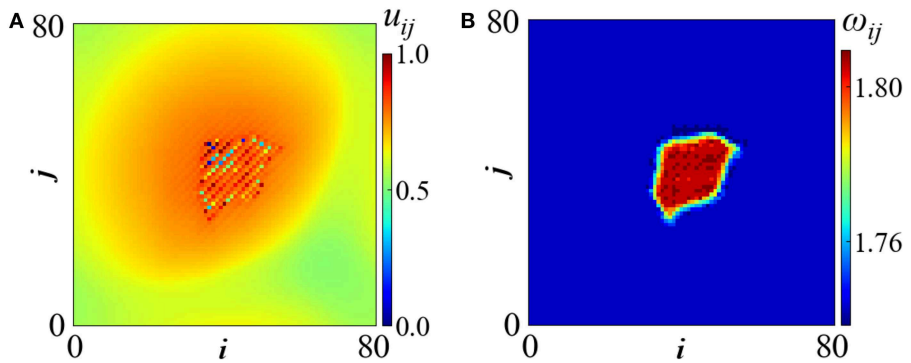

FIGURE 5 | Chimera state with slanted fractal deterministic connectivity: **(A)** u_{ij}-profile and **(B)** ω_{ij}-profile. Parameters are $\sigma = 0.2$ and $T_r = 0.1$. All other parameters are as in **Figure 2A**. Simulations start from random initial conditions.

fronts are similar to the size of the initiation connectivity pattern. A related video is added in the **Supplementary Material**[2].

For larger values of T_r coherent double spots and stripe chimeras are formed, surrounded by the incoherent domains (**Figure 8**). In the top row of **Figure 8** we can see the formation of a triple pattern (**Figure 8A**) composed by (i) a coherent stripe crossed by a traveling wave [57], (ii) an incoherent stripe surrounding the coherent region, while (iii) a third region consisting of traveling waves appears within the incoherent domain, at the top and bottom of the figure. The velocities of the traveling waves and the oscillator frequencies are different in the first and the third regions and this may support the idea of bistability. The presence of the incoherent region serves the purpose of continuity. Unlike the well known chimera patterns which is composed of two types of domains (coherent and incoherent), this is a curious chimera pattern which consists of three different domain types: coherent traveling waves with low velocity (region i), incoherent part (region ii) and coherent traveling waves with high velocity (region iii). The mean phase velocity distribution shows two maxima: one at the low frequencies which corresponds to the coherent domain and one in the high frequencies related to the high speed traveling waves. The intermediate ω values are attributed to the incoherent domain.

By increasing the coupling strength, $\sigma = 0.26$, the stripe splits into two coherent spots, around which incoherent domains develop (**Figure 8B**). Again, the two incoherent domains are separated by spatial traveling patterns. Here the mean phase velocity distribution shows only a distinct maximum in the high frequencies which corresponds to the traveling waves. The

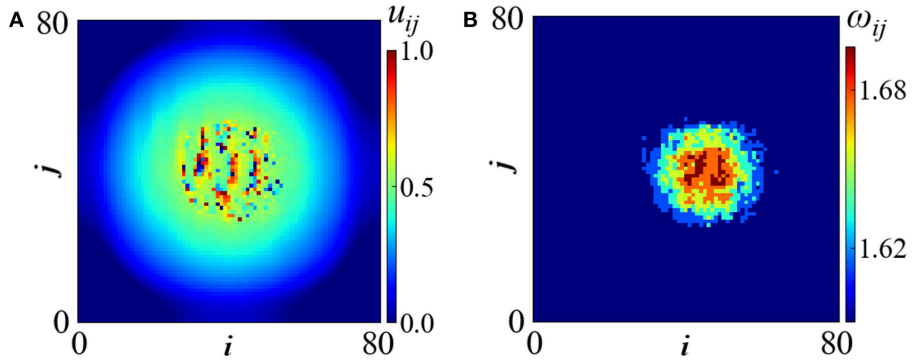

FIGURE 6 | Single mobile spot in random fractal connectivity. Parameters are $\sigma = 0.2$ and $T_r = 0.5$. All other parameters are as in **Figure 2A**. Simulations start from random initial conditions.

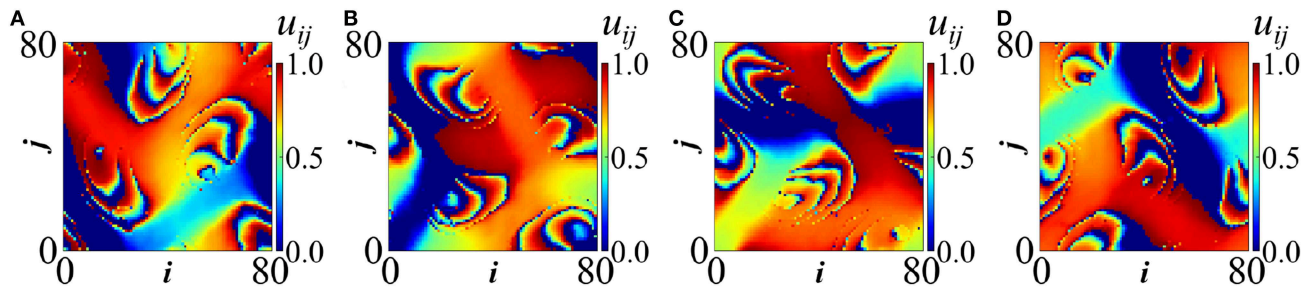

FIGURE 7 | Spiral wave chimeras around a coherent core for random hierarchical connectivity in LIF model; potential profiles are depicted at four instances: **(A)** $t = 3300$ **(B)** $t = 3360$ **(C)** $t = 3420$ and **(D)** $t = 3480$ (in time units). Parameters are $\sigma = 0.22$ and $T_r = 0.6$. All other parameters are as in **Figure 2A**. Simulations start from random initial conditions. A related video is included in the **Supplementary Material**.

two coherent spots have small sizes and their extent (size) is relatively small, not enough to produce a maximum in the low ω region in **Figure 8F**. Alternatively, the extent of "blue" regions in **Figure 8E** which characterize the coherent cores is similar to the extent of yellow regions which characterize the incoherent domains and therefore the spectrum in **Figure 8F** shows a plateau in the region of low mean phase velocities. The ω-profiles demonstrate that the coherent spots and the stripe acquire the lowest mean phase velocities, the incoherent domains have intermediate ω-values, while the traveling wave regions show the highest ω-values.

Related to the $\omega-$profiles in the coherent domains (spots and stripe) we may assume, similarly to the Kuramoto phase oscillators, that the coupling term contribution in Equation (1a) reduces to zero because oscillators in the coherent domains have a phase difference of zero to their nonlocal neighbors. Unlike the Kuramoto model, in the LIF model the coherent domains present $\omega-$ values close (but not equal) to the uncoupled system. In the incoherent domains the coupling term is not negligible (because the oscillators in the nonlocal neighborhood have different phases) and for the coupling strength we use in this study we observe that $\omega_{\text{incoh}} > \omega_{\text{coh}}$.

Calculations of the local order parameter in the u_{ij} profile is often used to test synchronization in systems of coupled oscillators [29]. The local order parameter r_{ij} around oscillator (i,j) is defined as $r_{ij} = \frac{1}{n_c}\sum_{k,l}\exp\left(i\,\phi(k,l)\right)$. The phase $\phi(k,l)$ of oscillator (k,l) is defined as $\phi(k,l) = \left[(2\,\pi\,u_{kl})/u_{\text{th}}\right]$, so that ϕ varies between 0 and 2π. The sum runs over the n_c first neighbors of the oscillator (i,j). In the present study the immediate neighborhood is defined as a (3×3)-square around the oscillator (i,j), and therefore $n_c = 8$. The local order parameters are depicted in **Figure 9A** for the state in **Figures 7A**, **9B** for the stripe of **Figures 8A**, **9C** for the double coherent spots of **Figure 8D**. The profile of the local order parameter confirms the conclusions on the chimera profiles in all three cases, with lighter colors indicating phase coherence and darker colors phase incoherence.

In particular for the case of the stripe and the double coherent spots (**Figures 9B,C**), the r_{ij}-values demonstrate coherence of the u_{ij} values in the regions of the stripe and the spots, respectively. To the best of our knowledge, these are new types of chimera manifested in 2D geometries, which allow freedom for coexistence of multiple stable domains with different oscillatory features in each domain.

5. CONCLUSIONS AND OPEN PROBLEMS

In the present study we report on how details of the hierarchical connectivity matrix modify the emerging chimera patterns in

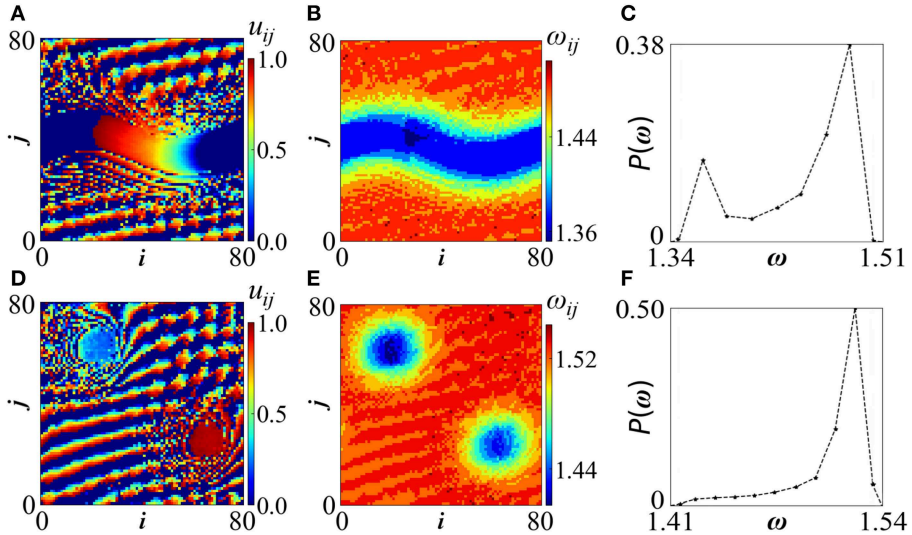

FIGURE 8 | Random hierarchical connectivity in LIF model. Top row: Stripe chimera for parameters $\sigma = 0.22$, $T_r = 2.0$. **(A)** u_{ij}-profiles, **(B)** ω_{ij}-profiles and **(C)** distribution of ω-values. The $P(\omega)$ spectrum present two distinguishable maxima: one at the high ω-region which correspond to the traveling waves with short wavelength and one in the low ω-values associated with the stripe. Bottom row: Double coherent spot chimera for $\sigma = 0.26$ and $T_r = 2.0$. **(D)** u_{ij}-profiles, **(E)** ω_{ij}-profiles and **(F)** distribution of ω-values. The $P(\omega)$ spectrum presents only distinguishable maximum at the high ω-region which correspond to the traveling waves with short wavelength. A peak in the low ω-values in **(F)** is not observable because the extent of the two coherent spots ["blue" regions in **(E)**] is of similar size to the extent of the incoherent domains ["yellow" regions in **(E)**] and therefore a plateau appears. The dashed lines in **(C,F)** serve as eye guides. All other parameters are as in **Figure 2A**. Simulations start from random initial conditions. Other related images are available in the **Supplementary Material**.

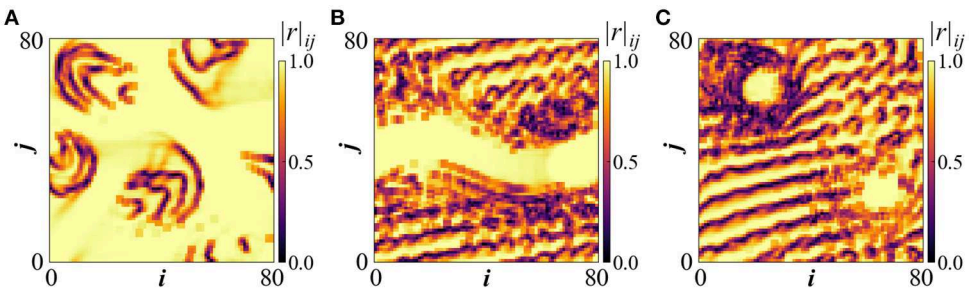

FIGURE 9 | The local order parameter r_{ij} for **(A)** the spiral wave chimera as depicted in **Figures 7A**, **(B)** the stripe chimera of **Figures 8A**, **(C)** the double coherent spots of **Figure 8D**.

2D toroidal geometry. Using as working model the Leaky Integrate-and-Fire oscillator, we present numerical evidence (see **Table 1**) that traces of the hierarchical connectivity motif are demonstrated only for small values of the coupling strength σ (**Figure 2**). For large σ values, the exchange between the oscillating elements is strong, the dynamics develop fast and erratic motion or traveling patterns emerge which destroy the formation of hierarchical ordering within the incoherent domains of the chimera states. A complete list of our simulation results is outlined in **Table 1**.

The introduction of asymmetric (not rotationally invariant) coupling kernels, in the form of deterministic or random fractals, has induced spiral wave chimeras and traveling or erratically moving chimeras. In particular, for connectivity schemes with random hierarchical kernels and for low refractory period, we report a novel spiral wave chimera with a coherent core which is different from the spiral wave chimeras reported in the literature which rotate around incoherent cores. For larger values of the refractory period we also report a peculiar type of chimera which include three types of domains: coherent (in the form of coherent spots or stripes), incoherent and traveling waves. These chimera states are stable and emerge also for small values of the coupling strength. For symmetric hierarchical coupling and large system sizes spiral wave multichimeras are possible. These are composed by ordered spiral waves on the torus rotating around multiple cores consisting of asynchronous oscillators.

Regarding traveling chimera states, to study quantitatively their ω-profiles in future studies it could be useful to use a comoving frame, which moves with the velocity of the traveling pattern. This way one could extract the correct frequencies, since

all nodes will be fixed either to the coherent or to the incoherent domains, without alternating between them.

From this study the rich variety of chimera patterns is evident, especially in 2D geometries, which give enough freedom for creation and stabilization of diverse forms. We have seen that by increasing the size of the system, e.g., from 81×81 to 243×243, it is possible to stabilize multichimera states, even for stochastic fractal connectivity. Apart from increasing the system size, other ways of pinning the traveling patterns (see e.g., Isele et al. [58] and Ruzzene et al. [59]) could be used in order to clarify the presence of hierarchical patterns in the $\omega-$ profile within the incoherent domains.

Another class of related problems concerns the dimensionality of the fractal kernels. In the present study flat fractals were considered with Hausdorff dimension $\ln 8/\ln 3 \approx 1.8928$ as connectivity matrices. It would be interesting to consider kernels with different dimensionality and study the chimera patterns which are produced. Other open problems include the introduction of hierarchical connectivity in three-dimensions to explore the chimera patterns and other synchronization phenomena which emerge. Further extensions include the use of realistic connectivity schemes obtained directly from MRI images in order to address applications related to synchronization of brain neurons.

DATA AVAILABILITY

All data generated for this study can be found in the manuscript and the **Supplementary Information**.

AUTHOR CONTRIBUTIONS

GA and AP formulated the problem and designed the study. GA performed the computations. Both authors discussed the results and contributed to writing the manuscript, read, and approved the final manuscript.

FUNDING

This work was supported by computational time granted from the Greek Research & Technology Network (GRNET) in the National HPC facility–ARIS–under project CoBrain3 (project ID: PR005014_taskp).

ACKNOWLEDGMENTS

The authors acknowledge helpful discussions with N. Tsigkri-Desmedt and I. Koulierakis. The authors would like to thank the reviewers for pointing out many interesting aspects of this work.

SUPPLEMENTARY MATERIAL

The Supplementary Material for this article can be found online at: https://www.frontiersin.org/articles/10.3389/fams.2019.00035/full#supplementary-material

Figure S1 | Depicts the distribution of ω values $P(\omega)$ of the oscillator which have local order parameter greater than 0.25 (these are about 90%).

Figure S2 | Depicts the distribution of ω values $P(\omega)$ of the oscillators which have local order parameter less than 0.25.

Figure S3 | Depicts the distribution of ω values $P(\omega)$ of the oscillators which have local order parameter greater than 0.5.

Figure S4 | Depicts the distribution of ω values $P(\omega)$ of the oscillators which have local order parameter less than 0.5.

Video S1 | Rotating fronts in synchronous background. Corresponds to **Figure 7**.

Video S2 | Creation of 4 asynchronous sports with evolving internal structure. Corresponds to **Figure 4**.

REFERENCES

1. Kuramoto Y. Reduction methods applied to nonlocally coupled oscillator systems. In: Hogan SJ, Champneys AR, Krauskopf AR, di Bernado M, Wilson RE, Osinga HM, et al., editors. *Nonlinear Dynamics and Chaos: Where Do We Go From Here?* Boca Raton, FL: CRC Press (2002). p. 209–27.
2. Kuramoto Y, Battogtokh D. Coexistence of coherence and incoherence in nonlocally coupled phase oscillators. *Nonlinear Phenom Comp*. (2002) **5**:380.
3. Abrams DM, Strogatz SH. Chimera states for coupled oscillators. *Phys Rev B*. (2004) **93**:174102. doi: 10.1103/PhysRevLett.93.174102
4. Hagerstrom AM, Murphy TE, Roy R, Hövel P, Omelchenko I, Schöll E. Experimental observation of chimeras in coupled-map lattices. *Nat Phys*. (2012) **8**:658. doi: 10.1038/nphys2372
5. Martens EA, Thutupalli S, Fourrière A, Hallatschek O. Chimera states in mechanical oscillator networks. *Proc Natl Acad Sci USA*. (2013) **110**:10563–67. doi: 10.1073/pnas.1302880110
6. Lazarides N, Neofotistos G, Tsironis GP. Chimeras in SQUID metamaterials. *Phys Rev B*. (2015) **91**:054303. doi: 10.1103/PhysRevB.91.054303
7. Gambuzza LV, Buscarino A, Chessari S, Fortuna L, Meucci R, Frasca M. Experimental investigation of chimera states with quiescent and synchronous domains in coupled electronic oscillators. *Phys Rev E*. (2014) **90**:032905. doi: 10.1103/PhysRevE.90.032905
8. Tinsley MR, Nkomo S, Showalter K. Chimera and phase-cluster states in populations of coupled chemical oscillators. *Nat Phys*. (2012) **8**:662–5. doi: 10.1038/nphys2371
9. Wickramasinghe M, Kiss IZ. Spatially organized dynamical states in chemical oscillator networks: Synchronization, dynamical differentiation, and chimera patterns. *PLoS ONE*. (2013) **8**:e80586. doi: 10.1371/journal.pone.0080586
10. Schmidt L, Schönleber K, Krischer K, García-Morales V. Coexistence of synchrony and incoherence in oscillatory media under nonlinear global coupling. *Chaos*. (2014) **24**:013102. doi: 10.1063/1.4858996
11. Cherry EM, Fenton FH. Visualization of spiral and scroll waves in simulated and experimental cardiac tissues. *N J Phys*. (2008) **10**:125016. doi: 10.1088/1367-2630/10/12/125016
12. Rattenborg NC, Amlaner CJ, Lima SL. Behavioral, neurophysiological and evolutionary perspectives on unihemispheric sleep. *Neurosci Biobehav Rev*. (2000) **24**:817–42. doi: 10.1016/S0149-7634(00)00039-7
13. Mormann F, Lehnertz K, David P, Elger CE. Mean phase coherence as a measure for phase synchronization and its application to the EEG of epilepsy patients. *Phys D*. (2000) **144**:358–369. doi: 10.1016/S0167-2789(00)00087-7
14. Mormann F, Kreuz T, Andrzejak RG, David P, Lehnertz K, Elger CE. Epileptic seizures are preceded by a decrease in synchronization. *Epilepsy Res*. (2003) **53**:173. doi: 10.1016/S0920-1211(03)00002-0
15. Andrzejak RG, Rummel C, Mormann F, Schindler K. All together now: analogies between chimera state collapses and epileptic seizures. *Sci Rep*. (2016) **6**:23000. doi: 10.1038/srep23000
16. Bansal K, Garcia JO, Tompson SH, Verstynen T, Vettel JM, Muldoon SF. Cognitive chimera states in human brain networks. *Sci Adv*. (2019) **5**:eaau8535. doi: 10.1126/sciadv.aau8535

17. Omelchenko I, Omel'chenko OE, Hövel P, Schöll E. When nonlocal coupling between oscillators becomes stronger: patched synchrony or multi-chimera states. *Phys Rev B*. (2013) **110**:224101. doi: 10.1103/PhysRevLett.110.224101
18. Omelchenko I, Provata A, Hizanidis J, Schöll E, Hövel P. Robustness of chimera states for coupled FitzHugh-Nagumo oscillators. *Phys Rev E*. (2015) **91**:022917. doi: 10.1103/PhysRevE.91.022917
19. Schmidt A, Kasimatis T, Hizanidis J, Provata A, Hövel P. Chimera patterns in two-dimensional networks of coupled neurons. *Phys Rev E*. (2017) **95**:032224. doi: 10.1103/PhysRevE.95.032224
20. Hizanidis J, Kanas V, Bezerianos A, Bountis T. Chimera states in networks of nonlocally coupled Hindmarsh-Rose neuron models. *Int J Bifurcat Chaos*. (2013) **24**:1450030. doi: 10.1142/S0218127414500308
21. Ulonska S, Omelchenko I, Zakharova A, Schöll E. Chimera states in networks of Van der Pol oscillators with hierarchical connectivities. *Chaos*. (2016) **26**:094825. doi: 10.1063/1.4962913
22. Olmi S, Martens EA, Thutupalli S, Torcini A. Intermittent chaotic chimeras for coupled rotators. *Phys Rev E*. (2015) **92**:030901. doi: 10.1103/PhysRevE.92.030901
23. Tsigkri-DeSmedt ND, Hizanidis J, Schöll E, Hövel P, Provata A. Chimeras in leaky integrate-and-fire neural networks: effects of reflecting connectivities. *Eur Phys J B*. (2017) **90**:139. doi: 10.1140/epjb/e2017-80162-0
24. Tsigkri-DeSmedt ND, Koulierakis I, Karakos G, Provata A. Synchronization patterns in Leaky Integrate-and-Fire neuron networks: merging nonlocal and diagonal connectivity. *Eur Phys J B*. (2018) **91**:305. doi: 10.1140/epjb/e2018-90478-8
25. Panaggio MJ, Abrams D. Chimera states: coexistence of coherence and incoherence in networks of coupled oscillators. *Nonlinearity*. (2015) **28**:R67–R87. doi: 10.1088/0951-7715/28/3/R67
26. Schöll E. Synchronization patterns and chimera states in complex networks: interplay of topology and dynamics. *Eur Phys J Spec Top*. (2016) **225**:891–919. doi: 10.1140/epjst/e2016-02646-3
27. Yao N, Zheng Z. Chimera states in spatiotemporal systems: theory and Applications. *Int J Mod Phys B*. (2016) **30**:1630002. doi: 10.1142/S0217979216300024
28. Majhi S, Bera BK, Ghosh D, Perc M. Chimera states in neuronal networks: a review. *Phys Life Rev*. (2018) **28**:100–21. doi: 10.1016/j.plrev.2018.09.003
29. Omel'Chenko OE. The mathematics behind chimera states. *Nonlinearity*. (2018) **31**:R121. doi: 10.1088/1361-6544/aaaa07
30. Omel'Chenko OE, Wolfrum M, Yanchuk S, Maistrenko YL, Sudakov O. Stationary patterns of coherence and incoherence in two-dimensional arrays of non-locally-coupled phase oscillators. *Phys Rev E*. (2012) **85**:036210. doi: 10.1103/PhysRevE.85.036210
31. Panaggio MJ, Abrams D. Chimera states on a flat torus. *Phys Rev B*. (2013) **110**:094102. doi: 10.1103/PhysRevLett.110.094102
32. Kundu S, Majhi S, Bera BK, Ghosh D, Lakshmanan M. Chimera states in two-dimensional networks of locally coupled oscillators. *Phys Rev E*. (2018) **97**:022201. doi: 10.1103/Phys-RevE.97.022201
33. Totz JF, Rode J, Tinsley MR, Showalter K, Engel H. Spiral wave chimera states in large populations of coupled chemical oscillators. *Nat Phys*. (2018) **14**:282–5. doi: 10.1038/s41567-017-0005-8
34. Paul B, Banerjee T. Chimeras in digital phase-locked loops. *Chaos*. (2019) **29**:013102. doi: 10.1063/1.5077052
35. Liu JZ, Zhang LD, Yue GH. Fractal dimension in human cerebellum measured by magnetic resonance imaging. *Biophys J*. (2003) **85**:4041–6. doi: 10.1016/S0006-3495(03)74817-6
36. Katsaloulis P, Verganelakis DA, Provata A. Fractal dimension and lacunarity of tractography images of the human brain. *Fractals*. (2009) **17**:181–9. doi: 10.1142/S0218348X09004284
37. Expert P, Lambiotte R, Chialvo DR, Christensen K, Jensen HJ, Sharp DJ, et al. Self-similar correlation function in brain resting-state functional magnetic resonance imaging. *J R Soc Int*. (2011) **8**:472–9. doi: 10.1098/rsif.2010.0416
38. Katsaloulis P, Ghosh A, Philippe AC, Provata A, Deriche R. Fractality in the neuron axonal topography of the human brain based on 3-D diffusion MRI. *Eur Phys J B*. (2012) **85**:150. doi: 10.1140/epjb/e2012-30045-y
39. Katsaloulis P, Hizanidis J, Verganelakis DA, Provata A. Complexity measures and noise effects on Diffusion Magnetic Resonance Imaging of the neuron axons network in the human brain. *Fluct Noise Lett*. (2012) **11**:1250032. doi: 10.1142/S0219477512500320
40. Hizanidis J, Panagakou E, Omelchenko I, Schöll E, Hövel P, Provata A. Chimera states in population dynamics: networks with fragmented and hierarchical connectivities. *Phys Rev E*. (2015) **92**:012915. doi: 10.1103/PhysRevE.92.012915
41. Tsigkri-DeSmedt ND, Hizanidis J, Hövel P, Provata A. Multi-chimera states and transitions in the Leaky Integrate-and- Fire model with nonlocal and hierarchical connectivity. *Eur Phys J Spec Top*. (2016) **225**:1149–64. doi: 10.1140/epjst/e2016-02661-4
42. Sawicki J, Omelchenko I, Zakharova A, Schöll E. Chimera states in complex networks: interplay of fractal topology and delay. *Eur Phys J Spec Top*. (2017) **226**:1883–92. doi: 10.1140/epjst/e2017-70036-8
43. Chouzouris T, Omelchenko I, Zakharova A, Hlinka J, Jiruska P, Schöll E. Chimera states in brain networks: empirical neural vs. modular fractal connectivity. *Chaos*. (2018) **28**:045112. doi: 10.1063/1.5009812
44. Sawicki J, Omelchenko I, Zakharova A, Schöll E. Delay-induced chimeras in neural networks with fractal topology. *Eur Phys J B*. (2019) **92**:54. doi: 10.1140/epjb/e2019-90309-6
45. Argyropoulos G, Kasimatis T, Provata A. Chimera patterns and subthreshold oscillations in two-dimensional networks of fractally coupled leaky integrate-and-fire neurons. *Phys Rev E*. (2019) **99**:022208. doi: 10.1103/PhysRevE.99.022208.
46. Brunel N, van Rossum MCW. Lapicque's 1907 paper: from frogs to integrate-and-fire. *Brain Res Bull*. (1999) **50**:303–4.
47. Abott LF. Lapicque's introduction of the integrate-and-fire model neuron (1907). *Biol Cybernet*. (2007) **97**:337–9.
48. Kuramoto Y. Collective synchronization of pulse-coupled oscillators and excitable units. *Phys D*. (1990) **50**:15–30.
49. Luccioli S, Politi A. Irregular collective behavior of heterogeneous neural networks. *Phys Rev E*. (2010) **105**:158104. doi: 10.1103/PhysRevLett.105.158104
50. Olmi S, Politi A, Torcini A. Collective chaos in pulse-coupled neural networks. *Eur Lett*. (2010) **92**:60007. doi: 10.1209/0295-5075/92/60007
51. Ullner E, Politi A, Torcini A. Ubiquity of collective irregular dynamics in balanced networks of spiking neurons. *Chaos*. (2018) **28**:081106. doi: 10.1063/1.5049902
52. Kasimatis T, Hizanidis J, Provata A. Three-dimensional chimera patterns in networks of spiking neuron oscillators. *Phys Rev E*. (2018) **97**:052213. doi: 10.1103/PhysRevE.97.052213
53. Mandelbrot BB. *The Fractal Geometry of Nature*. San Francisco, CA: W.H. Freeman and Co. (1982).
54. Takayasu H. *Fractals in Physical Science*. Manchester; New York, NY: Manchester University Press (1991).
55. Omel'Chenko OE, Wolfrum W, Knobloch E. Stability of spiral chimera states on a torus. *SIAM J Appl Dynam Syst*. (2018) **17**:97–127. doi: 10.1137/17M1141151
56. Martens S, Ryll C, Löber J, Tröltzsch F, Engel H. *Control of Traveling Localized Spots*. (2018). Available online at: https://arxivorg/abs/170304246 (accessed September 20, 2018).
57. Nkomo S, Tinsley MR, Showalter K. Chimera and chimera-like states in populations of nonlocally coupled homogeneous and heterogeneous chemical oscillators. *Chaos*. (2016) **26**:094826. doi: 10.1063/1.4962631
58. Isele T, Hizanidis J, Provata A, Hövel P. Controlling chimera states: the influence of excitable units. *Phys Rev E*. (2016) **93**:022217. doi: 10.1103/PhysRevE.93.022217
59. Ruzzene G, Omelchenko I, Schöll E, Zakharova A, Andrzejak RG. Controlling chimera states via minimal coupling modification. *Chaos*. (2019) **29**:0511031. doi: 10.1063/1.5097570

Conflict of Interest Statement: The authors declare that the research was conducted in the absence of any commercial or financial relationships that could be construed as a potential conflict of interest.

frontiers in Applied Mathematics and Statistics

ORIGINAL RESEARCH
published: 12 July 2019
doi: 10.3389/fams.2019.00033

Chimera States in Networks of Locally and Non-locally Coupled SQUIDs

Johanne Hizanidis, Nikos Lazarides and Giorgos P. Tsironis*

Department of Physics, University of Crete, Heraklion, Greece

Planar and linear arrays of SQUIDs (superconducting quantum interference devices) operate as non-linear magnetic metamaterials in microwaves. Such SQUID metamaterials are paradigmatic systems that serve as a test-bed for simulating several non-linear dynamics phenomena. SQUIDs are highly non-linear oscillators which are coupled together through magnetic dipole-dipole forces due to their mutual inductance; that coupling falls-off approximately as the inverse cube of their distance, i.e., it is non-local. However, it can be approximated by a local (nearest-neighbor) coupling which in many cases suffices for capturing the essentials of the dynamics of SQUID metamaterials. For either type of coupling, it is numerically demonstrated that chimera states as well as other spatially non-uniform states can be generated in SQUID metamaterials under time-dependent applied magnetic flux for appropriately chosen initial conditions. The mechanism for the emergence of these states is discussed in terms of the multistability property of the individual SQUIDs around their resonance frequency and the attractor crowding effect in systems of coupled non-linear oscillators. Interestingly, controlled generation of chimera states in SQUID metamaterials can be achieved in the presence of a constant (dc) flux gradient with the SQUID metamaterial initially at rest.

Keywords: SQUID, snaking resonance curve, SQUID metamaterials, magnetic metamaterials, coupled non-linear oscillators, chimera states, attractor crowding, synchronization-desynchronization transition

OPEN ACCESS

Edited by:
Ralph G. Andrzejak, Independent Researcher, Universitat Pompeu Fabra, Spain

Reviewed by:
Lev A. Smirnov, Institute of Applied Physics (RAS), Russia
Axel Hutt, German Weather Service, Germany

****Correspondence:***
Johanne Hizanidis
hizanidis@physics.uoc.gr

Specialty section:
This article was submitted to Dynamical Systems, a section of the journal Frontiers in Applied Mathematics and Statistics

Received: *12 December 2018*
Accepted: *24 June 2019*
Published: *12 July 2019*

Citation:
Hizanidis J, Lazarides N and Tsironis GP (2019) Chimera States in Networks of Locally and Non-locally Coupled SQUIDs. Front. Appl. Math. Stat. 5:33. doi: 10.3389/fams.2019.00033

1. INTRODUCTION

The notion of metamaterials refers to artificially structured media designed to achieve properties not available in natural materials. Originally they were comprising subwavelength resonant elements, such as the celebrated split-ring resonator (SRR). The latter, in its simplest version, is just a highly conducting metallic ring with a slit, that can be regarded as an effectively resistive–inductive–capacitive (*RLC*) electrical circuit. There has been a tremendous amount of activity in the field of metamaterials the last two decades, the results of which have been summarized in a number of review articles [1–8] and books [9–16]. One of metamaterial's most remarkable properties is that of the *negative refraction index*, which results from simultaneously negative dielectric permittivity and diamagnetic permeability.

An important subclass of metamaterials is that of superconducting ones [17, 18], in which the elementary units (i.e., the SRRs) are made by a superconducting material, typically Niobium (*Nb*) [19] or Niobium Nitride (*NbN*) [20], as well as perovskite superconductors such as yttrium barium copper oxide (*YBCO*) [21]. In superconductors, the dc resistance vanishes below a critical

temperature T_c; thus, below T_c, superconducting metamaterials have the advantage of ultra-low losses, a highly desirable feature for prospective applications. Moreover, when they are in the superconducting state, these metamaterials exhibit extreme sensitivity in external stimuli, such as the temperature and magnetic fields, which makes their thermal and magnetic tunability possible [22]. Going a step beyond, the superconducting SRRs can be replaced by SQUIDs [23, 24], where the acronym stands for Superconducting QUantum Interference Devices. The simplest version of such a device consists of a superconducting ring interrupted by a Josephson junction (JJ) [25], as shown schematically in **Figure 1A**; the most common type of a JJ is formed whenever two superconductors are separated by a thin insulating layer (superconductor / insulator / superconductor JJ). The current through the insulating layer and the voltage across the JJ are then determined by the celebrated Josephson relations. Through these relations, the JJ provides a strong and well-studied non-linearity to the SQUID, which makes the latter a unique non-linear oscillator that can be actually manipulated through multiple external means.

SQUID metamaterials are extended systems containing a large number of SQUIDs arranged in various configurations which, from the dynamical systems point of view, can be viewed theoretically as an assembly of weakly coupled non-linear oscillators that inherit the flexibility of their constituting elements (i.e, the SQUIDs). They present a non-linear dynamics laboratory in which numerous classical as well as quantum complex spatio-temporal phenomena can be explored. Recent experiments on SQUID metamaterials have revealed several extraordinary properties, such as negative permeability [26], broad-band tunability [26, 27], self-induced broad-band transparency [28], dynamic multistability and switching [29], as well as coherent oscillations [30]. Moreover, non-linear effects, such as localization of the discrete breather type [31] and non-linear band-opening (non-linear transmission) [32], as well as the emergence of counter-intuitive dynamic states referred to as chimera states in current literature [33–35], have been demonstrated numerically in SQUID metamaterial models [36].

The chimera states, in particular, which were first discovered in rings of non-locally and symmetrically coupled identical phase oscillators [37], have been reviewed thoroughly in recent articles [38–40], are characterized by the coexistence of synchronous and asynchronous clusters of oscillators; their discovery was followed by intense theoretical [41–61] and experimental [62–76] activities, in which chimera states have been observed experimentally or demonstrated numerically in a huge variety of physical and chemical systems.

Here, the possibility for generating chimera states in SQUID metamaterials driven by a time-dependent magnetic flux is demonstrated. These chimera states can be generated from a large variety of initial conditions, and they are characterized using well-established measures. Also, the present work is the first to demonstrate numerically the generation of chimera states while the system is "at rest" (i.e., with zero initial conditions) by using a temporally constant force gradient (i.e, a dc flux gradient) in addition to the time-dependent magnetic flux. In that case, controlled generation of chimera states can be achieved. The SQUIDs in such a metamaterial are coupled together through magnetic dipole-dipole forces due to their mutual inductance. This kind of coupling between SQUIDs falls-off approximately as the inverse cube of their center-to-center distance, and thus it is clearly non-local. However, due to the magnetic nature of the coupling, its strength is weak [27, 30], and thus a nearest-neighbor coupling approach (i.e., a local coupling approach) is often sufficient in capturing the essentials of the dynamics of SQUID metamaterials. Chimera states emerge in SQUID metamaterials with either non-local [33, 35] or local [34] coupling between SQUIDs.

In the next section (Methods), a model for a single SQUID that relies on the equivalent electrical circuit of **Figure 1B** is described, and the dynamic equation for the flux through the ring of the SQUID is derived and normalized. In the same section, the dynamic equations for a one-dimensional (1D) SQUID metamaterial with non-local coupling are derived, and subsequently they are reduced to the local coupling limit. In section 3 (Results), various types of chimera states are presented and characterized using appropriate measures. In this section, the possibility to generate chimera states with a dc flux gradient, is also explored. A brief discussion is given in section 4 (Discussion).

2. METHODS

2.1. The SQUID Oscillator

The simplest version of a SQUID consists of a superconducting ring interrupted by a JJ (**Figure 1A**), which can be modeled by the equivalent electrical circuit of **Figure 1B**; according to that model, the SQUID features a self-inductance L, a capacitance C, a resistance R, and a critical current I_c which characterizes an ideal JJ. A "real" JJ (brown-dashed square in **Figure 1B**) is however modeled as a parallel combination of an ideal JJ, the resistance R, and the capacitance C. When a time-dependent magnetic field is applied to the SQUID in a direction transverse to its ring, the flux threading the SQUID ring induces two types of currents; the supercurrent, which is lossless, and the so-called quasiparticle current which is subject to Ohmic losses. The latter roughly corresponds to the current through the branch containing the resistor R in **Figure 1B**. The (generally time-dependent) flux threading the ring of the SQUID is described in the model as a flux source, Φ_{ext}. Many variants of SQUIDs have been studied for several decades (since 1964) and they have found numerous applications in magnetic field sensors, biomagnetism, non-destructive evaluation, and gradiometers, among others [77, 78]. SQUIDs exhibit very rich dynamics including multistability, complex bifurcation structure, and chaotic behavior [79].

The magnetic flux Φ threading the ring of the SQUID is given by

$$\Phi = \Phi_{ext} + L\,I, \tag{1}$$

where Φ_{ext} is the external flux applied to the SQUID, and

$$I = -C\frac{d^2\Phi}{dt^2} - \frac{1}{R}\frac{d\Phi}{dt} - I_c\,\sin\left(2\pi\,\frac{\Phi}{\Phi_0}\right), \tag{2}$$

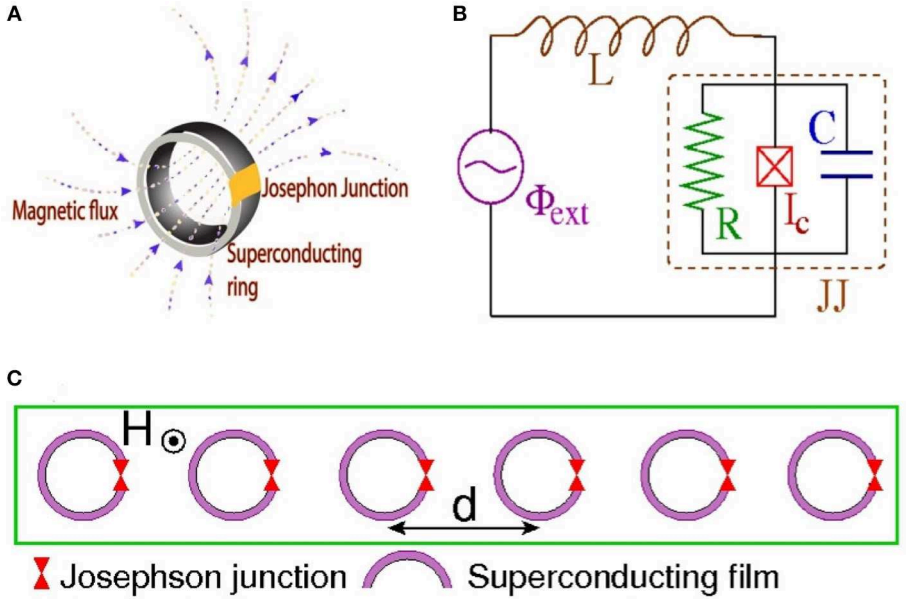

FIGURE 1 | (A) Schematic of a SQUID (superconducting quantum interference device) in a magnetic field. **(B)** Equivalent electrical circuit. **(C)** Schematic top view of a one-dimensional periodic array of SQUIDs in a magnetic field H.

is the total current induced in the SQUID as provided by the resistively and capacitively shunted junction (RCSJ) model of the JJ [80] (the part of the circuit in **Figure 1B** contained in the brown-dashed square), Φ_0 is the flux quantum, and t is the temporal variable. The three terms in the right-hand-side of Equation (2) correspond to the current through the capacitor C, the current through the resistor R, and the supercurrent through the ideal JJ, respectively. The combination of Equations (1) and (2) gives

$$C\frac{d^2\Phi}{dt^2} + \frac{1}{R}\frac{d\Phi}{dt} + I_c \sin\left(2\pi\frac{\Phi}{\Phi_0}\right) + \frac{\Phi - \Phi_{ext}}{L} = 0. \quad (3)$$

Note that losses decrease with increasing Ohmic resistance R, which is a peculiarity of the SQUID device. The external flux usually consists of a constant (dc) term Φ_{dc} and a sinusoidal (ac) term of amplitude Φ_{ac} and frequency ω, i.e., it is of the form

$$\Phi_{ext} = \Phi_{dc} + \Phi_{ac}\cos(\omega t). \quad (4)$$

The normalized form of Equation (3) be obtained by using the relations

$$\phi = \frac{\Phi}{\Phi_0}, \quad \phi_{ac,dc} = \frac{\Phi_{ac,dc}}{\Phi_0}, \quad \tau = \omega_{LC}\, t, \quad \Omega = \frac{\omega}{\omega_{LC}}, \quad (5)$$

where $\omega_{LC} = 1/\sqrt{LC}$ is the inductive-capacitive ($L\,C$) SQUID frequency (geometrical frequency), and the definitions

$$\beta = \frac{I_c L}{\Phi_0} = \frac{\beta_L}{2\pi}, \qquad \gamma = \frac{1}{R}\sqrt{\frac{L}{C}}. \quad (6)$$

for the rescaled SQUID parameter and the loss coefficient, respectively. Thus, we get

$$\ddot{\phi} + \gamma\dot{\phi} + \phi + \beta\sin(2\pi\phi) = \phi_{dc} + \phi_{ac}\cos(\Omega\tau). \quad (7)$$

By substituting $\gamma = 0$ and $\phi_{ext} = 0$ and $\beta\sin(2\pi\phi) \simeq \beta_L\phi$ into Equation (7), we get $\ddot{\phi} + \Omega_{SQ}^2\phi = 0$, with $\Omega_{SQ} = \sqrt{1+\beta_L}$ being the linear eigenfrequency (resonance frequency) of the SQUID. Equation (7) can be also written as

$$\ddot{\phi} + \gamma\dot{\phi} = -\frac{du_{SQ}}{d\phi}, \quad (8)$$

where

$$u_{SQ} = -\phi_{ext}(\tau)\phi + \frac{1}{2}\left[\phi^2 - \frac{\beta}{\pi}\cos(2\pi\phi)\right], \quad (9)$$

is the normalized SQUID potential, and

$$\phi_{ext}(\tau) = \phi_{dc} + \phi_{ac}\cos(\Omega\tau), \quad (10)$$

is the normalized external flux. The SQUID potential u_{SQ} given by Equation (9) is time-dependent for $\phi_{ac} \neq 0$ and $\Omega \neq 0$. Here, parameter values of β_L less than unity ($\beta_L < 1$) are considered, in accordance with recent experiments; in that case, u_{SQ} is a single-well, although non-linear potential. For $\phi_{ext} = \phi_{dc}$, there is no time-dependence; however, the shape of u_{SQ} varies with varying ϕ_{dc}, as it can be seen in **Figure 2**. The potential u_{SQ} is symmetric around a particular ϕ for integer and half-integer values of ϕ_{dc}. In **Figures 2A,C,E**, the potential u_{SQ} is symmetric around $\phi =$ 0, 0.5, and 1, respectively. For all the other values of ϕ_{dc}, the potential u_{SQ} is asymmetric; this asymmetry of u_{SQ} allows for

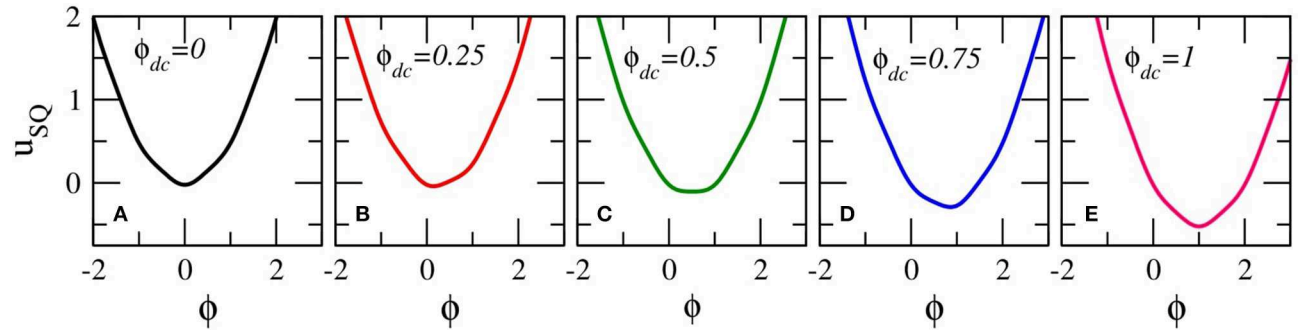

FIGURE 2 | SQUID potential curves $u_{SQ}(\phi)$ for $\beta_L = 0.86$, $\phi_{ac} = 0$, and **(A)** $\phi_{dc} = 0$; **(B)** $\phi_{dc} = 0.25$; **(C)** $\phi_{dc} = 0.5$; **(D)** $\phi_{dc} = 0.75$; **(E)** $\phi_{dc} = 1.0$.

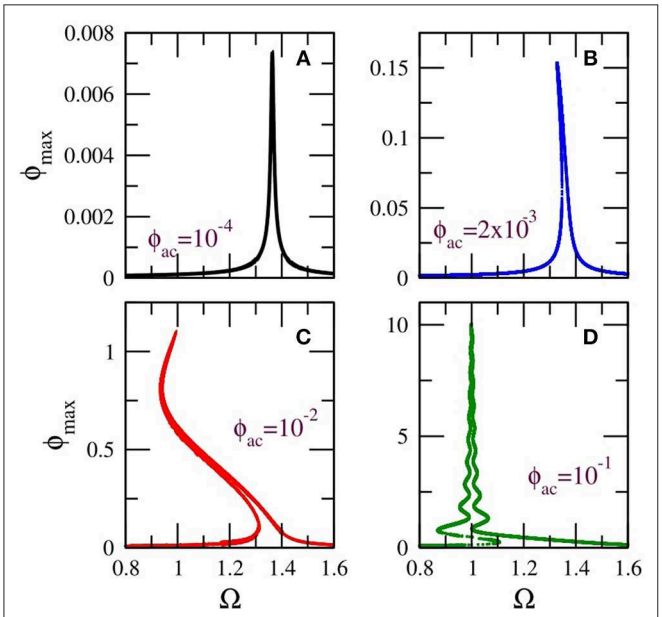

FIGURE 3 | Flux amplitude–driving frequency ($\phi_{max} - \Omega$) curves for a SQUID with $\beta_L = 0.86$, $\gamma = 0.01$, $\phi_{dc} = 0$, and **(A)** $\phi_{ac} = 10^{-4}$, **(B)** $\phi_{ac} = 2 \times 10^{-3}$, **(C)** $\phi_{ac} = 10^{-2}$, **(D)** $\phi_{ac} = 10^{-1}$.

chaotic behavior to appear in an ac and dc driven single SQUID through period-doubling bifurcation cascades. Such cascades and the subsequent transition to chaos are prevented by a symmetric u_{SQ} which renders the SQUID a symmetric system in which period-doubling bifurcations are suppressed [81]. Actually, suppression of period-doubling bifurcation cascades due to symmetry occurs in a large class of systems, including the sinusoidally driven-damped pendulum.

For zero dc flux, the strength of the SQUID non-linearity increases with increasing ac flux amplitude ϕ_{ac}. This effect is illustrated in **Figure 3** in which the flux amplitude—driving frequency ($\phi_{max} - \Omega$) curves, i.e., the resonance curves, for four values of ϕ_{ac} spanning four orders of magnitude are shown (for $\phi_{dc} = 0$). In **Figure 3A**, for $\phi_{ac} = 0.0001$, the SQUID is in the linear regime and thus its $\phi_{max} - \Omega$ curve is apparently symmetric around the linear SQUID eigenfrequency, $\Omega_{SQ} = \sqrt{1+\beta_L} \simeq 1.364$. Weak non-linear effects begin to appear in **Figure 3B**, for $\phi_{ac} = 0.002$, in which the curve is slightly bended to the left. In **Figure 3C**, for $\phi_{ac} = 0.01$, the non-linear effects are already strong enough to generate a multistable $\phi_{max} - \Omega$ curve. In **Figure 3D**, for $\phi_{ac} = 0.1$, the SQUID is in the strongly non-linear regime and the $\phi_{max} - \Omega$ curve has acquired a *snake-like form*. Indeed, the curve "snakes" back and forth within a narrow frequency region via successive saddle-node bifurcations [79]. Note that in **Figures 3C,D**, the frequency region with the highest multistability is located around the geometrical frequency of the SQUID, i.e., at $\Omega \simeq 1$ (the LC frequency in normalized units). Inasmuch the frequency at which ϕ_{max} is highest can be identified with the "resonance" frequency of the SQUID, it can be observed that this resonance frequency lowers with increasing ϕ_{ac} from the linear SQUID eigenfrequency Ω_{SQ} to the inductive-capacitive (geometrical) frequency $\Omega \simeq 1$. Thus, the resonance frequency of the SQUID, where its multistability is highest, can be actually tuned by non-linearity, i.e., by varying the ac flux amplitude ϕ_{ac}. Note that the multistability of the SQUID is a purely dynamic effect, which is not related to any local minima of the SQUID potential (which is actually single-welled for the values of β_L considered here, i.e., for $\beta_L < 1$).

For $\phi_{dc} \neq 0$, chaotic behavior appears in wide frequency intervals below the geometrical frequency ($\Omega = 1$) for relatively high ϕ_{ac}. As it was mentioned above, the SQUID potential u_{SQ} is asymmetric for $\phi_{dc} \neq 0$, and thus the SQUID can make transitions to chaos through period-doubling cascades [79]. In the bifurcation diagram shown in **Figure 4A**, the flux ϕ is plotted at the end of each driving period $T = 2\pi/\Omega$ for several tenths of driving periods (transients have been rejected) as a function of the driving frequency Ω. This bifurcation diagram reveals multistability as well as a reverse period-doubling cascade leading to chaos. That reverse cascade, specifically, begins at $\Omega = 0.64$ with a stable period-2 solution (i.e., whose period is two times that of the driving period T). A period-doubling occurs at $\Omega = 0.638$ resulting in a stable period-4 solution. The next period-doubling, at $\Omega = 0.62$, results in a stable period-8 solution. The last period-doubling bifurcation which is visible in this scale occurs at $\Omega = 0.614$ and results in a stable period-16 solution. More and more period-doubling bifurcations very close to each other lead eventually to chaos at $\Omega = 0.6132$. Note that another stable multiperiodic solution is present in the frequency interval

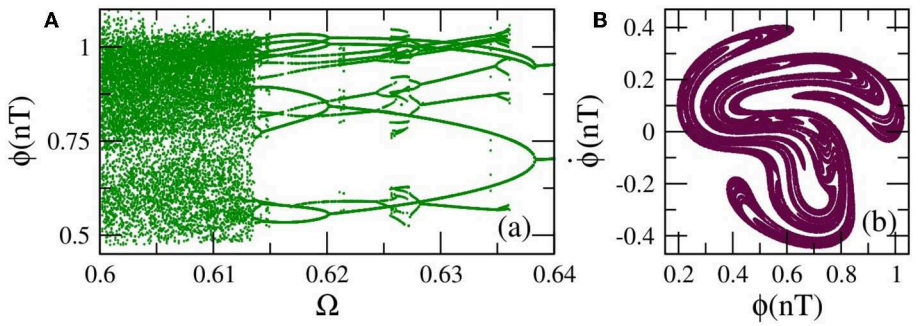

FIGURE 4 | (A) Bifurcation diagram of $\phi(nT)$ as a function of the driving frequency Ω, for $\beta_L = 0.86$, $\gamma = 0.01$, $\phi_{dc} = 0.36$, and $\phi_{ac} = 0.18$. **(B)** A typical chaotic attractor on the $\phi - \dot{\phi}$ phase-plane for $\Omega = 0.6$. The other parameters are as in **(A)**.

shown in **Figure 4A**. A typical chaotic attractor of the SQUID is shown on the $\phi - \dot{\phi}$ phase plane in **Figure 4B** for $\Omega = 0.6$.

2.2. SQUID Metamaterials: Modeling

2.2.1. Flux Dynamics Equations

Consider a one-dimensional periodic arrangement of N identical SQUIDs in a transverse magnetic field **H** as in **Figure 1C**, whose center-to-center distance is d and they are coupled through (non-local) magnetic dipole-dipole forces [33]. The magnetic flux Φ_n threading the ring of the $n-$th SQUID is

$$\Phi_n = \Phi_{ext} + L\, I_n + L \sum_{m \neq n} \lambda_{|m-n|} I_m, \tag{11}$$

where $n, m = 1, ..., N$, Φ_{ext} is the external flux in each SQUID, $\lambda_{|m-n|} = M_{|m-n|}/L$ is the dimensionless coupling coefficient between the SQUIDs at the sites m and n, with $M_{|m-n|}$ being their mutual inductance, and

$$-I_n = C\frac{d^2\Phi_n}{dt^2} + \frac{1}{R}\frac{d\Phi_n}{dt} + I_c \sin\left(2\pi\frac{\Phi_n}{\Phi_0}\right) \tag{12}$$

is the current in the $n-$th SQUID as given by the RCSJ model [80]. The combination of Equations (11) and (12) gives

$$C\frac{d^2\Phi_n}{dt^2} + \frac{1}{R}\frac{d\Phi_n}{dt} + I_c \sin\left(2\pi\frac{\Phi_n}{\Phi_0}\right) + \frac{1}{L}\sum_{m=1}^{N}\left(\hat{\Lambda}^{-1}\right)_{nm}(\Phi_m - \Phi_{ext}) = 0, \tag{13}$$

where $\hat{\Lambda}^{-1}$ is the inverse of the symmetric $N \times N$ coupling matrix with elements

$$\hat{\Lambda}_{nm} = \begin{cases} 1, & \text{if } m = n; \\ \lambda_{|m-n|} = \lambda_1 |m-n|^{-3}, & \text{if } m \neq n, \end{cases} \tag{14}$$

with λ_1 being the coupling coefficient between nearest neighboring SQUIDs. Note that due to the geometry of the SQUID metamaterial considered here, which is planar, and according to standard conventions for loops carrying current flowing in the same direction, the mutual inductance $M_{|m-n|}$ between the $n-$th and the $m-$th SQUIDs is negative ($M_{|m-n|} < 0$ for any n, m with $n \neq m$). Thus, since $L > 0$, the coupling strength $\lambda_{|m-n|}$ is negative. The dependence of the coupling strength on the center-to-center distance between SQUIDs in Equation (14) is due to their mutual inductance $M_{|m-n|}$, which can be obtained using basic expressions from electromagnetism. The magnetic field generated by a wire loop, at a distance d greater than its dimensions, is given by the Biot-Savart law as $B = \frac{\mu_0}{4\pi}\frac{\pi r_w^2 I_w}{d^3}$, where I_w is the current in the wire, r_w is the radius of the loop, which approximate the SQUID geometry, d is the distance from the center of the loop, and μ_0 is the permeability of the vacuum. The magnitude of the mutual inductance between two such (identical) loops lying on the same plane is given by

$$M = \frac{B\pi r_w^2}{I_w} = \frac{\mu_0}{4\pi}\frac{(\pi r_w^2)^2}{d^3} \propto d^{-3}, \tag{15}$$

where it is assumed that the field B is constant over the area of each loop, πr_w^2. For square loops of side a, the radius r_w should be replaced by $a/\sqrt{\pi}$. Equation (15) explains qualitatively the inverse cube distance-dependence of the coupling strength $\lambda_{|m-n|}$ between SQUIDs.

In normalized form Equation (13) reads ($n = 1, ..., N$)

$$\ddot{\phi}_n + \gamma\dot{\phi}_n + \beta\sin(2\pi\phi_n) = \sum_{m=1}^{N}\left(\hat{\Lambda}^{-1}\right)_{nm}(\phi_{ext} - \phi_m), \tag{16}$$

where Equation (5) and the definitions Equation (6) have been used. When nearest-neighbor coupling is only taken into account, Equation (16) reduces to the simpler form

$$\ddot{\phi}_n + \gamma\dot{\phi}_n + \phi_n + \beta\sin(2\pi\phi_n) = \lambda(\phi_{n-1} + \phi_{n+1}) + (1 - 2\lambda)\phi_{ext}, \tag{17}$$

where $\lambda = \lambda_1$.

2.2.2. Local and Non-local Linear Frequency Dispersion

Equation (11) with $\Phi_{ext} = 0$ can be written in matrix form as

$$L\,\hat{\Lambda}\vec{I} = \vec{\Phi}, \tag{18}$$

where the elements of the coupling matrix $\hat{\Lambda}$ are given in Equation (14), and $\vec{I}$, $\vec{\Phi}$ are $N-$dimensional vectors with components I_n, Φ_n, respectively. The linearized equation for the current in the $n-$th SQUID, in the lossless case ($R \to \infty$), is given from Equation (12) as

$$-\vec{I} = C\frac{d^2}{dt^2}\vec{\Phi} + 2\pi\frac{I_c}{\Phi_0}\vec{\Phi}, \tag{19}$$

where the approximation $\sin(x) \simeq x$ has been employed. By substituting Equation (19) into Equation (18), we get

$$\hat{\Lambda}\left(\frac{1}{\omega_{LC}^2}\frac{d^2}{dt^2}\vec{\Phi} + \beta_L\vec{\Phi}\right) + \vec{\Phi} = 0. \tag{20}$$

In component form, the corresponding equation reads

$$\sum_m \hat{\Lambda}_{nm}\left(\frac{1}{\omega_{LC}^2}\frac{d^2}{dt^2}\Phi_m + \beta_L\Phi_m\right) + \Phi_n = 0, \tag{21}$$

or, in normalized form

$$\sum_m \hat{\Lambda}_{nm}\left(\frac{1}{\omega_{LC}^2}\ddot{\phi}_m + \beta_L\phi_m\right) + \phi_n = 0, \tag{22}$$

where the overdots denote derivation with respect to the normalized time $\tau = \omega_{LC}t$.

Substitute the trial (plane wave) solution

$$\phi_n = \exp^{i(\kappa n - \Omega\tau)}, \tag{23}$$

where κ is the dimensionless wavenumber (in units of d^{-1}), into Equation (22) to obtain

$$\Omega^2 = \frac{1}{S}\left(1 + \beta_L S\right), \tag{24}$$

where

$$S = \sum_m \hat{\Lambda}_{nm}\exp^{i\kappa(m-n)}. \tag{25}$$

It can be shown that, for the infinite system, the function S is

$$S = 1 + 2\lambda\sum_{s=1}^{\infty}\frac{\cos(\kappa s)}{|s|^3} = 1 + 2\lambda Ci_3(\kappa), \tag{26}$$

where $s = m - n$, and $Ci_3(\kappa)$ is a Clausen function. Putting Equation (26) into Equation (24), we obtain the non-local frequency dispersion for the 1D SQUID metamaterial as

$$\Omega_\kappa = \sqrt{\frac{\Omega_{SQ}^2 + 2\lambda\beta_L Ci_3(\kappa)}{1 + 2\lambda Ci_3(\kappa)}}, \tag{27}$$

where $\Omega_{SQ}^2 = 1 + \beta_L$. In the case of local (nearest-neighbor) coupling the Clausen function $Ci_3(\kappa)$ is replaced by $\cos(\kappa)$. Then, by neglecting terms of order λ^2 or higher, the local frequency dispersion

$$\Omega_\kappa \simeq \sqrt{\Omega_{SQ}^2 - 2\lambda\cos(\kappa)} \tag{28}$$

is obtained.

The linear frequency dispersion $\Omega = \Omega_\kappa$, calculated for non-local and local coupling from Equations (27) and (28), respectively, is plotted in **Figure 5** for three values of the coupling coefficient λ. The differences between the non-local and local dispersion are rather small, especially for low values of λ, i.e., for $\lambda = -0.02$ (**Figure 5A**), which are mostly considered here. Although the linear frequency bands are narrow, the bandwidth $\Delta\Omega = \Omega_{max} - \Omega_{min}$ increases with increasing λ. For simplicity, the bandwidth $\Delta\Omega$ can be estimated from Equation (28); from that equation the minimum and maximum frequencies of the band can be approximated by $\Omega_{min,max} \simeq \Omega_{SQ}\left(1 \pm \frac{\lambda}{\Omega_{SQ}^2}\right)$, so that

$$\Delta\Omega \simeq \frac{2|\lambda|}{\Omega_{SQ}}. \tag{29}$$

That is, the bandwidth is roughly proportional to the magnitude of λ. Note that for physically relevant parameters, the minimum frequency of the linear band is well above the geometrical (i.e., inductive-capacitive) frequency of the SQUIDs in the metamaterial. Thus, for strong non-linearity, for which the resonance frequency of the SQUIDs is close to the geometrical one ($\Omega = 1$), no plane waves can be excited. It is this frequency region where localized and other spatially inhomogeneous states, such as chimera states are expected to emerge (given also the extreme multistability of individual SQUIDs there).

3. RESULTS

3.1. Chimeras and Other Spatially Inhomogeneous States

Equation (16) are integrated numerically in time with free-end boundary conditions ($\phi_{N+1} = \phi_0 = 0$) using a fourth-order Runge-Kutta algorithm with time-step $h = 0.02$. The initial conditions have been chosen so that they lead to chimera states. It should be noted that chimera states can be obtained from a huge variety of initial conditions. Here we choose

$$\phi_n(\tau = 0) = \begin{cases} 1, \text{ for } n_\ell < n \leq n_r; \\ 0, \text{ otherwise,} \end{cases} \tag{30}$$

$$\dot{\phi}_n(\tau = 0) = 0, \tag{31}$$

with $n_\ell = 18$ and $n_r = 36$. The number of SQUIDs in the metamaterial in all calculations below is $N = 54$. Equation (16) are first integrated in time for a relatively long time-interval, 10^7 T time-units, where $T = 2\pi/\Omega$ is the driving period, so that the system has reached a steady-state. While the SQUID metamaterial is in the steady-state, Equation (16) are integrated for $\tau_{sst} = 1000$ T more time-units. Then, the profiles of the

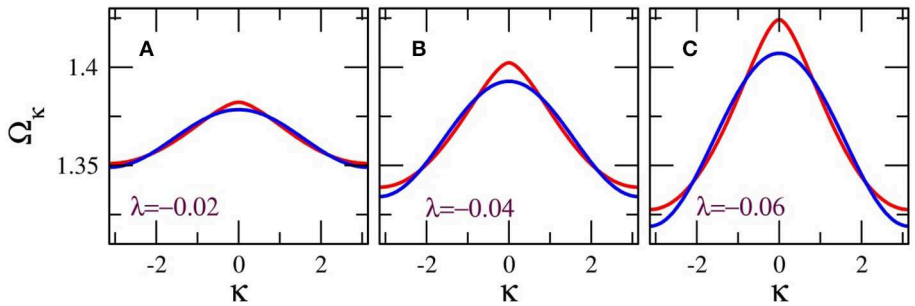

FIGURE 5 | Linear frequency dispersion $\Omega = \Omega_\kappa$ for non-local (red) and local (blue) coupling, for $\beta_L = 0.86$, and **(A)** $\lambda = -0.02$, **(B)** $\lambda = -0.04$; **(C)** $\lambda = -0.06$.

time-derivatives of the fluxes, averaged over the driving period T, i.e.,

$$\langle \dot{\phi}_n \rangle_T = \frac{1}{T} \int_0^T \dot{\phi}_n \, d\tau, \quad n = 1, ..., N, \tag{32}$$

are mapped as a function of τ. Such maps are shown in **Figure 6**, for several values of the ac flux amplitude, ϕ_{ac}. In these maps, areas with uniform colorization indicate that the SQUID oscillators there are synchronized, while areas with non-uniform colorization indicate that they are desynchronized.

In **Figures 6A,B**, i.e., for low values of ϕ_{ac}, chimera states are not excited since the $\langle \dot{\phi}_n \rangle_T$ are practically zero during the steady-state integration time. However, this does not mean that the state of the SQUID metamaterial is spatially homogeneous, as we shall see below. For higher values of ϕ_{ac}, chimera states begin to appear, in which one or more desynchronized clusters of SQUID oscillators roughly in the middle of the SQUID metamaterial are visible (**Figures 6C–E**). For even higher values of ϕ_{ac}, as can be seen in **Figure 6F**, the whole SQUID metamaterial is desynchronized. In order to quantify the degree of synchronization for SQUID metamaterials at a particular time-instant τ, the magnitude of the complex synchronization (Kuramoto) parameter r is calculated, where

$$r(\tau) = \left| \Psi(\tau) \right| = \frac{1}{N} \left| \sum_n e^{i[2\pi \phi_n(\tau)]} \right|. \tag{33}$$

Note that the phase in the earlier equation, which is enclosed in the square brackets, $2\pi\phi_n(\tau)$, or $2\pi\Phi_n(\tau)/\Phi_0$ in natural units, is actually the argument of the sine term in Equation (13). Below, two averages of $r(\tau)$ are used for the characterization of a particular state of SQUID metamaterials, i.e., the average of $r(\tau)$ over the driving period T, $\langle r \rangle_T(\tau)$, and the average of $r(\tau)$ over the steady-state integration time $\langle r \rangle_{sst}$. These are defined, respectively, as

$$\left\langle r(\tau) \right\rangle_T = \frac{1}{T} \int_0^T r(\tau) \, d\tau, \qquad \langle r \rangle_{sst} = \frac{1}{\tau_{sst}} \int_0^{\tau_{sst}} r(\tau) \, d\tau. \tag{34}$$

The calculated $\langle r \rangle_T(\tau)$ for the states shown in **Figure 6**, clarify further their nature. In **Figure 7A**, $\langle r \rangle_T(\tau)$ is plotted as a function of time τ for all the six states presented in **Figure 6**. It can be seen that for $\phi_{ac} = 0.02$ and 0.04 (black and red curves), calculated for the states of the SQUID metamaterial in **Figures 6A,B**, respectively, $\langle r \rangle_T(\tau)$ is constant in time, although less than unity. For such states, $\langle r \rangle_T(\tau) = \langle r \rangle_{sst}$, where $\langle r \rangle_{sst}$ can be inferred from **Figure 7B** for the curves of interest to be $\langle r \rangle_{sst} \simeq 0.972$ and $\langle r \rangle_{sst} \simeq 0.894$ for $\phi_{ac} = 0.02$ and 0.04, respectively. The lack of fluctuations indicates that these states consist of "clusters" in which the SQUID oscillators are synchronized together. However, the clusters are not synchronized to each other, resulting in a partially synchronized state with $\langle r \rangle_T(\tau) < 1$. The exact nature of these partially synchronized states can be clarified by plotting the flux profiles ϕ_n at the end of the steady-state integration time as shown in **Figures 7C,D**. In these figures, it can be observed that all but a few SQUID oscillators are synchronized; in addition, those few SQUIDs execute high-amplitude flux oscillations. Moreover, it has been verified that the frequency of all the flux oscillations is that of the driving, Ω. Such states can be classified as discrete breathers/multi-breathers, i.e., spatially localized and time-periodic excitations which have been proved to emerge generically in non-linear networks of weakly coupled oscillators [82]. In the present case, the multibreathers shown in **Figures 7C,D** can be further characterized as *dissipative* ones [83], since they emerge through a delicate balance of input power and intrinsic losses. They have been investigated in some detail in SQUID metamaterials in one and two dimensions [31, 84–86], as well as in SQUID metamaterials on two-dimensional Lieb lattices [87].

The corresponding $\langle r \rangle_T(\tau)$ for the states shown in **Figures 6C–F**, are shown in **Figure 7A** as green, blue, orange, and brown curves, respectively. In these curves there are apparently fluctuations around their temporal average over the steady-state integration time (shown in **Figure 7B**). These fluctuations are typically associated with the level of metastability of the chimera states [88, 89]; an appropriate measure of metastability for SQUID metamaterials is the full-width half-maximum (FWHM) of the distribution of $\langle r \rangle_T$ [33]. The FWHM can be used to compare the metastability levels of different chimera states. For synchronized (spatially homogeneous) and partially synchronized states, such as those in **Figures 6A,B**, the FWHM of the corresponding distribution of the values of $\langle r \rangle_T$ is practically zero.

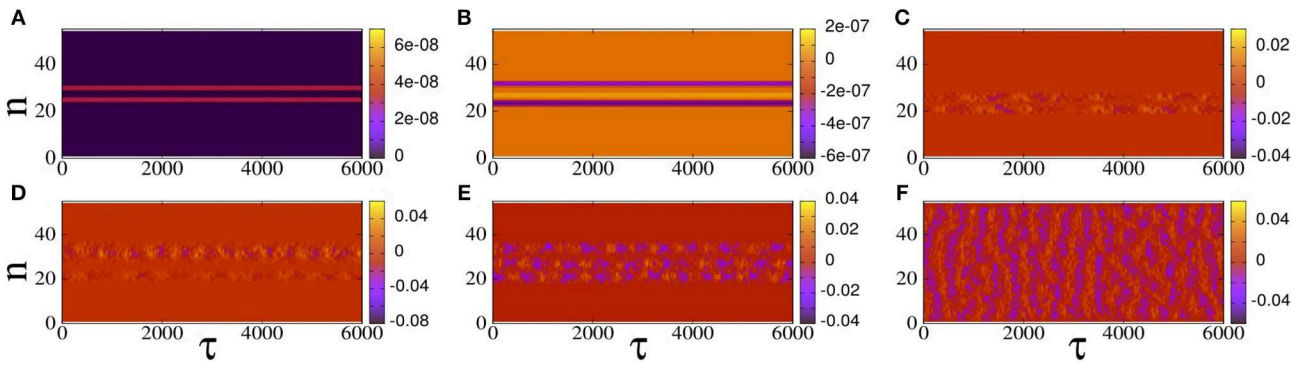

FIGURE 6 | Maps of $\langle\dot{\phi}_n\rangle(\tau)$ on the $n-\tau$ plane for $\beta_L = 0.86$, $\gamma = 0.01$, $\lambda = -0.02$, $\Omega = 1.01$, $N = 54$, $\phi_{dc} = 0$, and **(A)** $\phi_{ac} = 0.02$, **(B)** $\phi_{ac} = 0.04$, **(C)** $\phi_{ac} = 0.06$, **(D)** $\phi_{ac} = 0.08$, **(E)** $\phi_{ac} = 0.10$, **(F)** $\phi_{ac} = 0.12$.

Another set of initial conditions which gives rise to chimera states is of the form [34]

$$\phi_n(\tau = 0) = \frac{1}{2}\cos\left(\frac{2j\pi n}{N}\right), \qquad \dot{\phi}_n(\tau = 0) = 0, \quad n = 1, ..., N. \tag{35}$$

The initial conditions in Equation (35) allow for generating multiclustered chimera states, in which the number of clusters depends on j. In **Figures 8A,B**, maps of $\langle\dot{\phi}_n\rangle_T$ on the $n-\tau$ plane for $j = 1$ and $j = 2$, respectively, are shown. In **Figure 8A**, three large clusters can be distinguished; in the two of them, the SQUID oscillators are synchronized, while in the third one, in between the two sychronized clusters, the SQUID oscillators are desynchronized. The flux profile ϕ_n of that state at the end of the steady-state integration time $\tau_{sst} = 6,000$, is shown in **Figure 8C** as blue circles (the black curve is a guide to the eye) along with the initial condition (red curve). It can be seen that two more desynchronized clusters at the ends of the metamaterial, which are rather small (they consist of only a few SQUIDs each), are visible. Obviously, the synchronized clusters correspond to the spatial interval indicated by the almost horizontal segments in the ϕ_n profile. The corresponding $\langle\dot{\phi}_n\rangle_T$ map and flux profile ϕ_n for $j = 2$ is shown in **Figures 8B,D**, respectively. In this case, a number of six (6) synchronized clusters and seven (7) desynchronized clusters are visible in both **Figures 8B,D**. In **Figure 8D**, the red curve is the initial condition from Equation (35) with $j = 2$. Chimera states with even more "heads" can be generated from the initial condition Equation (35) for $j > 2$ in larger systems (here $N = 54$).

Similar chimera states can be generated with local (nearest-neighbor) coupling between the SQUIDs of the metamaterial. For that purpose, Equation (17) is integrated in time using a fourth order Runge-Kutta algorithm with free-end boundary conditions and the initial conditions of Equation (30). As above, in order to eliminate transients and reach a steady-state, Equation (17) is integrated for 10^7 T time units and the results are discarded. Then, Equation (17) is integrated for $\tau_{sst} = 10^3$ T more time units (steady-state integration time), and $\langle\dot{\phi}_n\rangle_T$ is mapped on the $n-\tau$ plane (**Figure 9**). The emerged states are very similar to those shown in **Figure 6**, which is the case of non-local coupling between the SQUIDs. In particular, the states shown in **Figures 9A–C**, have been generated for exactly the same parameters and initial-boundary conditions as those in **Figures 6C,E,F**, respectively, i.e, for $\phi_{ac} = 0.06$, 0.1, and 0.12. Note that the state of the SQUID metamaterial for $\phi_{ac} = 0.12$ is completely desynchronized both in **Figures 6F**, **9C**. One may also compare the plots of the corresponding $\langle r\rangle_T$ as a function of τ, which are shown in **Figure 9D** for the local coupling case. The averages of r over the steady-state integration time τ_{sst} for $\phi_{ac} = 0.06$, 0.1, 0.12 are respectively, $\langle r\rangle_{sst} = 0.757$, 0.656, 0.136 for the non-local coupling case and $\langle r\rangle_{sst} = 0.743$, 0.656, 0.146 for the local coupling case. The probability distribution function of the values of $\langle r\rangle_T$, $pdf(\langle r\rangle_T)$, for the three states in **Figures 9A–C** are shown in **Figures 9E–G**, respectively. As it was mentioned above, the FWHM of such a distribution is a measure of the metastability of the corresponding chimera state. The FWHM for the distributions in **Figures 9E,F**, calculated for the chimera states shown in **Figures 9A,B**, are respectively 0.003 and 0.0215. Thus, it can be concluded that the chimera state of **Figure 9B** is more metastable than that in **Figure 9A**. The distribution in **Figure 9G** has a FWHM much larger than the ones of the distributions in **Figures 9E,F** as expected, since it has been calculated for the completely desynchronized state of **Figure 9C**. Note that 10^6 values of $\langle r\rangle_T$ have been used to obtain each of the three distributions. Also, these distributions are normalized such that their area sums to unity.

The chimera states do not result from destabilization of the synchronized state of the SQUID metamaterial; instead, they coexist with the latter, which can be reached simply by integrating the relevant flux dynamics equations with zero initial conditions, i.e., with $\phi_n(\tau = 0) = 0$ and $\dot{\phi}_n(\tau = 0) = 0$ for any n. In order to reach a chimera state, on the other hand, appropriately chosen initial conditions, such as those in Equations (30) or (35) have to be used. However, one cannot expect that the synchronized state is stable over the whole external parameter space, i.e., the ac flux amplitude ϕ_{ac}, the frequency of the ac flux field Ω, and the dc flux bias ϕ_{dc}. In order to explore the stability of the synchronized state of the SQUID metamaterial, the magnitude of the synchronization parameter averaged over the steady-state integration time, $\langle r\rangle_{sst}$, is calculated and then

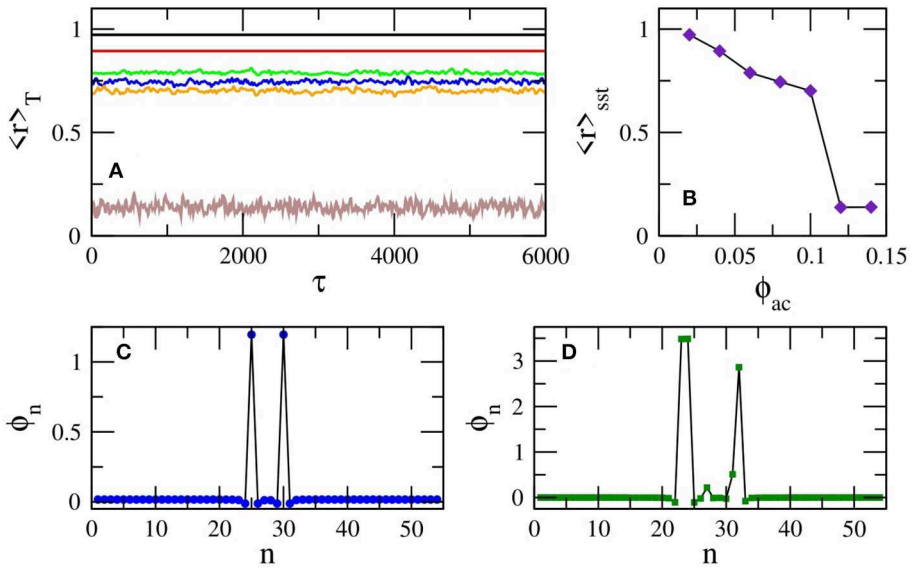

FIGURE 7 | (A) The magnitude of the synchronization parameter averaged over the driving period, $\langle r \rangle_T$, as a function of time τ for $\beta_L = 0.86$, $\gamma = 0.01$, $\lambda = -0.02$, $\Omega = 1.01$, $N = 54$, $\phi_{dc} = 0$, and $\phi_{ac} = 0.02$ (black), $\phi_{ac} = 0.04$ (red), $\phi_{ac} = 0.06$ (green), $\phi_{ac} = 0.08$ (blue), $\phi_{ac} = 0.10$ (orange), $\phi_{ac} = 0.12$ (brown). **(B)** The magnitude of the synchronization parameter averaged over the steady-state integration time τ_{sst}, $\langle r \rangle_{sst}$, as a function of the ac flux amplitude ϕ_{ac}. The other parameters are as in **(A)**. **(C)** The flux profile ϕ_n for $\phi_{ac} = 0.02$ and the other parameters as in **(A)**. **(D)** The flux profile ϕ_n for $\phi_{ac} = 0.04$ and the other parameters as in **(A)**.

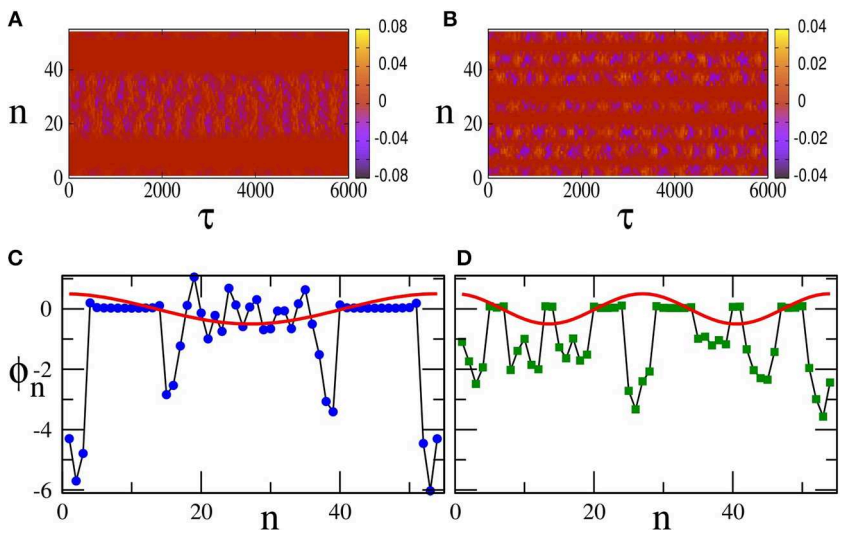

FIGURE 8 | (A) Map of $\langle \dot{\phi}_n \rangle_T$ on the $n - \tau$ plane for $\beta_L = 0.86$, $\gamma = 0.01$, $\lambda = -0.02$, $\Omega = 1.01$, $N = 54$, $\phi_{dc} = 0$, $\phi_{ac} = 0.1$, and initial conditions given by Equation (35) with $j = 1$. **(B)** Same as in **(A)** with initial conditions given by Equation (35) with $j = 2$. **(C)** Flux profile ϕ_n at the end of the steady-state integration time (blue circles, the black line is a guided to the eye), obtained with the initial conditions Equation (35) with $j = 1$ (red curve). **(D)** Flux profile ϕ_n at the end of the steady-state integration time (blue circles, the black line is a guided to the eye), obtained with the initial conditions Equation (35) with $j = 2$ (red curve).

mapped on the $\phi_{dc} - \phi_{ac}$ parameter plane. For each pair of ϕ_{ac} and ϕ_{dc} values, the SQUID metamaterial is initialized with zeros (it is at "rest"). Once again, the frequency Ω is chosen to be very close to the geometrical resonance Ω_{LC} ($\Omega \simeq 1$). In **Figure 10**, maps of $\langle r \rangle_{sst}$ on the $\phi_{dc} - \phi_{ac}$ plane are shown for four driving frequencies Ω around unity. These maps are a kind of *"synchronization phase diagrams"*, in which $\langle r \rangle_{sst} = 1$ indicates a synchronized state while $\langle r \rangle_{sst} < 1$ indicates a partially or completely desynchronized state. In all subfigures, but perhaps most clearly seen in **Figure 10C** (for $\Omega = 1.01$) there are abrupt transitions between completely synchronized (red areas) and completely desynchronized (light blue areas) states. It can

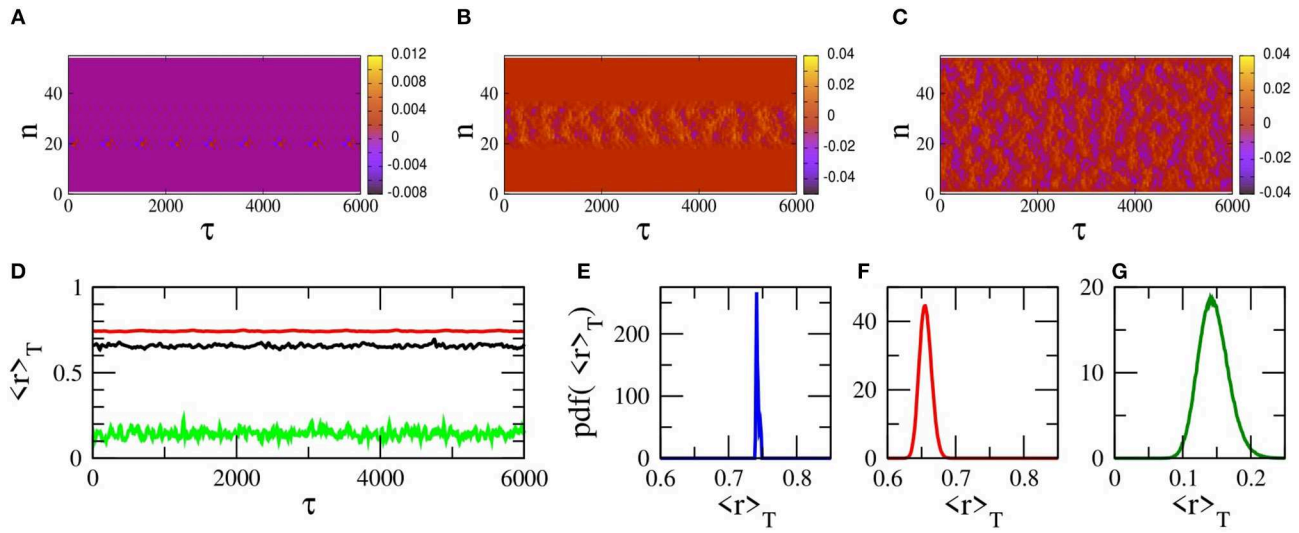

FIGURE 9 | (A) Map of $\langle \dot{\phi}_n \rangle_T$ on the $n - \tau$ plane for $\beta_L = 0.86$, $\gamma = 0.01$, $\lambda = -0.02$, $\Omega = 1.01$, $N = 54$, $\phi_{dc} = 0$, $\phi_{ac} = 0.06$, and initial conditions given by Equation (30). **(B)** Same as in **(A)** but with $\phi_{ac} = 0.10$. **(C)** Same as in **(A,B)** but with $\phi_{ac} = 0.12$. **(D)** The magnitude of the synchronization parameter averaged over the driving period, $\langle r \rangle_T$, as a function of time τ for $\phi_{ac} = 0.06$ (red), $\phi_{ac} = 0.1$ (black), and $\phi_{ac} = 0.12$ (green). The other parameters are as in **(A)**. **(E)** The distribution of 10^6 values of $\langle r \rangle_T$, $pdf(\langle r \rangle_T)$, for the chimera state shown in **(A)**. **(F)** Same as in **(E)** for the chimera state shown in **(B)**. **(G)** Same as in **(E,F)** for the completely desynchronized state shown in **(C)**.

be verified by inspection of the flux profiles (not shown) that these synchronization-desynchronization transitions do not go through a stage in which chimera states are generated; instead, the destabilization of a synchronized state results either in a completely desynchronized state (light blue areas) or a clustered state (green areas). Thus, it seems that chimera states cannot be generated when the SQUID metamaterial is initially at "rest," i.e., with zero initial conditions. As we shall see in the next subsection, this is not true for a position-dependent external flux $\phi_{ext} = \phi_{ext}(n)$.

3.2. Chimera Generation by dc Flux Gradients

3.2.1. Modified Flux Dynamics Equations

In obtaining the results of **Figure 10**, a spatially homogeneous dc flux ϕ_{dc} over the whole SQUID metamaterial is considered. Although, all the chimera states presented here are generated at $\phi_{dc} = 0$, such states can be also generated in the presence of a spatially constant, non-zero ϕ_{dc}, by using appropriate initial conditions (not shown here). In this subsection, the generation of chimera states in SQUID metamaterials driven by an ac flux and biased by a dc flux gradient is demonstrated, for the SQUID metamaterial being initially at "rest." The application of a dc flux gradient along the SQUID metamaterial is experimentally feasible with the set-up of Zhang et al. [28]. Consider the SQUID metamaterial model in section 2.2.1 in the case of local coupling (for simplicity), in which the dc flux is assumed to be position-dependent, i.e., $\phi_{dc} = \phi_n^{dc}$. Then, Equation (17) can be easily modified to become

$$\ddot{\phi}_n + \gamma \dot{\phi}_n + \phi_n + \beta \sin(2\pi\phi_n) = \phi_n^{eff}(\tau) + \lambda(\phi_{n-1} + \phi_{n+1}), \quad (36)$$

where

$$\phi_n^{eff} = \phi_n^{ext} - \lambda(\phi_{n-1}^{ext} + \phi_{n+1}^{ext}), \quad (37)$$

with

$$\phi_n^{ext} = \phi_n^{dc} + \phi_{ac}\cos(\Omega\tau). \quad (38)$$

In the following, the dc flux function ϕ_n^{dc} is assumed to be of the form

$$\phi_n^{dc} = \frac{n-1}{N-1}\phi_{max}^{dc}, \qquad n = 1, ..., N, \quad (39)$$

so that the dc flux bias increases linearly from zero (for the SQUID at $n = 1$) to ϕ_{max}^{dc} (for the SQUID at the $n = N$).

3.2.2. Controlled Generation of Chimera States

Equations (36) are integrated numerically in time with free-end boundary conditions (Equation 36) using a fourth-order Runge-Kutta algorithm with time-step $h = 0.02$. The SQUID metamaterial is initially at "rest," i.e.,

$$\phi_n(\tau = 0) = 0, \qquad \dot{\phi}_n(\tau = 0) = 0, \quad n = 1, ..., N. \quad (40)$$

This system is integrated for 10^5 T time units to eliminate the transients and then for more $\tau_{sst} = 10^5$ T time units during which the temporal averages $\langle r \rangle_{sst}$ and $\langle r \rangle_T(\tau)$ are calculated. Note that the transients die-out faster in this case since the SQUID metamaterial is initialized with zeros. Typical flux profiles ϕ_n, plotted at the end of the steady-state integration time are shown in **Figures 11A–I**. The varying parameter in this case is ϕ_{max}^{dc}, which actually determines the gradient of the dc flux. The state of

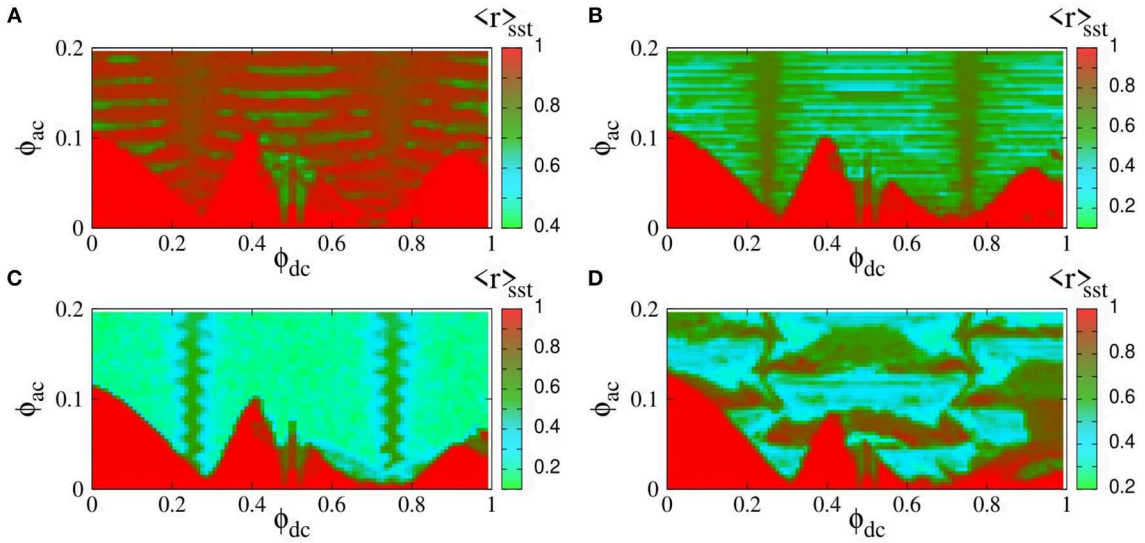

FIGURE 10 | Map of the magnitude of the synchronization parameter averaged over the steady-state integration time, $\langle r \rangle_{sst}$, on the dc flux bias–ac flux amplitude ($\phi_{dc} - \phi_{ac}$) parameter plane, for $\beta_L = 0.86$, $\gamma = 0.01$, $\lambda = -0.02$, $N = 54$, and **(A)** $\Omega = 1.03$, **(B)** $\Omega = 1.02$, **(C)** $\Omega = 1.01$, **(D)** $\Omega = 0.982$.

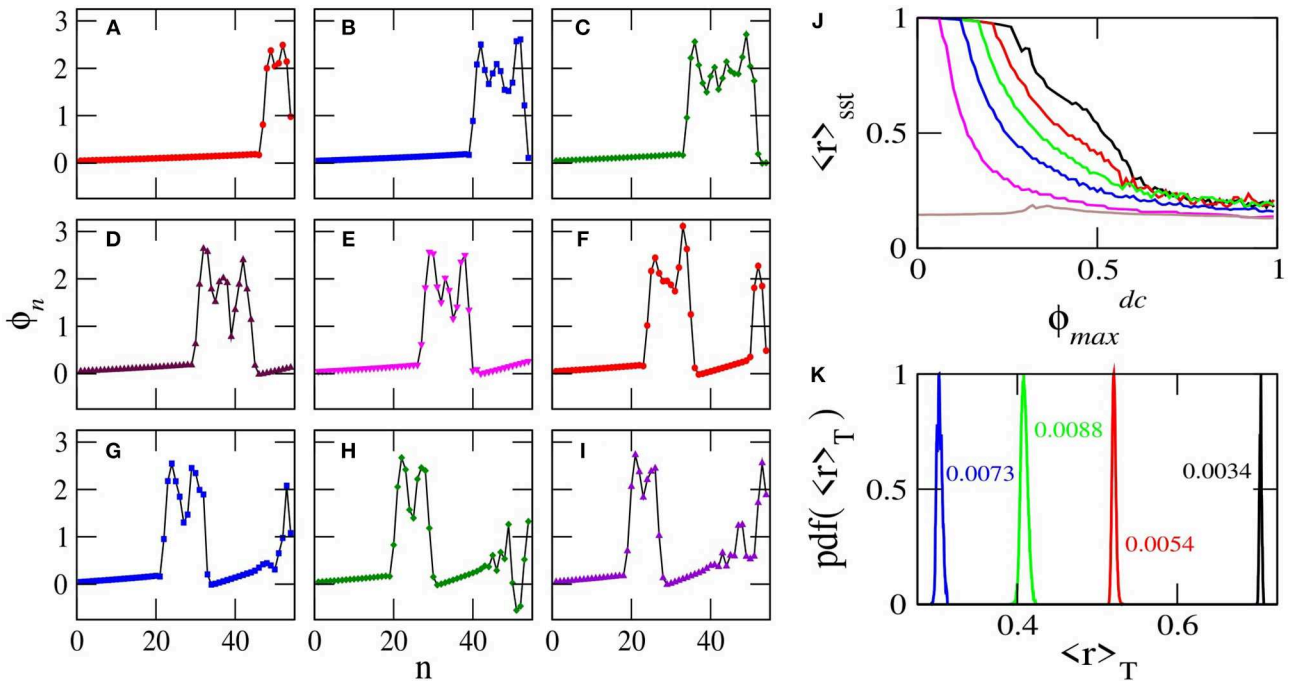

FIGURE 11 | Flux profiles ϕ_n as a function of n for $\beta_L = 0.86$, $\gamma = 0.01$, $\lambda = -0.02$, $N = 54$, $\phi_{ac} = 0.04$, $\Omega = 1.01$, and **(A)** $\phi_{max}^{dc} = 0.25$; **(B)** 0.30; **(C)** 0.35; **(D)** 0.40; **(E)** 0.45; **(F)** 0.50; **(G)** 0.55; **(H)** 0.60; **(I)** 0.65. **(J)** The magnitude of the synchronization parameter averaged over the steady-state integration time $\langle r \rangle_{sst}$ as a function of ϕ_{max}^{dc} for the parameters of **(A–I)** but with $\phi_{ac} = 0.02$ (black), 0.04 (red), 0.06 (green), 0.08 (blue), 0.10 (magenta), 0.12 (brown). **(K)** Distributions of the values of $\langle r \rangle_T$ for $\phi_{ac} = 0.04$, and $\phi_{max}^{dc} = 0.30$ (black), 0.40 (red), 0.50 (green), 0.60 (blue). The other parameters as in **(A–I)**. The numbers next to the distributions are the corresponding full-width half-maximums.

the SQUID metamaterial remains almost homogeneous in space for ϕ_{max}^{dc} increasing from zero to $\phi_{max}^{dc} = 0.22$. At that critical value of ϕ_{max}^{dc}, the spatially homogeneous (almost synchronized) state breaks down, for several SQUIDs close to $n = N$ become desynchronized with the rest (because the dc flux is higher at this end). The number of desynchronized SQUIDs for $\phi_{max}^{dc} = 0.25$ is about $6 - 7$ (**Figure 11A**). For further increasing ϕ_{max}^{dc}, more and more SQUIDs become desynchronized, until they form a well-defined desynchronized cluster (**Figure 11B** for $\phi_{max}^{dc} = 0.30$). As ϕ_{max}^{dc} continues to increase, the desynchronized cluster clearly

shifts to the left, i.e., toward $n = 1$ (**Figures 11C–E**). Further increase of ϕ^{dc}_{max} generates a second desynchronized cluster around $n = N$ for $\phi^{dc}_{max} = 0.50$ (**Figure 11F**), which persists for values of ϕ^{dc}_{max} at least up to 0.65. With the formation of the second desynchronized cluster, the first one clearly becomes smaller and smaller with increasing ϕ^{dc}_{max} (see **Figures 11F–I**). Above, the expression "almost homogeneous" was used instead of simply "homogeneous," because complete homogeneity is not possible due to the dc flux gradient. However, for $\phi^{dc}_{max} < 0.22$, the degree of homogeneity (synchronization) is more than 99%, i.e., the values of the synchronization parameter $\langle r\rangle_{sst}$ are higher than 0.99 ($\langle r\rangle_{sst} > 0.99$). The dependence of $\langle r\rangle_{sst}$ on ϕ^{dc}_{max} for several values of the ac flux amplitude ϕ_{ac} is shown in **Figure 11J**. The SQUID metamaterial remains in an almost synchronized state (with $\langle r\rangle_{sst} > 0.96$ below a critical value of ϕ^{dc}_{max}, which depends on the ac flux amplitude ϕ_{ac}. That critical value of ϕ^{dc}_{max} is lower for higher ϕ_{ac}. For values of ϕ^{dc}_{max} higher than the critical one, $\langle r\rangle_{sst}$ gradually decreases until it saturates at $\langle r\rangle_{sst} \simeq 0.12$. For $\phi_{ac} = 0.12$, the SQUID metamaterial is in a completely desynchronized state for any value of ϕ^{dc}_{max} (brown curve). The distributions of the values of $\langle r\rangle_T$, obtained during the steady-state integration time, are shown in **Figure 11K** for $\phi^{dc}_{max} = 0.30$ (black), 0.40 (red), 0.50 (green), and 0.60 (blue). As expected, the maximum of the distributions shifts to lower $\langle r\rangle_T$ with increasing ϕ^{dc}_{max}. These distributions have been divided by their maximum value for easiness of presentation, and the number next to each distribution is its full-width half-maximum (FWHM).

Two typical "synchronization phase diagrams," in which $\langle r\rangle_{sst}$ is mapped on the $\phi_{ac} - \phi^{dc}_{max}$ parameter plane, are shown in **Figures 12A,B** for $\lambda = -0.02$ and $\lambda = -0.06$, respectively. The frequency of the driving ac field has been chosen once again to be very close to the geometrical resonance of a single SQUID oscillator, i.e., at $\Omega = 1.01$. For each point on the $\phi_{ac}-\phi^{dc}_{max}$ plane, Equation (36) are integrated in time with a standard fourth order Runge-Kutta algorithm using the initial conditions of Equation (40), with a time-step $h = 0.02$. First, Equation (36) are integrated for 10^5 T time-units to eliminate transients, and then they are integrated for $\tau_{sst} = 10^5$ T more time-units during which $\langle r\rangle_{sst}$ is calculated. A comparison between **Figures 12A,B** reveals that the increase of the coupling strength between nearest-neighboring SQUIDs from $\lambda = -0.02$ to $\lambda = -0.06$ results in relatively moderate, quantitative differences only. In both **Figures 12A,B**, for values of ϕ_{ac} and ϕ^{dc}_{max} in the red areas, the state of the SQUID metamaterial is synchronized. For values of ϕ_{ac} and ϕ^{dc}_{max} in the dark-green, light-green and light-blue areas, the state of the SQUID metamaterial is either completely desynchronized, or a chimera state with one or more desynchronized clusters. In order to obtain more information about these states, additional measures should be used, such as the incoherence index S and the chimera index η.The definitions of these two measures follow closely those of previous works [90, 91], with the only difference being the choice of the relevant parameter on which subsequent calculations are performed. Specifically, here the time-derivative of the normalized fluxes through the loops of the SQUIDs, averaged over the driving period T, $\langle\dot{\phi}_n\rangle_T(\tau)$, is chosen as the relevant variable. Note that a similar definition of the chimera index, using the magnitude of the synchronization (Kuramoto) parameter as the relevant variable, has been also proposed [88].

The definitions for S and η employed here are as follows: First, define

$$\nu_n(\tau) \equiv \langle\dot{\phi}_n\rangle_T(\tau), \tag{41}$$

where the angular brackets denote averaging over T, and

$$\bar{\nu}_n(\tau) \equiv \frac{1}{n_0+1}\sum_{j=n-n_0/2}^{n+n_0/2}\nu_j(\tau), \tag{42}$$

the local spatial average of $\nu_n(\tau)$ in a region of length $n_0 + 1$ around the site n at time τ ($n_0 < N$ is an integer). Then, the local standard deviation of $\nu_n(\tau)$ is defined as

$$\sigma_n(\tau) \equiv \left\langle\sqrt{\frac{1}{n_0+1}\sum_{j=n-n_0/2}^{n+n_0/2}\left(\nu_j-\bar{\nu}_n\right)^2}\right\rangle_{sst}, \tag{43}$$

where the large angular brackets denote averaging over the steady-state integration time. The *index of incoherence* is then defined as

$$S = 1 - \frac{1}{N}\sum_{n=1}^{N} s_n, \tag{44}$$

where $s_n = \Theta(\delta - \sigma_n)$ with Θ being the Theta function, and δ a predefined threshold that is reasonably small. The index S takes its values in $[0, 1]$, with 0 and 1 corresponding to synchronized and desynchronized states, respectively, while all other values between them indicate the existence of a chimera or multi-chimera state. Finally, the *chimera index* is defined as

$$\eta = \sum_{n=1}^{N}|s_n - s_{n+1}|/2, \tag{45}$$

and takes positive integer values. The chimera index η gives the number of desynchronized clusters of a (multi-)chimera state, except in the case of a completely desynchronized state where it gives zero. In **Figure 13**, the incoherence index S and the chimera index η are mapped on the $\phi_{ac}-\phi^{dc}_{max}$ plane for the same parameters as in **Figure 12A**.

Figures 13A,B provide more information about the state of the SQUID metamaterial at a particular point on the $\phi_{ac} - \phi^{dc}_{max}$ plane. In **Figure 13A**, for values of ϕ_{ac} and ϕ^{dc}_{max} in the light-green area ($S = 0$) the SQUID metamaterial is in a synchronized state (see the corresponding area in **Figure 13B** in which $\eta = 0$). For values of ϕ_{ac} and ϕ^{dc}_{max} in the red area ($S = 1$), the SQUID metamaterial is completely desynchronized (the corresponding area in **Figure 13B** has $\eta = 0$ due to technical reasons). For values of ϕ_{ac} and ϕ^{dc}_{max} in one of the other areas, the SQUID metamaterial is in a chimera state with one, two, or three desynchronized clusters, as it can be inferred from **Figure 13B**.

Using the combined information from **Figures 12**, **13**, the form of the steady-state of a SQUID metamaterial can be predicted for any physically relevant value of ϕ_{ac} and ϕ^{dc}_{max}. In

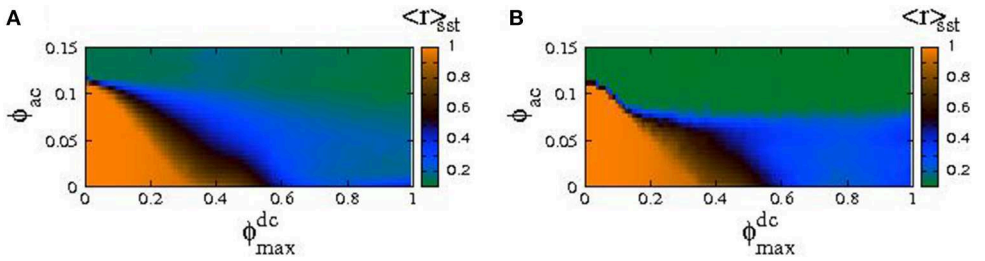

FIGURE 12 | The magnitude of the synchronization parameter averaged over the steady-state integration time $\langle r \rangle_{sst}$ mapped as a function of the ac flux amplitude and the maximum dc flux bias ($\phi_{ac} - \phi^{dc}_{max}$ plane), for $\beta_L = 0.86$, $\gamma = 0.01$, $N = 54$, $\Omega = 1.01$, and **(A)** $\lambda = -0.02$, **(B)** $\lambda = -0.06$.

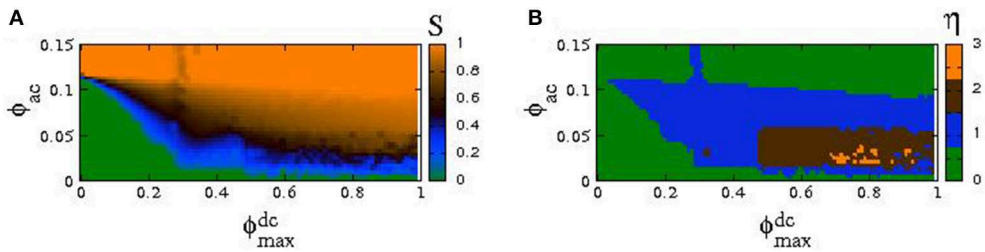

FIGURE 13 | The index of incoherence S **(A)** and the chimera index η **(B)** are mapped on the $\phi_{ac} - \phi^{dc}_{max}$ plane, for the same parameters as in **Figure 12A** and $n_0 = 4$, $\delta = 10^{-4}$.

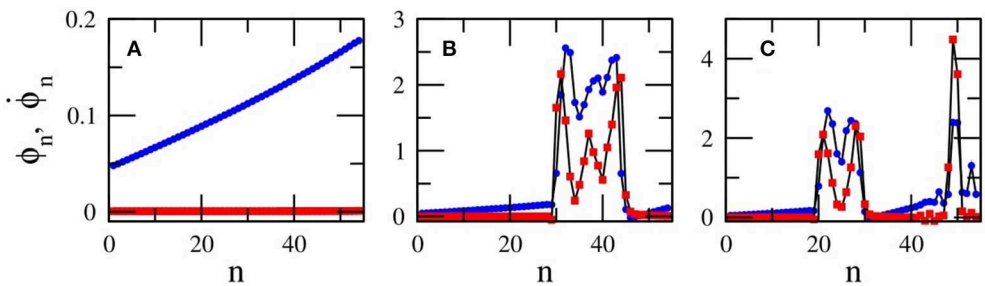

FIGURE 14 | Flux and voltage profiles ϕ_n (blue) and $v_n = \dot{\phi}_n$ (red), respectively, as a function of n for $\beta_L = 0.86$, $\gamma = 0.01$, $\Omega = 1.01$, $\phi_{ac} = 0.04$, and **(A)** $\phi^{dc}_{max} = 0.2$, **(B)** $\phi^{dc}_{max} = 0.4$, **(C)** $\phi^{dc}_{max} = 0.6$.

Figure 14, three flux profiles ϕ_n are shown as a function of n, along with the corresponding profiles of their time-derivatives, $\dot{\phi}_n$. The profiles in **Figures 14A–C**, are obtained for $\phi_{ac} = 0.04$ and $\phi^{dc}_{max} = 0.2$, 0.4, and 0.6, respectively, which are located in the light-green, light-blue, and dark-green area of **Figure 14B**. As it is expected, the state in **Figure 14A** is an almost synchronized one, in **Figure 14B** is a chimera state with one desynchronized cluster, while in **Figure 14C** is a chimera state with two desynchronized clusters. At this point, the use of the expression "almost synchronized" should be explained. In the presence of a dc flux gradient, it is impossible for a SQUID metamaterial to reach a completely synchronized state. This is because each SQUID is subject to a different dc flux, which modifies accordingly its resonance (eigen-)frequency. As a result, the flux oscillation amplitudes of the SQUIDs, whose oscillations are driven by the ac flux field of amplitude ϕ_{ac} and frequency Ω, are slightly different. On the other hand, the maximum of the flux oscillations for all the SQUIDs is attained at the same time. Indeed, as can be observed in **Figure 14A**. the flux profile ϕ_n is not horizontal, as it should be in the case of complete synchronization. Instead, that profile increases almost linearly from $n = 1$ to $n = N$ (that increase is related to the dc flux gradient). However, the voltage profile $\dot{\phi}_n$ is zero for any n, indicating that all the SQUID oscillators are in phase. Since, in such a state of the SQUID metamaterial there is phase synchronization but no amplitude synchronization, the synchronization is not complete. However, the value of $\langle r \rangle_{sst}$ in such a state is in the worst case higher than 0.96 for moderately high values of $\phi_{ac} = 0.02 - 0.10$ (**Figure 11J**), which is a very high degree of global synchronization. Furthermore, the synchronized clusters in the chimera state profiles in **Figures 14B,C**, whose length coincides with that of the horizontal segments of the $\dot{\phi}_n$ profiles, also exhibit a very high degree of global synchronization ($\langle r \rangle_{sst} > 0.96$).

4. DISCUSSION

The emergence of chimera and multi-chimera states in a 1D SQUID metamaterial driven by an ac flux field is demonstrated numerically, using a well-established model that relies on equivalent electrical circuits. Chimera states may emerge both with local coupling between SQUID (nearest-neighbor coupling) and non-local coupling between SQUIDs which falls-off as the inverse cube of their center-to-center distance. A large variety of initial conditions can generate chimera states which persist for very long times. In the previous section, the expression "steady-state integration time" is used repeatedly; however, in some cases this may not be very accurate, since chimera states are generally metastable and sudden changes may occur at any instant of time-integration which results in sudden jumps the synchronization parameter $\langle r \rangle_T$ [33]. For the chimera states presented here, however, no such sudden changes have been observed. Along with the ac flux field, a dc flux bias, the same at any SQUID, can be also applied to the 1D SQUID metamaterial. Chimera states can be generated in that case as well, although not shown here. Although a large volume of analytical and numerical studies on the existence and properties of chimera states for a variety of non-linear mathematical models of coupled oscillators exists, there are comparatively very few studies in which the oscillators are periodically (i.e., sinusoidally) driven. Some of the latter studies include an array of locally coupled bistable Duffing oscillators with a common sinusoidal forcing [92], in networks of non-locally coupled van der Pol-Duffing oscillators excited by a sinusoidal drive [93], and locally coupled extended Duffing oscillators with harmonic forcing [94].

The emergence of those counter-intuitive states, their form and their global degree of synchronization depends crucially on the initial conditions. If the SQUID metamaterial is initialized with zeros, the generation of chimera states does not seem to be possible for spatially constant dc flux bias ϕ_{dc}. In that case, synchronization-desynchronization and reverse synchronization-desynchronization transitions may occur by varying the ac flux amplitude ϕ_{ac} or the dc flux bias ϕ_{dc}. In the former transition, a completely synchronized state suddenly becomes a completely desynchronized one. The replacement of the spatially constant dc flux bias by a position-dependent one, ϕ_n^{dc}, makes possible the generation of chimera states from zero initial conditions. In the latter case, it is possible to generate chimera states whose characteristics depend on the external parameters, such as the dc flux gradient, and the amplitude and frequency of the ac flux field. Specifically, given that the SQUID metamaterial is initially "at rest" ($\phi_n(\tau = 0) = \dot{\phi}_n(\tau = 0) = 0$ for any n), the values of the external parameters determine whether a chimera state will be generated, its degree of synchronization and its multiplicity, as well as the location and the size of its desynchronized cluster(s). It is in this sense that we use the term "controlled generation of chimera states" in the beginning of this section.

Here, the driving frequency is always chosen to be very close to the geometrical frequency of the individual SQUIDs. In the case of relatively strong non-linearity, considered here, the resonance frequency of individual SQUIDs is shifted to practically around the geometrical frequency. That is, for relatively strong non-linearity, the driving frequency was chosen so that the SQUIDs are at resonance. For a single SQUID driven close to its resonance, the relatively strong non-linearity makes it highly multistable; then, several stable and unstable single SQUID states may coexist (see the snake-like curves presented in section 2.1). This dynamic multistability effect is of major importance for the emergence of chimera states in SQUID metamaterials, as it is explained below.

The dynamic complexity of N SQUIDs which are coupled together increases with increasing N; this effect has been described in the past for certain arrays of coupled non-linear oscillators as attractor crowding [95, 96]. This complexity is visible already for two coupled SQUIDs, where the number of stable states close to the geometrical resonance increases more than two times compared to that of a single SQUID [34]; some of these states can even be chaotic. Interestingly, the existence of homoclinic chaos in a pair of coupled SQUIDs has been proved by analytical means [97, 98]. It has been argued that the number of stable limit cycles (i.e., periodic solutions) in such systems scales with the number of oscillators N as $(N-1)!$. As a result, their basins of attraction crowd more and more tightly in phase space with increasing N. The multistability of individual SQUIDs around the resonance frequency enhances the attractor crowding effect in SQUID metamaterial. Apart from the large number of periodic solutions (limit cycles), a number of coexisting chaotic solutions may also appear as in the two-SQUID system. All these states are available for each SQUID to occupy. Then, with appropriate initialization of the SQUID metamaterial, or by applying a dc flux gradient to it, a number of SQUIDs that belong to the same cluster may occupy a chaotic state. The flux oscillations of these SQUIDs then generally differ in both their amplitude and phase, resulting for that cluster to be desynchronized. Alternatingly, a number of SQUIDs that belong to the same cluster may find themselves in a region of phase-space with a high density of periodic solutions. Then, the flux in these SQUID oscillators may jump irregularly from one periodic state to another resulting in effectively random dynamics and in effect for that cluster to be desynchronized. At the same time, the other cluster(s) of SQUIDs can remain synchronized and, as a result, a chimera state emerges.

AUTHOR CONTRIBUTIONS

NL conceived the structure of the manuscript. JH and NL performed the simulations. All authors listed performed data analysis and have made intellectual contribution to the work, and approved it for publication.

ACKNOWLEDGMENTS

This research has been financially supported by the General Secretariat for Research and Technology (GSRT) and the Hellenic Foundation for Research and Innovation (HFRI) (Code: 203).

REFERENCES

1. Smith DR, Pendry JB, Wiltshire. Metamaterials and negative refractive index. *Science* (2004) **305**:788–92. doi: 10.1126/science.1096796
2. Linden S, Enkrich C, Dolling G, Klein MW, Zhou J, Koschny T, et al. Photonic metamaterials: magnetism at optical frequencies. *IEEE J Selec Top Quant Electron.* (2006) **12**:1097–105. doi: 10.1109/JSTQE.2006.880600
3. Padilla WJ, Basov DN, Smith DR. Negative refractive index metamaterials. *Mater Today.* (2006) **9**:28–35. doi: 10.1016/S1369-7021(06)71573-5
4. Shalaev VM. Optical negative-index metamaterials. *Nature Photon.* (2007) **1**:41–8. doi: 10.1038/nphoton.2006.49
5. Litchinitser NM, Shalaev VM. Photonic metamaterials. *Laser Phys Lett.* (2008) **5**:411–20. doi: 10.1002/lapl.200810015
6. Soukoulis CM, Wegener M. Past achievements and future challenges in the development of three-dimensional photonic metamaterials. *Nature Photon.* (2011) **5**:523–30. doi: 10.1038/nphoton.2011.154
7. Liu Y, Zhang X. Metamaterials: a new frontier of science and technology. *Chem Soc Rev.* (2011) **40**:2494–507. doi: 10.1039/c0cs00184h
8. Simovski CR, Belov PA, Atrashchenko AV, Kivshar YS. Wire metamaterials: physics and applications. *Adv Mater.* (2012) **24**:4229–48. doi: 10.1002/adma.201200931
9. Engheta N, Ziolkowski RW. *Metamaterials: Physics and Engineering Explorations*. New Jersey, NJ: Wiley-IEEE Press (2006).
10. Pendry JB. *Fundamentals and Applications of Negative Refraction in Metamaterials*. New Jersey, NY: Princeton University Press (2007).
11. Ramakrishna SA, Grzegorczyk T. *Physics and Applications of Negative Refractive Index Materials*. New York, NY: SPIE and CRC Press (2009).
12. Cui TJ, Smith DR, Liu R. *Metamaterials Theory, Design and Applications*. New York, NY: Springer (2010).
13. Cai W, Shalaev V. *Optical Metamaterials, Fundamentals and Applications*. Heidelberg: Springer (2010).
14. Solymar L, Shamonina E. *Waves in Metamaterials*. New York, NY: Oxford University Press (2009).
15. Noginov MA, Podolskiy VA. *Tutorials in Metamaterials*. Boca Raton, FL: Taylor & Francis (2012).
16. Tong XC. *Functional Metamaterials and Metadevices, Springer Series in Materials Science*, Vol. 262. Cham: Springer International Publishing AG (2018).
17. Anlage SM. The physics and applications of superconducting metamaterials. *J Opt.* (2011) **13**:024001–10. doi: 10.1088/2040-8978/13/2/024001
18. Jung P, Ustinov AV, Anlage SM. Progress in superconducting metamaterials. *Supercond Sci Technol.* (2014) **27**:073001. doi: 10.1088/0953-2048/27/7/073001
19. Jin B, Zhang C, Engelbrecht S, Pimenov A, Wu J, Xu Q, et al. Low loss and magnetic field-tunable superconducting terahertz metamaterials. *Opt Express.* (2010) **18**:17504–9. doi: 10.1364/OE.18.017504
20. Zhang CH, Wu JB, Jin BB, Ji ZM, Kang L, Xu WW, et al. Low-loss terahertz metamaterial from superconducting niobium nitride films. *Opt Express.* (2012) **20**:42–7. doi: 10.1364/OE.20.000042
21. Gu J, Singh R, Tian Z, Cao W, Xing Q, He MX, et al. Terahertz superconductor metamaterial. *Appl Phys Lett.* (2010) **97**:071102. doi: 10.1063/1.3479909
22. Zhang X, Gu J, Han J, Zhang W. Tailoring electromagnetic responses in terahertz superconducting metamaterials. *Front Optoelectron.* (2014) **8**:44–56. doi: 10.1007/s12200-014-0439-x
23. Du C, Chen H, Li S. Quantum left-handed metamaterial from superconducting quantum-interference devices. *Phys Rev B.* (2006) **74**:113105–4. doi: 10.1103/PhysRevB.74.113105
24. Lazarides N, Tsironis GP. RF superconducting quantum interference device metamaterials. *Appl Phys Lett.* (2007) **90**:163501. doi: 10.1063/1.2722682
25. Josephson B. Possible new effects in superconductive tunnelling. *Phys Lett A.* (1962) **1**:251–5. doi: 10.1016/0031-9163(62)91369-0
26. Butz S, Jung P, Filippenko LV, Koshelets VP, Ustinov AV. A one-dimensional tunable magnetic metamaterial. *Opt Express.* (2013) **21**:22540–8. doi: 10.1364/OE.21.022540
27. Trepanier M, Zhang D, Mukhanov O, Anlage SM. Realization and modeling of RF superconducting quantum interference device metamaterials. *Phys Rev X.* (2013) **3**:041029. doi: 10.1103/PhysRevX.3.041029
28. Zhang D, Trepanier M, Mukhanov O, Anlage SM. Broadband transparency of macroscopic quantum superconducting metamaterials. *Phys Rev X.* (2015) **5**:041045. doi: 10.1103/PhysRevX.5.041045
29. Jung P, Butz S, Marthaler M, Fistul MV, Leppäkangas J, Koshelets VP, et al. Multistability and switching in a superconducting metamaterial. *Nat Commun.* (2014) **5**:3730. doi: 10.1038/ncomms4730
30. Trepanier M, Zhang D, Mukhanov O, Koshelets VP, Jung P, Butz S, et al. Coherent oscillations of driven rf squid metamaterials. *Phys Rev E.* (2017) **95**:050201. doi: 10.1103/PhysRevE.95.050201
31. Lazarides N, Tsironis GP, Eleftheriou M. Dissipative discrete breathers in RF squid metamaterials. *Nonlinear Phenom Complex Syst.* (2008) **11**:250–8. Available online at: http://www.j-npcs.org/abstracts/vol2008/v11no2/v11no2p250.html
32. Tsironis GP, Lazarides N, Margaris I. Wide-band tuneability, nonlinear transmission, and dynamic multistability in squid metamaterials. *Appl Phys A.* (2014) **117**:579–88. doi: 10.1007/s00339-014-8706-7
33. Lazarides N, Neofotistos G, Tsironis GP. Chimeras in squid metamaterials. *Phys Rev B.* (2015) **91**:054303. doi: 10.1103/PhysRevB.91.054303
34. Hizanidis J, Lazarides N, Tsironis GP. Robust chimera states in squid metamaterials with local interactions. *Phys Rev E.* (2016) **94**:032219. doi: 10.1103/PhysRevE.94.032219
35. Hizanidis J, Lazarides N, Neofotistos G, Tsironis G. Chimera states and synchronization in magnetically driven squid metamaterials. *Eur Phys J Spec Top.* (2016) **225**:1231–43. doi: 10.1140/epjst/e2016-02668-9
36. Lazarides N, Tsironis GP. Superconducting metamaterials. *Phys Rep.* (2018) **752**:1–67. doi: 10.1016/j.physrep.2018.06.005
37. Kuramoto Y, Battogtokh D. Coexistence of coherence and incoherence in nonlocally coupled phase oscillators. *Nonlinear Phenom Complex Syst.* (2002) **5**:380–5. Available online at: http://www.j-npcs.org/online/vol2002/v5no4/v5no4p380.pdf
38. Panaggio MJ, Abrams DM. Chimera states: coexistence of coherence and incoherence in network of coulped oscillators. *Nonlinearity.* (2015) **28**:R67–87. doi: 10.1088/0951-7715/28/3/R67
39. Schöll E. Synchronization patterns and chimera states in complex networks: interplay of topology and dynamics. *Eur Phys J Spec Top.* (2016) **225**:891–919. doi: 10.1140/epjst/e2016-02646-3
40. Yao N, Zheng Z. Chimera states in spatiotemporal systems: theory and applications. *Int J Mod Phys B.* (2016) **30**:1630002. doi: 10.1142/S0217979216300024
41. Abrams DM, Strogatz SH. Chimera states for coupled oscillators. *Phys Rev Lett.* (2004) **93**:174102. doi: 10.1103/PhysRevLett.93.174102
42. Kuramoto Y, Shima SI, Battogtokh D, Shiogai Y. Mean-field theory revives in self-oscillatory fields with non-local coupling. *Prog Theor Phys Suppl.* (2006) **161**:127–43. doi: 10.1143/PTPS.161.127
43. Omel'chenko OE, Maistrenko YL, Tass PA. Chimera states: the natural link between coherence and incoherence. *Phys Rev Lett.* (2008) **100**:044105. doi: 10.1103/PhysRevLett.100.044105
44. Abrams DM, Mirollo R, Strogatz SH, Wiley DA. Solvable model for chimera states of coupled oscillators. *Phys Rev Lett.* (2008) **101**:084103. doi: 10.1103/PhysRevLett.101.084103
45. Pikovsky A, Rosenblum M. Partially integrable dynamics of hierarchical populations of coupled oscillators. *Phys Rev Lett.* (2008) **101**:264103. doi: 10.1103/PhysRevLett.101.264103
46. Ott E, Antonsen TM. Long time evolution of phase oscillator systems. *Chaos.* (2009) **19**:023117. doi: 10.1063/1.3136851

47. Martens EA, Laing CR, Strogatz SH. Solvable model of spiral wave chimeras. *Phys Rev Lett.* (2010) **104**:044101. doi: 10.1103/PhysRevLett.104.044101
48. Omelchenko I, Maistrenko Y, Hövel P, Schöll E. Loss of coherence in dynamical networks: spatial chaos and chimera states. *Phys Rev Lett.* (2011) **106**:234102. doi: 10.1103/PhysRevLett.106.234102
49. Yao N, Huang ZG, Lai YC, Zheng ZG. Robustness of chimera states in complex dynamical systems. *Sci Rep.* (2013) **3**:3522. doi: 10.1038/srep03522
50. Omelchenko I, Omel'chenko OE, Hövel P, Schöll E. When nonlocal coupling between oscillators becomes stronger: matched synchrony or multichimera states. *Phys Rev Lett.* (2013) **110**:224101. doi: 10.1103/PhysRevLett.110.224101
51. Hizanidis J, Kanas V, Bezerianos A, Bountis T. Chimera states in networks of nonlocally coupled hindmarsh-rose neuron models. *Int J Bifurcation Chaos.* (2014) **24**:1450030. doi: 10.1142/S0218127414500308
52. Zakharova A, Kapeller M, Schöll E. Chimera death: symmetry breaking in dynamical networks. *Phys Rev Lett.* (2014) **112**:154101. doi: 10.1103/PhysRevLett.112.154101
53. Bountis T, Kanas V, Hizanidis J, Bezerianos A. Chimera states in a two-population network of coupled pendulum-like elements. *Eur Phys J Spec Top.* (2014) **223**:721–8. doi: 10.1140/epjst/e2014-02137-7
54. Yeldesbay A, Pikovsky A, Rosenblum M. Chimeralike states in an ensemble of globally coupled oscillators. *Phys Rev Lett.* (2014) **112**:144103. doi: 10.1103/PhysRevLett.112.144103
55. Haugland SW, Schmidt L, Krischer K. Self-organized alternating chimera states in oscillatory media. *Sci Rep.* (2015) **5**:9883. doi: 10.1038/srep09883
56. Bera BK, Ghosh D, Lakshmanan M. Chimera states in bursting neurons. *Phys Rev E.* (2016) **93**:012205. doi: 10.1103/PhysRevE.93.012205
57. Shena J, Hizanidis J, Kovanis V, Tsironis GP. Turbulent chimeras in large semiconductor laser arrays. *Sci Rep.* (2017) **7**:42116. doi: 10.1038/srep42116
58. Sawicki J, Omelchenko I, Zakharova A, Schöll E. Chimera states in complex networks: interplay of fractal topology and delay. *Eur Phys J Spec Top.* (2017) **226**:1883–92. doi: 10.1140/epjst/e2017-70036-8
59. Ghosh S, Jalan S. Engineering chimera patterns in networks using heterogeneous delays. *Chaos.* (2018) **28**:071103. doi: 10.1063/1.5042133
60. Shepelev IA, Vadivasova TE. Inducing and destruction of chimeras and chimera-like states by an external harmonic force. *Phys Lett A.* (2018) **382**:690–6. doi: 10.1016/j.physleta.2017.12.055
61. Banerjee A, Sikder D. Transient chaos generates small chimeras. *Phys Rev E.* (2018) **98**:032220. doi: 10.1103/PhysRevE.98.032220
62. Tinsley MR, Nkomo S, Showalter K. Chimera and phase-cluster states in populations of coupled chemical oscillators. *Nat Phys.* (2012) **8**:662–5. doi: 10.1038/nphys2371
63. Hagerstrom AM, Murphy TE, Roy R, Hövel P, Omelchenko I, Schöll E. Experimental observation of chimeras coulped-map lattices. *Nat Phys.* (2012) **8**:658–61. doi: 10.1038/nphys2372
64. Wickramasinghe M, Kiss IZ. Spatially organized dynamical states in chemical oscillator networks: synchronization, dynamical differentiation, and chimera patterns. *PLoS ONE* (2013) **8**:e80586. doi: 10.1371/journal.pone.0080586
65. Nkomo S, Tinsley MR, Showalter K. Chimera states in populations of nonlocally coupled chemical oscillators. *Phys Rev Lett.* (2013) **110**:244102. doi: 10.1103/PhysRevLett.110.244102
66. Martens EA, Thutupalli S, Fourriére A, Hallatschek O. Chimera states in mechanical oscillator networks. *Proc Natl Acad Sci USA.* (2013) **110**:10563–7. doi: 10.1073/pnas.1302880110
67. Schönleber K, Zensen C, Heinrich A, Krischer K. Patern formation during the oscillatory photoelectrodissolution of n-type silicon: turbulence, clusters and chimeras. *New J Phys.* (2014) **16**:063024. doi: 10.1088/1367-2630/16/6/063024
68. Viktorov EA, Habruseva T, Hegarty SP, Huyet G, Kelleher B. Coherence and incoherence in an optical comb. *Phys Rev Lett.* (2014) **112**:224101. doi: 10.1103/PhysRevLett.112.224101
69. Rosin DP, Rontani D, Haynes ND, Schöll E, Gauthier DJ. Transient scaling and resurgence of chimera states in coupled boolean phase oscillators. *Phys Rev E.* (2014) **90**:030902. doi: 10.1103/PhysRevE.90.030902
70. Schmidt L, Schönleber K, Krischer K, García-Morales V. Coexistence of synchrony and incoherence in oscillatory media under nonlinear global coupling. *Chaos.* (2014) **24**:013102. doi: 10.1063/1.4858996
71. Gambuzza LV, Buscarino A, Chessari S, Fortuna L, Meucci R, Frasca M. Experimental investigation of chimera states with quiescent and synchronous domains in coupled electronic oscillators. *Phys Rev E.* (2014) **90**:032905. doi: 10.1103/PhysRevE.90.032905
72. Kapitaniak T, Kuzma P, Wojewoda J, Czolczynski K, Maistrenko Y. Imperfect chimera states for coupled pendula. *Sci Rep.* (2014) **4**:6379. doi: 10.1038/srep06379
73. Larger L, Penkovsky B, Maistrenko Y. Laser chimeras as a paradigm for multistable patterns in complex systems. *Nat Comms.* (2015) **6**:7752. doi: 10.1038/ncomms8752
74. Hart JD, Bansal K, Murphy TE, Roy R. Experimental observation of chimera and cluster states in a minimal globally coupled network. *Chaos.* (2016) **26**:094801. doi: 10.1063/1.4953662
75. English LQ, Zampetaki A, Kevrekidis PG, Skowronski K, Fritz CB, Abdoulkary S. Analysis and observation of moving domain fronts in a ring of coupled electronic self-oscillators. *Chaos.* (2017) **27**:103125. doi: 10.1063/1.5009088
76. Totz JF, Rode J, Tinsley MR, Showalter K, Engel H. Spiral wave chimera states in large populations of coupled chemical oscillators. *Nat Phys.* (2018) **14**:282–5. doi: 10.1038/s41567-017-0005-8
77. Clarke J, Braginski AI. *The SQUID Handbook Vol. I: Fundamentals and Technology of SQUIDs and SQUID Systems*. Weinheim: Wiley-VCH (2004).
78. Clarke J, Braginski AI. *The SQUID Handbook Vol. II: Applications of SQUIDs and SQUID Systems*. Weinheim: Wiley-VCH (2004).
79. Hizanidis J, Lazarides N, Tsironis GP. Flux bias-controlled chaos and extreme multistability in squid oscillators. *Chaos.* (2018) **28**:063117. doi: 10.1063/1.5020949
80. Likharev KK. *Dynamics of Josephson Junctions and Circuits*. Philadelphia, PA: Gordon and Breach (1986).
81. Swift JW, Wiesenfeld K. Suppression of period doubling in symmetric systems. *Phys Rev Lett.* (1984) **52**:705. doi: 10.1103/PhysRevLett.52.705
82. Flach S, Gorbach AV. Discrete breathers–advances in theory and applications. *Phys Rep.* (2008) **467**:1–116. doi: 10.1016/j.physrep.2008.05.002
83. Flach S, Gorbach A. Discrete breathers with dissipation. *Lect Notes Phys.* (2008) **751**:289–320. doi: 10.1007/978-3-540-78217-9_11
84. Tsironis GP, Lazarides N, Eleftheriou M. Dissipative breathers in rf squid metamaterials. *PIERS Online.* (2009) **5**:26–30. doi: 10.2529/PIERS081006095539
85. Lazarides N, Tsironis GP. Intrinsic localization in nonlinear and superconducting metamaterials. *Proc SPIE.* (2012) **8423**:84231K. doi: 10.1117/12.922708
86. Lazarides N, Tsironis GP. Nonlinear localization in metamaterials. In: Shadrivov I, Lapine M, Kivshar YS, editors. *Nonlinear, Tunable and Active Metamaterials*. Cham: Springer International Publishing (2015). p. 281–301.
87. Lazarides N, Tsironis GP. Multistable dissipative breathers and collective states in squid lieb metamaterials. *Phys Rev E.* (2018) **98**:012207. doi: 10.1103/PhysRevE.98.012207
88. Shanahan M. Metastable chimera states in community-structured oscillator networks. *Chaos.* (2010) **20**:013108. doi: 10.1063/1.3305451
89. Wildie M, Shanahan M. Metastability and chimera states in modular delay and pulse-coupled oscillator networks. *Chaos.* (2012) **22**:043131. doi: 10.1063/1.4766592
90. Gopal R, Chandrasekar VK, Venkatesan A, Lakshmanan M. Observation and characterization of chimera states in coupled dynamical systems with nonlocal coupling. *Phys Rev E.* (2014) **89**:052914. doi: 10.1103/PhysRevE.89.052914
91. Gopal R, Chandrasekar VK, Venkatesan A, Lakshmanan M. Chimera at the phase-flip transition of an ensemble of identical nonlinear oscillators. *Commun Nonlinear Sci Numer Simulat.* (2018) **59**:30–46. doi: 10.1016/j.cnsns.2017.11.005
92. Chandrasekar VK, Suresh R, Senthilkumar DV, Lakshmanan M. Coexisting coherent and incoherent domains near saddle-node bifurcation. *EPL.* (2015) **111**:60008. doi: 10.1209/0295-5075/111/60008

93. Dudkowski D, Maistrenko Yu, Kapitaniak T. Occurrence and stability of chimera states in coupled externally excited oscillators. *Chaos.* (2016) **26**:116306. doi: 10.1063/1.4967386
94. Clerc MG, Coulibaly S, Ferré MA, Rojas RG. Chimera states in a Duffing oscillators chain coupled to nearest neighbors. *Chaos.* (2018) **28**:083126. doi: 10.1063/1.5025038
95. Wiesenfeld K, Hadley P. Attractor crowding in oscillator arrays. *Phys Rev Lett.* (1989) **62**:1335–8. doi: 10.1103/PhysRevLett.62.1335
96. Tsang KY, Wiesenfeld K. Attractor crowding in josephson junction arrays. *Appl Phys Lett.* (1990) **56**:495–7. doi: 10.1063/1.102774
97. Agaoglou M, Rothos VM, Susanto H. Homoclinic chaos in a pair of parametrically-driven coupled squids. *J Phys Conf Series.* (2015) **574**:012027. doi: 10.1088/1742-6596/574/1/012027
98. Agaoglou M, Rothos VM, Susanto H. Homoclinic chaos in coupled squids. *Chaos Solit Fract.* (2017) **99**:133–40. doi: 10.1016/j.chaos.2017.04.003

Conflict of Interest Statement: The authors declare that the research was conducted in the absence of any commercial or financial relationships that could be construed as a potential conflict of interest.

frontiers in Applied Mathematics and Statistics

ORIGINAL RESEARCH
published: 27 March 2019
doi: 10.3389/fams.2019.00015

Chimera States in Ecological Network Under Weighted Mean-Field Dispersal of Species

*Suman Saha, Nandadulal Bairagi and Syamal Kumar Dana**

Department of Mathematics, Centre for Mathematical Biology and Ecology, Jadavpur University, Kolkata, India

In ecological landscapes, species tend to migrate between nearby patches in search of a better survivability condition. By this dispersal process, they form connectivity between the patches and thereby may develop various correlated or partially correlated population dynamics among species living in the patches. We explore various possible emergent collective population patterns using a simple ecological network model of all-to-all connected patches where we use a particular type of dispersal process that is controlled by a weighted mean-field diffusion to include the failed migration between the interacting patches. We represent the population dynamics of both the predator and prey in each patch by a modified Rosenzweig-MacArthur (mRM) model that incorporates an additional effect of habitat complexity. Our theoretical investigations on the network dynamics, using numerical and to some extent, analytical techniques, show various complex patterns, namely, 2-cluster, 3-cluster and multicluster states, and chimera states, besides synchrony (1-cluster) and homogeneous steady states (HSS) in a migrating metapopulation. An important observation is that addition of habitat complexity in the Rosenzweig-MacArthur (RM) model makes qualitative changes in the collective behaviors. Especially to mention that it shrinks the region of synchrony and broadens the region of HSS, in parameter space and, thereby leads to better survival probabilities and increased population persistence in a natural ecosystem.

Keywords: ecological network, habitat complexity, weighted mean-field diffusion, homogeneous steady states, synchrony, clustering, amplitude mediated chimera

OPEN ACCESS

Edited by:
Eckehard Schöll, Technische Universität Berlin, Germany

Reviewed by:
Tanmoy Banerjee, University of Burdwan, India
Konstantin Blyuss, University of Sussex, United Kingdom
Bernd Blasius, University of Oldenburg, Germany

****Correspondence:***
Syamal Kumar Dana
syamaldana@gmail.com

Specialty section:
This article was submitted to Dynamical Systems, a section of the journal Frontiers in Applied Mathematics and Statistics

Received: *07 September 2018*
Accepted: *05 March 2019*
Published: *27 March 2019*

Citation:
Saha S, Bairagi N and Dana SK (2019) Chimera States in Ecological Network Under Weighted Mean-Field Dispersal of Species. Front. Appl. Math. Stat. 5:15. doi: 10.3389/fams.2019.00015

1. INTRODUCTION

Dispersal is a natural tendency of species in search of a better survival condition against scarcity of food, high population density, intense grazing, or extreme climate changes. An important question in ecology is how dispersal between patches can influence the intrinsic as well as the collective behavior of the interacting species, and thereby make a balance and control of populations [1]. Earlier studies [2–6] showed that dispersal can lower the burden of high population density and reduce the chances of global extinction [7, 8], as species can migrate from over-populated patches to empty or sparsely populated patches. Population migration in fragmented patches is described as metapopulation dynamics [9, 10]. In isolated patches, species may survive in a non-equilibrium state, namely, in a state of stable limit cycle oscillation [11–13]. In an ecological landscape, dispersal or migration-driven spatial synchrony is a most likely event [14–18] as usually seen in dynamical networks, in general, when many agents or oscillatory units interact via diffusion [19]. Examples of spatial synchrony are abundant in population dynamics [18]. In a synchronous state, species in all patches of a metapopulation fluctuate in a common rhythm; then if one goes extinct,

all others are likely to follow the same fate. Synchrony may thus deteriorate the chances of survivability in a situation of an imminent crisis [10, 20–22]. Dispersal driven population stability is another expected and well-known possibility in ecological patches. Such diffusion induced stabilization of oscillation by breaking a synchrony is an established phenomenon [23–28] in dynamical networks as well when a homogeneous steady state (HSS) or inhomogeneous steady states (IHSS) may emerge. Species may develop more persistence or less chances of extinction [29] when populations stop oscillating and stabilized to a constant size. This fact may be explained from the experience of dynamical system studies that a stable steady state as an analog of population stability is robust to external perturbation. Besides synchrony and population stability, many long-lived transient complex patterns, spiral waves, chaos may emerge [30] in a spatially extended ecosystem; stable complex spatial patterns such as spots, stripes, and holes are also seen in natural vegetations [31]. In dynamical networks, partial synchrony such as clustered states [32–34] and chimera patterns [35–37] are well-known transient or stable patterns. This encourages theoretical studies by the ecological community to search for such complex patterns in a metapopulation, if they exists at all, which may be undertaken as possible strategies to enhance survivability of species from the edge of extinction through a recolonization process. We treat here a migration-driven ecological network model as a dynamical network and use the known theoretical techniques to explore various possible collective states using the globally connected network structure and a special type of migration process as explained below.

We focus on clustered states and chimera states in our investigation. Existence of clustered states and chimera states are not reported so far in experiments in ecology, to the best of our knowledge. However, chimera states were first observed in a network of non-locally coupled phase oscillators in 2002 [35, 36], but later reported in networks of limit cycle systems [38, 39], and then, most surprisingly, in networks of globally coupled oscillators [40–42]. Synchrony usually emerges in both amplitude and phase of all identical oscillators in a network above a critical coupling when all the oscillators develop a common rhythm. In chimera states, the synchronous population of identical oscillators splits into two subgroups above a critical coupling when one subgroup is synchronized completely while the other subgroup remains asynchronous. It was an unexpected behavior for a homogeneous network and more surprising in a globally coupled network whose all-to-all connectivity structure is symmetric. Such a symmetry-breaking partial synchrony was difficult to explain in the beginning. The reason behind the emergence of such a coexisting pattern of synchronous and asynchronous subpopulations in a network is more or less understood very recently [33, 34]. Most importantly, such incongruous pattern really exists and found in nature [43] that makes an expectation of such complex patterns in dispersal-driven ecological network too. Besides chimera patterns, clustered patterns may also emerge. In clustered states, the whole ensemble of oscillators splits into subgroups of oscillators [32–34], but in contrast to chimera states, each subgroup is now synchronous. However, there exists no synchrony between the subgroups. Moreover, the number of oscillators in each subgroup may not be identical. Usually species in ecological systems survive mostly in steady states; the population may also oscillate and survive in a non-equilibrium state although chances of extinction prevails. Quite a few theoretical studies were reported on 2-clustered death and multiclustered death states [46] and chimera states [44, 45, 47] and also spiral chimera states [48] in ecological networks using a variety of coupling, non-local, distance dependent power-law coupling and a purely diffusive coupling. For non-local coupling [44], an emergence of chimeralike states was seen where a synchronous or coherent population splits into one coherent subpopulation in oscillatory states and another subpopulation in coexisting steady states and oscillatory states. For the distance dependent power-law connectivity between the patches [45], amplitude chimera (AC) states were reported. The amplitudes of the oscillating incoherent subpopulation did not show any amplitude variation, but showed a phase lag in oscillation of population between the incoherent patches. Both the studies used the RM prey-predator interaction model [49] to represent the local dynamics of each connected patch. Alternatively, we explore chimera states using a globally coupled network structure where dynamics of each ecological patch is represented by the RM model, but with additional effect of habitat complexity. We use the weighted mean-field diffusion as a migration process to define the links between the patches. Such a interactive diffusion process was first introduced [50, 51] for quorum sensing of genetic oscillators and also used [52] for dynamical networks, in general. Recently, the weighted mean-field diffusion was interpreted [46, 53] as a very relevant migration process that explains nicely the failed or misdirected migration of species in a dispersal-driven metapopulation. Thereby the authors observed HSS, IHSS, and multiclustered-death states in a RM model based ecological network of smaller size. We extend the work in a similar globally coupled network with larger number of patches, when we observe additional complexity in population patterns, namely, 2-cluster, 3-cluster, multiclustered, and amplitude modulated chimera (AMC) states for low to moderate migration rate. We mainly focus in the low to moderate dispersal rates and low strength of mean-field factor when such complexity arises. For large migration, we find HSS, in other words, population stability, as usual. However, a significant region of synchronous oscillatory state also exists between the clustered states and HSS for an intermediate range of dispersal, in parameter space. Furthermore, we introduce an additional effect of habitat complexity in the local dynamics of patches that broadens the region of HSS, in parameter space and, shrinks the region of parameter space for synchrony, especially, for low migration of prey and high migration of predator. We explain the ecological consequence of our observed dynamical properties in the discussion.

2. GLOBALLY COUPLED NETWORK OF PREDATOR-PREY SYSTEMS WITH HABITAT COMPLEXITY

Habitat complexity is ubiquitous and found both in terrestrial and aquatic ecosystem in variable degree. For example, presence

of sea grass, salt marshes, coral reefs make marine habitat complex and predator's success is greatly determined by the degree/strength of the physical and structural complexity of habitat. There are plenty of laboratory and field experiments [54–58] which confirm that structural complexity of the habitat has significant influence on predator-prey interaction. The common hypothesis is that habitat complexity reduces predation rates by decreasing encounter rates between predator and prey, thereby enhances persistence of the interacting species. The physical structure of the habitat also reduces the available space for the interacting species and thereby reduces the carrying capacity of the environment [59]. Taking into account the effect of habitat complexity on predation rate and environmental carrying capacity in explicit way, the following model was proposed [59]:

$$\begin{aligned}\dot{x} &= rx(1-\frac{x}{(1-c_1)K}) - \frac{\alpha(1-c_2)xy}{1+\alpha(1-c_2)hx},\\ \dot{y} &= \frac{\theta\alpha(1-c_2)xy}{1+\alpha(1-c_2)hx} - dy,\end{aligned} \tag{1}$$

where x_i and y_i represent, respectively, the prey and predator population densities at time t. Here r is the intrinsic growth rate of prey, K is the environmental carrying capacity, $\theta(0 < \theta < 1)$ is the conversion efficiency of the predator and d is the food-independent death rate of predator. The parameters α and h represent the prey attack rate and handling time, respectively. The effect of habitat complexity on the carrying capacity is represented by the parameter $c_1(0 < c_1 < 1)$ and the effect of habitat complexity on predator's functional response is represented by the parameter $c_2(0 < c_2 < 1)$. We call this model as a modified Rosenzweig-MacArthur (mRM) predator-prey model. The model parameters can be easily rescaled so as to retain the original form of the RM model [49]. In the rescaled model, one will be unable to track the specific effect of the habitat parameters hidden in the rescaled parameters and hence we keep them distinctly visible here. Further explanation and illustration of the model can be seen in Jana and Bairagi [59]. All parameters are assumed positive from the biological viewpoint.

We extend the one patch model to N all-to-all connected network of patches, where the local dynamics of each patch is governed by the mRM model. The network dynamics is represented by

$$\begin{aligned}\dot{x_i} &= rx_i(1-\frac{x_i}{(1-c_1)K}) - \frac{\alpha(1-c_2)x_iy_i}{1+\alpha(1-c_2)hx_i} + \epsilon_1(q\bar{x}-x_i),\\ \dot{y_i} &= \frac{\theta\alpha(1-c_2)x_iy_i}{1+\alpha(1-c_2)hx_i} - dy_i + \epsilon_2(q\bar{y}-y_i),\end{aligned} \tag{2}$$

where $i = 1, 2, \ldots, N$ is the patch or node index. All the patches are assumed identical meaning that individual patches have identical intrinsic dynamics as decided by their identical parameters. The weighted mean-field diffusion of species between the patches is considered to control the dispersal-guided diffusion process between the patches. In a metapopulation ecology, the weighted mean-field coupling is justifiable when the dispersal probability of a species from a randomly selected patch is assumed to be a fraction of its mean density. This type of dispersal of species has been interpreted [44, 53] as failed, misdirected migration or a partial death of species during a migration. The mean population densities of prey and predators are defined as $\bar{x} = \frac{1}{N}\sum_{i=1}^{N} x_i$ and $\bar{y} = \frac{1}{N}\sum_{i=1}^{N} y_i$, respectively. The dispersal of both prey and predator between the patches follows a diffusion process governed by their respective mean-field densities with a weight factor q $(0 < q < 1)$ that measures the dispersal fraction of the mean population density. The parameters ϵ_1 and ϵ_2 represent the dispersal rates of prey and predator population, respectively. We investigate numerically and, to some extent, analytically the emergent collective states of species in the network by varying the dispersal rates (ϵ_1, ϵ_2) and the weighted mean-field parameter q. There is no spatial identity of the patches in a global coupling since all nodes have equal distance from each other and have equal degree distribution and therefore each node has equal priority, representing a symmetric and homogeneous network. We emphasize on the role of habitat complexity parameters $c_{1,2}$ and show that habitat complexities make qualitative changes in the characteristic features of collective dynamics.

3. COLLECTIVE STATES: NUMERICAL RESULTS

Numerical simulations are initiated with pseudo-randomly generated initial conditions, where all prey and predator densities are uniformly distributed, respectively, on the interval (100, 400) and (20, 50) in all patches. The model parameters of the mRM model are set [59] as $r = 2.65$, $K = 898$, $h = 0.0437$, $\theta = 0.215$, $\alpha = 0.045$, $c_1 = 0.01$, $c_2 = 0.1$, $d = 0.12$ so that the dynamics of an isolated patch exhibits relaxation type oscillation as shown in **Figure 1A**; the oscillation never reaches a zero population. Our choice of model parameters is guided by a notion [11] that slow-fast time scale in variation of prey and predator populations is a necessary condition for sptial synchrony in a metapopulation in the weaker dispersal regime. In a similar study, the RM model was considered earlier [46] in search of synchrony and population stability where the model parameters of an isolated patch were also chosen for relaxation type oscillation.

In this present study, a network of $N = 100$ globally connected patches is considered and migration of both the prey and predators are allowed between the patches. To explore all the possible collective states, several phase diagrams are plotted in the 2-parameter planes using the following quantitative measures to identify various collective states, HSS, synchrony, clusters and chimera states. A steady state in the network is identified by estimating the standard deviations of the predator and prey populations in each patch and averaging them as

$$\Delta_{ASD} = \frac{1}{N}\sum_{i=1}^{N}\sqrt{\frac{1}{2}\left[(\langle x_i^2\rangle - \langle x_i\rangle^2) + (\langle y_i^2\rangle - \langle y_i\rangle^2)\right]}. \tag{3}$$

Here $\langle . \rangle$ denotes time average. A steady state is identified when Δ_{ASD} is zero and it has a finite non-zero value in oscillatory states. Number of unique steady states in case of HSS is one.

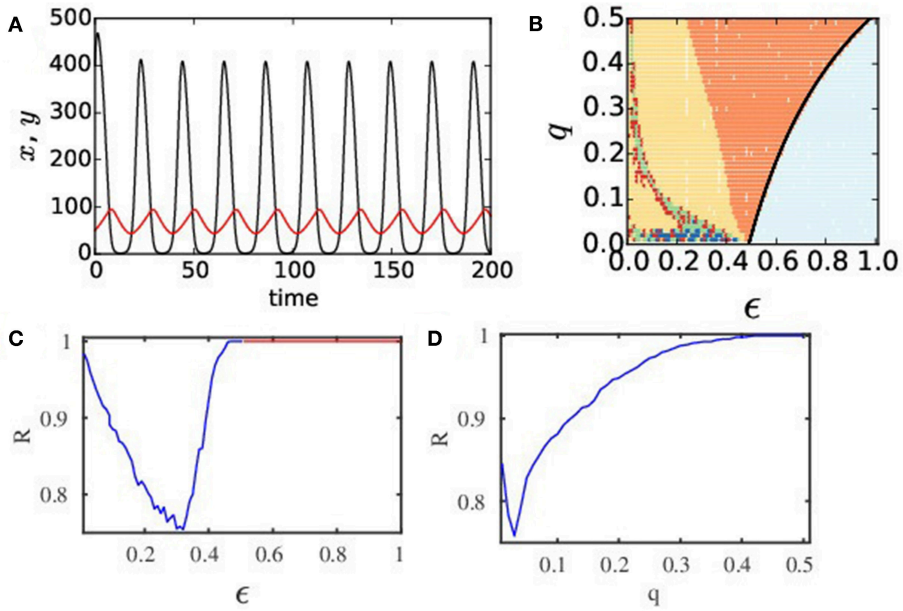

FIGURE 1 | (Color online) **(A)** Temporal dynamics of an isolated patch. It is governed by the mRM model where black and red lines denote prey and predator populations, respectively. The intrinsic dynamics of an isolated patch is relaxation type ($x > 0$ and $y > 0$) for the choice of parameters $r = 2.65$, $K = 898$, $h = 0.0437$, $\theta = 0.215$, $\alpha = 0.045$, $c_1 = 0.01$, $c_2 = 0.1$, and $d = 0.12$. **(B)** Phase diagram in a $q - \epsilon$ plane of the ecological network of $N = 100$ nodes where $\epsilon_1 = \epsilon_2 = \epsilon$. Different colors depict diverse collective states: light blue for HSS, orange for global synchrony (1-cluster), yellow for 2-cluster states; red indicates 3-cluster; green represents higher cluster states; blue for chimera state. **(C)** R vs. ϵ plot ($q = 0.02$) shows global synchrony ($R = 1$, blue line) for $0.45 < \epsilon \leq 0.5$, HSS for $\epsilon > 0.5$ ($R = 1$, red line). For $\epsilon < 0.45$ ($R < 1$), partial synchronization, clustering, or chimera states are observed. **(D)** R vs. q plot shows effect of q on synchrony ($\epsilon = 0.31$).

For global coherence (1-cluster) or synchrony measure, we use the complex Kuramoto order parameter (R) [60] defined by

$$Re^{j\Phi} = \frac{1}{n}\sum_{i=1}^{n} e^{j\phi_i}, \tag{4}$$

where $j = \sqrt{-1}$, ϕ_i is the instantaneous phase of the ith patch. ϕ_i is determined by $\phi_i = \arctan(\frac{y_i - y^*}{x_i - x^*})$, where (x^*, y^*) is the non-zero fixed point of the system (2). When all patches are synchronized, $R = 1$ and in an incoherent state $R = 0$, while $0 < R < 1$ implies partial synchronization or clustering and even chimera states, which are further classified by other measures as described below.

For a more precise classification of clustered states (when $R \neq 1$), we use a clustering index (CI) [61],

$$CI = \frac{max(n)}{N}u, \tag{5}$$

where $u = 1 - \Psi(\sigma - p)$, $p = max(n) - \bar{n}$, and $\Psi(.)$ is the Heaviside step function; σ is an arbitrary small number, $n(t)$ is the number of distinct states counted (using a standard numerical routine) at every instant of time t in the time evolution of the network and $\bar{n}$ denotes the average in a long run. The $max(n)$ is the largest possible value of $n(t)$. We calculate the number of cluster states by rounding the value $\bar{n}$. In clustered states, $0 < R < 1$ and $CI = 0$. In chimera states, however, these measures are given by $0 < CI < 1$ and $0 < R < 1$.

The chimera state is finally characterized by a local order parameter (L_i), which presents an overview about the local degree of incoherency. The local order parameter of the ith oscillator is defined as Bera et al. [62]

$$L_i = \left| \frac{1}{2\delta} \sum_{|i-k| \leq \delta} e^{j\phi_k} \right|, i = 1, 2, \ldots, N, j = \sqrt{-1}, \tag{6}$$

where δ is the nearest neighbor on both sides of the ith oscillator (we choose $\delta = 5$) and ϕ_i is the instantaneous phase of the ith patch. $L_i \approx 1$ indicates that the ith oscillator belongs to the coherent subgroup of the chimera state, i.e., $L_i = 1$ means maximum ordering or coherency. In contrary, $L_i \approx 0$ means ith oscillator belongs to the incoherent neighbors. For each oscillatory patch, the local order parameter L_i is computed for a long time interval. For a confirmation of the chimera states, we employ a long time mean of phase velocity of each oscillatory patch. For ith oscillator, it is given by Banerjee et al. [63]

$$\Omega_i = \frac{2\pi M_i}{\Delta t}, \; i = 1, 2, \ldots, N, \tag{7}$$

where M_i is the number of periods of the ith oscillator in the long time interval Δt. Basically, it gives an impression about the distribution of oscillatory frequency of a group of oscillators. In an AMC state, Ω_i is identical for the coherent subgroup of oscillators and scattered for the incoherent subgroup. In AC states, Ω_i shows no distribution for both the subgroups.

To get a glimpse of a broader scenario of the collective dynamics of the network, we first approximate a symmetric case with identical dispersal rates ($\epsilon_1 = \epsilon_2 = \epsilon$) of both the predator and prey, without losing the essential dynamical features. We consider an approximation of equal weighted mean-field diffusion rates q for both the species. We consider an asymmetry in dispersal rates ($\epsilon_1 \neq \epsilon_2$), at a later stage. We first draw a phase diagram in a $q - \epsilon$ plane in **Figure 1B** that gives an overview of different collective states denoted by colors. A unique state of complete coherence (1-cluster) is seen (orange) in a large region of parameter space, where populations of both species in all patches oscillate in a common rythm and the population densities in all patches are identical in time. The parameter region of complete coherence (orange) is seen to form a typical arnold-toungue-like structure [64], which has a tip at a very small q value, but the region broadens with increasing dispersal rate ϵ and for increasingly larger q values. This coherent state (1-cluster) represents a globally synchronous state. From the ecological viewpoint, both prey and predator species follow a coherent oscillation in their temporal behavior. In such a coherent state, the network becomes vulnerable to external attack or perturbation. If population in any one of the patches goes extinct at any arbitrary instant of time then all other patches will follow the same trend, and thus enhances the possibility of a global extinction. For larger dispersal ϵ, the coherent region (orange) changes to a globally stable steady state or HSS (light blue region), as shown in the right side of the phase diagram. The transition to HSS occurs via reverse Hopf bifurcation: the analytically drawn Hopf line (black line) closely matches with the numerically drawn line of separation that delineates the HSS region (light blue) from the coherent region (orange). In the HSS region, both species reach a constant density in all the patches; they coexist with non-zero identical population density in each patch and they are safe. In dynamical sense, a stable steady state has the ability to return to its original stable state after a transient time under a perturbation and thus HSS signifies robustness of a population to external attacks. Besides these coherent oscillatory state (synchrony) and the HSS, we find regions of 2-cluster (yellow), 3-cluster (red), and multi-cluster (green) states. A symmetry-breaking line (black circles) delineates the regions of synchrony and 2-cluster states as obtained from numerical simulations of a reduced 2-patch system (see **Appendix** in Supplementary Material) and it closely fits to the separating line (boundary of orange and yellow regions) as designated by numerical simulations of the full system. In clustered states, all the patches split into coherent subgroups. In a coherent subgroup or a cluster, species oscillate coherently with almost identical population density at any time instant, however, the subgroups remain incoherent between themselves. We notice complex patterns such as chimera states (blue) for low q and a range of ϵ values. The complexity in collective behavior is clearly visible in the lower range of q values, and hence we focus on this range of q values, in the next section. Before that we elaborate the nature of transition to synchrony from an initial state of incoherence. For this, we plot the order parameter R (**Figure 1C**) against ϵ that decreases first, indicating a decreasing level of coherence with higher clusters and emergence of chimera states. Then R increases for increasing ϵ, indicating a decrease in cluster size, but finally $R = 1$ when the network transits to synchrony (blue line) at $\epsilon = 0.45$ and it continues until $\epsilon = 0.5$. The HSS (red line) is reached (where $R = 1$) for $\epsilon > 0.50$. The transition to synchrony is also checked with a variation of q for a fixed dispersal rate $\epsilon = 0.31$ as shown in **Figure 1D**. It follows a monotonic increase to $R = 1$, indicating existence of clustered and chimera states before reaching synchrony.

A globally coupled network based on the RM model using the weighted mean-field controlled dispersal was investigated earlier [44, 46], in exhaustive details, numerically as well as analytically, in two coupled patches to establish the evolution of spatial synchrony and population stability, HSS and two regions of transcritical bifurcation, in parameter space. They made an extension to a 16-patch network to present two more emergent IHSS states, 2-clustered death and multiclustered-death states [28, 46]. We reproduce some of the previous results, mainly, synchrony, HSS and two additional transcritical bifurcations (see **Appendix** in Supplementary Material) for larger values of $\epsilon_{1,2}$, which we do not focus here. Taking earlier experience [46] into consideration, we rather focus our investigations on the lower range of q values and weaker dispersal rates where complex patterns (green, red, blue regions) really evolve as shown in **Figure 1B** and as detailed in **Figures 2A,B**. Existence of complex patterns, clustered states, multiclustered states and chimera states, in non-equilibrium states, is absent in the earlier study [46]. In a metapopulation, emergence of such complex oscillatory patterns may play crucial role on the survival probability of species. The main difference in our results lies in the choice of low q and ϵ values.

Now we focus on the lower range of q in search of complexity of collective behaviors. Selecting a lower value of q (0.02), as an example, and varying both the dispersal rates $\epsilon_{1,2}$, two separate phase diagrams (**Figure 2**) are drawn in the $\epsilon_1 - \epsilon_2$ plane using the quantitative measures defined above. **Figure 2A** presents collective dynamical scenarios of the network of predatory-prey interactions represented by the original RM model; a comparative picture of the collective states in the network represented by the mRM patches is presented in **Figure 2B**. In both the cases, we obtain regions of HSS (light blue), spatial synchrony (orange) and 2-cluster (yellow), multiclustered (green) and chimera patterns (blue) by numerically simulating the full system of $N = 100$ patches. We attempt an analytical stability analysis of the full system to derive the separating boundaries of different complex patterns in the phase diagrams. So far we are unable to do the stability analysis of the full system ($N = 100$), however, we are able to reduce the network to a 2-dimensional 1-patch system at HSS and then do the stability analysis of equilibrium points of the reduced system. Thereby we draw (see **Appendix** in Supplementary Material) the Hopf bifurcation lines (black lines) in **Figures 2A,B** that almost match the border of HSS and synchrony as obtained from simulation of the full system. Similarly, we check the separating line of synchrony and 2-cluster states, in parameter space, by reducing the full system to a 2-cluster system (see **Appendix** in Supplementary Material). We numerically simulate the 4-dimensional reduced system to put a demarcation boundary

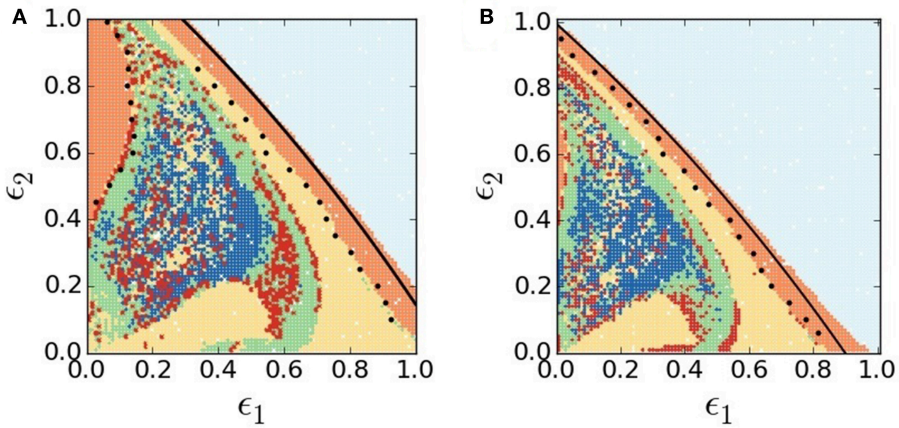

FIGURE 2 | (Color online) Collective dynamical states in ϵ_1-ϵ_2 parameter plane. **(A)** Original RM network model ($c_1 = c_2 = 0$), **(B)** modified RM network model ($c_1 = 0.01$, $c_2 = 0.1$). Different colors depict various collective states: HSS (light blue), global synchrony (orange), 2-cluster (yellow), 3-cluster (red dots), higher cluster (green), and chimera states (blue). Black circles on both phase diagrams denote the symmetry-breaking line from synchrony (1-cluster) to 2-cluster state as obtained from numerical simulations of a reduced 2-patch mode. Other system parameters are same for both the models: $r = 2.65$, $K = 898$, $h = 0.0437$, $\theta = 0.215$, $\alpha = 0.045$, $d = 0.12$, $q = 0.02$, and $N = 100$.

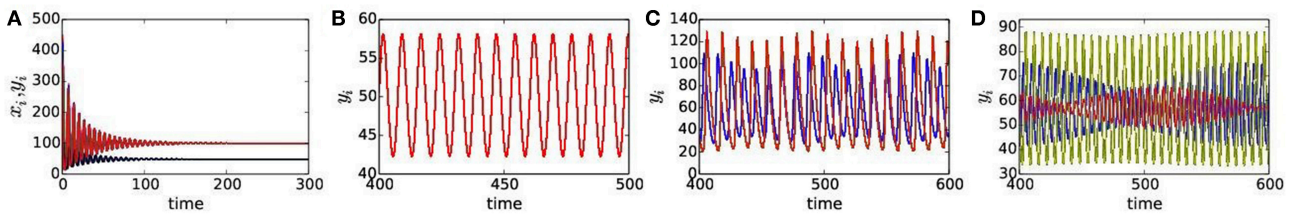

FIGURE 3 | (Color online) Temporal dynamics of prey and predator in presence of habitat complexity for different dispersal rates: **(A)** HSS for $\epsilon_1 = 0.71$, $\epsilon_2 = 0.63$, **(B)** synchronous state for $\epsilon_1 = 0.66$, $\epsilon_2 = 0.3$, **(C)** 2-cluster states for $\epsilon_1 = 0.3$, $\epsilon_2 = 0.11$, and **(D)** 3-cluster states for $\epsilon_1 = 0.4$ $\epsilon_2 = 0.44$. Other parameters are chosen as per in **Figure 2B** for the mRM based network.

between synchrony and 2-cluster state (black circles), which shows an almost matching with the separating line obtained from a simulation of the full system. Using the reduced system, we depict a similar demarcation boundary of synchrony (orange region) and 2-cluster state by putting a border of black circles at the top left of **Figure 2A**.

Now we draw an attention to significant changes in our results by the addition of habitat complexity. **Figures 2A,B** apparently look similar since both the plots show large regions of HSS (light blue) and regions of synchrony (orange) and 2-cluster (yellow) states. A closer inspection, however, reveals noticeable qualitative changes in collective dynamics in presence of habitat complexity. **Figure 2B** clearly shows a larger area of HSS in the $\epsilon_1 - \epsilon_2$ parameter plane compared to **Figure 2A**. Changes in other regions of clustered states (yellow, red dots, green) and chimera states (blue) are also noticed. In the HSS region, both prey and predator population densities become stable at a non-zero steady state in all patches, as confirmed by their temporal dynamics in **Figure 3A**, although isolated patches were in oscillatory states. This represents a globally stable steady state (cf. $R = 1$, red line in **Figure 1C**). The weighted mean-field-controlled dispersal of species plays an important role in the emergence of this HSS state. The non-zero fixed point explains its ecological relevance as a coexistence of both prey and predator populations with non-zero constant densities. This leads to a better survivability condition of both the species in HSS since it is a robust state against external or environmental perturbations. Obviously, the presence of habitat complexity enhances persistence of species by increasing the region of HSS in parameter space and thereby supports the experimental results [54–58]. In the lower range of dispersal rates, all patches are driven out of the HSS state and enter into an oscillatory state (orange color), yet they maintain a coherent state. A transition from the HSS state (light blue) to the globally synchronous oscillatory state (orange) is seen immediately below the HSS region via Hopf bifurcation in **Figure 2**. Both the prey and predators start oscillating in a globally synchronous state (orange), where all patches oscillate in one common rhythm, as illustrated in the temporal dynamics of the patches in **Figure 3B**. The oscillation in all the $N = 100$ patches show a single period limit cycle. As mentioned above, extinction probability is higher in case of coherent oscillatory populations as population may go extinct due to additional environmental perturbation when population density is at the nadir of a cycle [5, 6, 20]. If population in one patch goes

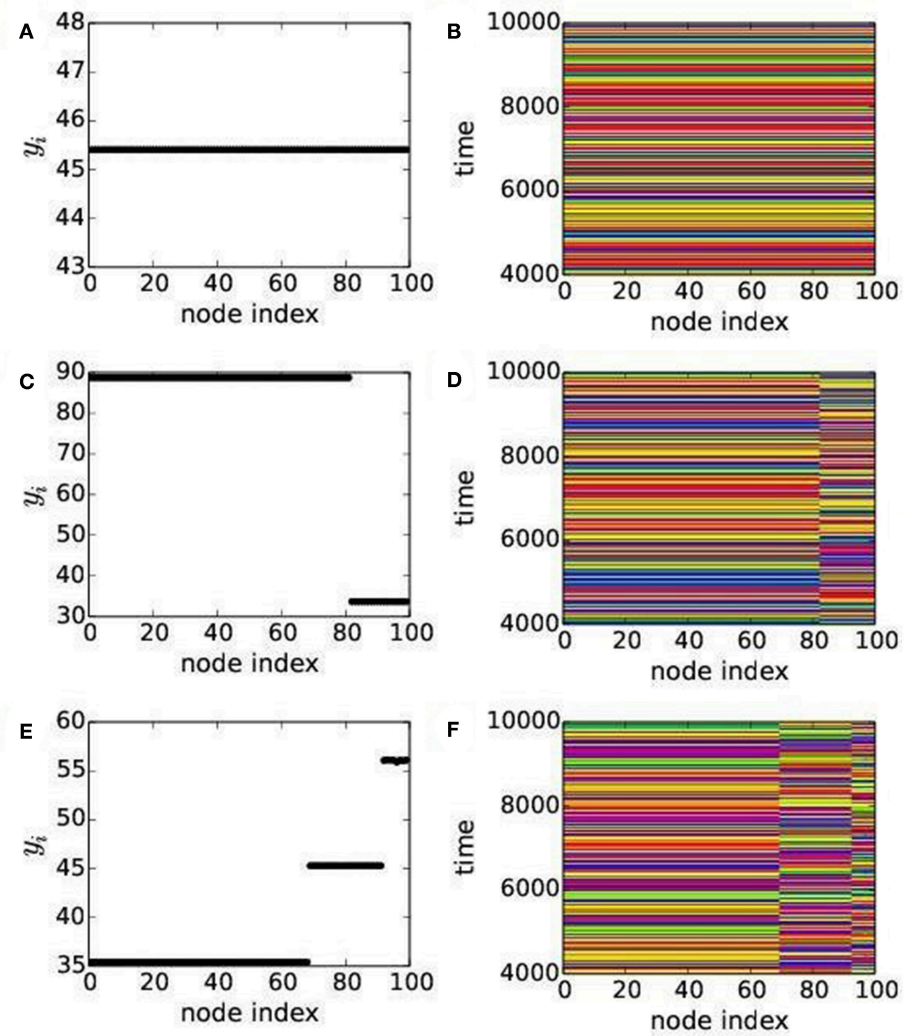

FIGURE 4 | (Color online) Collective dynamics of predators in all N(=100) patches. Left and right panels show, respectively, snapshots and spatio-temporal asymptotic dynamics of predators in 100 patches. **(A,B)** show snapshot and spatio-temporal of 1-cluster state for $\epsilon_1 = 0.66$, $\epsilon_2 = 0.3$. **(C,D)** represent snapshot and spatio-temporal of 2-cluster states for $\epsilon_1 = 0.3$, $\epsilon_2 = 0.11$. **(E,F)** represent snapshot and spatio-temporal of 3-cluster states for $\epsilon_1 = 0.4$, $\epsilon_2 = 0.44$. System parameters are as chosen in **Figure 2B** with $q = 0.02$ for the mRM based network.

extinct for some external perturbations, it will be followed by the populations of all other patches in the network, causing global extinction of the species. In this sense, synchrony is always a curse for ecological systems. A reasonably large region of globally synchronous state also exists in the lower range of prey dispersal rate and larger predator movement as seen (top left) in **Figure 2A**. This synchronous state is almost vanished in the same parameter region in **Figure 2B**. The presence of habitat complexity thus incurs another qualitative change and thereby improves the survivability condition by breaking the synchrony and inducing multi-clustered states (green) and chimera states (blue) in this region of the $\epsilon_1 - \epsilon_2$ parameter plane.

For weaker dispersal rates, below the synchronous state (orange), regions of 2-cluster states (yellow), 3-clustered (scattered red dots), multi-clustered (green) states and chimera states (blue) are seen in both the phase diagrams in **Figure 2**. For further illustration of collective states, we select dispersal parameters from different colored regions of the phase diagram **Figure 2B**, representing the mRM based network, and present their respective temporal dynamics, snapshots, spatio-temporal dynamics and also plots of local order parameter L_i and mean phase velocity Ω_i. The temporal dynamics of both predator and prey populations in all patches are plotted in **Figures 3C,D** for 2-cluster and 3-cluster states, respectively, which are quasiperiodic in nature in both the states. Snapshots of predator population in all patches (indicated by node indices) are plotted in **Figures 4A,C,E**, showing 1-cluster (synchrony), 2-cluster and 3-cluster states, respectively, for different choices of (ϵ_1, ϵ_2). One coherent group (1-cluster) splits into 2- and 3-coherent subgroups of unequal number of patches (node indices); each subgroup have identical population density (y_i level), in the snapshot, but there exist different levels of densities for different

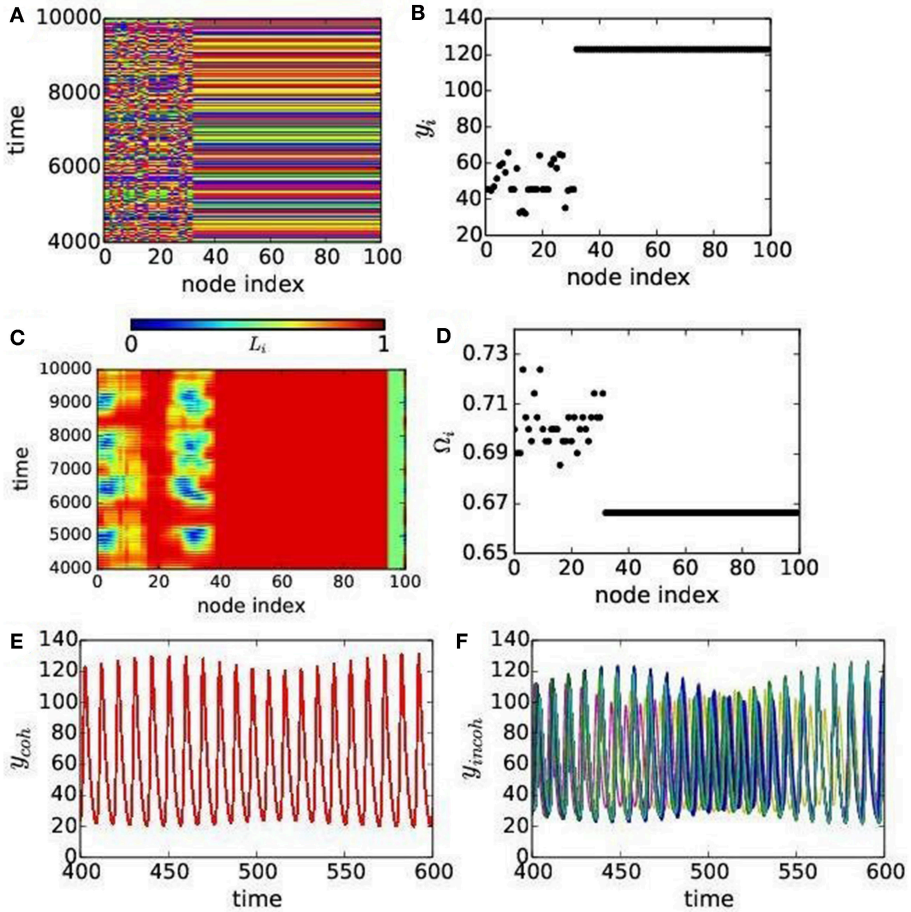

FIGURE 5 | (Color online) Chimera states for the dispersal rates $\epsilon_1 = 0.29$, $\epsilon_2 = 0.22$. **(A)** Spatio-temporal plots and **(B)** snap shot of predator population. **(C)** Local order parameter L_i and **(D)** mean phase velocity Ω_i. **(E)** Temporal dynamics of coherent patches and **(F)** the same for incoherent patches. Other parameters are as chosen in **Figure 2B** for the mRM network.

subgroups. Corresponding spatio-temporal plots presented in **Figures 4B,D,F** also confirm the collective states of 1-cluster, 2-cluster, and 3-cluster, respectively. Clearly, the subgroups in each 2-, 3-cluster states have no coherence.

Multi-clustered states (green color) and chimera states (blue color) are present in smaller islands, but clearly noticeable in parameter space as shown in **Figure 2** for both the cases. A spatio-temporal plot of y_i population in all the patches in **Figure 5A** shows chimera pattern with two subgroups: one coherently oscillating and another oscillating incoherently. The spatio-temporal plot of the local order parameter L_i (node index) presented in **Figure 5C** is in agreement with **Figure 5A**. This chimera pattern is further confirmed by a snapshot in **Figure 5B** that shows coherence in predator densities y_i in all the patches, while a smaller subgroup of patches show random distribution. The mean phase velocity is plotted in **Figure 5D** that shows a distribution for the incoherent patches in the same subgroup while they are identical for the coherent patches. This identifies the chimera states as amplitude mediated, i.e., as a case of AMC. The temporal dynamics of all the coherent and incoherent patches are presented in **Figures 5E,F**, respectively. The coherent patches show identical oscillation, while oscillation in the incoherent patches have varying amplitude, but both are of quasiperiodic nature. We have checked the quasiperiodicity using a Poincáre plot, which we do not present here.

4. DISCUSSION

A globally connected network structure is considered here as an approximate model for studies of metapopulation dynamics in ecological networks [14, 65]. Although a number of complex natural processes is involved in ecological systems, a deterministic model approach, as proposed here, can still be used to extract reliable information on the complexity of population dynamics [65]. Here we assume that all the patches in the network have all-to-all connectivity by the process of dispersal of species and the predator-prey interaction in each patch is governed by the mRM model, where the local dynamics exhibits stable limit cycle oscillation in isolation. Both the prey and predator species have freedom to migrate within the patches [11–13] and the migration of both species depends upon its average or mean population density. The diffusion or

the migration process between the patches is controlled by the weighted mean-field density of each species [50, 53, 66]. Such a weighted mean-field guided diffusion process was initiated in quorum sensing of synthetic genetic oscillators [50, 51] and later on, it has been applied to other generic dynamical models to realize HSS in coupled oscillatory systems [52, 67]. We used the weighted mean-field diffusion process to describe a dispersal-driven metapopulation since it is more realistic in a perspective of partial loss of population during migration of species as suggested earlier [46, 53], however, extended their results [46] in a search of complex patterns.

A basic question in ecological network study is—how such a diffusion process of dispersal of species can influence the collective dynamics of the network and if it can originate complex spatio-temporal patterns? Another important question is how does complexity in collective spatio-temporal pattern help an ecological landscape and most importantly, if it can, at all, improve the survivability and persistence of species when such complex collective states may emerge? To address the questions, we first plotted a two parameter phase diagram in the dispersal rate and weighted mean-field parameter plane under an approximation of identical dispersal rates of both species. The phase diagram gave an overview of the collective dynamics of the ecological network as shown by different colors under varying weighted mean-field diffusion and dispersal rate. A spatial synchrony prevailed in a large region of the parameter space along with a significantly large region of 2-cluster and HSS. However, we observed smaller regions of complex collective patterns such as 2-cluster, 3-cluster, multi-cluster, and chimera states in the lower range of weighted mean-field diffusion constant. To have a closer look on the complex dynamics for lower values of the weighted mean-field diffusion constant, another phase diagram was plotted with respect to the dispersal rates of prey and predator species for a low value of weighted mean-field constant. It showed prominent regions of complex patterns in a parameter plane of dispersal rates: 2-cluster, 3-cluster, multi-clustered, and chimera states in the region of low weighted mean-field constant. Existence of complex collective patterns were identified using several quantitative measures, namely, Kuramoto order parameter, clustering index, local order parameter and mean phase velocity. Spatio-temporal plots, snapshots of predator, and prey population dynamics of all patches gave us confirmation of our claims of the variety of collective states, especially, information about clustered states and chimera states. A transition from synchronous oscillatory state to HSS occurred via reverse Hopf bifurcation for higher dispersal rates as confirmed by a stability analysis of the reduced system at HSS (**Appendix** in Supplementary Material). A representative example of emergent complex patterns for a low q value is presented here, however, it has been found true for a range of q values.

Another important question that we tried to address is the role of habitat complexity on the emergence of complex patterns. For a comparative understanding of the collective dynamics in presence and absence of habitat complexity, a phase diagram in the same parameter plane of dispersal rates was added using the ecological network where each node was represented by the original RM model without having habitat complexity parameter. The region of HSS had been enlarged significantly, in parameter space, by the addition of habitat complexity in our proposed mRM model, indicating an increased parameter region of dispersal rates that provided an improved condition of persistence. Furthermore, in the absence of habitat complexity, a region of synchrony that existed for lower rates of dispersal of prey and higher dispersal of predator, disseminated into larger varieties of complex patterns in presence of habitat complexity. By decreasing the parameter space for spatial synchrony, species in an ecological landscape were allowed to a large variety of dispersal possibilities that may reduce the risk of extinction.

Habitat complexity has no specific role in the origin of complex patterns. In fact, we showed in a comparative study that complex patterns originate for both cases: in absence and presence of habitat complexity. Complexity in collective states may be attributed to the choice of low q and ϵ values. Finally, we mention that all the complex patterns emerge, in non-equilibrium states, in our globally coupled ecological network. How complex oscillatory patterns help improving survivability or persistence of species is a future question of investigation to address.

AUTHOR CONTRIBUTIONS

SS formulated the problem, did the simulations and wrote the manuscript. SD and NB worked on rewriting and improving the manuscript.

ACKNOWLEDGMENTS

SS, NB, and SD acknowledge support by the DST-SERB (India), Grant No. EMR/2016/001078. SD also acknowledges support by the University Grants Commission (India) under Emeritus Fellow scheme. The authors are thankful to the editor and reviewers for their useful suggestions and comments. Authors acknowledge valuable discussions with Dibakar Ghosh, Indian Statistical Institute, Kolkata.

SUPPLEMENTARY MATERIAL

The Supplementary Material for this article can be found online at: https://www.frontiersin.org/articles/10.3389/fams.2019.00015/full#supplementary-material

REFERENCES

1. Earn DJ, Levin SA, Rohani P. Coherence and conservation. *Science*. (2000) **290**:1360–4. doi: 10.1126/science.290.5495.1360
2. Jansen VAA. The dynamics of two diffusively coupled predator-prey populations. *Theor Popul Biol*. (2001) **59**:119–31. doi: 10.1006/tpbi.2000.1506
3. Hudgens BR, Haddad NM. Predicting which species will benefit from corridors in fragmented landscapes from population growth models. *Am Nat*. (2003) **161**:808–20. doi: 10.1086/374343
4. Roy M, Holt RD, Barfield M. Temporal autocorrelation can enhance the persistence and abundance of metapopulations comprised of coupled sinks. *Am Nat*. (2005) **166**:246–61. doi: 10.1086/431286

5. Holland MD, Hastings A. Strong effect of dispersal network structure on ecological dynamics. *Nature.* (2008) **456**:792. doi: 10.1038/nature07395
6. Gupta A, Banerjee T, Dutta PS. Increased persistence via asynchrony in oscillating ecological populations with long-range interaction. *Phys Rev E.* (2017) 96:042202. doi: 10.1103/PhysRevE.96.042202
7. Heino M, Kaitala V, Ranta E, Lindstrom J. Synchronous dynamics and rates of extinction in spatially structured populations. *Proc R Soc Lond B Biol Sci.* (1997) **264**:481–6. doi: 10.1098/rspb.1997.0069
8. Johst K, Brandl R, Eber S. Metapopulation persistence in dynamic landscapes: the role of dispersal distance. *Oikos.* (2002) **98**:263–70. doi: 10.1034/j.1600-0706.2002.980208.x
9. Levins R. Extinction. In: Miura RM, editor. *Some Mathematical Questions in Biology: Lectures on Mathematics in the Life Sciences*. Providence, RI: American Mathematical Society (1970). p. 75–108.
10. Fahrig L. Effects of habitat fragmentation on biodiversity. *Annu Rev Ecol Evol Syst.* (2003) **34**:487–515. doi: 10.1146/annurev.ecolsys.34.011802.132419
11. Goldwyn EE, Hastings A. When can dispersal synchronize populations? *Theor Popul Biol.* (2008) **73**:395–402. doi: 10.1016/j.tpb.2007.11.012
12. Goldwyn EE, Hastings A. Small heterogeneity has large effects on synchronization of ecological oscillators. *Bull Math Biol.* (2009) **71**:130–44. doi: 10.1007/s11538-008-9355-9
13. Goldwyn EE, Hastings A. The roles of the Moran effect and dispersal in synchronizing oscillating populations. *J Theor Biol.* (2011) **289**:237–46. doi: 10.1016/j.jtbi.2011.08.033
14. Blasius B, Huppert A, Stone L. Complex dynamics and phase synchronization in spatially extended ecological systems. *Nature.* (1999) **399**:354. doi: 10.1038/20676
15. Pajunen VI and Pajunen I. Long-term dynamics in rock pool daphnia metapopulations. *Ecography.* (2003) **26**:731–8. doi: 10.1111/j.0906-7590.2003.03542.x
16. Roy M, Harding K, Holt RD. Generalizing levins metapopulation model in explicit space: models of intermediate complexity. *J Theor Biol.* (2008) **255**:152–61. doi: 10.1016/j.jtbi.2008.07.022
17. Wall E, Guichard F, Humphries AR. Synchronization in ecological systems by weak dispersal coupling with time delay. *Theor Ecol.* (2013) **6**:405–18. doi: 10.1007/s12080-013-0176-6
18. Liebhold A, Koenig WD, Bjornstad ON. Spatial synchrony in population dynamics. *Annu Rev Ecol Evol Syst.* (2004) **35**:467–90. doi: 10.1146/annurev.ecolsys.34.011802.132516
19. Strogatz S. *Sync: How Order Emerges From Chaos in the Universe, Nature, and Daily Life*. New York, NY: Hyperion (2003).
20. Holyoak M, Lawler SP. Persistence of an extinction-prone predator-prey interaction through metapopulation dynamics. *Ecology.* (1996) **77**:1867–79. doi: 10.2307/2265790
21. Ranta E, Kaitala V, Lundberg P. The spatial dimension in population fluctuations. *Science.* (1997) **278**:1621–3. doi: 10.1126/science.278.5343.1621
22. Hanski I. Metapopulation dynamics. *Nature.* (1998) **396**:41. doi: 10.1038/23876
23. Saxena G, Prasad A, Ramaswamy R. Amplitude Death: the emergence of stationarity in coupled nonlinear systems. *Phys Rep.* (2012) **521**:205–30. doi: 10.1016/j.physrep.2012.09.003
24. Koseska A, Volkov E, Kurths J. Oscillation quenching mechanisms: amplitude vs. oscillation death. *Phys Rep.* (2013) **531**:173-200. doi: 10.1016/j.physrep.2013.06.001
25. Hens CR, Olusola OI, Pal P, Dana SK. Oscillation death in diffusively coupled oscillators by local repulsive link. *Phys Rev E.* (2013) **88**:034902. doi: 10.1103/PhysRevE.88.034902
26. Hens CR, Pal P, Bhowmick SK, Roy PK, Sen A, Dana SK. Diverse routes of transition from amplitude to oscillation death in coupled oscillators under additional repulsive links. *Phys Rev E.* (2014) **89**:032901. doi: 10.1103/PhysRevE.89.032901
27. Nandan M, Hens CR, Pal P, Dana SK. Transition from amplitude to oscillation death in a network of oscillators. *Chaos.* (2014) **24**:043103. doi: 10.1063/1.4897446
28. Mishra A, Saha S, Roy PK, Kapitaniak T, Dana SK. Multicluster oscillation death and chimeralike states in globally coupled Josephson Junctions. *Chaos.* (2017) **27**:023110. doi: 10.1063/1.4976147
29. Steiner CF, Stockwell RD, Kalaimani V, Aqel Z. Population synchrony and stability in environmentally forced metacommunities. *Oikos.* (2013) **122**:1195. doi: 10.1111/j.1600-0706.2012.20936.x
30. Drake JA, Staelens P, Wieczynski D. *Encyclopedia of Theoretical Ecology*. Hastings A, Gross L, editors. Berkeley, CA: University of California Press (2012). p. 60-3.
31. Hardenberg JV, Meron E, Shachak M, Zarmi Y. Diversity of vegetation patterns and desertification. *Phys Rev Lett.* (2001) **87**:198101. doi: 10.1103/PhysRevLett.87.198101
32. Jalan S, Amritkar RE. Self-organized and driven phase synchronization in coupled maps. *Phys Rev Lett.* (2003) **90**:014101. doi: 10.1103/PhysRevLett.90.014101
33. Pecora LM, Sorrentino F, Hagerstrom AM, Murphy TE, Roy R. Cluster synchronization and isolated desynchronization in complex networks with symmetries. *Nat Commun.* (2014) **5**:4079. doi: 10.1038/ncomms5079
34. Sorrentino F, Pecora LM, Hagerstrom AM, Murphy TE, Roy R. Complete characterization of the stability of cluster synchronization in complex dynamical networks. *Sci Adv.* (2016) **2**:e1501737 doi: 10.1126/sciadv.1501737
35. Kuramoto Y, Battogtokh D. Coexistence of coherence and incoherence in nonlocally coupled phase oscillators. *Nonlinear Phenom Complex Syst.* (2002) **5**:380.
36. Abrams DM, Strogatz SH. Chimera states for coupled oscillators. *Phys Rev Lett.* (2004) **93**:174102. doi: 10.1103/PhysRevLett.93.174102
37. Sethia GC, Sen A, Atay FM. Clustered chimera states in delay-coupled oscillator systems. *Phys Rev Lett.* (2008) **100**:144102. doi: 10.1103/PhysRevLett.100.144102
38. Omelchenko I, Maistrenko YL, Hövel P, Schöll E. Loss of coherence in dynamical networks: spatial chaos and chimera states. *Phys Rev Lett.* (2011) **106**:234102. doi: 10.1103/PhysRevLett.106.234102
39. Sethia GC, Sen A, Johnston GL. Amplitude-mediated chimera states. *Phys Rev E.* (2013) **88**:042917. doi: 10.1103/PhysRevE.88.042917
40. Sethia GC, Sen A. Chimera states: the existence criteria revisited. *Phys Rev Lett.* (2014) **112**:144101. doi: 10.1103/PhysRevLett.112.144101
41. Yeldesbay A, Pikovsky A, Rosenblum M. Chimeralike states in an ensemble of globally coupled oscillators. *Phys Rev Lett.* (2014) **112**:144103. doi: 10.1103/PhysRevLett.112.144103
42. Mishra A, Hens CR, Bose M, Roy PK, Dana SK. Chimeralike states in a network of oscillators under attractive and repulsive global coupling. *Phys Rev E.* (2015) **92**:062920. doi: 10.1103/PhysRevE.92.062920
43. Panaggio M, Abrams DM. Chimera states: Coexistence of coherence and incoherence in networks of coupled oscillators. *Nonlinearity.* (2015) **28**:R67–87. doi: 10.1088/0951-7715/28/3/R67
44. Dutta PS, Banerjee T. Spatial coexistence of synchronized oscillation and death: a chimeralike state. *Phys Rev E.* (2015) **92**:042919. doi: 10.1103/PhysRevE.92.042919
45. Banerjee T, Dutta PS, Zakharova A, Schöll E. Chimera patterns induced by distance-dependent power-law coupling in ecological networks. *Phys Rev E.* (2016) **94**:032206. doi: 10.1103/PhysRevE.94.032206
46. Arumugam R, Dutta PS, Banerjee T. Dispersal-induced synchrony, temporal stability, and clustering in a mean-field coupled Rosenzweig-MacArthur model. *Chaos.* (2015) **25**:103121. doi: 10.1063/1.4933300
47. Hizanidis J, Panagakou E, Panagakou E, Omelchenko I, Provata A, Scöll E, et al. Chimera states in population dynamics: networks with fragmented and hierarchical connectivities. *Phys Rev E.* (2015) **92**:012915. doi: 10.1103/PhysRevE.92.012915
48. Kundu S, Majhi S, Muruganandam P, Ghosh D, Diffusion induced spiral wave chimeras in ecological system. *Eur Phys J Spec Top.* (2018) **227**:983–93. doi: 10.1140/epjst/e2018-800011-1
49. Rosenzweig ML, MacArthur RH. Graphical representation and stability conditions of predator-prey interactions. *Am Nat.* (1963) **97**:209–23. doi: 10.1086/282272

50. Ullner E, Zaikin A, Volkov EI, García-Ojalvo J. Multistability and clustering in a population of synthetic genetic oscillators via phase-repulsive cell-to-cell communication. *Phys Rev Lett*. (2007) **99**:148103. doi: 10.1103/PhysRevLett.99.148103
51. Hellen EH, Dana SK, Zhurov B, Volkov E. Electronic implementation of a repressilator with quorum sensing feedback. *PLoS ONE*. (2013) 8:e62997. doi: 10.1371/journal.pone.0062997
52. Sharma A, Shrimali MD, Dana SK. Phase-flip transition in nonlinear oscillators coupled by dynamic environment. *Chaos*. (2012) **22**:023147. doi: 10.1063/1.4729459
53. Banerjee T, Dutta PS, Gupta A. Mean-field dispersion-induced spatial synchrony, oscillation and amplitude death, and temporal stability in an ecological model. *Phys Rev E*. (2015) **91**:052919. doi: 10.1103/PhysRevE.91.052919
54. Johnson, WD. Predation, habitat complexity and variation in density dependent mortality of temperate reef fishes. *Ecology*. (2006) **87**:1179–188. doi: 10.1890/0012-9658(2006)87[1179:PHCAVI]2.0.CO;2
55. Manatunge J, Asaeda T, Priyadarshana T. The influence of structural complexity on fish-zooplankton interactions: a study using artificial submerged macrophytes. *Environ Biol Fish*. (2000) **58**:425–38. doi: 10.1023/A:1007691425268
56. Savino, JF, Stein, RA. Behavior of fish predators and their prey: habitat choice between open water and dense vegetation. *Environ Biol Fish*. (1989) **24**:287–93. doi: 10.1007/BF00001402
57. August PV. The role of habitat complexity and heterogeneity in structuring tropical mammal communities. *Ecology*. (1983) **64**:1495–507. doi: 10.2307/1937504
58. Crowder LB, Cooper WE. Habitat structural complexity and the interaction between bluegills and their prey. *Ecology*. (1982) **63**:1802–13. doi: 10.2307/1940122
59. Jana D, Bairagi N. Habitat complexity, dispersal and metapopulations: macroscopic study of a predator-prey system. *Ecol Complex*. (2014) **17**:131–9. doi: 10.1016/j.ecocom.2013.11.006
60. Kuramoto Y. *Chemical Oscillations, Waves, and Turbulence*. Berlin; Heidelberg: Springer-Verlag (2012). p. 19. doi: 10.1007/978-3-642-69689-3
61. Mishra A, Saha S, Hens CR, Roy PK, Bose M, Louodop P, et al. Coherent libration to coherent rotational dynamics via chimeralike states and clustering in a Josephson junction array. *Phys Rev E*. (2017) **95**:010201(R). doi: 10.1103/PhysRevE.95.010201
62. Bera BK, Ghosh D, Banerjee T. Imperfect traveling chimera states induced by local synaptic gradient coupling. *Phys Rev E*. (2016) **94**:012215. doi: 10.1103/PhysRevE.94.012215
63. Banerjee T, Biswas D, Ghosh D, Schöll E, Zakharova A. Networks of coupled oscillators: From phase to amplitude chimeras. *Chaos*. (2018) **28**:113124. doi: 10.1063/1.5054181
64. Pikovsky A, Osipov GV, Rosenblum M, Zaks M, Kurths J. Attractor-repeller collision and eyelet intermittency at the transition to phase synchronization. *Phys Rev Lett*.(1997) **79**:47. doi: 10.1103/PhysRevLett.79.47
65. McCredie May GM. *Stability and Complexity in Model Ecosystems, Vol. 6*. Princeton, NJ: University Press (2001).
66. Garcia-Ojalvo J, Elowitz MB, Strogatz SH. Modeling a synthetic multicellular clock: repressilators coupled by quorum sensing. *Proc Natl Acad Sci USA*. (2004) **101**:10955. doi: 10.1073/pnas.0307095101
67. Sharma A, Shrimali MD. Amplitude death with mean-field diffusion. *Phys Rev E*. (2012) **85**:057204. doi: 10.1103/PhysRevE.85.057204
68. Ermentrout B. *Simulating, Analyzing, and Animating Dynamical Systems: A Guide to Xppaut for Researchers and Students (Software, Environments, Tools)*. Philadelphia, PA: SIAM Press (2002). doi: 10.1137/1.9780898718195

Conflict of Interest Statement: The authors declare that the research was conducted in the absence of any commercial or financial relationships that could be construed as a potential conflict of interest.

frontiers in Applied Mathematics and Statistics

ORIGINAL RESEARCH
published: 09 April 2019
doi: 10.3389/fams.2019.00016

Chimera and Anticoordination States in Learning Dynamics

Haydée Lugo[1]*, *Juan Carlos González-Avella*[2] *and Maxi San Miguel*[3]

[1] ICAE, Department of Economic Analysis, Complutense University of Madrid, Madrid, Spain, [2] APSL S.L, Edifici Europa - Planta baja Galileo Galilei, Palma de Mallorca, Spain, [3] IFISC (CSIC-UIB), Campus Universitat Illes Balears, Palma de Mallorca, Spain

In many real-life situations, individuals are dared to simultaneously achieve social objectives of acceptance or approval and strategic objectives of coordination. Since these two objectives may take place in different environments, a two-layer network is the simple and natural framework for the study of such kind of dynamical situations. In this paper we present a model in which the state of the agents corresponds to one of two possible strategies. They change their states by interaction with their neighbors in the network. Inside each layer the agents interact by a social pressure mechanism, while between the layers the agents interact via a coordination game. From an evolutionary approach, we focus on the asymptotic solutions for all-to-all interactions across and inside the layers and for any initial distribution of strategies. We find new asymptotic configurations which do not exist in a single isolated social network analysis. We report the emergence and existence of chimera states in which two different collective states coexist in the network. Namely, one layer reaches a state of full coordination while the other remains in a dynamical state of coexistence of strategies. In addition, the system may also reach a state of global anticoordination where a full coordination is reached inside each layer but with opposite strategies in each of the two network layers. We trace back the emergence of chimera states and global anticoordination states to the agents inertia against social pressure, referred here to as the level of skepticism, along with the degree of risk taken into account in a general coordination game.

Keywords: multilayer network, coordination games, chimera states, anticoordination states, skepticism

OPEN ACCESS

Edited by:
Eckehard Schöll, Technische Universität Berlin, Germany

Reviewed by:
Ugo Merlone, University of Turin, Italy
Sajad Jafari, Amirkabir University of Technology, Iran

***Correspondence:**
Haydée Lugo
hlugo@ucm.es

Specialty section:
This article was submitted to Dynamical Systems, a section of the journal Frontiers in Applied Mathematics and Statistics

Received: *12 December 2018*
Accepted: *19 March 2018*
Published: *09 April 2019*

Citation:
Lugo H, González-Avella JC and San Miguel M (2019) Chimera and Anticoordination States in Learning Dynamics. Front. Appl. Math. Stat. 5:16. doi: 10.3389/fams.2019.00016

1. INTRODUCTION

The chimeric states refer to the emergence of a hybrid state in a coupled dynamic system in which one domain of the system exhibits a coherent behavior in combination with another domain that displays an incoherent behavior. The coexistence of coherent and incoherent states has received much attention as an intriguing manifestation of collective behavior. This interesting behavior was first observed by Kuramoto et al. [1] and then named it as chimera state [2]. Although the literature about chimera states started with the study of interacting populations of oscillators in dynamical systems [3–7], it has been dizzily expanded to many fields in physics, chemistry, biology, etc (see [8–20]). Also in social systems, situations of two interacting populations in which one exhibits a coherent or synchronized behavior while the other is incoherent or desynchronized are commonly observed [21, 22]. This phenomena has also been addressed from the conceptual framework of chimera states. Models based on individual interactions have been introduced for opinion formation and cultural dissemination [21] and [22] in order to analyze the emergence of

localized coherent or chimeras states behavior in social contexts. The systems considered consist in two populations of social agents mutually coupled through global interaction fields that account for the state of the majority of the agents in each population. The internal interactions in each group have a condition that allow for non-interacting states. Two examples of such dynamics have been analyzed: (i) Axelrod's model for social influence [23], and (ii) a discrete version of a bounded confidence model for opinion formation [24]. In both systems, there are localized coherent states for some parameter values, in which a group reaches a homogenous or consensus state, while the other group remains in a disordered or polarized state. In this paper we contribute further to the study of chimera states in social systems, searching for them in the context of models of social coordination and learning dynamics [25].

The goal of reaching coordination has become one of the most important challenges in modern societies: In spite of the fact that individuals are now more connected and handle more information due to technological progress, it seems that coordination to reach consensus is becoming an increasingly difficult goal. It is common to observe how some societies become polarized either by economics concerns, ideological or political opinions, or, the collective behavior leads the population to states in which one part reaches a consensus while the other part behaves in an unstable manner, or it displays a dynamical coexistence of states. It can be argued that such diversity of outcomes is the result of a constant search for achieving simultaneously two different kinds of aims, namely, social and economic aims. On one side, individuals, influenced by others, seek for social acceptance and recognition and on the other side they attempt to get higher gains. Whenever the social and economic concerns take place in two different social networks or environments, the population unavoidably splits into two disjoint target groups. For instance, we can consider a country divided into two regions. Between the regions the habitants search for fulfilling economic aims and inside each region they search for social aims of approval and acceptance.

Here we present a simple model to illustrate such situation in which individuals of a population divided into two groups are dared to coordinate in order to accomplish their social and economic goals. Our framework for studying such kind of population is a two-layer network. Each layer corresponds to a group of the population and the interactions within the group aim to satisfy social concerns, while interactions between agents of different layers aim to satisfy economic concerns. In our system, the economic goal turns out to be reached when agents play the same strategy. Since there will be as many consensus as numbers of possible strategies a coordination problem arises. This situation is an important issue in economics, being analyzed in many theoretical and experimental studies. From the game-theoretical approach this situation has being modeled as a non-cooperative game called coordination game, [26–30]. In our framework, the individuals play a pairwise two-person two-strategy coordination game.

In a social context, there is a wide number of theoretical models and empirical evidences that explain and show how the social influence can lead individuals to modify their behaviors, attitudes or beliefs, and as results, collective behaviors of consensus, polarization, or diversity may arise, [31], [32], [33]. Here, we consider an alternative model of social influence based on the popularity of the strategies instead of the payoffs. Agents search for social goals of acceptance or approval of the strategy they use in their interlayer interactions.

There are a number of studies on population games with binary choices and externalities in discrete time (e.g., [34–36]). Within this literature, an interesting recent contribution by Dal Forno and Merlone [37] considers the dynamical effect in discrete time of a reference group in a system of two-group population. They consider the reference group as a "model" in which the behavior of such group affects the other population's dynamics. Our study follows the two-group population model described in Lugo and San Miguel [38]. Both models study the dynamics of a system of two-group population with binary choices in discrete time and obtain results that can not be obtained in a single isolated system. However, our model differs from Dal Forno and Merlone [37] in several aspects, in particular in two main points. A first one is where the binary choice game takes place. In our model individuals in one population play the two-strategy coordination game with the individuals in the other population, instead of playing a game inside each population as in the model of Dal Forno and Merlone [37]. A second main difference is where the social influence takes place. In our model, it takes place inside each population. In terms of the approach of Dal Forno and Merlone [37], we may say that each group serves as its own reference group.

Despite the simplicity of our model, the accomplishment of social goals can be difficult to achieve because there is skepticism in people to be influenced by the popularity of the opposite strategy of their partners. The previous work of Lugo and San Miguel [38] that considers such population searching for social and strategic objectives shows that for an initial uniform distribution of two possible strategies the skepticism to follow the opposite strategy and the local connectivity are the driving forces to accomplish full coordination for this two-layer network. Here, we consider the role of different initial conditions leading to different asymptotic states of the dynamics and we determine the basin of attraction of these states. As one of our main results, we find two asymptotic states with non-trivial collective behavior which can not be found in a single isolated network analysis. A first outcome is a social analog of a chimera state with coexistence of coherent and incoherent states. In our model, one layer can reach a homogeneous state of full coordination while the other remains in a dynamical state of coexistence of strategies. The second non-trivial asymptotic state is the anticoordination or polarization state in which the system reaches coordination with a different strategy in each layer.

The paper is organized as follows. Section 2 introduces the general frame of our model. Based on a two-layer network, we describe the kind of interactions inside and between layers and the dynamical rule for individuals to update their strategies. Section 3 describes the possible asymptotic solutions of the collective dynamics reached by the system, as well as the basins of attraction to reach these solutions. In particular we describe the non-trivial chimera and anticoordination states and their basins

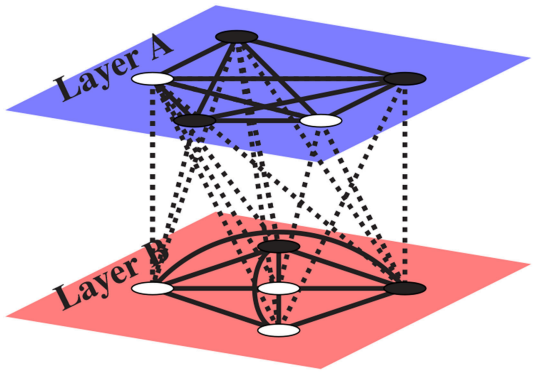

FIGURE 1 | Sketch of a two-layer network. The nodes are connected to each other in a pairwise manner both inside the layers (intralayer links) and across the layers A and B (interlayer links). Dotted lines describe the interlayer interactions and the solid lines describe the intralayer interactions. Black nodes stand for the agents playing strategy L, while white nodes stand for the agents playing strategy R in a coordination game.

of attraction. Section 4 shows bifurcation diagrams, in section 4.1 for the case of a symmetric coordination game and in section 4.2 for the case of an asymmetric coordination game. Finally, section 5 summarizes our conclusions. In the Appendix, we present a mean-field theory for the time evolution of the system in the infinite size limit.

2. METHODS

We consider an individual based model consisting in a population in which individuals interact in two different groups, A and B of sizes N_A and N_B respectively. We take $N_A = N_B = N$. Using the frame of a two-layer network (see **Figure 1**), inside each layer the individuals interact with social objectives and between layers they interact with strategic or economic objectives, as described in the following.

2.1. Interactions Between the Layers: Coordination Games

In Game Theory, the coordination game is a prototype model of a non-cooperative game in which players share the goal of coordinating on any of the feasible actions, [26–30]. It has multiple pure strategy Nash equilibria, and hence, a problem of equilibrium selection arises. In our model, players between the layers play a two-person, two-strategy coordination game.

The strategic interaction proceeds as follows. In each time step, each agent in a layer plays with each agent in the other layer a pairwise coordination game. **Table 1** shows the payoff normal form representation of a coordination game: For example if one agent plays L and the other plays R, the payoff for the former is 0, and $-b$ for the latter. We focus our analysis on two parametric settings, a pure or symmetric coordination game (SCG) in which $s = 0$ and $b = 0$ and a general or asymmetric coordination game (ACG) in which $s = 1$ and $b > 0$. The profiles (L, L) and (R, R) are the two pure strategy Nash equilibria in both settings.

TABLE 1 | Payoff matrix for a two-person, two-strategy coordination game.

	L	R
L	$1, 1$	$0, -b$
R	$-b, 0$	$1+s, 1+s$

A problem of equilibrium selection is present in both settings. In the symmetric coordination game both equilibria are equivalent, in the sense that the payoff of each player for coordinating either on L or R is equal to 1. However, in the general coordination game, the payoff is equal to 2 for coordinating on (R, R) and 1 for coordinating on (L, L). Then, the higher payoff is achieved when agents coordinate on R. The profile (R, R) is the socially efficient solution and it is known in game theory, as the *Pareto (payoff) dominant* equilibrium. However, when $b > 1$, the profile (L, L) becomes the *risk dominant* equilibrium, in the sense of [30]. When players coordinate on (L, L), the cost of a unilateral deviation is $1 + b$ and when they coordinate on (R, R) the cost of a unilateral deviation is 2. The cost of deviation from L to R is greater than the cost of deviation from R to L, if $1 + b > 2$, or equivalently, if $b > 1$. In this case, by the criterion of *risk dominance*, when $b > 1$, the agents select the profile (L, L) since the socially efficient solution (R, R) turns risky. The parameter b becomes a measure of the risk for playing the strategy R. For a complete review, see [29].

2.2. Interactions Inside the Layers: the Effect of Social Pressure

Inside each layer, searching for social acceptance and approval, each agent observes the strategies being played by her partners. An agent may not feel at ease with her strategy when such strategy is not as popular as she wants in her social environment. The level of skepticism in the population is calibrated by a threshold T that determines the effect of the social pressure exerted on an individual. The criterion used by each player i is to measure how well she is doing by comparing the share of agents who are playing the opposite strategy to hers, denoted by d_i, with the threshold $T \in [0, 1]$. We may distinguish two types of populations. *Herding population*, for $T < 0.5$, in which individuals are influenced by low levels of popularity of the opposite strategy, and, *skeptical population*, for $T > 0.5$, where the social pressure has a weak effect on individuals: a feeling of disapproval only arises for high levels of popularity of the opposite strategy. Therefore, when $d_i > T$, the social pressure is effective because player i generates a feeling of non-acceptance about the strategy she is currently playing and she is willing to revise it.

2.3. Inter-layer and Intra-layer Objectives: The Degree of Satisfaction

In the interactions across and inside the layers agents intend to satisfy two different objectives: social objectives of acceptance and approval, and strategic objectives of coordination. These objectives give rise into two different sources of satisfaction: strategic satisfaction in terms of the monetary payoff obtained

TABLE 2 | Degrees of satisfaction according to the fulfilment of social and strategical objectives.

S	P1	P2	U
$\pi_i = (1+s)N$	$\pi_i = (1+s)N$	$\pi_i < (1+s)N$	$\pi_i < (1+s)N$
$d_i < T$	$d_i > T$	$d_i < T$	$d_i > T$

in the coordination game and social satisfaction in terms of the popularity of the current strategies. Therefore, there are four degrees of satisfaction described in **Table 2**, where π_i is the aggregate payoff that agent i in a layer gets playing with all the other agents in the other layer.

The value of s is derived from the parametric setting of the coordination game. When $s = 0$ the equality $\pi_i = N$ shows the total payoff when player i coordinates with all the members of the other layer in the symmetric game. Then we say that agent i is strategically satisfied. In the case of a general coordination game, $s = 1$, an agent is strategically satisfied when the coordination is on the socially efficient solution, i.e., the Pareto dominant strategy. Then, the total payoff is $\pi_i = 2N$. Besides, when $d_i < T$ the share of agents inside the layer of player i who play the same strategy as she does is high enough so the player i feels socially satisfied with her current strategy. This means that her social objectives of acceptance and approval are fulfilled. Then, the level of satisfaction of agent i can be: S (satisfied) when she is both socially ($d_i < T$) and strategically ($\pi_i = (1+s)N$) satisfied, P1 or P2 (partially satisfied) when she is either socially ($d_i < T$) or strategically ($\pi_i = (1+s)N$) satisfied and is U (unsatisfied) when she is both socially ($d_i > T$) and strategically ($\pi_i < (1+s)N$) unsatisfied.

2.4. Learning Dynamics

The learning dynamics in the system is described by the update rule used to change strategy: at each elementary time step each player plays the coordination game with all the members in the other layer. Once the game is over and an aggregate payoff is assigned to each player, each agent observes and measures the popularity of her strategy in her own group. As a result, a level of satisfaction arises. Then, she might change her strategy impelled by her level of satisfaction. The process is repeated setting aggregate payoffs to zero. The synchronous update rule in which each player can change her current strategy according to her level of satisfaction is described as follows,

1. If her level of satisfaction is S, she remains with the same strategy.
2. If her level of satisfaction is P1 or P2, she imitates the strategy of her best performing agent inside the layer in case that such agent has received a larger payoff than the player herself, otherwise she remains with the same strategy.
3. If her level of satisfaction is U, she changes her current strategy.

Although the update rule takes place inside the layers, individuals change their strategies by both social and strategic considerations. The imitation of the best performing individuals in her social environment aims to capture the individual behavior observed in many complex real life situations. This learning dynamics was first implemented in Lugo and San Miguel [38] to study the effect of local interactions on a two-layer network with an initial uniformly distribution of strategies and also, in González-Avella et al. [39] to study the emergence of polarization in a skeptical population for any initial distribution of strategies.

3. RESULTS

3.1. Asymptotic Solutions

Analytical equations for our model and their asymptotic solutions are discussed in the Appendix. For the general case of the asymmetric coordination game these solutions, described below, are the following:

Solution I: Coordination in strategy L: All agents in both layer play strategy L. It is linearly stable and exists for any $T \in [0, 1]$.

Solution II: Coordination in strategy R: All agents in both layer play strategy R. It is linearly stable and exists for any $T \in [0, 1]$.

Solutions III: Coexistence of strategies. These solution exist for any $T \neq 1$ and it occurs in two ways:

(1) unstable fixed points and,
(2) family of marginally stable periodic solutions.

Solutions III-a and III-b: Chimera solutions. This is an interesting case of coexistence of two distinct solutions, namely, solutions I and III. One of the layers goes to the absorbing state of coordination in strategy L, namely layer A for Solution III-a and layer B for solution III-b, while the other layer goes to a dynamical state of coexistence of strategies, solution III type (2). We also find the case of coexistence of two solutions in which one layer coordinates in L and the other layer remains disordered with both strategies coexisting in the same proportion [Solution III type (1)]. Chimera solutions only appear when agents are playing the asymmetric coordination game. They exist for almost any $T < 0.5$ and almost any $b > 0$.

Although the strategies L and R are not equivalent in the asymmetric coordination game because the first is the socially undesired and the second the socially desired outcome, solutions III-a and III-b are equivalent in the sense that the layer reaching the absorbing state L is determined by the initial conditions of strategies in the two layers. We refer to these solutions as chimera states because of the coexistence of an ordered layer and a disordered layer. The disordered layer can be in a dynamical state [solution III (2)] or in a configuration in which the number of agents playing each strategy is equal and constant in time [solution III (1)].

Solutions IV Anticoordination states, layer A coordinates in strategy L while layer B in strategy R.

Solutions V Anticoordination states, layer A coordinates in strategy R while layer B in strategy L.

Solutions IV and V exist and they are linearly unstable and exist for almost all $T \in [0.5, 1]$.

We summarize in **Figure 2** the domain of existence of the different asymptotic solutions for the general case of the asymmetric coordination game as a function of the threshold T

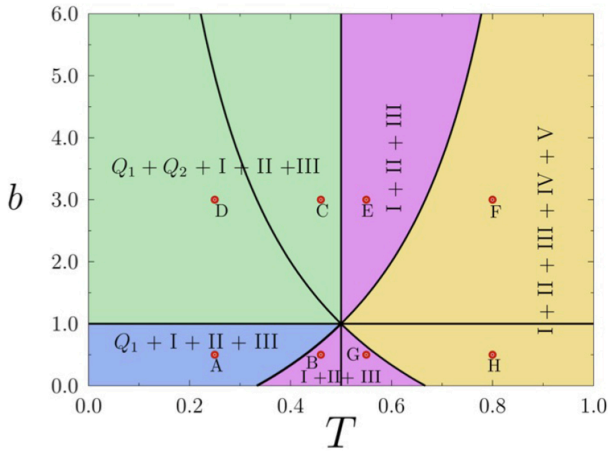

FIGURE 2 | Domain of existence of the different asymptotic solutions in the Asymmetric Coordination Game (ACG) as a function of the threshold T and the risk parameter b as obtained from the analytic solution of the equations discussed in the Appendix. The two curves ($T = \frac{1+b}{3+b}$ and $1 - T = \frac{1+b}{3+b}$) and the two lines ($b = 1$, $T = 0.5$) divide the figure in eight zones from (A) to (H). In each of these zones the asymptotic solutions that exist are indicated. The red dots correspond to values of T and b used in **Figure 5**.

TABLE 3 | Asymptotic states and associated values of x_{aa}, x_{bb}, and n_{AB}.

Asymptotic state	n_{AB}	x_{aa}	x_{bb}	Solution	SCG	ACG
Coordination	0	0	0	I	✓	✓
		1	1	II	✓	✓
Anticoordination	1	0	1	IV	✓	✓
		1	0	V	✓	✓
Coexistence of strategies	$\frac{1}{2}$	$\frac{1}{2}$	$\frac{1}{2}$	III	✓	✓
	$\frac{4(1+b)}{(3+b)^2}$	$\frac{1+b}{3+b}$	$\frac{1+b}{3+b}$		✗	✓
	u+v -2uv	u, 1-u	v, 1-v		✓	✓
Chimera states	v,1-v	0	v, 1-v	III-a	✗	✓
	$\frac{1}{2}$	0	$\frac{1}{2}$		✗	✓
	u, 1-u	u, 1-u	0	III-b	✗	✓
	$\frac{1}{2}$	$\frac{1}{2}$	0		✗	✓

The last two columns indicate existence or non-existence of the state in the Symmetric Coordination Game (SCG) and in the Asymmetric Coordination Game (ACG). The parameter b corresponds to the risk parameter of the ACG and the numbers $u, 1-u$ and $v, 1-v$ for $u, v \in (0, 1)$ describe the family of periodic solutions in layer A and layer B respectively. Chimera states in which the three variables x_{aa}, x_{bb}, and n_{AB} take constant values, either 0 or 1/2, correspond to the case in which the disordered layer is in a solution III (1).

and the risk b parameters. For this general case the parameters of the pay-off matrix take the values $s = 1$ and $b > 0$ for any $T \in [0, 1]$. Asymptotic solutions of the dynamics depend on initial conditions (see below **Figure 5**), and in this sense we refer to Q_1 as those chimera states, solutions III-a and III-b, that are reached from initial conditions such that ${x_{aa}}^0 + {x_{bb}}^0 < 1$, where ${x_{aa}}^0$ and ${x_{bb}}^0$ are the initial conditions for x_{aa} and x_{bb} respectively. Likewise we refer to Q_2 as those chimera states, solutions III-a and III-b, that are reached from initial conditions such that ${x_{aa}}^0 + {x_{bb}}^0 > 1$. It turns out that solutions Q_1 exist for $b > 0$, zones A, C, and D in **Figure 2**, while Q_2 only exist for $b > 1$, zones D and C. The range of values of b and T in which the system reaches solutions Q_1, Q_2, I ,II and III corresponds to zones C and D in the Figure. The difference between zones C and D refers to the areas of the basins of attraction of each solution, as explained in section 3.2. For the case of symmetric coordination game, the parameters take the values $s = 0$ and $b = 0$. The asymptotic solutions in this case are the same as those for the asymmetric coordination game except for Solutions III-a and III-b, the Chimera states. Chimera states could not be found for any level of skepticism in the case of the symmetric coordination game.

Given that the agent population is divided in two layers, A and B, we define x_{aa} as the fraction of individuals playing strategy R in layer A, and x_{bb} as the fraction of individuals playing strategy R in layer B. To describe the different asymptotic solutions we also introduce the order parameter n_{AB} giving the density of inter-layer active links, i.e., the proportion of links connecting agents in different layers with opposite strategies. The order parameter n_{AB} can be written in terms of x_{aa} and x_{bb} by,

$$n_{AB} = x_{aa}(1 - x_{bb}) + x_{bb}(1 - x_{aa})$$

The different solutions described in terms of the asymptotic values of n_{AB}, x_{aa}, and x_{bb} are shown in **Table 3**. These solutions follow from the mean-field analysis described in the Appendix. We next describe these solutions as obtained from numerical simulations. In these simulations, we have fixed the system size $N_A + N_B = 2000$ where $N_A = N_B = 1000$.

Figure 3 shows the time evolution of x_{aa} and x_{bb}, as obtained from the simulation of our individual based model, for different initial conditions that lead to the asymptotic solutions I, II, III, III-a, III-b, IV, and V. **Figures 3A–G** correspond to the symmetric coordination game (SCG), while chimeras states appearing in the asymmetric coordination game (ACG) are shown in **Figures 3H–J**. In **Figures 3A,B** the order parameter $n_{AB} = 0$, indicates that the system goes to an absorbing state in which the agents in both layers play the same strategy. **Figure 3A** shows that after a short transient time the fractions $x_{aa} = x_{bb} = 0$ and the density of inter-layer active links is $n_{AB} = 0$ corresponding to solution I, while for **Figure 3B** after a short transient time the fractions $x_{aa} = x_{bb} = 1$ and $n_{AB} = 0$ corresponding to solution II.

In **Figure 3C** (solution IV) and **Figure 3D** (solution V), the value $n_{AB} = 1$ indicates that in both cases the system goes to an anticoordination absorbing state, i.e., agents in each layer are playing opposite strategies. This state of anticoordination can emerge only in skeptical populations where $T > 0.5$. It is interesting to notice that the layer with an initial higher proportion of R is the layer that ends playing L. A complete analysis of the anticoordination solutions for a skeptical two-group population can be found in González-Avella et al. [39].

It is important to note that there exist absorbing states other than solutions I, II, IV, and V. They correspond to an unstable fixed point $x_{aa} = x_{bb} = r$ of the dynamics for $0 < r < 1$. These solution correspond to the classification (1) of Solution III, namely, $r = 1/2$ in the SCG for all $T \in (0, 1)$ and in the ACG for $T < 1/2$, or the fixed point $r = \frac{1+b}{3+b}$ in ACG when $T > 1/2$.

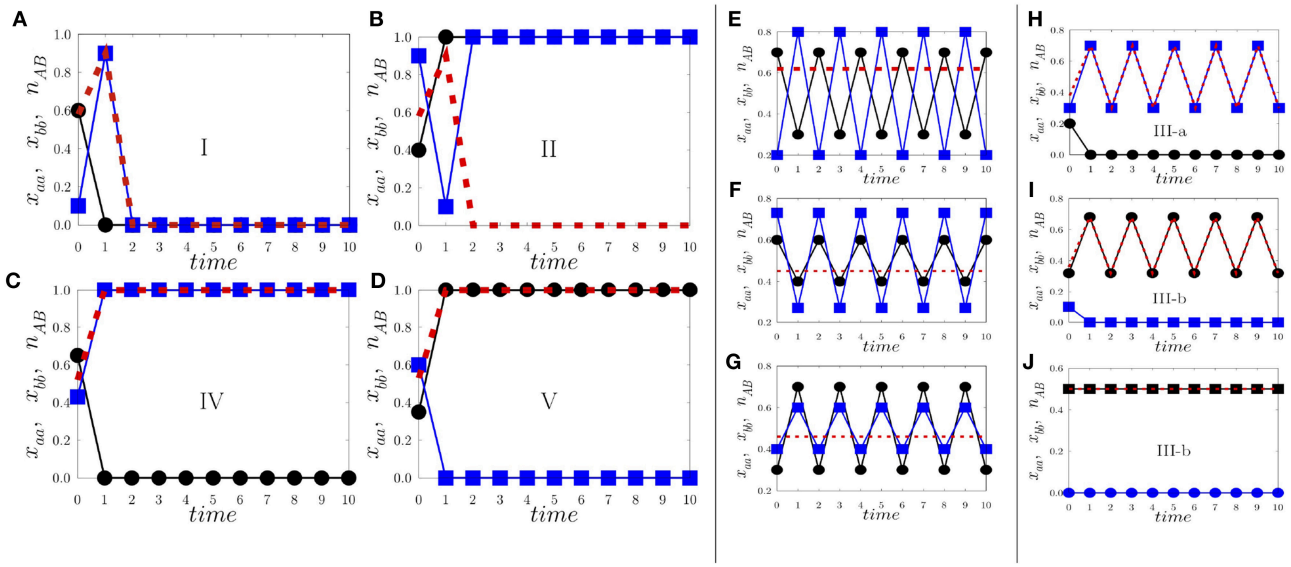

FIGURE 3 | Time evolution of x_{aa} (circles), x_{bb} (squares) and the density of active inter-layer links n_{AB} (dashed lines). **(A–D)** Show the time evolution to coordination (solutions I and II) and anticoordination states (solutions IV and V) for symmetric game ($s = 0, b = 0$) with $T = 0.75$. **(E–G)** Show the phase and anti-phase oscillations [solutions III (2)] of the fraction of strategies x_{aa} and x_{bb} for symmetric game ($s = 0, b = 0$) with $T = 0.25$. **(H–J)** Show the temporal evolution of x_{aa} and x_{bb} and the active inter-layer links n_{AB}, for the asymmetric coordination game ($s = 1, b = 0.5$) with $T = 0.25$. **(H,I)** Show the chimera states, solution III-a and III-b respectively and **(J)** shows the case when the initial and the final states are the same when $x_{aa} = 0$ and $x_{bb} = 0.5$.

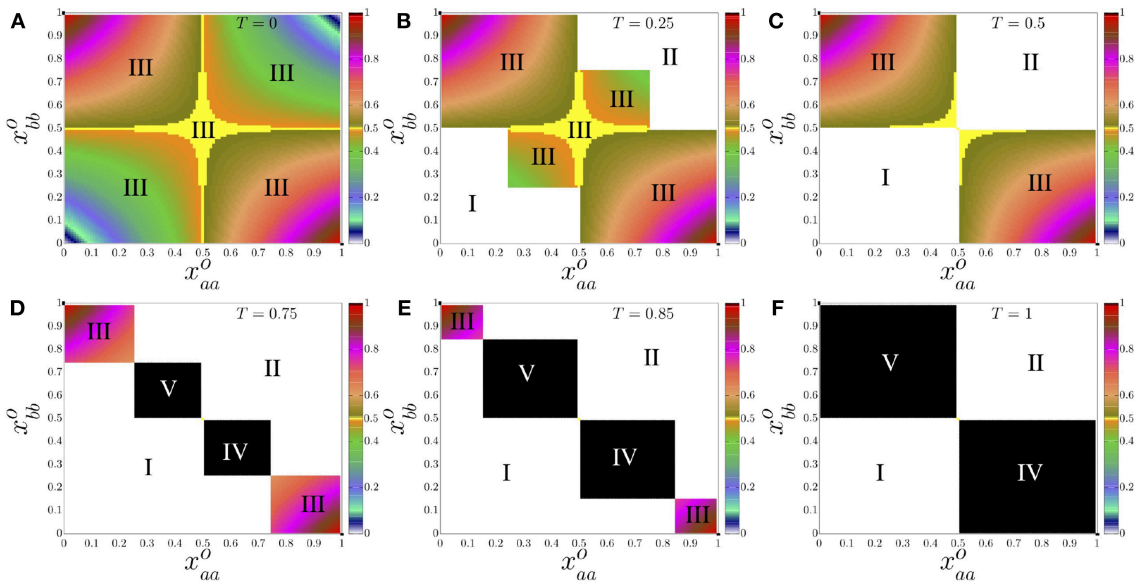

FIGURE 4 | Plot in color scale of the fraction of active links between layer A and B in the asymptotic solution of the dynamics as a function of the initial density of x_{aa} and x_{bb} for the Symmetric Coordination Game ($s = 0$, $b = 0$). The color scale defines the values of the fraction of actives links, $n_{AB} = 1$ black color and $n_{AB} = 0$ white color. Asymptotic solutions are as indicated. **(A–F)** Correspond to different values of T: **(A)** $T = 0$, **(B)** $T = 0.25$, **(C)** $T = 0.5$, **(D)** $T = 0.75$, **(E)** $T = 0.85$, and **(F)** $T = 1$. System size, $N_A + N_B = 1000 + 1000 = 2000$.

Figures 3E–G display the temporal evolution of the system for marginally stable periodic solutions [solutions III (2)] in the case of the symmetric coordination game. The asymptotic dynamical configurations show phase (**Figures 3F,G**) and anti-phase (**Figure 3E**) oscillations of strategies between the two layers. Note that $0 < n_{AB} < 1$ remains constant during these oscillations.

The Chimera solutions are illustrated in **Figures 3H–J** for the ACG with parameter values $T = 0.25$, $b = 0.5$. **Figure 3H** corresponds to a solution III-a, in which all agents play strategy L in layer A, i.e., $x_{aa} = 0$ while a configuration of dynamical coexistence of strategies takes place in layer B, i.e., $0 < x_{bb} < 1$. Note that the fraction of agents that choose to play strategy

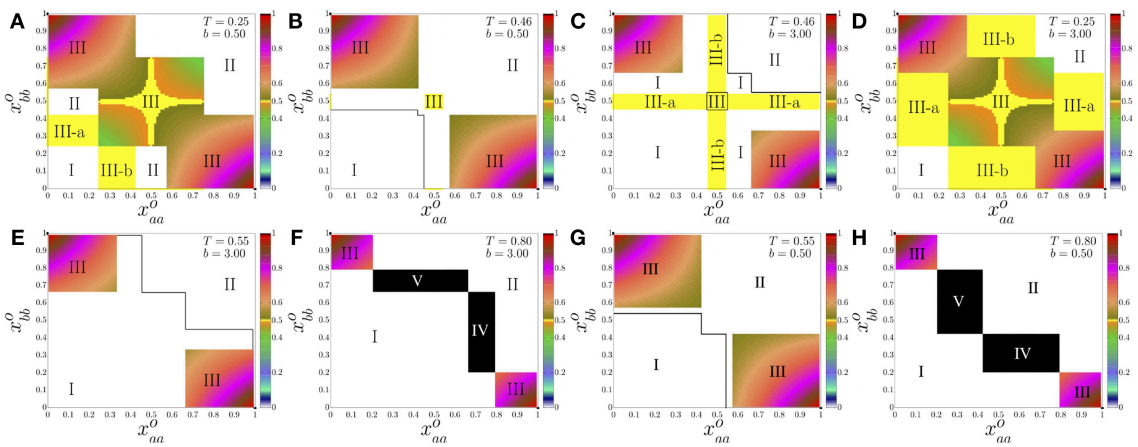

FIGURE 5 | Plot in color scale of the fraction of active links between layer A and B in the asymptotic solution of the dynamics as a function of the initial density of x_{aa} and x_{bb} for the Asymmetric Coordination Game. The color scale defines the values of the fraction of actives links, $n_{AB} = 1$ black color and $n_{AB} = 0$ white color. Asymptotic solutions are as indicated. **(A–H)** Correspond to the values of the threshold T and parameter b indicated by red dots in **Figure 2**. **(A)** $T = 0.25, b = 0.50$, **(B)** $T = 0.46, b = 0.50$, **(C)** $T = 0.25, b = 0.30$, **(D)** $T = 0.25, b = 3.00$, **(E)** $T = 0.55, b = 3.00$, **(F)** $T = 0.80, b = 3.00$, **(G)** $T = 0.55, b = 0.50$, **(H)** $T = 0.80, b = 0.50$. System size, $N_A + N_B = 1000 + 1000 = 2000$.

L or R in layer B changes over time, so that we also observe an oscillation of n_{AB}. **Figure 3I** corresponds to a solution III-b. In this case the behavior is similar to the one in **Figure 3H**, but now the L coordinating absorbing state occurs in layer B, while the dynamical coexistence of strategies appears in layer A. We also notice that possibly similar solutions with $x_{aa} \neq 0$ constant, and x_{bb} oscillating are not found in our model due to the non-equivalence of the L and R strategies in the ACG. In **Figure 3J** we illustrate the particular case of a chimera state in which one layer coordinates in L, in this case layer B, while the other layer remains in a solution III (1) in which agents in that layer start and continue playing for all times both strategies with equal proportions.

The particular collective behaviors described by solutions III-a and III-b, are the social analog of a chimera state arising in two interacting populations of oscillators observed in dynamical systems. In general a chimera state describes a situation where two populations that interact with each other, one exhibits a coherent or synchronized behavior while the other is incoherent or desynchronized. Likewise we have two populations of interacting agents such that one reaches an absorbing state, while the other remains in a dynamically disordered state. The chimera states only arise in our system when the population is *herding* ($T < 0.5$) and play an asymmetric coordination game. This means that beside the initial distribution of strategies, a herding behavior is the underlying mechanism that allows to reach chimera states when the two Nash equilibria of the coordination game are not equivalent in terms of payoff.

3.2. Basins of Attraction: The Global Picture

Depending on the initial conditions for x_{aa} and x_{bb}, the system reaches different asymptotic solutions characterized by their value of the order parameter n_{AB}. Extensive numerical simulations of our individual based model are summarized in **Figures 4**, **5** that show the basins of attraction of the different asymptotic solutions in terms of the initial densities of x_{aa} and x_{bb}, and for different values of the threshold parameter T for the SCG and for different values of T and b for the ACG, respectively. The color code defines the solutions in terms of the fraction of inter-layer active links. Both figures show how the basins of attraction in terms of the initial conditions are determined by the value of the threshold parameter T in the case of the SCG and the threshold T along with the parameter b in the case of the ACG.

4. BIFURCATION DIAGRAMS

In this section we consider possible transitions among the different solutions discussed before. These transitions are described by means of bifurcations diagrams obtained in terms of the control parameters T and b.

4.1. Symmetric Coordination Game

We have shown in the previous section that the solution obtained for the SCG, and for a fixed initial condition, depends on the value of the threshold parameter T, so that by varying T we find transitions among those solutions. Examples of these transitions are shown in **Figures 6A–C**. These are bifurcation diagrams that give the average of the fractions of inter-layer active links n_{AB} or $1 - n_{AB}$ as a function of the threshold T. These bifurcation diagrams describe transitions that occur, for threshold values of T, between solutions III to I, III to V, and I to V, respectively for different fixed values of the initial conditions. Each panel shows two examples. We also find subsequent transitions among three solutions. For instance, the bifurcation diagram **Figure 7A** for the average of n_{AB}, illustrates a first transition between solution III and solution I, followed by a second transition between I and V as T increases. These results show the effect of the

skepticism on the collective behavior in a two-layer network. Tuning the level of skepticism from the limit value $T = 0$, where the population is extremely *herding* to the limit value $T = 1$ where the population is extremely *skeptical*. **Figure 4** indicates that the system goes from a state of complete coexistence of strategies, Solution III for almost all initial conditions, to states of anticoordination, Solutions IV and V, and states of global coordination, Solutions I and II.

4.2. Asymmetric Coordination Game

As discussed before, **Figure 2** shows for the ACG case a phase diagram, obtained from a mean field theoretical approach, indicating domains of existence of different asymptotic solutions in the b - T parameter space. In comparison with the SCG case, the additional parameter b allows for new transitions that occur for a threshold value of b and fixed T, including transition to chimera states. Examples of these transitions are shown in **Figures 6D–G**. **Figure 6D** shows a transition between a state of anticoordination IV and a state of full coordination I and **Figure 6G** shows a transition between a state of full coordination II and a state of anticoordination V, while **Figures 6E,F** show transitions between a state of coordination II or dynamical coexistence III and a chimera state III-a. On the other hand, **Figure 7B** shows an example of subsequent transitions as T increases for fixed $b = 3$, with a first transition between a state of dynamical coexistence III and a chimera state III-a, followed by a transition between III-a and a state of full coordination II and a final transition between II and a state of anticoordination IV.

A different form of bifurcation diagrams can be obtained by considering the area of the basin of attraction of a given solution in the parameter space of the initial conditions ${x_{aa}}^0$ and ${x_{bb}}^0$. Results for this area are indicated in **Table 4** for the chimera states Q_1 and Q_2 and the different zones of the T-b parameter space of **Figure 2**. We recall that Q_1 are those solutions III-a and III-b reached from initial conditions such that ${x_{aa}}^0 + {x_{bb}}^0 < 1$, while Q_2 are those obtained when ${x_{aa}}^0 + {x_{bb}}^0 > 1$. The areas of the basins of attractions A_{Q_1}, A_{Q_2} for Q_1 and Q_2 respectively are plotted vs. T and b in **Figure 8**. Using A_{Q_1}, A_{Q_2} as order parameters, these figures show bifurcation diagrams for the transition from existence $A_Q \neq 0$ to non-existence $A_Q = 0$ of a chimera state.

Figures 8A,B show a threshold value $T = 0.5$, so that chimera states exist for $T < 0.5$ in agreement with the phase diagram of **Figure 2**. They also show that as T increases the areas of the basin of attraction of chimera states first increase until a certain value of T and then they decrease to become zero for $T = 0.5$. In addition **Figures 8C,D** identify a threshold value of b for the existence of chimera states. For Q_2 chimeras this is fixed at $b = 1$ independently of T, while for Q_1 it depends on T, with Q_1 chimera states existing for all values of b and T small enough. For both Q_1 and Q_2 we also identify a characteristic T-dependent value of b beyond which the area of the basin of attraction remains constant.

More generally and on a qualitative basis, it follows from **Figures 4**, **5** that, for any fixed b, the basins of attraction of solution III and chimeras states disappear as T increases, so that and in the limiting case of $T = 1$, only Solutions I, II, IV and V can be reached by the system. Another interesting limiting case is the one of the risk parameter $b \to \infty$, where it is extremely *risky* to play strategy R. It can be expected that in this limit solution I becomes preponderant. Indeed, we show in **Figure 9**, as compared with **Figure 5**, that the basin of attraction of solution I increases, solution II disappears and solution III and chimeras remain for fixed values of $T < 0.5$. When both parameters b and T increase, solutions II, III, IV, and V disappear and the basin of attraction of solution I increases. In the limit case, $T = 1$ and $b \to \infty$, solution I becomes the main solution in the system for almost every initial condition.

TABLE 4 | Areas of the basin of attraction of chimera states in the parameter space of initial conditions of x_{aa} and x_{bb} according to the zones described in **Figure 2**.

Zones	Ranges	A_{Q_1}	A_{Q_2}
A	$T < \frac{1+b}{3+b} < 0.5$	$2\left(\frac{1+b}{3+b} - T\right)T$	0
B	$\frac{1+b}{3+b} < T < 0.5$	0	0
C	$1 - \frac{1+b}{3+b} < T < 0.5$	$2(1-2T)T$	$2(1-2T)T$
D	$T < 1 - \frac{1+b}{3+b} < 0.5$	$2\left(\frac{1+b}{3+b} - T\right)T$	$2\left(2\frac{1+b}{3+b} - 1\right)T$

5. CONCLUSIONS

We have considered a model of evolutionary game of a population divided into two groups where individuals are searching to fulfil their social and strategic objectives. The frame for this situation has been a multilayer network of two layers. Interactions within each layer aim to fulfill social objectives associated with learning dynamics, while interactions across layer consist in a coordination game, therefore involving strategic objectives. Our analysis, based on a mean-field theoretical approach and corroborated by numerical simulations of the model, reveals the existence of collective behaviors commonly observed on nature but impossible to find on a single isolated network analysis. In our multilayer framework we find states different of those of global coordination or dynamical states of coexistence of the strategies. Namely, in the multilayer coordination challenge, anticoordination and chimera states solution emerge. In the former the dynamics of the system polarizes the population, with each layer coordinating in a different strategy. This can also happen in the asymmetric coordination game where the two strategies correspond to different Nash equilibria: the socially efficient or Pareto dominant, and the risk dominant equilibrium. In the chimera states one layer coordinates in the risk dominant equilibrium, while the second remains disordered, that is with coexistence of the two strategies. This coexistence can be time independent or in the form of periodic solutions.

In connection with the standard notion of chimera states in two populations of dynamical oscillators having global or long range interactions [2, 8, 14, 40], we note that in our evolutionary game theory framework we also have the basic ingredients of two non-linear dynamical systems which are globally coupled.

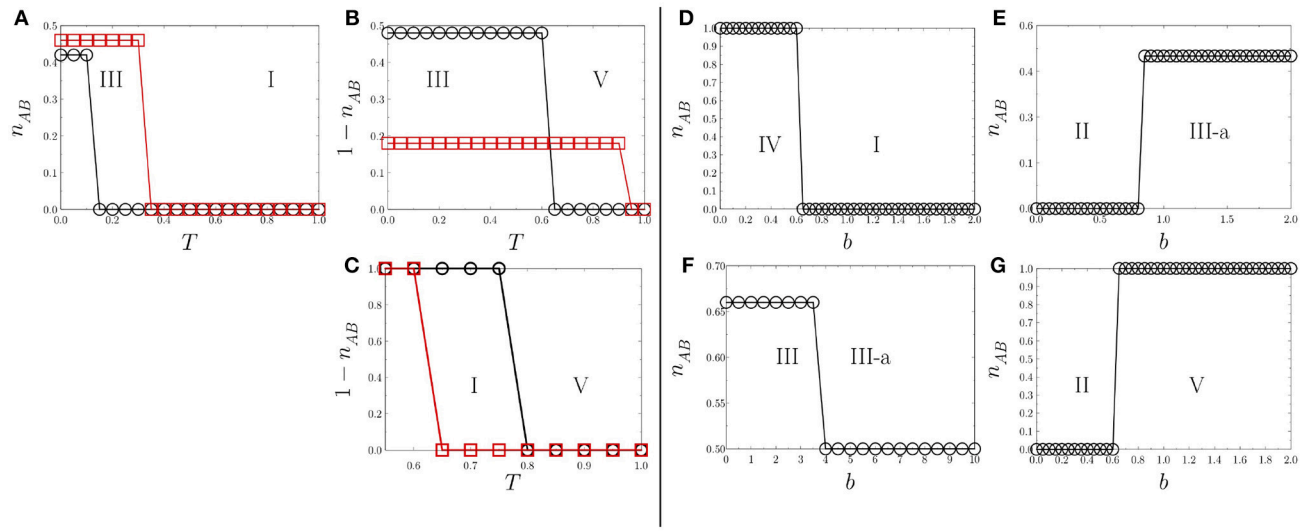

FIGURE 6 | Bifurcation diagrams for the average of n_{AB} as function of T for fixed initial conditions for the SCG, **(A–C)**, and for the ACG, **(D–G)**. **(A):** $x_{aa} = 0.40$ and $x_{bb} = 0.10$ (circles), $x_{aa} = 0, 40$ and $x_{bb} = 0.30$ (squares). **(B):** $x_{aa} = 0.40$ and $x_{bb} = 0.60$ (circles), $x_{aa} = 0, 10$ and $x_{bb} = 0.90$ (squares). **(C):** $x_{aa} = 0.25$ and $x_{bb} = 0.51$ (circles), $x_{aa} = 0, 37$ and $x_{bb} = 0.52$ (squares). **(D):** $x_{aa} = 0.30$ and $x_{bb} = 0.45$ with $T = 0.75$. **(E):** $x_{aa} = 0.10$ and $x_{bb} = 0.48$ with $T = 0.15$. **(F):** $x_{aa} = 0.25$ and $x_{bb} = 0.1$ with $T = 0.7$. **(G):** $x_{aa} = 0.45$ and $x_{bb} = 0.65$ with $T = 0.75$.

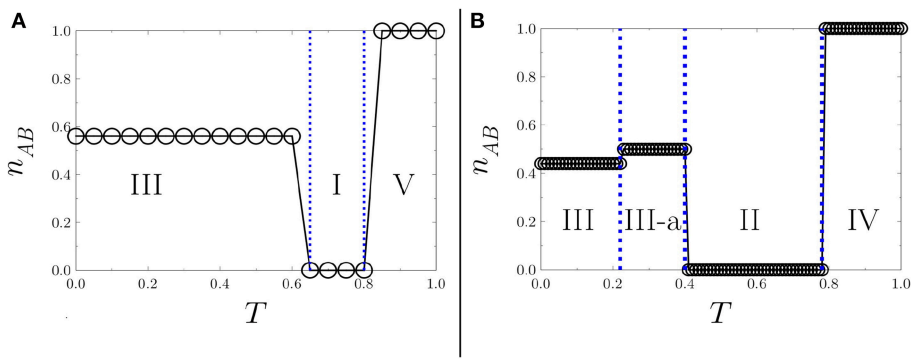

FIGURE 7 | (A): Bifurcation diagram among solutions III, I, and V of the average of n_{AB} as function of T in the SCG for a fixed initial condition $x_{aa} = 0.20$ and $x_{bb} = 0.60$. **(B):** Bifurcation diagram among solutions III, III-a, II, and IV of the average of n_{AB} as function of T for a fixed initial condition $x_{aa} = 0.78$ and $x_{bb} = 0.60$ where the risk parameter $b = 3$ in the ACG.

In chimera states of coupled oscillators, one population is in a coherent state and coexists with the other population in an incoherent state. In our social analog of the chimera state we have interpreted the coordination states in one layer as a coherent or ordered state, while we identify the incoherent state with the layer that exhibits coexistence of the two strategies. In most cases this coexistence is of dynamical nature, being the disordered layer in an active dynamical state of oscillation between the two possible strategies. Our model only incorporates two possible individual states of the agents, but we envisage that in social models including more individual states or strategies, such as those in reference [21, 22], the disordered state would show a richer dynamical behavior, since the individual elements can dynamically visit a large number of possible states. In this case the disordered or incoherent population would have a dynamical behavior similar to those found in populations of dynamical oscillators.

We observe chimera states only for the asymmetric coordination game where the coherent state reached is in the socially least desired coordination state. For herding individuals, the presence of a degree of risk in coordinating on the socially efficient outcome has an effect on the emergence of chimera states. However, for skeptical individuals, the anticoordination states are present in both symmetric and asymmetric coordination games. While the presence of two layers in the network is a consequence of the type of interaction that individuals have inside and across the layers, the actual factors that play a key role for the existence of chimera and

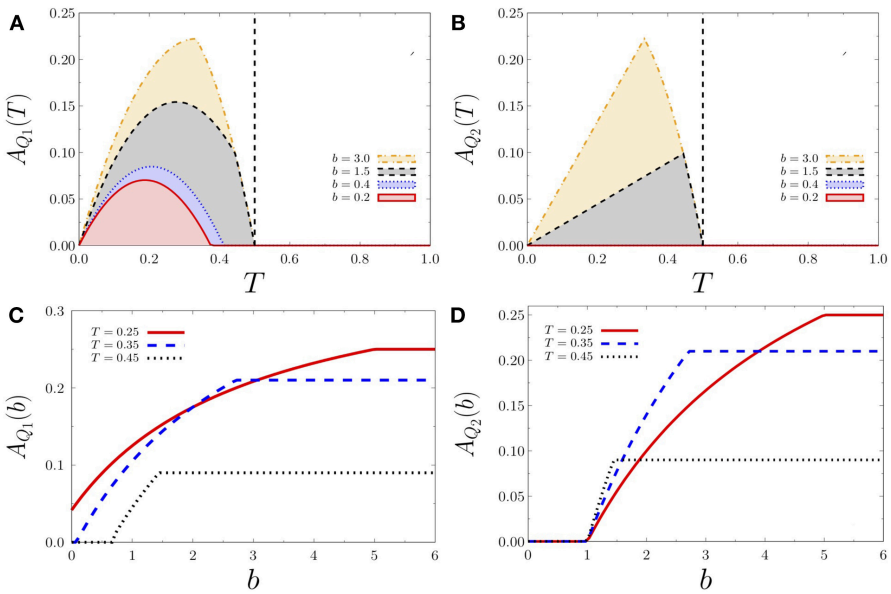

FIGURE 8 | Sizes of the basins of attraction of chimera states categorized by Q_1 and Q_2, denoted by A_{Q_1} and A_{Q_2}, as function of T for different values of b **(A,B)** and as function of b for different values of T **(C,D)**.

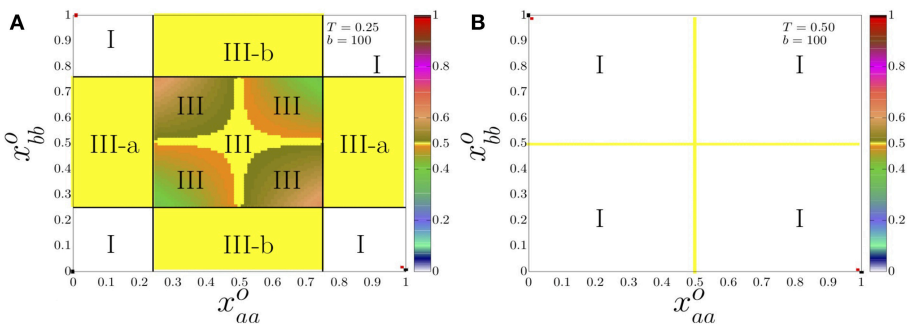

FIGURE 9 | Plot in color scale of the fraction of active links between layer A and B in the asymptotic solution of the dynamics as a function of the initial density of x_{aa} and x_{bb} for the Asymmetric Coordination Game. The color scale defines the values of the fraction of actives links, $n_{AB} = 1$ black color and $n_{AB} = 0$ white color. Asymptotic solutions are as indicated. **(A):** $b = 100$, $T = 0.25$, and **(B):** $b = 100$, $T = 0.50$.

anticoordination states are the level of skepticism and the existence of a risk parameter on the coordination game.

In the context of coordination in social systems, our contribution brings a more realistic insight about the consequences of a collective behavior that makes a distinction between social and strategic objectives. This collective behavior may lead herding societies to chimera states and skeptical societies to polarized states of anticoordination.

AUTHOR CONTRIBUTIONS

All authors conceived the study and designed the numerical simulations, HL and JG-A performed the numerical and analytical calculations, all authors analyzed the results, wrote, and reviewed the paper.

ACKNOWLEDGMENTS

HL acknowledges financial support from Ministerio de Economía y Competitividad (Spain) under Project No. ECO2016-75992-P. MS acknowledges financial support from Agencia Estatal de Investigación (AEI, Spain) and Fondo Europeo de Desarrollo Regional under Project ESoTECoS Grant No. FIS2015-63628-C2-2-R (AEI/FEDER,UE) and the Spanish State Research Agency, through the María de Maeztu Program for Units of Excellence in R&D (MDM-2017-0711).

SUPPLEMENTARY MATERIAL

The Supplementary Material for this article can be found online at: https://www.frontiersin.org/articles/10.3389/fams.2019.00016/full#supplementary-material

REFERENCES

1. Kuramoto Y, Battogtokh D. Coexistence of coherence and incoherence in nonlocally coupled phase oscillators. *Nonlinear Phenom Complex Syst.* (2002) **5**:380–5.
2. Abrams DM, Strogatz SH. Chimera states for coupled oscillators. *Phys Rev Lett.* (2004) **93**:174102. doi: 10.1103/physrevlett.93.174102
3. Martens EA, Panaggio MJ, Abrams DM. Basins of attraction for chimera states: fast track communication. *New J Phys.* (2016) **18**:022002. doi: 10.1088/1367-2630/18/2/022002
4. Rakshit S, Bera BK, Perc M, Ghosh D. Basin stability for chimera states. *Sci Rep.* (2017) **7**:2412. doi: 10.1038/s41598-017-02409-5
5. Suda Y, Okuda K. Persistent chimera states in nonlocally coupled phase oscillators. *Phys. Rev. E* (2015) **92**:060901. doi: 10.1103/sphysreve.92.060901
6. Panaggio MJ, Abrams DM. Chimera states: coexistence of coherence and incoherence in networks of coupled oscillators. *Nonlinearity*(2015) **28**:R67–87. doi: 10.1088/0951-7715/28/3/r67
7. Kundu S, Majhi S, Bera BK, Ghosh D, Lakshmanan, M. Chimera states in two-dimensional networks of locally coupled oscillators. *Phys Rev E.* (2018) **97**:022201. doi: 10.1103/PhysRevE.97.022201
8. Omelchenko I, Maistrenko Y, Hovel P, Scholl E. Loss of coherence in dynamical networks: spatial chaos and chimera states. *Phys Rev Lett.* (2011) **106**:234102. doi: 10.1103/physrevlett.106.234102
9. Hizanidis J, Kouvaris Nikos E, Zamora-López G, Díaz-Guilera A, Antonopoulos CG. Chimera-like states in modular neural networks. *Sci Rep*. (2016) **6**:19845. doi: 10.1038/srep19845
10. Banerjee T, Dutta PS, Zakharova A, Schöll E. Chimera patterns induced by distance-dependent power-law coupling in ecological networks. *Phys Rev E.* (2016) **94**:032206. doi: 10.1103/PhysRevE.94.032206
11. Röhm A, Böhm F, Lüdge K. Small chimera states without multistability in a globally delay-coupled network of four lasers. *Phys Rev E.* (2016) **94**:042204. doi: 10.1103/PhysRevE.94.042204
12. Bastidas VM, Omelchenko I, Zakharova A, Schöll E, Brandes T. Quantum signatures of chimera states. *Phys Rev E.* (2015) **92**:062924. doi: 10.1103/PhysRevE.92.062924
13. Viennot D, Aubourg L. Quantum chimera states. *Phys Lett A*. (2016) **380**:678. doi: 10.1016/j.physleta.2015.11.022
14. Tinsley MR, Nkomo S, Showalter S. Chimera and phase-cluster states in populations of coupled chemical oscillators. *Nat Phys*. (2012) **8**:662–5. doi: 10.1038/nphys2371
15. Nkomo S, Tinsley MR, Showalter K. Chimera states in populations of nonlocally coupled chemical oscillators *Phys Rev Lett*. (2013) **110**:244102. doi: 10.1103/PhysRevLett.110.244102
16. Rattenborg NC, Amlaner CJ, Lima SL. Behavioral, neurophysiological and evolutionary perspectives on unihemispheric sleep. *Neurosci Biobehav Rev*. (2000) **24**:817–42. doi: 10.1016/S0149-7634(00)00039-7
17. Laing CR, Chow CC. Stationary bumps in networks of spiking neurons. *Neural Comput*. (2001) **13**:1473. doi: 10.1162/089976601750264974
18. Sakaguchi H. Instability of synchronized motion in nonlocally coupled neural oscillators. *Phys Rev E*. (2006) **73**:031907. doi: 10.1103/PhysRevE.73.031907
19. Panaggio MJ, Abrams DM. Chimera states: coexistence of coherence and incoherence in networks of coupled oscillators. *Nonlinearity* (2015) **28**:R67. doi: 10.1088/0951-7715/28/3/R67
20. Yao N, Zheng Z. Chimera states in spatiotemporal systems: theory and applications. *Int J Mod Phys*. (2016) bf B30:1630002 . doi: 10.1142/S0217979216300024
21. González-Avella JC, Cosenza MG, San Miguel M. A model for cross-cultural reciprocal interactions through mass media *PLOS ONE*. (2012) **7**:e51035. doi: 10.1371/journal.pone.0051035
22. González-Avella JC, Cosenza MG, San Miguel M. Localized coherence in two interacting populations of social agents. *Physica A*. (2014) **399**:24–30. doi: 10.1016/j.physa.2013.12.035
23. Axelrod R. The dissemination of culture: a model with local convergence and global polarization. *J Conflict Res*. (1997) **41**:203–26. doi: 10.1177/0022002797041002001
24. Deffuant D, Neau F, Amblard G. Weisbuch. Mixing beliefs among interacting agents. *Adv Complex Syst*. (2000) **3**:87–98. doi: 10.1142/S0219525900000078
25. González-Avella JC, Eguíluz VM, Marsili M, Vega-Redondo F, San Miguel M. Threshold learning dynamics in social networks. *PLoS ONE.* (2011) **6**:e20207. doi: 10.1371/journal.pone.0020207
26. Ellison G. Learning, local interaction, and coordination. *Econometrica.* (1993) **61**:1047–71. doi: 10.2307/2951493
27. Vega-Redondo F. *Economics and the Theory of Games*. Cambridge: Cambridge University Press (2003).
28. Goeree JK Holt CA. Coordination games. In: *The Encyclopedia of Cognitive Science*, Vol 2. L. Nagel, ed., London: Nature Publishing Group; McMillan (2002). p. 204–8.
29. Weidenholzer S. Coordination games and local interactions: a survey of the game theoretic literature. *Games.* (2010) **1**:551–85. doi: 10.3390/g1040551
30. Harsanyi J, Selten R. *A General Theory of Equilibrium Selection in Games*.Cambridge, MA: The MIT Press (1988).
31. Flache A, Mas M, Feliciani T, Chattoe-Brown E, Deffuant G, Huet S, et al. Models of social influence: towards the next frontiers. *J Artif Soc Soc Simul.* (2017) **20**:2. doi: 10.18564/jasss.3521
32. Flache A, Macy MW. Local convergence and global diversity: from interpersonal to social influence. *J. Conflict Resol.* (2011) **55**:970–95. doi: 10.1177/0022002711414371
33. Friedkin NE, Johnsen EC. *Social Influence Network Theory*. New York, NY: Cambridge University Press (2011).
34. Bischi GI, Merlone U. Global dynamics in binary choice models with social influence. *J Math Sociol.* (2009) **33**:277–302. doi: 10.1080/00222500902979963
35. Bischi, GI, Gardini L, Merlone U. Impulsivity in binary choices and the emergence of periodicity. *Discrete Dyn Nat Soc.* **2009**:407913. doi: 10.1155/2009/407913
36. Dal Forno A, Merlone U. Heterogeneous society in binary choices with externalities. *Dyn Games Appl.* (2018). p. 1–25. doi: 10.1007/s13235-018-0270-x
37. Dal Forno A, Merlone U. Reference group influence on binary choices dynamics. *Decisions Econ Finan.* (2018). **41**:427–45. doi: 10.1007/s10203-018-0216-1
38. Lugo H, San Miguel M. Learning and coordinating in a multilayer network. *Sci. Rep.* (2015) **5**:7776. doi: 10.1038/srep07776
39. González-Avella JC, Lugo H, San Miguel M. Coordination in a skeptical two-group population. *J Econ Interact Coord.* (2018) **14**:203–14. doi: 10.1007/s11403-018-0223-x
40. Laing CR. Chimeras in networks of planar oscillators. *Phys Rev E.* (2010) **81**:066221. doi: 10.1103/PhysRevE.81.066221

Conflict of Interest Statement: The authors declare that the research was conducted in the absence of any commercial or financial relationships that could be construed as a potential conflict of interest.

Advantages of publishing in Frontiers

OPEN ACCESS
Articles are free to read for greatest visibility and readership

FAST PUBLICATION
Around 90 days from submission to decision

HIGH QUALITY PEER-REVIEW
Rigorous, collaborative, and constructive peer-review

TRANSPARENT PEER-REVIEW
Editors and reviewers acknowledged by name on published articles

Frontiers
Avenue du Tribunal-Fédéral 34
1005 Lausanne | Switzerland

Visit us: www.frontiersin.org
Contact us: info@frontiersin.org | +41 21 510 17 00

REPRODUCIBILITY OF RESEARCH
Support open data and methods to enhance research reproducibility

DIGITAL PUBLISHING
Articles designed for optimal readership across devices

FOLLOW US
@frontiersin

IMPACT METRICS
Advanced article metrics track visibility across digital media

EXTENSIVE PROMOTION
Marketing and promotion of impactful research

LOOP RESEARCH NETWORK
Our network increases your article's readership